Analysis of the ballistic responses of the fibres of woven material at the microscopic scale based on numerical homogenization

Quoc Hoan Pham

No d'ordre : 109224

UNIVERSITÉ DE LILLE

UNITÉ DE MÉCANIQUE DE LILLE

ÉCOLE DOCTORALE SCIENCES POUR L'INGÉNIEUR (SPI)

Rapport de thèse pour l'obtention du grade de

Docteur de l'Université de Lille

Spécialité : Mécanique, énergétique, génie des procédés, génie civil

Présente par

Quoc Hoan PHAM

Sujet de thèse :

Analyse des réponses balistiques des fibres d'un matériau tissé à l'échelle microscopique basée sur l'homogénéisation numérique

Analysis of the ballistic responses of the fibres of woven material at the microscopic scale based on numerical homogenization

---

Date de soutenance : le 29 janvier 2021

M. A. SAOUAB, Professeur	Université de Havre	Président du jury
M. J.F. FERRERO, Professeur	Université Toulouse III	Rapporteur
Mme N. BAHLOULI, Professeure	Université de Strasbourg	Rapporteuse
M. L. RABET, Professeur	Ecole Royale Militaire, Bruxelles	Examinateur
M. A. IMAD, Professeur	Université de Lille	Directeur de thèse
M. T. KANIT, MCF-HDR	Université de Lille	Co-directeur
M. C. HA-MINH, MCF	ENS Paris-Saclay	Invité

Remerciements

Je voudrais remercier vivement le Professeur Abdellatif IMAD qui a dirigé cette thèse. Il m'a soutenu, suivi et a su orienter mes recherches tout au long de ma thèse.

Je tiens particulièrement à remercier Monsieur Toufik KANIT pour ces années de travail. Il a su me donner la liberté nécessaire pour accomplir mon travail tout en gardant un œil critique et informé. Sa disponibilité et ses pertinents conseils ont contribué indéniablement à l'aboutissement de ces travaux.

Mes remerciements vont à Monsieur Cuong HA-MINH et Monsieur Tuan Long CHU qui ont co-supervisé cette thèse. Leurs contributions m'ont été d'une aide précieuse.

Je voudrais exprimer ma gratitude à Madame Nadia BAHLOULI et à Monsieur Jean-François FERRERO pour avoir accepté de rapporter sur le manuscrit. Je tiens également à remercier Monsieur Abdelghani SAOUAB pour avoir présidé le jury de soutenance. Je remercie Monsieur Luc RABET pour examiner mon travail. Leur présence parmi les membres de jury m'a fait un grand plaisir.

Un grand merci à Shafiq, Rachid, Moussa, Essosnam et Nada qui m'ont aidé dans la partie sur l'homogénéisation; particulièrement pour leur esprit chaleureux et leur grande patience. Merci beaucoup mes amis!

Je remercie également toutes les personnes avec lesquelles j'ai travaillé: Lionel, Muzzamal, Karim, Amine, Reda ainsi que tous les chercheurs, enseignants et personnels administratifs de mon laboratoire. Sans toutefois oublier Mouna, Nesrine, Hajar, Amani et les doctorants que j'ai rencontrés pendant les séjours scientifiques.

Enfin, je réserve un merci tout particulier à ma chère famille qui m'a soutenu pendant toutes ces années. Je leur envoie tout l'amour du monde.

Résumé

Analyse des réponses balistiques des fibres d'un matériau tissé à l'échelle microscopique basée sur l'homogénéisation numérique

Cette thèse est consacrée à l'étude du comportement balistique d'un matériau tissé en utilisant une approche microscopique basée sur la technique d'homogénéisation numérique. En effet, lors d'un chargement balistique, le projectile agit localement sur la zone affectée du tissu engendrant ainsi une compression transversale des fibres. Ce phénomène a été modélisé, à l'échelle des fibres, en prenant en compte les effets des interactions fibre-fibre et l'évolution de la fraction volumique d'un fil au cours du chargement. Cette modélisation a conduit à établir une loi de comportement mécanique non-linéaire décrivant l'évolution des contraintes et des déformations apparentes dans un fil soumis à une compression transversale. La technique d'homogénéisation numérique, basée sur un volume élémentaire représentatif (VER) périodique, a été utilisée en vue d'une modélisation prenant en compte le vide entre les fibres. Cette démarche a conduit à établir une loi puissance entre la déformation apparente et la fraction volumique pour un fil sollicité en compression transversale. La technique d'homogénéisation numérique a également été utilisée pour analyser le comportement microscopique des fibres soumises à un impact balistique selon une approche multi-échelle. La notion de fibre équivelante représentant un ensemble de fibres a été introduite afin de gagner du temps de calcul. Cette analyse a conduit à une meilleure compréhension des phénomènes physiques se produisant lors d'un impact balistique d'un fil à l'échelle des fibres. Ensuite, cette modélisation a été appliquée au cas d'un tissu soumis à un impact balistique à une échelle mésoscopique (échelle d'un fil) combinée à une échelle microscopique (échelle d'une fibre) dans la zone affectée par l'impact. Cette modélisation a été validée par confrontation avec des données expérimentales, en termes de l'évolution la vitesse du projectile. Les évolutions de l'énergie, de la force d'impact, des interactions fibres-fibres et de la rupture locale des fibres ont été aussi analysées.

Abstract

Analysis of the ballistic responses of the fibres of woven material at the microscopic scale based on numerical homogenization

This thesis is dedicated to the study of the ballistic behaviour of woven material using a microscopic approach based on the numerical homogenization technique. Indeed, during ballistic impact, the projectile locally strikes the fabric on the impact zone, thus generating a transverse compression of the fibres. This phenomenon has been modelled, at the fibre scale, taking into account the effects of fibre-fibre interactions and the evolution of the volume fraction of yarn during loading. From this modelling, a non-linear mechanical behaviour law describing the evolution of apparent stress and strain in a yarn subjected to transverse compression was obtained. Then, based on a periodic Representative Volume Element (RVE), a numerical homogenization technique taking into account the void between fibres was used for modelling. A power law between the apparent deformation and the volume fraction for a yarn subjected to transverse compression was deduced based on this approach. Numerical homogenization technique was also utilised to analyse the microscopic behaviour of fibres subjected to ballistic impact based on a multi-scale approach. The notion of an equivalent fibre representing a set of fibres was introduced in order to gain computation time. The analysis has provided a better understanding of the physical phenomena occurring during the ballistic impact of one single yarn at the fibre scale. Then, this model was applied to the case of one fabric subjected to ballistic impact at a mesoscopic scale (yarn scale) combined with a microscopic scale (fibre scale) in the impact zone. This model was validated by comparison with experimental data, in terms of the evolution of projectile velocity. The evolution of energy, impact force, fibre-fibre interactions and local fibre failure are also analysed.

Table of contents

List of figures

List of tables

Introduction générale

Contexte de l'étude

La problématique de l'impact balistique introduit des phénomènes complexes du fait d'une forte interaction entre le projectile, la protection et la cible. Dans la littérature, plusieurs études expérimentales, analytiques et numériques ont été réalisées. Ces travaux de recherche ont porté essentiellement sur les performances balistiques des protections en vue d'assurer leur allégement et leur résistance mécanique. On note aussi, l'intérêt porté au comportement dynamique des projectiles dans l'objectif de mieux cerner à la fois les matériaux utilisés ainsi que leurs morphologies. Quant aux cibles, des études antérieures ont porté sur l'utilisation des matériaux témoins tels que la gélatine ou la plasticine pour simuler le corps humain dans le cadre des investigations expérimentales. Mais, la plupart des nombreux travaux de recherche a porté sur l'étude des performances balistiques des protections. En effet, le choix des matériaux utilisés pour une meilleure protection des cibles constitue un souci permanent. Dans ce domaine, on note l'utilisation d'une diversité de matériaux pour la protection balistique tels que les matériaux composites et les multi-matériaux (granulats, céramiques, etc.).

Mais, l'emploi des équipements souples de protection constitue une part importante dans les travaux de recherche antérieurs. En effet, les matériaux tissés utilisant des fibres de haute performance font l'objet de plusieurs investigations, tels que les fibres de Kevlar, Twaron, etc. Des approches expérimentale, analytique et numérique ont été développées en vue d'une caractérisation mécanique des textiles soumis à un chargement balistique. La compréhension et la maîtrise de la chronologie et des mécanismes de dommage constituent un des objectifs essentiels. La performance balistique est évaluée à partir de la situation de la perforation ou non-perforation des tissus lors de l'impact. La complexité de la mise en œuvre des essais expérimentaux a conduit manifestement au recours à l'utilisation de la modélisation numérique. Cette voie de recherche a été encouragée par le développement des moyens de calculs. On note un nombre important de travaux déjà publiés portant sur le développement de modèles numériques pour la description et la prédiction de la tenue mécanique des tissus soumis à un impact balistique. A ce stade, nous pouvons classer les modèles numériques à partir de l'échelle d'analyse retenue, à savoir :

- Une modélisation macroscopique qui est développée à l'échelle du tissu.
- Une modélisation mésoscopique qui s'inscrit à l'échelle du fil.
- Une modélisation microscopique à l'échelle d'une fibre
- Une modélisation multi-échelle : Macro/Méso (tissu/fil) ou Méso/Micro (fil/fibre)

Le présent travail de ma thèse de doctorat s'inscrit dans la continuité thématique de l'équipe de recherche de l'Unité de Mécanique de Lille, Joseph Boussinseq (UML) de l'université de Lille. Depuis quelques années, nous enregistrons quatre travaux de thèse déjà soutenues :

- La thèse de Cuong HA MINH, soutenue en 2011, porte sur le thème « Comportement mécanique des matériaux tissés soumis à un impact balistique : approches expérimentale, numérique et analytique », dans le cadre d'une collaboration Université de Lille/ENSAIT de Roubaix.
- La thèse de Jan VAN ROEY, soutenue en 2011, porte sur le thème « Etude du comportement dynamique des matériaux granulaires et tissés : étude expérimentale et simulation numérique », dans le cadre d'une collaboration Université de Lille/Ecole Royale Militaire, Bruxelles, Belgique.
- La thèse de Tuan-Long CHU, soutenue en 2016, porte sur le thème « Etude du comportement mécanique d'un matériau tissé soumis à un impact balistique basée sur une approche multi-échelle », Université de Lille
- La thèse de Lionel GILSON, soutenue en 2017, porte sur le thème « Etude du comportement mécanique des multi-matériaux soumis à un impact balistique : approches expérimentale et numérique », dans le cadre d'une collaboration Université de Lille/Ecole Royale Militaire, Bruxelles, Belgique.

Objectif de la thèse

Cette thèse est consacrée à l'étude du comportement balistique d'un matériau tissé en utilisant une approche microscopique basée sur la technique d'homogénéisation numérique. En effet, lors d'un chargement balistique, le projectile agit localement sur la zone affectée du tissu engendrant ainsi une compression transversale des fibres. Ce phénomène a été modélisé, à l'échelle des fibres, en prenant en compte les effets des interactions fibre-fibre et l'évolution de la fraction volumique d'un fil au cours du chargement. Cette modélisation a conduit à établir une loi de comportement mécanique

non-linéaire décrivant l'évolution des contraintes et des déformations apparentes dans un fil soumis à une compression transversale. La technique d'homogénéisation numérique, basée sur un Volume Élémentaire Représentatif (VER) périodique, a été utilisée en vue d'une modélisation prenant en compte le vide entre les fibres. Cette démarche a conduit à établir une loi puissance entre la déformation apparente et la fraction volumique pour un fil sollicité en compression transversale. La technique d'homogénéisation numérique a également été utilisée pour analyser le comportement microscopique des fibres soumises à un impact balistique selon une approche multi-échelle. La notion de fibre équivelante représentant un ensemble de fibres a été introduite afin de gagner du temps de calcul. Cette analyse a conduit à une meilleure compréhension des phénomènes physiques se produisant lors d'un impact balistique d'un fil à l'échelle des fibres. Ensuite, cette modélisation a été appliquée au cas d'un tissu soumis à un impact balistique à une échelle mésoscopique (échelle d'un fil) combinée à une échelle microscopique (échelle d'une fibre) dans la zone affectée par l'impact. Cette modélisation a été validée par confrontation avec des données expérimentales, en termes de l'évolution la vitesse du projectile. Les évolutions de l'énergie, de la force d'impact, des interactions fibres-fibres et de la rupture locale des fibres ont été aussi analysées.

Structuration du rapport

Le présent rapport est l'aboutissement de mes travaux de recherche de thèse de doctorat. Je l'ai structuré en quatre chapitres principaux :

- **Chapitre I :** Analyse bibliographique

Ce chapitre présente l'état de l'art des études sur les performances balistiques des matériaux tissés. Nous avons abordé les principaux mécanismes de réponses de ces matériaux soumis à un impact balistique décrits dans la littérature, tels que la formation et la propagation des ondes de déformation d'un fil, ainsi que les réponses globales et locales d'un tissu au cours de l'impact. Dans un second temps, nous avons présenté les facteurs qui influencent les performances balistiques des tissus. En effet, cette performance est influencée par une combinaison de nombreux paramètres tels que les propriétés physiques et mécaniques des fils et des tissus, la friction projectile/tissu et fil/fil, les propriétés physiques et mécaniques des projectiles, etc.

Aussi, nous avons présenté une synthèse des principales investigations portant sur les modélisations numériques concernant l'impact balistique d'un tissu. Ces modèles sont classés selon quatre échelles : échelle macroscopique, échelle mésoscopique, échelle microscopique et multi-échelle (macro/méso, méso/micro). Les avantages et les inconvénients de chaque modèle sont mis en évidence et discutés.

Un focus a été mis sur les travaux portant sur la modélisation microscopique à l'échelle d'une fibre. Pour cela, nous avons présenté les réponses mécaniques d'une ou plusieurs fibres soumises à une compression transversale, à partir des résultats expérimentaux, analytiques et numériques. Ensuite, plusieurs des travaux expérimentaux et numériques sont passés en revue.

- **Chapitre II :** Analyse numérique microscopique de la compression transversale des fibres

Dans ce chapitre, le comportement en compression transversale microscopique des fibres est analysé. En effet, l'étude de la compression à cette échelle est motivée par l'action du projectile dans la zone affectée par l'impact. Une modélisation numérique a été développée dans quatre configurations, à savoir: (i) une seule fibre, (ii) deux fibres, (iii) un bloc de fibres et (iv) un fil. Des calculs numériques sont effectués dans le cas d'une compression transversale en utilisant l'hypothèse d'une déformation plane 2D. De plus, la convergence du maillage est étudiée en vue de vérifier le nombre optimal d'éléments finis pour une section transversale d'une fibre. Les interactions avec la friction entre chaque fibre sont prises en compte. On note bien l'existence d'une évolution non-linéaire de la contrainte et déformation apparentes dans le cas de la compression transversale d'une et de deux fibres. Cette modélisation a été vérifiée dans le cas de deux fibres en Kevlar (Kevlar® KM2, Kevlar® 49). Dans le cas d'un bloc de fibres, nous avons étudié les effets de la friction sur les réponses mécaniques en termes de courbes contrainte-déformation apparentes. Les résultats numériques ont été validés par confrontation avec des données expérimentales.

La modélisation numérique a été appliquée pour analyser le comportement d'un fil composé de 400 fibres soumis à une compression transverse, en prenant en compte l'aspect elliptique du fil. La réponse mécanique en termes de courbes Force-Déplacement a mis en évidence l'existence de deux zones principales : (i) zone de réarrangement des

fibres où la fraction volumique des fibres est constante, (ii) zone de comportement non-linéaire correspondant à la compression des fibres où la fraction volumique des fibres augmente avec le déplacement. Ce constat a conduit à l'établissement d'une corrélation entre la déformation effective apparente et la fraction volumique.

- **Chapitre III :** Homogénéisation numérique du comportement en compression de fibres

Dans ce chapitre, le comportement en compression transversale des fibres est étudié en utilisant une approche d'homogénéisation élémentaire numérique. Tout d'abord, dans la première partie, un aperçu de la méthode d'homogénéisation numérique est présenté. Le concept d'homogénéisation numérique et les notions les plus importantes, en particulier, le volume élémentaire représentatif (VER) et les conditions aux limites, sont présentés en détail. Plusieurs résultats de travaux antérieurs, portant sur l'application de la méthode d'homogénéisation aux matériaux tissés, ont été exposés dans cette partie.

Dans la seconde partie, la méthode d'homogénéisation numérique est développée pour évaluer les propriétés effectives dans le cas de fibres et d'un fil soumis à une compression transversale. Ces lois de comportement homogénéisées sont implémentées dans le logiciel ABAQUS via un sous-programme utilisateur et validées par comparaison avec les résultats des modèles microscopiques. Cette approche a permis de proposer un matériau homogène équivalent (MHE) pour un fil et a conduit à des résultats très intéressants en termes de courbes contrainte-déformation apparentes. Cette modélisation constitue une voie prometteuse pour être utilisée en vue d'établir un modèle robuste pour l'étude de l'impact sur les matériaux tissés.

- **Chapitre IV :** Modélisation microscopique d'un tissu soumis à un impact balistique

Dans ce chapitre, le comportement du matériau tissé soumis à un impact balistique (vitesse d'impact de 245 m/s) est étudié en utilisant une approche microscopique dans le cas (i) d'un seul fil ondulé et (ii) d'un tissu. Dans le cas d'un seul fil ondulé, deux modèles numériques à l'échelle des fibres dans lesquels les 400 fibres sont représentées respectivement par 42 et 98 fibres équivalentes sont réalisés. Les deux modèles sont comparés en analysant les énergies des fils, la propagation des ondes transversales et la vitesse du projectile en fonction du temps. Les forces à l'échelle de chaque fibre sont analysées. Les résultats sont comparés à ceux obtenus via une modélisation

mésoscopique. Les ruptures des fibres au cours de l'impact sont analysées ce qui permet d'avoir accès à des informations très intéressantes dans le processus d'endommagement d'un fil au contact d'un projectile.

Par la suite, un modèle multi-échelle micro-mésoscopique de tissu a été développée. En effet, nous considérons un tissu avec deux fils primaires qui sont modélisés à l'échelle microscopique (échelle des fibres) et le reste est basé sur un modèle mésoscopique. Cette démarche permet de mieux analyser les mécanismes physiques se produisant dans la zone du tissu affectée par l'impact sous le projectile. Elle met en évidence les phénomènes de glissement et les ruptures des fibres, ainsi que les interactions entre fibre/fibre et fibres/fils. Cette modélisation multi-échelle (micro/méso) a été comparée à une modélisation mésoscopique.

Le présent manuscrit contient une introduction générale, une conclusion et des perspectives. A la fin du manuscrit, une liste des références bibliographiques est présentée.

Introduction

Context

The assessment of ballistic impact problems is challenging due to the complicated interactions between the projectile, the protection and the target. In the literature, several experimental, analytical and numerical studies have been carried out. These works mainly investigated the ballistic performance of the protections in order to ensure their lightweight and mechanical resistance. The importance of the dynamic behaviour of projectiles in order to better understand both their materials and morphologies has also been noted. For the targets, previous studies have concentrated on the use of sample materials, such as gelatine and plasticine, to simulate the human body in experimental investigations. Of these three areas, most previous research has focused on the study of the performance of ballistic protection. Indeed, the choice of materials used for better target protection poses a permanent concern. In this domain, a variety of materials for ballistic protection, such as composite materials and multi-materials (aggregates, ceramics and so on), has been noted.

The use of flexible protective equipment is an essential component of the previous research in this area. Indeed, woven materials using high-performance fibres, such as Kevlar and Twaron, have been investigated. Experimental, analytical and numerical approaches have been developed to predict the mechanical behaviour of textile fabrics subjected to ballistic impact. Understanding and predicting the evolution and mechanisms of damage are one of the essential objectives. Ballistic performance is evaluated in the case of the perforation or non-perforation of the tissues during impact. The complexity of such experiments has led to a clear need for numerical modelling. This approach has been facilitated by the development of computational resources. There is a significant number of works already published relating to the development of numerical models for the description and prediction of the response of fabrics subjected to ballistic impact. Based on the scale, the numerical models can be classified as follows:

- Macroscopic models developed at the fabric scale;
- Mesoscopic models performed at the yarn scale;
- Microscopic models developed at fibre scale;

- Multi-scale models composed of macro/meso (fabric/yarn) or meso/micro (yarn/fibre) scales.

The work of this PhD thesis is part of the thematic continuity of the research of the Unité de Mécanique de Lille, Joseph Boussinseq (UML) - University of Lille. There are four theses already defended:

- Cuong HA-MINH (defended in 2011): "Mechanical behaviour of woven materials subjected to ballistic impact: experimental, numerical and analytical approaches", as part of a collaboration between the University of Lille and ENSAIT de Roubaix.
- Jan VAN ROEY (defended in 2011): "Study of the dynamic behaviour of granular and woven materials: experimental study and numerical simulation", as part of a collaboration between the University of Lille and the Royal Military Academy, Brussels, Belgium.
- Tuan-Long CHU (defended in 2016): "Study of the mechanical behaviour of a woven material subjected to a ballistic impact based on a multi-scale approach", University of Lille, France.
- Lionel GILSON (defended in 2017): "Study of the mechanical behaviour of multi-materials subjected to ballistic impact: experimental and numerical approaches", as part of a collaboration between the University of Lille and the Royal Military Academy, Brussels, Belgium.

Objective of thesis

This thesis is dedicated to the study of the ballistic behaviour of woven materials using a microscopic approach based on a numerical homogenization technique. Indeed, during ballistic impact, the projectile locally strikes the fabric on the impact zone, thus generating a transverse compression of the fibres. This phenomenon has been modelled, at the fibre scale, considering the effects of fibre-fibre interactions and the evolution of the volume fraction of yarn during loading. From this modelling, a non-linear mechanical behaviour law describing the evolution of the apparent stress and strain in a yarn subjected to transverse compression was obtained. Then, based on a periodic Representative Volume Element (RVE), a numerical homogenization technique considering the void between fibres was used for modelling. A power law between the

apparent deformation and the volume fraction for a yarn subjected to transverse compression was deduced based on this approach. Numerical homogenization technique was also utilised to analyse the microscopic behaviour of fibres subjected to ballistic impact based on a multi-scale approach. The notion of an equivalent fibre representing a set of fibres was introduced in order to gain computation time. The analysis provided a better understanding of the physical phenomena occurring during the ballistic impact of one single yarn at the fibre scale. This model was then applied to the case of one fabric subjected to ballistic impact at a mesoscopic scale (yarn scale) combined with a microscopic scale (fibre scale) in the impact zone. This model was validated by comparison with experimental data, in terms of the evolution of projectile velocity. The evolution of energy, impact force, fibre-fibre interactions and local fibre failure were also analysed.

Structure of thesis

This thesis is the culmination of my doctoral research and is divided into four main chapters:

- **Chapter 1**: Bibliography analysis

This chapter presents the state-of-the-art regarding studies on the ballistic performance of woven materials. The main response mechanisms of these materials subjected to ballistic impact described in the literature, such as the formation and propagation of deformation waves of yarn, as well as the global and local responses of fabrics during impact, are discussed. We then present the factors that influence the ballistic performance of the tissue. Indeed, this performance is influenced by a combination of many parameters, including the physical and mechanical properties of yarns and fabrics, projectile/fabric and yarn/yarn friction, physical and mechanical properties of projectiles.

A summary of the main numerical modelling investigation concerning the ballistic impact of fabrics is also presented. These models are classified into four scales: macroscopic scale, mesoscopic scale, microscopic scale and multi-scale (macro/meso, meso/micro). The advantages and disadvantages of each model are highlighted and discussed.

Previous works based on microscopic modelling at the fibre scale are featured. For this purpose, we present the mechanical responses of one or more fibres subjected to transverse compression, based on experimental, analytical and numerical results. Some experimental and numerical works are also reviewed.

- **Chapter 2**: Numerical analysis of microscopic transverse compressive behaviour of fibres

In this chapter, the microscopic transverse compressive behaviour of fibres is analysed. Indeed, the study of compression on this scale is motivated by the responses of the projectile in the area affected by the impact. Numerical modelling is developed in four configurations: (i) a single fibre; (ii) two fibres; (iii) a block of fibres; (iv) a yarn. Numerical calculations are performed in the case of transverse compression using the assumption of 2D plane strain. In addition, the mesh convergence is studied in order to find the optimal number of finite elements for a cross-section of a fibre. The interactions with the friction between each fibre are considered. Non-linear evolution of the nominal stress and strain in the case of transverse compression of one and two fibres is obtained. This modelling is verified in the case of two Kevlar fibres (Kevlar® KM2 and Kevlar® 49). In the case of a block of fibres, we investigate the effects of friction on mechanical responses in terms of apparent stress-strain curves. The numerical results are validated by comparison with the experimental data.

Numerical modelling is applied to analyse the behaviour of one yarn composed of 400 fibres subjected to transverse compression, considering the elliptical shape the cross-section of the yarn. The mechanical response in terms of force-displacement curves clearly shows two main zones: (i) a zone of rearrangement of fibres where the volume fraction of the fibres is constant, (ii) a zone of non-linear behaviour corresponding to the compression of fibres where the volume fraction of the fibres increases with displacement. A relationship between the apparent effective strain and the volume fraction is also obtained.

- **Chapter 3**: Homogenization of transverse compressive behaviour of fibres

In this chapter, the transverse compression behaviour of fibres is studied using a numerical elementary homogenization approach. In the first part, an overview of the numerical homogenization method is presented. The concept of numerical

homogenization and the most important notions, including the Representative Volume Element (RVE) and boundary conditions, are presented in detail. Several results of previous works concerning the application of the homogenization method on woven materials are presented in this section.

In the second part, the numerical homogenization method is developed to evaluate the effective properties in the case of a block of fibres and one yarn subjected to transverse compression. These homogenized behaviour laws are implemented in the ABAQUS software via a user-defined subroutine and validated by comparison with the results of microscopic models. An Effective Homogenized Material (EHM) for one yarn is proposed, leading to exciting results in terms of apparent stress-strain curves. This modelling allows for a robust model for the study of the impact of woven materials.

- **Chapter 4**: Microscopic behaviour of a fabric subjected to ballistic impact

In this chapter, the behaviour of the woven material subjected to a ballistic impact (impact velocity of 245 m/s) is studied using a microscopic approach in the case of (i) a single crimped yarn and (ii) one fabric. In the case of a single crimped yarn, two numerical fibre-scale models, in which 400 fibres are represented by 42 and 98 equivalent fibres, respectively, are conducted. The two models are compared by analysing the energies of the yarn, the propagation of the transverse waves and the velocity of the projectile versus time. The tension forces of each fibre are observed. The results are compared with those obtained via mesoscopic modelling. Fibre failure during impact is analysed, resulting in exciting information regarding the damage process of the yarn in contact with a projectile.

Subsequently, a micro-mesoscopic multi-scale model of tissue is developed. Indeed, we consider a fabric with two primary yarns modelled at the microscopic scale (fibre scale) and the rest is modelled as a mesoscopic model. This approach allows for a better analysis of the physical mechanisms occurring in the impact zone under the projectile. It highlights the sliding phenomena and fibre failure, as well as the fibre-fibre and fibre-yarn interactions. This multi-scale model is also compared with a validated mesoscopic model.

This thesis contains a general introduction, conclusion and perspectives. At the end of the thesis, a list of bibliographic references is presented.

Chapter I

Bibliography Analysis

Abstract

This chapter presents the state of the art regarding studies on the ballistic performance of woven materials. The main response mechanisms of these materials subjected to ballistic impact described in the literature, such as the formation and propagation of deformation waves of yarn, as well as the global and local responses of fabrics during impact, are discussed. We then present the factors that influence the ballistic performance of the tissue. Indeed, this performance is influenced by a combination of many parameters, including the physical and mechanical properties of yarns and fabrics, projectile/fabric and yarn/yarn friction, physical and mechanical properties of projectiles.

A summary of the main numerical modelling investigation concerning the ballistic impact of fabrics is also presented. These models are classified into four scales: macroscopic scale, mesoscopic scale, microscopic scale and multi-scale (macro/meso, meso/micro). The advantages and disadvantages of each model are highlighted and discussed.

Previous works based on microscopic modelling at the fibre scale are featured. For this purpose, we present the mechanical responses of one or more fibres subjected to transverse compression, based on experimental, analytical and numerical results. Some experimental and numerical works are also reviewed.

Résumé

Ce chapitre présente l'état de l'art des études sur les performances balistiques des matériaux tissés. Nous avons abordé les principaux mécanismes de réponses de ces matériaux soumis à un impact balistique décrits dans la littérature, tels que la formation et la propagation des ondes de déformation d'un fil, ainsi que les réponses globales et locales d'un tissu au cours de l'impact. Dans un second temps, nous avons présenté les facteurs qui influencent les performances balistiques des tissus. En effet, cette performance est influencée par une combinaison de nombreux paramètres tels que les propriétés physiques et mécaniques des fils et des tissus, la friction projectile/tissu et fil/fil, les propriétés physiques et mécaniques des projectiles, etc.

Aussi, nous avons présenté une synthèse des principales investigations portant sur les modélisations numériques concernant l'impact balistique d'un tissu. Ces modèles sont classés selon quatre échelles : échelle macroscopique, échelle mésoscopique, échelle microscopique et multi-échelle (macro/méso, méso/micro). Les avantages et les inconvénients de chaque modèle sont mis en évidence et discutés.

Un focus a été mis sur les travaux portant sur la modélisation microscopique à l'échelle d'une fibre. Pour cela, nous avons présenté les réponses mécaniques d'une ou plusieurs fibres soumises à une compression transversale, à partir des résultats expérimentaux, analytiques et numériques. Ensuite, plusieurs travaux expérimentaux et numériques sont passés en revue.

Contents

I.1 Ballistic impact phenomenon

I.1.1 Introduction

Nowadays, high-performance ballistic materials have become familiar and have gradually replaced metals, in particular or specific applications, thanks to their flexibility and high strength-to-weight ratio. These applications, requiring exceptional resistance, are commonly niche products, such as lightweight composite materials for aircraft, ballistic fibres, and bullet or body armour.

It is well known that the impact phenomenon can be classified into four types based on the range of impact velocity as follows: (i) low-velocity impact (up to 30 m/s), (ii) high-velocity impact (from 30 to 200 m/s), (iii) ballistic velocity impact (more than 200 m/s) and (iv) hypervelocity impact (more than 15 000 m/s) [1,2]. The ballistic impact response of a woven fabric is a complex process due to the rapid impact velocity, the very short period, and the complicated structure. Figure I.1 presents an example of soft body armour and a ballistic test. In this test, a hemispherical head projectile strikes a Kevlar fabric resulting in fibre failure and the formation of a deformation pyramid.

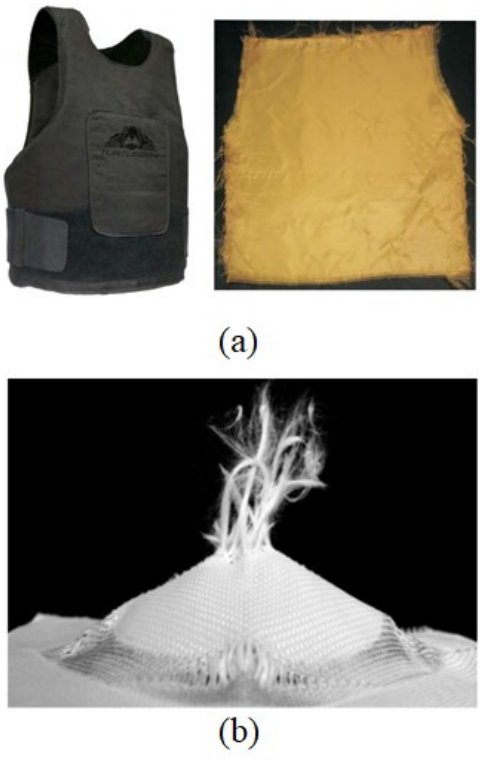

Figure I.1 (a) Soft body armour [3, 4], (b) a ballistic test [5].

The ballistic performance of woven fabrics has been studied for decades by analytical, experimental, and numerical approaches [6, 7]. It should be noted that a fabric

consists of a bundle of yarns, while the yarn is comprised of hundreds of fibres. Therefore, the ballistic impact phenomenon has been mainly analysed on three scales: (i) macroscopic (fabric) scale, (ii) mesoscopic (yarn) scale and (iii) microscopic (fibre) scale. On the macroscopic scale, the fabric is considered as a homogeneous plate, while on the mesoscopic one, the fabric is divided into homogeneous yarns.

I.1.2 Ballistic impact responses

In this section, a general presentation on the ballistic impact response of textile materials is introduced. Firstly the impact response of one yarn is presented via the analytical theory well-known in the literature. Then, the main deformation mechanisms of woven fabric are illustrated.

Ballistic impact response of one yarn

The theory of the ballistic impact of one yarn was first studied in reference [8] by Stone in 1955. Afterwards, Smith *et al.* developed the theory with a series of articles from 1955 to 1965, see the references [9-12]. In their works, the formation and propagation of deformation waves were analytically investigated. Figure I.2 presents an experiment of one yarn subjected to transverse impact, and a schematic of the deformation wave. Indeed, when a projectile strikes the yarn with an initial velocity V, two waves propagate from the impact point: (i) longitudinal and (ii) transverse waves.

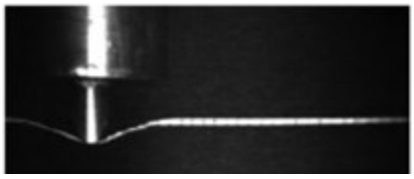

(a)

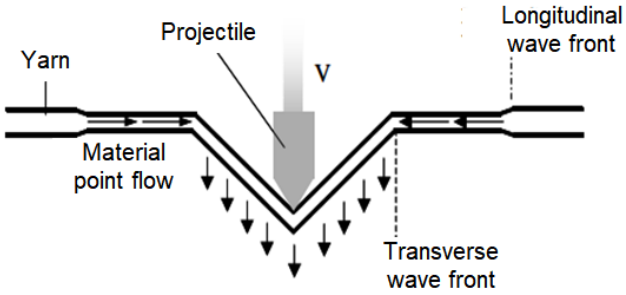

(b)

Figure I.2 Projectile impact onto one yarn: (a) an experiment [13] , (b) schematic of deformation waves [7].

- Longitudinal wave travels down the yarn axis at the sound speed material. The material points behind the longitudinal wave front are under strain and thus flow towards the impact point. The propagation speed is a function of Young's modulus and material density, as shown in the following equation:

$$V_l = \sqrt{\frac{E}{\rho}} \tag{I.1}$$

- As the projectile pushes the yarn, material points are deflected in the projectile direction. The transverse wave V_t travels much slower than the longitudinal one (one order magnitude). A V-shape zone near the impact point is induced. However, this wave does not strain the yarn further [14]. The speed of the transverse wave is calculated as the function of the longitudinal wave and the elastic strain ε (Equation I.2). The strain can be found from the projectile velocity V_p in Equation I.3 [9, 11], as follows:

$$V_t = V_l\left(\sqrt{\varepsilon(1+\varepsilon)} - \varepsilon\right) \tag{I.2}$$

$$V_p = V_l\sqrt{\varepsilon\left(2\sqrt{\varepsilon(1+\varepsilon} - \varepsilon\right)} \tag{I.3}$$

Figure I.3 presents an experiment of one Kevlar KM2 yarn subjected to transverse impact in the work of Hudspeth *et al.* [15]. In this work, a razor blade impactor struck the yarn with an initial velocity of 145 m/s. The yarn length was 850 cm. Two sides of the yarn were fixed via aluminium clamps. The propagation of deformation waves was captured from the resulting high-speed image sequence. Indeed, during the impact process, the yarn is tensile by the longitudinal wave. Moreover, from the impact point, a V-shape zone is induced due to the transverse wave.

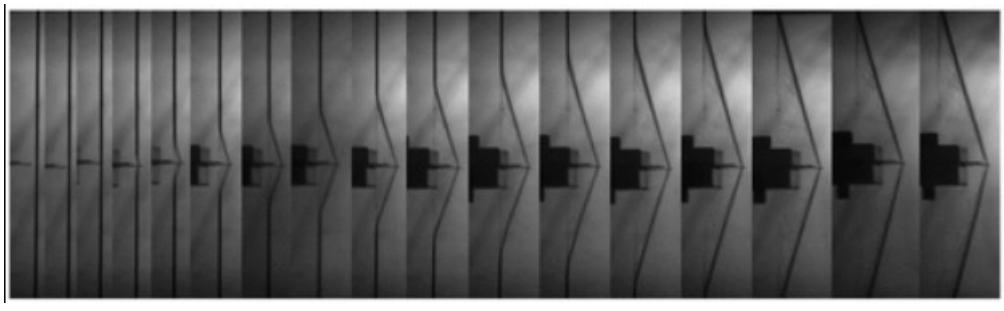

Figure I.3 An experiment of a razor blade impacts into Kevlar KM2 yarn [15].

The deformation of a Kevlar KM2 yarn subjected to transverse impact at the striking speed of 53 m/s is shown in Figure I.4 [13]. The 305-mm-long yarn was fixed at two sides and collided by a tapered aluminium cylinder. The high-speed images of the yarn deformation show that up to 20 μs, the yarn was laterally compressed. Then a triangular zone was formed, which extended with time. It can be observed that in the time, the triangular zones were almost similar. Material particles moved downwards along the yarn direction first because the longitudinal wave propagated faster than the transverse one. Then, the transverse wave arrived, and the material particles moved perpendicular to the fibre direction.

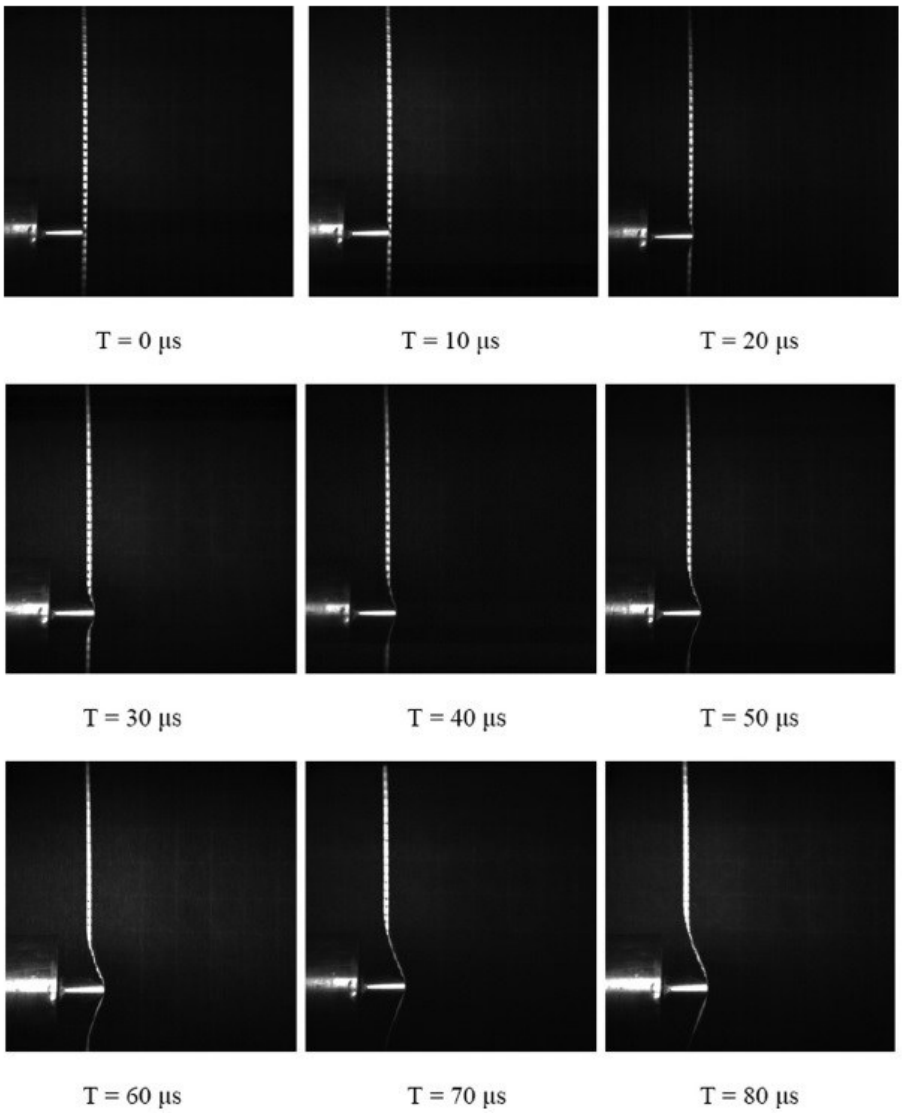

(a)

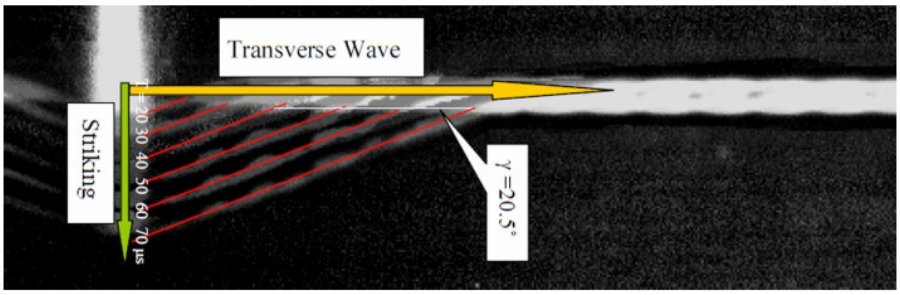

(b)

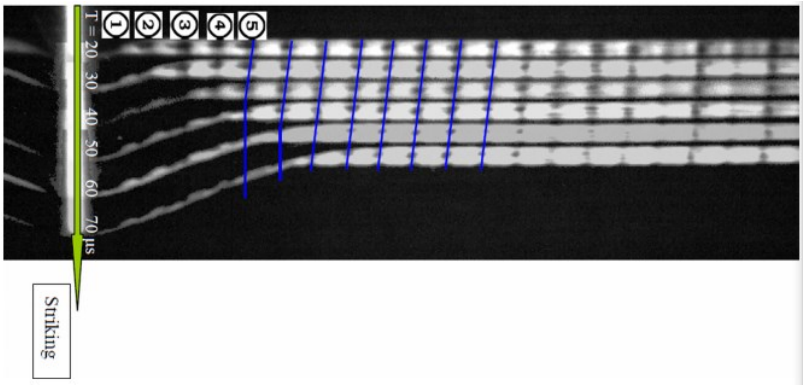

(c)

Figure I.4 Deformation of Kevlar KM2 yarn subjected to transverse impact (a) deformation at the striking speed of 53 m/s, (b) evolution of triangle shape, (c) movement of material particles [13].

Ballistic impact response of one fabric

Figure I.5 presents the ballistic impact response of one fabric. Once the projectile strikes the fabric, its energy is transferred to the target. Normally, during this process, the general response of the target is a combination of global and local responses [16]. While in the local response, the deformation is concentrated in the impact zone, for the global one, the deformation spreads to the whole of the fabric.

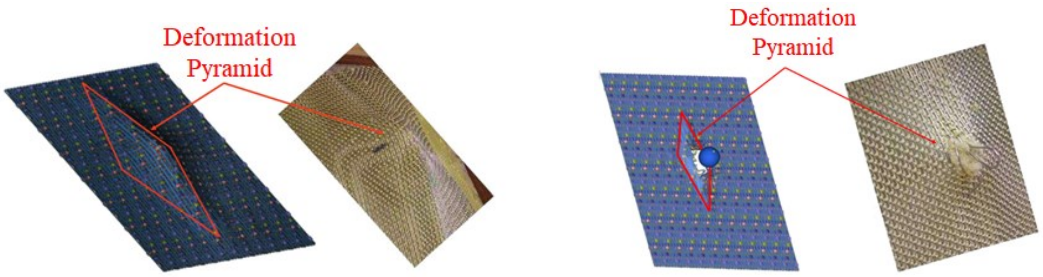

(a) (b)

Figure I.5 Ballistic impact responses (a) Global response (b) local response [17, 18].

The transition of the two response modes can be determined by the ballistic limit or V50. This value is the striking velocity at which the fabric is perforated with the probability of 50%. Figure I.6 presents an example of a V0-V100 curve. From this curve, the ballistic limit can be detected.

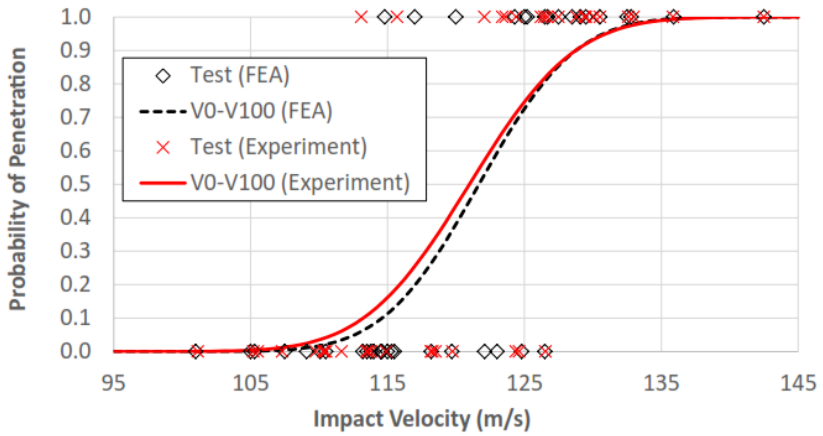

Figure I.6 An example of V_0-V_{100} curves [19].

The global response is dominant in the case of a low-velocity impact, inferior to the ballistic limit. This reaction depends on the fabric dimension and concerns the transfer of the deformation wave and the formation cone. In this case, the projectile is trapped, and no penetration occurs. Thus, the fabric absorbs the whole impact energy. The impact duration is long enough for the energy of the projectile to be transferred and spread through the fabric. Two waves are generated and reach the boundaries of the fabric:

- A longitudinal wave is initiated when the projectile strikes the fabric. This one travels at the speed of sound in the yarns directly in contact with the projectile (primary yarns). These yarns are stretched, and the material moves in-plane towards the impact point [16].
- A transverse wave is generated when the primary yarns start to move along the impact direction and transmit their displacement to the other ones (called secondary yarns). The deflection moves with a much slower speed than the longitudinal one outside the impact zone resulting in a deformation pyramid [16, 20].

The local response is characterised by the local damage mechanisms within the impact zone, such as shear, perforation, shear plugging, and fibre breakage. In this case, the striking velocity is higher than the ballistic limit. As the projectile penetrates the

fabric, the projectile energy is partially absorbed, and residual velocity is observed (Figure I.7). It should be noted that two scenarios can be observed:

- Low-velocity perforation: the velocity is higher than the ballistic limit. Despite yarn failure, longitudinal and transverse waves still propagate. In comparison with the global reaction, the impact pyramid is smaller, and the impact zone is narrower.
- High-velocity perforation: in this case, the velocity is much higher. There is not enough time for the fabric to be deformed. The fabric is immediately penetrated.

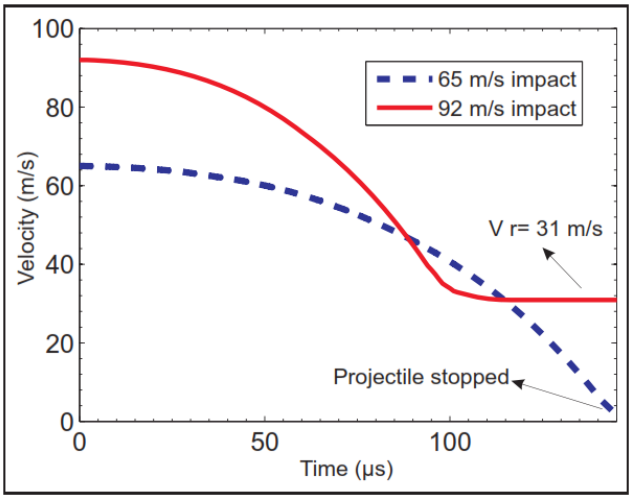

Figure I.7 Projectile velocity in the case of perforation and non-perforation impact [21].

From the energetic point of view, after impacting the fabric, the projectile velocity is reduced, leading to the loss of projectile kinetic energy. Assuming that the projectile is rigid, the loss of projectile kinetic energy ΔE_{pk} is absorbed by the fabric and converted into fabric deformation energy E_{fd}, fabric kinetic energy E_{fk} and energy lost in frictional sliding E_f [22, 23], as shown in the Equation I.4:

$$\Delta E_{pk} = E_{fd} + E_{fk} + E_f \tag{I.4}$$

The loss of projectile kinetic energy can be determined from ballistic experiments in the relationship with an initial and residual velocity of the projectile [22, 24-26] or in the function of time by a method taken from the work of Starratt *et al.* [27]. While the deformation energy relates to the energy of the primary yarns and the secondary yarns in the deformed zone, the kinetic energy is determined by the energy of the material in the impact pyramid zone [4, 28]. These energies can be obtained from the following equations:

$$\Delta E_{pk} = \frac{1}{2} m\left(v_i^2 - v_r^2\right) \tag{I.5}$$

$$\Delta E_{pk}(t) = \frac{1}{2} m\left(v_i^2 - v_p^2(t)\right) \tag{I.6}$$

$$E_{fd} = \frac{1}{2} \int_{V_d} E\varepsilon^2 dV \tag{I.7}$$

$$E_{fk} = \frac{1}{2} \rho \int_{V_p} v^2 dV \tag{I.8}$$

Where V_d is the deformed volume, V_p is the volume of the deformed pyramid, m stands for the mass of the projectile, and v, v_i, v_r are the velocity, the initial velocity and the residual velocity of the projectile, respectively. E, and ε denote the Young's modulus and strain of the material, respectively.

I.2 Influencing factors

In the previous sections, the ballistic performance has been introduced. In this section, factors influencing the ballistic performance are presented. The ballistic performance of the fabric is influenced by a combination of many factors, such as projectile velocity, projectile properties, properties of the fabric, and boundary conditions [6, 7, 29-31]. Here, three factors are focussed upon: (i) material properties, (ii) friction and (iii) fabric structure.

I.2.1 Influence of material properties

Fibre and yarn properties, such as Young's modulus and density, play an essential role in determining the behaviour of the fabric. The amount of energy absorbed depends on Young's modulus and the density of the material. Moreover, the deformation of the yarn is affected by the sound speed of the material, which is a function of the material's Young's modulus and density.

In 1999, Cunniff [32] introduced the product of the specific fibre toughness and strain wave velocity $U^* = \frac{\sigma\varepsilon}{2\rho}\sqrt{\frac{E}{\rho}}$ for evaluating the ballistic performance of fibres [6]. It clearly shows that a high Young's modulus, and high ratio of Young's modulus to density, determine a better ballistic performance.

Figure I.8 shows the effect of yarn stiffness and strength combination in the work of Rao *et al.* [33]. The authors conducted a numerical model of a rigid sphere impacting onto a plain-weave Kevlar KM2 fabric with four different material parameters. A quasi-static friction experiment was also incorporated into the model. The material with higher stiffness but lower strength was not penetrated, whereas the material with lower stiffness and higher strength was penetrated. In the case of the same strength, the higher stiffness material presented a better resistance and determined the initiation of the damage, while with the same stiffness, the higher strength material decelerates the projectile faster, resulting in a lower residual velocity.

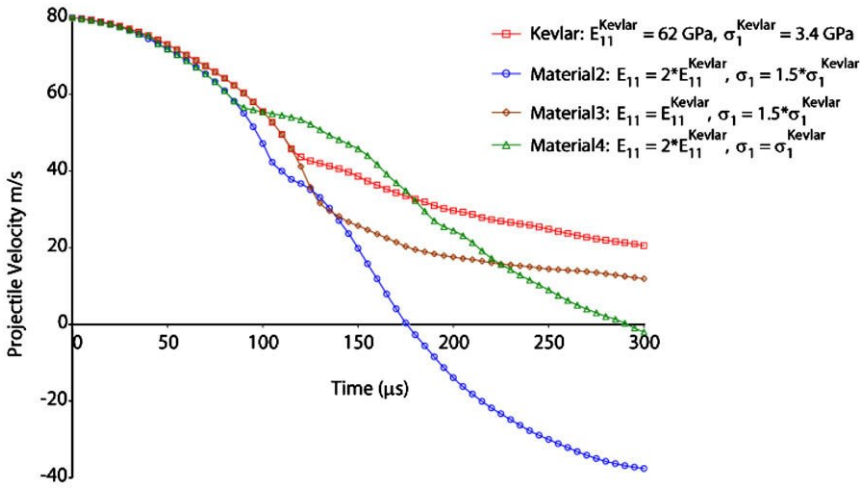

Figure I.8 The effect of material properties to the projectile velocity [33].

The effect of yarn transverse properties was numerically studied by Ha Minh *et al.* in 2012 [21]. Poisson's ratio, transverse Young's, and the shear moduli were investigated in the case of one Kevlar KM2 single crimp yarn and one Kevlar KM2 fabric. The effect was insignificant except for premature damages of yarns caused by the case of very low Young's modulus, or that of very high shear modulus.

I.2.2 Influence of friction coefficient

Friction, including yarn-yarn, fibre-fibre, and projectile-yarn friction, has a vital contribution to the absorbed energy. Briscoe *et al.* [26] studied the effect of aramid fabrics surface friction to their ballistic performance with different fabric weaves, and levels of inter-fibre, and inter-yarn friction. The experiments showed that in a fabric with higher inter-yarn friction, a larger amount of energy is dissipated. Using a yarn pull-out method, many researchers [34-37] have measured the friction of yarns. They found that

yarn-yarn friction determines the expansion of the pull-out zone, and then the dissipated energy during the pull-out and damage process.

Many authors have also conducted numerical investigations. Duan *et al.* have published many articles studying the effect of friction on the ballistic performance of 2D Kevlar KM2 plain-woven fabrics [22, 38-40]. Friction in yarn-yarn and projectile-yarn contacts has been defined. Figure I.9 clearly shows that friction sharply affects the evolution of the projectile velocity. The authors concluded that the higher the friction is, the higher amount of impact energy is absorbed. The relative yarn-yarn motion is prevented by yarn-yarn friction. Thus, yarn-yarn friction leads to the early failure of the fabric. However, the projectile-yarn friction distributes the maximum stress along the periphery of the contact zone. Therefore, yarn breakage is delayed, and the amount of energy absorbed by the fabric increases.

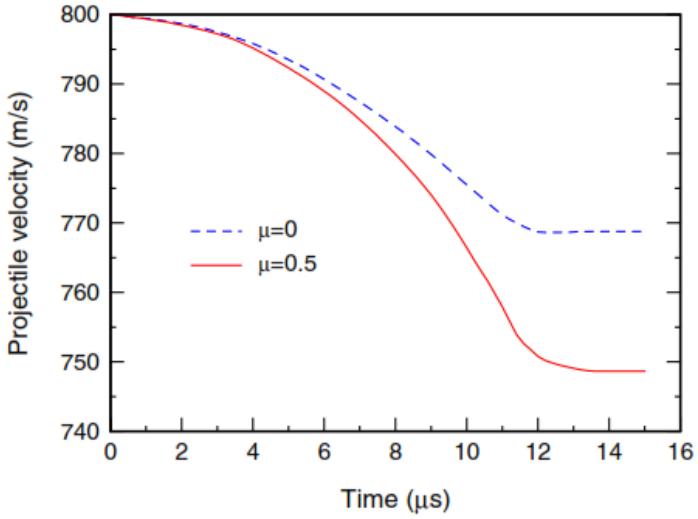

Figure I.9 Time development of the projectile velocity for the two different friction conditions [22].

Figure I.10 presents the effects of friction in the case of 3D interlock fabric [41]. In this work, Ha Minh *et al*. [41] introduced a new tool in order to represent the geometry of fabrics and investigate the friction effect. Results indicated that the fabric performance increased with the effect of friction. The yarn-yarn friction maintained the structural packing, while the yarn-projectile maintained the number of yarns loading the projectile by preventing yarns slipping out of the surface.

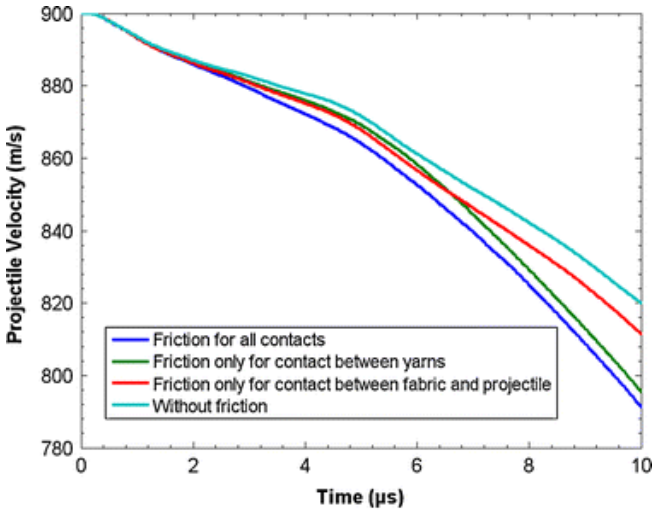

(a)

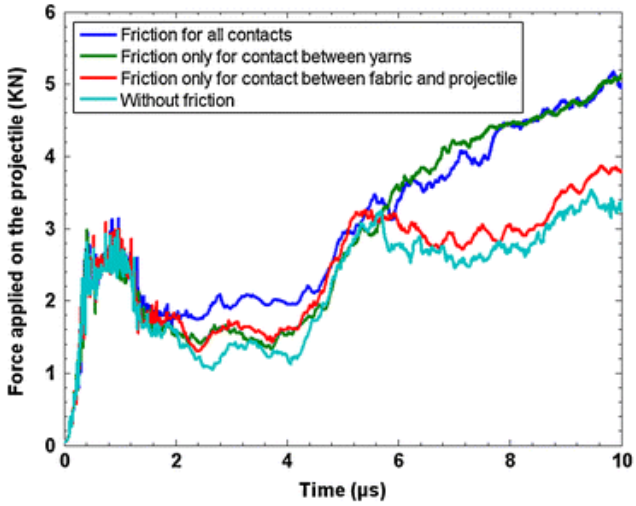

(b)

Figure I.10 Evolution versus time of: (a**)** Projectile velocity; (b) Force applied on the projectile [41].

The effect of yarn-yarn friction on the responses and the roles of both primary and secondary yarns on the failure of fabrics were investigated by Chu *et al*. [42]. The results showed that more impact energy and loading are shared by the secondary yarns, resulting in the prolongation of primary yarn's failure in the case of more yarn-yarn friction. Besides, a value of friction beyond a coefficient of static friction of 0.8, and a coefficient of kinetic friction of 0.75, causes more stress concentration on the primary yarns leading to an earlier failure of the fabric (Figure I.11).

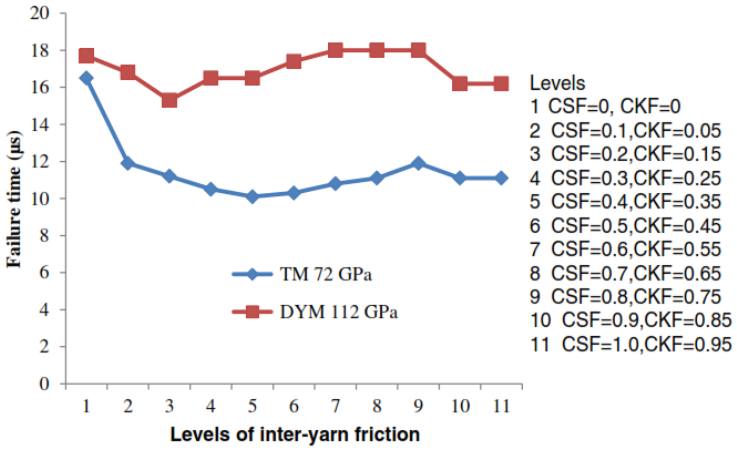

Figure I.11 The trends of failure time of fabrics with the increase of the inter-yarn friction [42].

I.2.3 Influence of projectile properties

Projectile geometry determines its ability and how it penetrates the fabric [7]. This effect has been numerically and experimentally studied. Blunt and pointed bullets perform differently. While pointed bullets have a better ability to slide through the fabric, blunt bullets decelerate faster [35, 43]. Tan and Lim *et al.* [44, 45] analysed four different types of nose shapes including hemispherical, flat, ogival, and conical, as shown in Figure I.12. Different mechanisms of yarn rupture, fibrillation, failure by friction, and bowing were found in each case..

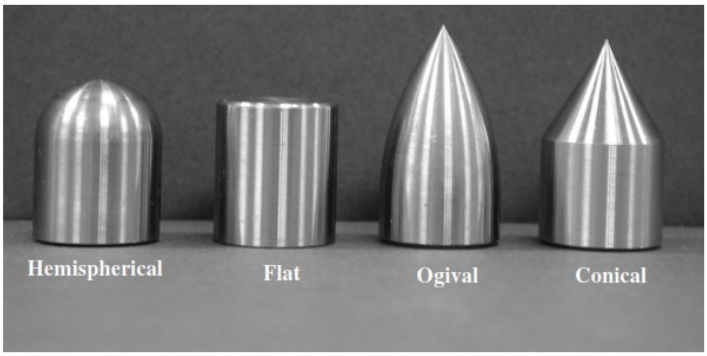

Figure I.12 Shape of projectiles used [44].

Figure I.13 shows the amount of energy absorbed by different kinds of projectile nose shapes. The least amount of yarn pull-out was observed in the case of ogival and conical bullets due to their better ability to wedge through the fabric. Therefore, lower projectile energy was absorbed by the fabric. However, in the case of hemispherical and plat shape bullets, more filaments were damaged. It is noted that hemispherical projectiles perforate the fabric mainly by longitudinal failure, while flat projectiles are

able to induce shear failure due to their angled edges and constant cross-section. Bowing is a significant mode of fabric perforation for the sharper conical and ogival projectiles.

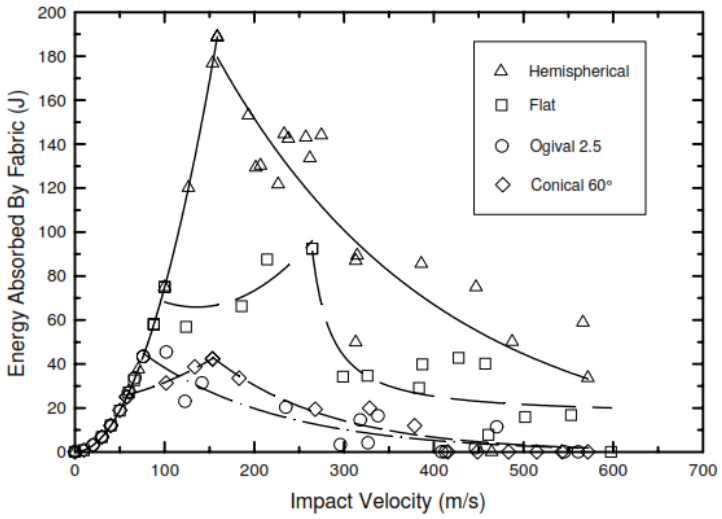

Figure I.13 Energy absorbed by fabric against impact velocity of projectiles [46].

From the numerical point of view, Nilakantan *et al.* [47, 48] investigated the effect of projectile size and shape by varying the size of six projectiles of spherical, cylindrical, and conical shapes. The mass and velocity were the same for all cases. These works confirmed the result of the experimental works. The order of impact performance of the fabric from lowest to highest residual projectile velocity was as follows: cylinder, sphere, and cone (Figure I.14). In the case of the same shape, the larger bullets caused a lower residual velocity [47].

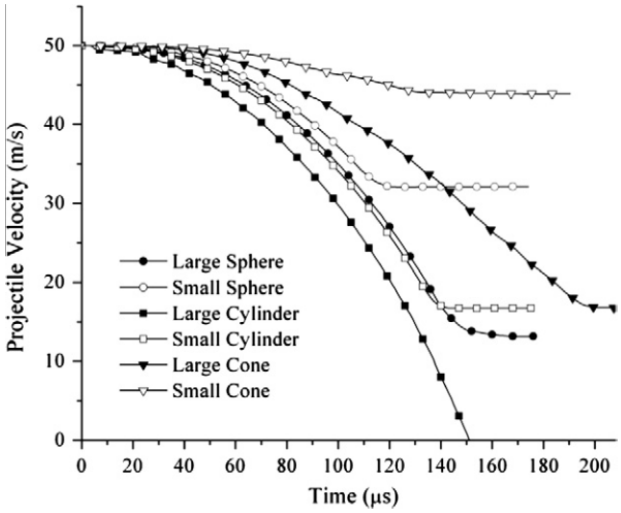

Figure I.14 Comparison of projectile velocity histories [47].

I.3 Numerical modelling of ballistic impact response

The ballistic performance of the fabric is very complex due to the complicated structure and rapid impact velocity. Thus, the number of experimental works is limited and unable to predict all of the mechanisms. Additionally, the cost of the experiment is very high. Therefore, numerical modelling has been conducted alongside experimental and analytical approaches.

Figure I.15 presents three main modelling scales of a fabric:

- Macroscopic model (fabric scale): the fabric is considered as a homogeneous plate.
- Mesoscopic model (yarn scale): the fabric is divided into yarns which are considered as a homogeneous body.
- Microscopic model (fibre scale): the fabric is considered on the scale of fibres.

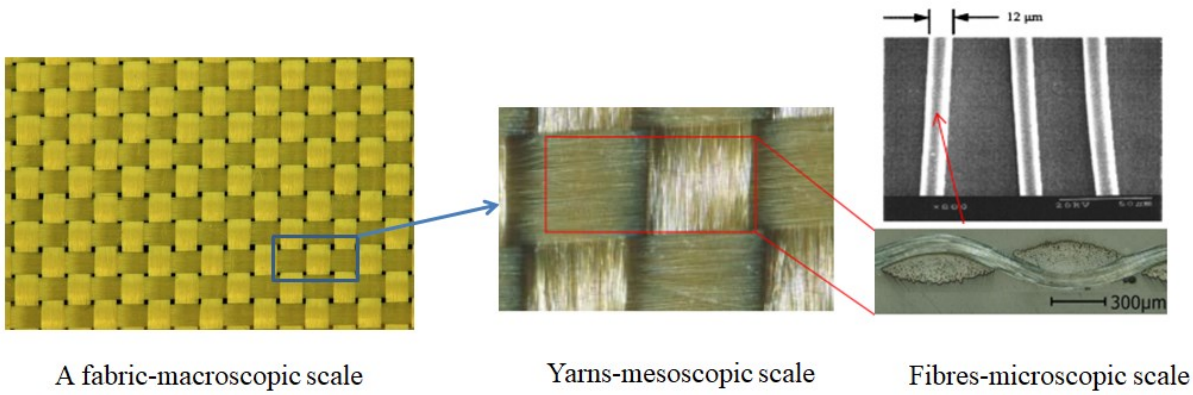

Figure I.15 Multi-scale problem of a fabric [49].

Besides, in order to gain computation time, a multi-scale model, such as macro-mesoscopic or meso-microscopic model, has also been developed. In this model, the fabric is divided into two zones: (i) local zone which is modelled on a finer scale, and (ii) global zone, which is modelled on a coarser scale.

I.3.1 Macroscopic model

Macroscopic models of 2D woven fabrics subjected to ballistic impact were firstly developed by Roylance *et al.* in a series of papers [29, 30, 50-54]. The authors assumed warp and weft yarns as no-mass beam elements forming a regular grid. The masses were concentrated in the intersection point of the beam system. The results showed that projectile energy is mostly transferred to the primary yarns as kinetic and deformation energy. A similar model of plain-woven fabric was also developed by Shim *et al.* [55]

using pin-jointed fibre elements. The model was able to predict the deformation and tearing manner of the fabric, but not the slippage of yarns.

Figure I.16 shows the macroscopic model conducted by Lim *et al.* [56]. The authors investigated a finite element model of a Twaron fabric subjected to ballistic impact using membrane elements. The material was assumed to be isotropic, elasto plastic, and strain-rate-dependent. Failure criterion and penalty contact were also implemented. The results closely correlated with the experimental data in terms of absorbed energy and residual velocity of the projectile. The formation of a deformation impact pyramid and the transverse deflection profile were observed (Figure I.17).

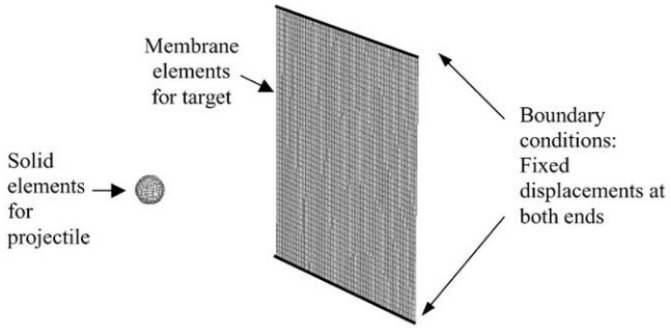

Figure I.16 Macroscopic model using membrane element [56].

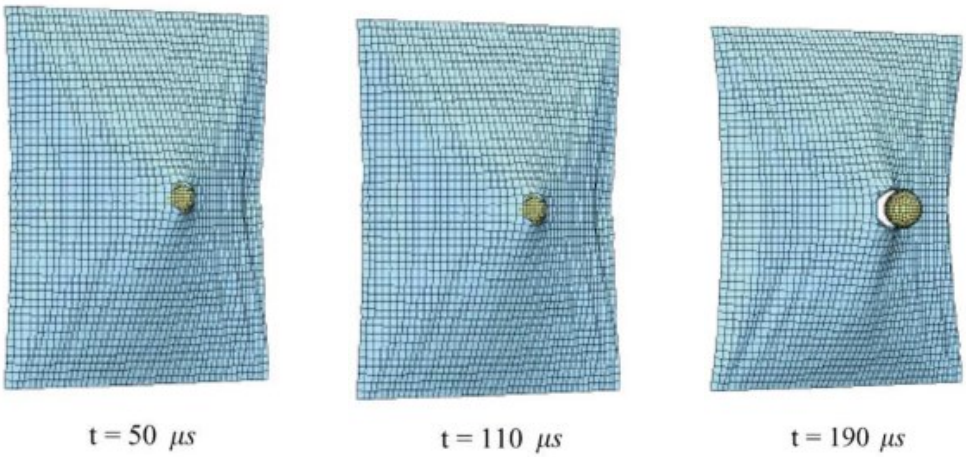

Figure I.17 Development of perforation v = 206m/s [56].

Ivanov *et al.* [57] integrated the crimping of the fibres as well as the trellis mechanisms in their macroscopic model. The fabric was modelled by eight layers of shell elements. The deformation pyramid and projectile residual velocity were also observed to be in good agreement with the experimental data.

Figure I.18 presents the macroscopic model in the works of Ha Minh *et al.* [58, 59]. The authors considered the fabric as a homogeneous plate represented by 3D shell

elements. The plate was assumed as orthotropic, and its properties were the same as one single yarn. The mass density was calculated to ensure that the mass of the homogeneous plate and the real fabric were the same. The authors concluded that the macroscopic model was able to predict global reactions, such as energy absorbed, the formation of deformation pyramid, and projectile time-velocity, as well as the residual velocity. The macroscopic model, especially, can provide the main damage failure zones: the motion of primary yarns, localised damage zone around the impact zone, or narrowing of the fabric due to projectile penetration (Figure I.18). However, the interactions between yarns, such as yarn pull-out or yarn sliding, cannot be observed due to the homogeneity [59].

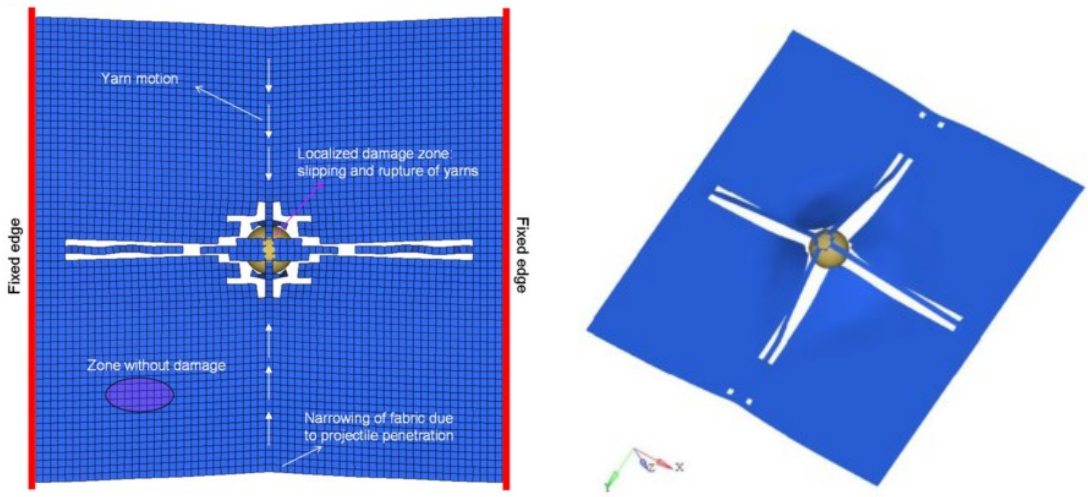

Figure I.18 Damage phase and deformed configuration of a fabric subjected to a 245m/s ballistic impact [59].

I.3.2 Mesoscopic model

As the macroscopic model cannot predict local behaviour of the fabric, it is necessary, therefore, to develop the mesoscopic model in which the weaving parameters and yarn-yarn interactions are considered. Normally, a yarn is considered as a transversely orthotropic material. The axis of material symmetry is parallel to the yarn's longitudinal axis. Since the 2000s, many authors have conducted finite element numerical models. Two types of elements are mainly used: solid and 3D shell elements.

Gu [60] conducted one of the first mesoscopic models. The conically cylindrical steel projectile and yarns were meshed with solid elements. The actual structure of a real multi-layer fabric was obtained by representing crimps of yarns. The residual projectile velocity, the deformation, and the damage of the fabric and yarns were predicted with a good agreement with experimental results.

Figure I.19 presents the mesoscopic model of Duan *et al.* [22, 38-40] using solid elements. Details of the finite element mesh are discussed in reference [38]. The yarn cross-section was discretised into twelve elements. Along with a yarn crimp, ten elements were used to describe this parameter. Yarns were assumed as transversely orthotropic with a Poisson's ratio of zero. The authors investigated the effects of yarn-yarn, and fabric-projectile friction, as well as the effects of boundary conditions (three cases of fixation of fabric edges: four edges free, four edges clamped, and two edges clamped) on the ballistic behaviour. Results showed that the higher the friction, the lower the residual projectile velocity. The friction also contributed to the amount of impact energy absorbed (Figure I.20). This amount increased in the presence of higher friction. It also showed that the fabric with four edges clamped slowed down the projectile the quickest. However, the projectile was slowed down the most effectively in the case of four edges free [40].

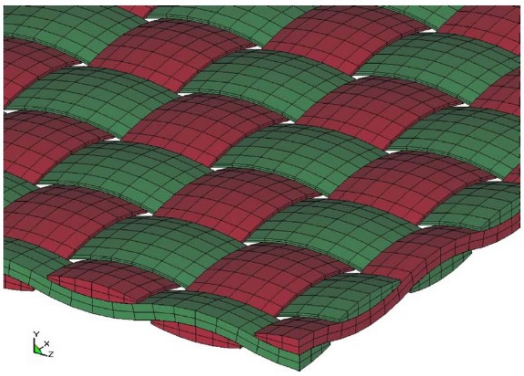

Figure I.19 Mesoscopic model of a fabric using solid element [38].

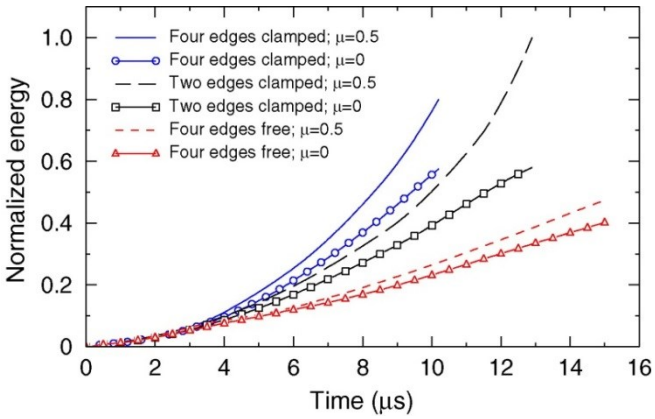

Figure I.20 The loss of projectile kinetic energy as a function of time for the three different boundary conditions [38].

Rao *et al.* [33, 61] conducted modelling of 2D and 3D Kevlar KM2 fabrics using the mesh of, and failure criterion, proposed by Duan. The fibre volume fraction was

considered in order to recalculate the density of yarns. The results confirmed the influence of friction on ballistic performance. It was also noted that near the ballistic limit, the yarn-yarn friction is more critical than the fabric-projectile friction.

Nilakantan *et al.* [19, 47, 48, 62-66] developed new models based on the above works of Duan and Rao in order to evaluate the probabilistic and deterministic impact response of the fabric. Here, one through-thickness element was adopted instead of two. Except for the four elements used in reference [19], five elements were used to discretise the yarn cross-section [62]. The authors also adopted a new mesh [67] in order to introduce a new "thermal growth" method. This method has the capacity to generate the realistic virtual microstructures of woven fabrics.

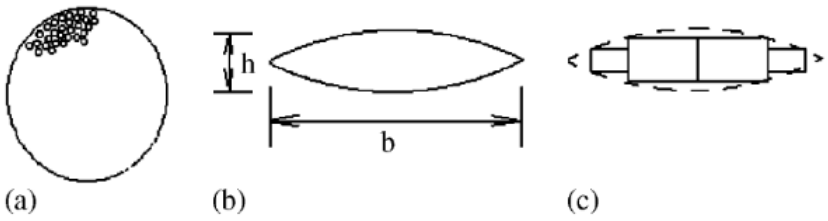

Figure I.21 (a) Circular cross-section of a free yarn; (b) cross-section of an interwoven yarn; (c) cross-sections of an in-woven yarn approximated by rectangular cross-sections of four shell elements.

Besides solid elements, shell elements have also been used in order to reduce the computation time. In 2007, the first model was proposed by Barauskas *et al.* [68] using thin shell elements. The width of the cross-section of yarns was modelled by four shell elements with different thicknesses (Figure I.21). This model not only gains computation time, but also satisfies the level of accuracy.

Ha Minh *et al.* developed some mesoscopic models of Kevlar fabrics inspired by the idea of using shell elements (Figure I.22). In references [3, 59], the authors compared the results of models using meshes with four and eight shell elements per cross-section of yarn (Figure I.23). The results showed that four-elements-models were sufficient to predict the ballistic performance. On the other hand, the authors underlined that in the work of Barauskas [68], the number of integration points through the thickness of one element should be two instead of one in order to better predict the bending resistance of yarns.

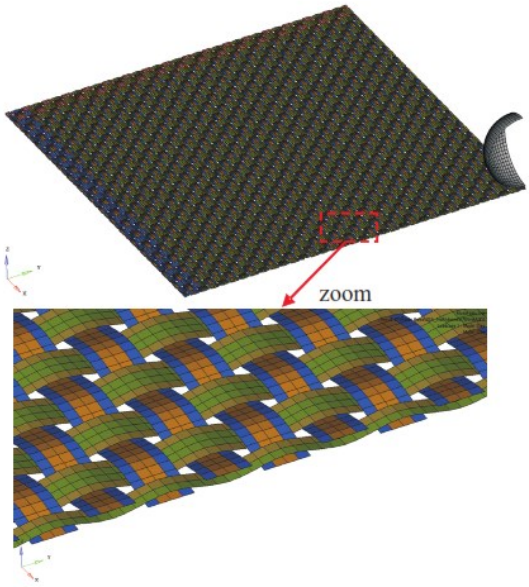

Figure I.22 Mesoscopic model of a fabric using 3D shell element [21]

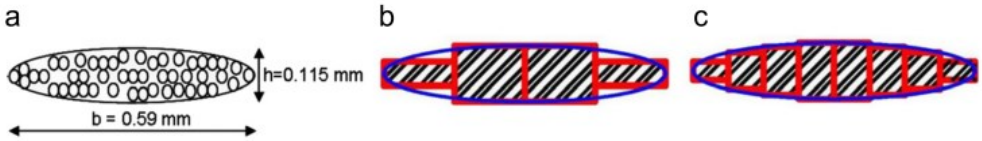

Figure I.23 Cross-section of yarn by shell element (a) a real yarn (b) model of 4 elements (c) model of 4 elements [59].

Figure I.24 shows that the higher the impact velocity is, the closer the behaviour of the macroscopic model is to the behaviour of the mesoscopic one. The reason is that in the case of ballistic impact velocity, the primary yarns mainly stop the projectile; therefore, the behaviours of both models come mostly from the primary yarns.

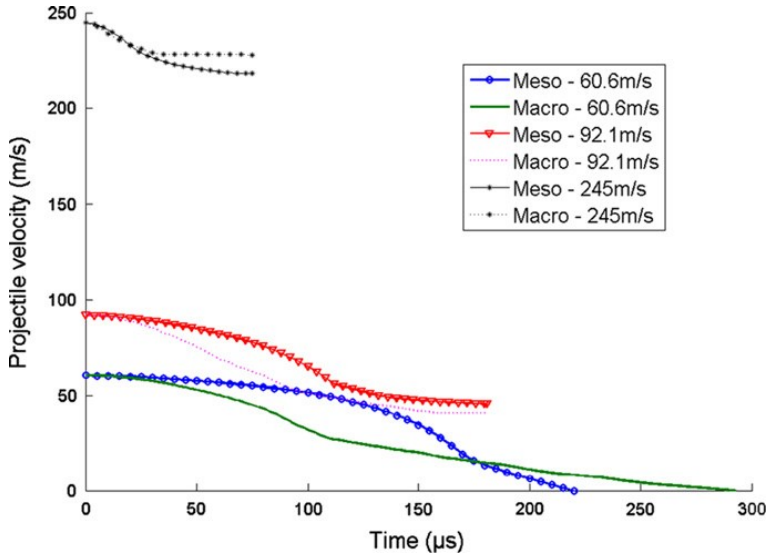

Figure I.24 Projectile velocity evolution versus time [59].

Chu *et al.* [23, 28] also conducted two mesoscopic models of Kevlar woven fabric. Reference [23] investigated the effect of yarn properties on the ballistic performance of a 2D fabric. The effect of yarn density was insignificant, while a very high longitudinal Young's modulus may lead to the premature failure of primary yarns and perforation of the fabric (Figure I.25). The authors also analysed local and global localisation of the failure phenomenon of 3D interlock fabrics in reference [28]. The results showed that impact localisation significantly affects the ballistic performance. The fabric centre impact is more significant than the case of the fabric quarter-centre impact (Figure I.26).

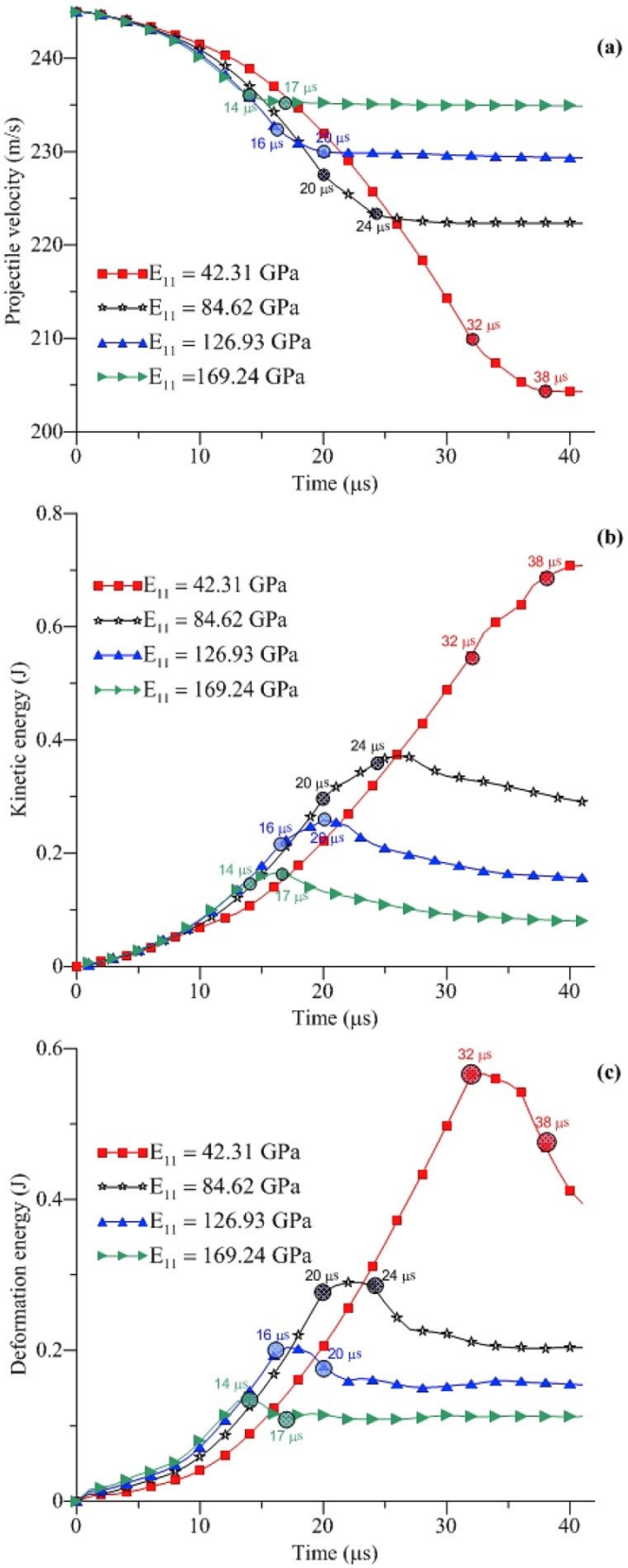

Figure I.25 Time histories of projectile velocity and fabric energies with different longitudinal Young's moduli E_{11} in the perforation impact case: (a) Projectile velocity, (b) Kinetic energy, (c) Deformation energy [23].

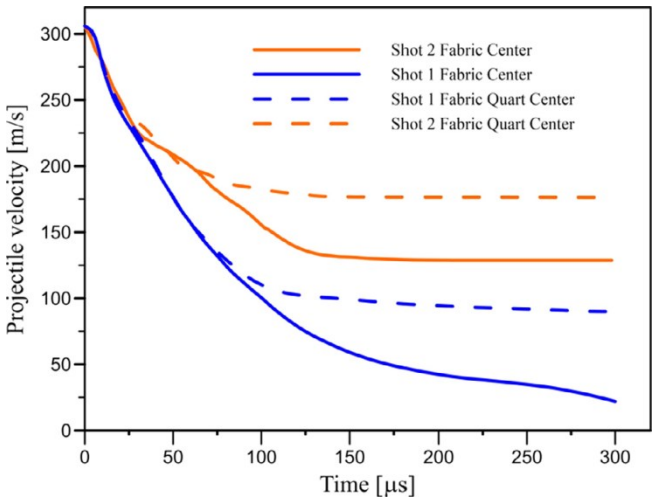

Figure I.26 Comparison of two global locations impact [28, 69]

I.3.3 Macro-meso multi-scale model

Although the mesoscopic model is more realistic than the macroscopic one as it can predict local responses of fabrics, the mesoscopic model consumes more computational resources. On the other hand, the macroscopic models can describe basic and global impact responses of fabrics with low computation time. Therefore, it is necessary to develop a macro-meso multi-scale model which not only can predict impact problems as accurately as the mesoscopic one, but also gains computation time.

Figure I.27 illustrates the configuration of a multi-scale model. The model is comprised of (i) a local and (ii) a global region [61, 68]:

- Local region: a mesoscopic model with finer mesh is applied in this region in order to capture the local reactions of the fabrics. In this region, damage and slippage of yarns occur.
- Global region: a macroscopic model is applied. In this region, no damage occurs. Thus, a coarser mesh is used.

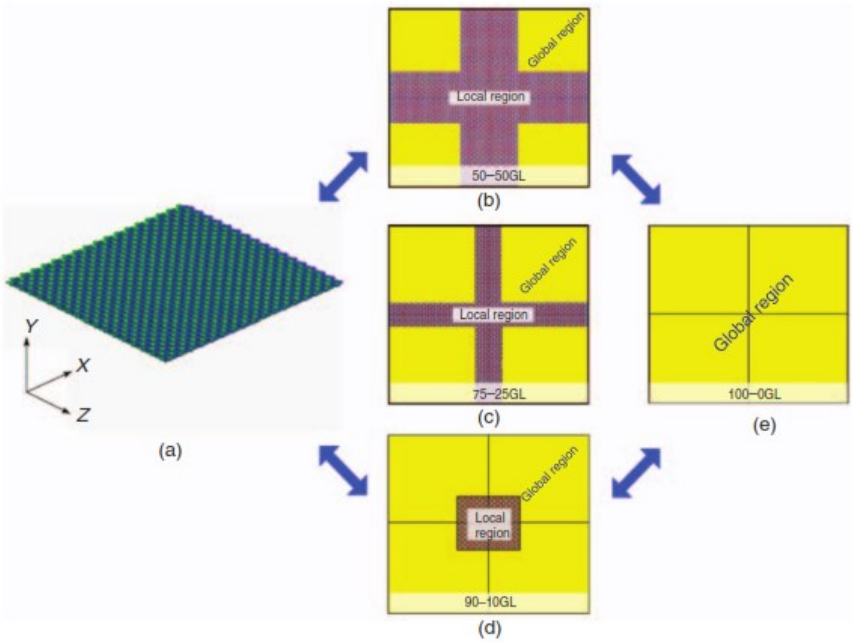

Figure I.27 The conceptualisation of the global/local model [61]

Barauskas *et al.* [68] used tied constraint to connect the two zones. In order to maintain the continuity between local and global zones, the speeds of wave propagation in the two regions were made the same by adjusting the material properties. Rao *et al.* [61] proposed that both the areal density and transverse wave propagation velocity must be the same across the two regions. Thus, the effective density and stiffness of the global region were adjusted, while those of the global region were maintained.

Figure I.28 presents a multi-scale model conducted by Ha Minh *et al.* [58]. The authors used shell elements in order to minimise the computation time by varying the ratio of macroscopic and mesoscopic areas: 75.3–24.7%, 65.5–34.5%, and 56.3–43.7%. The mass density of each region was calculated to ensure that the mass of the multi-scale plate was equal to the real fabric. Acoustic impedance through material cross-section was calculated as proposed in the work of Rao *et al.* [61].

$$Z = A\sqrt{E\rho} \tag{I.9}$$

Where A is the cross-section area of the interface, E is Young's modulus, and ρ is the mass density.

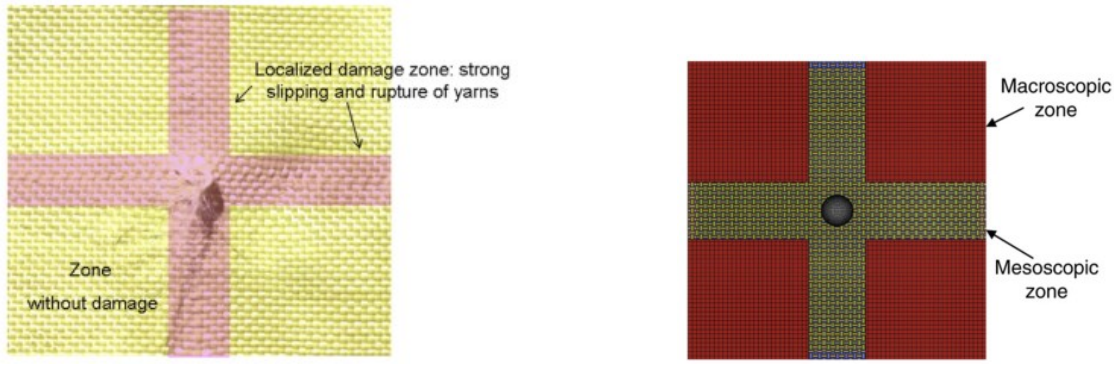

(a) (b)

Figure I.28 Macro-meso multi-scale model: (a) A fabric after impacted (b) global view of the model [58]

The three configurations above were compared with the mesoscopic model (Figure I.29). The authors concluded that the 65.5–34.5% multi-scale model is the pertinent one providing an acceptable precision and a low computation time.

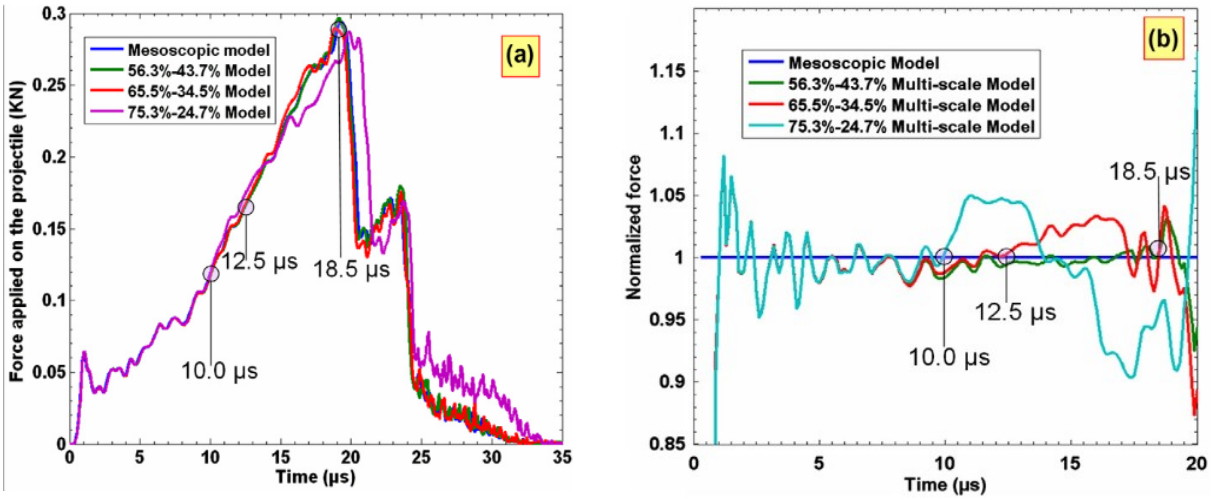

Figure I.29 (a) Force applied on the projectile versus the time in the impact velocity case 60 m/s; (b) normalised force curves [58].

In 2019, López-Gálvez *et al*. [70] conducted a "centre square" multi-scale model using isotropic hypothesis in which the yarns were assumed as an isotropic material. In this model, the impact zone was modelled on the mesoscopic scale while the rest was modelled as a macroscopic model, as shown in Figure I.30a. The results in the case of the isotropic and orthotropic hypotheses, including residual velocity and absorbed energy, were compared in a wide range from low to high velocities. A good fit was obtained. The isotropic model reduced the computational time by up to 60% (Figure I.30b).

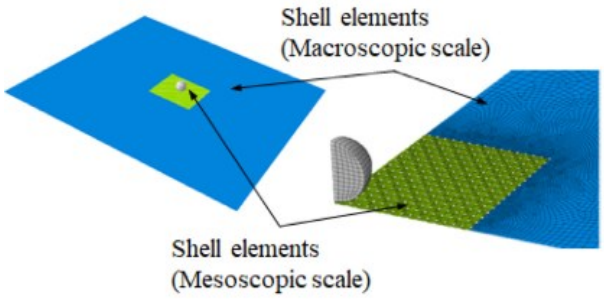

(a)

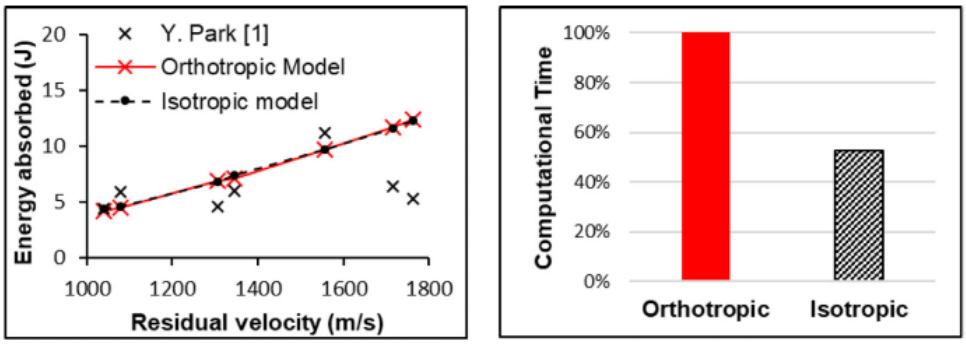

(b)

Figure I.30 (a) Schematic of centre square multi-scale model. (b) Absorbed energy and calculation time required by the isotropic and orthotropic model [70].

I.3.4 Microscopic model

As both the macroscopic and mesoscopic cannot describe the interactions between fibres during the impact process, simulation of fabrics on the fibres scale has also been investigated. Some authors have proposed the notion of an equivalent fibre which can represent a group of fibres. Furthermore, some microscopic models of a single yarn have been conducted.

Zhou *et al.* [71] proposed a new numerical method called the "Digital Element Method". Each fibre was presented by a frictionless pin-connected rod element chain (Figure I.31). Wang *et al.* [72] studied the ballistic impact and penetration of a textile fabric following this method. A yarn was modelled as an assembly of 1–19 digital fibres. This method is able to predict micro-scale phenomena such as fibre failure, fibre–fibre friction, fibre-to-projectile compression, and fibre-to-fibre compression (Figure I.32). However, contact width and longitudinal shear deformation cannot be modelled because rod elements cannot justify the effect of Poisson's ration.

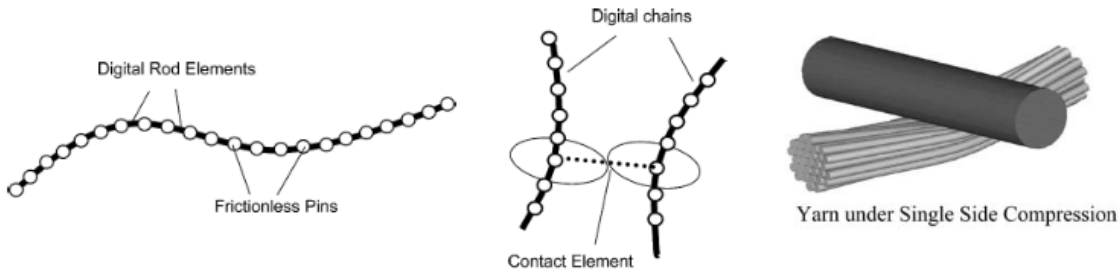

Figure I.31 Digital element fibres [71].

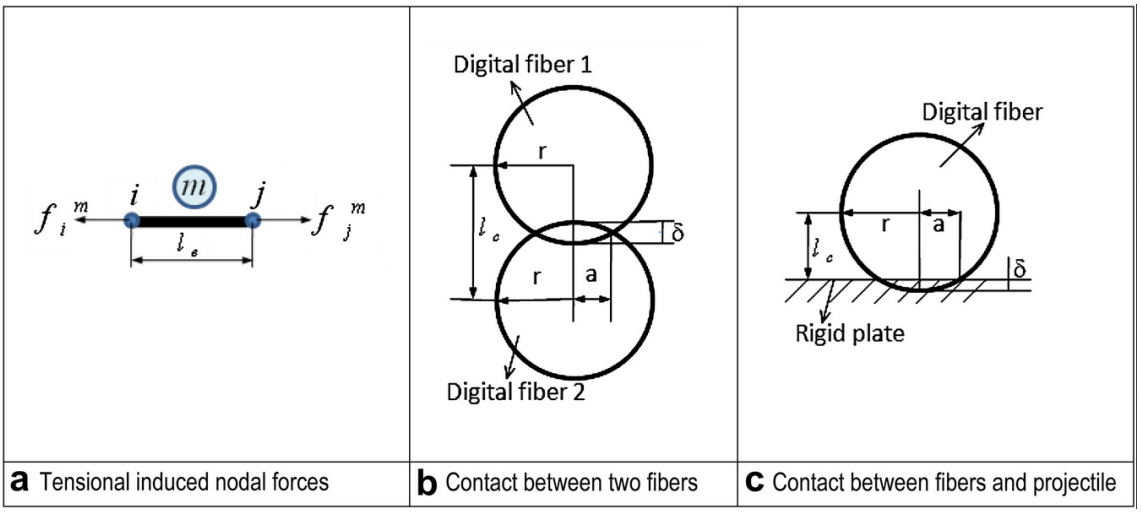

Figure I.32 Nodal force calculations [72].

Grujicic *et al.* [73] improved the approach of Wang *et al.* [72] to determine the ballistic performance of a Kevlar KM2 fabric subjected to a spherical projectile: its penetration resistance, overall deflection, deformation, and damage response. The effect of the fibre's transverse properties and fibre–fibre friction were also investigated. Figure I.33 shows the variation of residual velocity with the initial velocity of the projectile in the three cases of transverse-response conditions. However, besides the models of Zhou and Wang [71, 72], only a sub-yarn model has been developed using a small number of fibres (1 to 30) depicting the yarn instead of hundreds of fibres (Figure I.34). Therefore, these models cannot predict the behaviour of one single fibre on the microscopic scale.

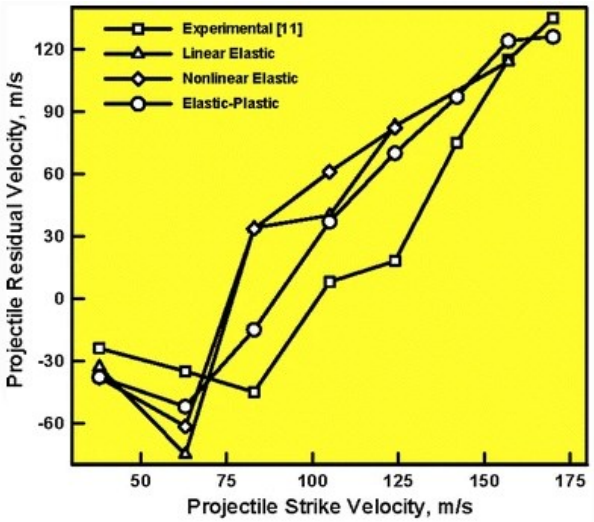

Figure I.33 The variation of residual velocity with the initial velocity of the projectile in the three cases of transverse-response conditions [73].

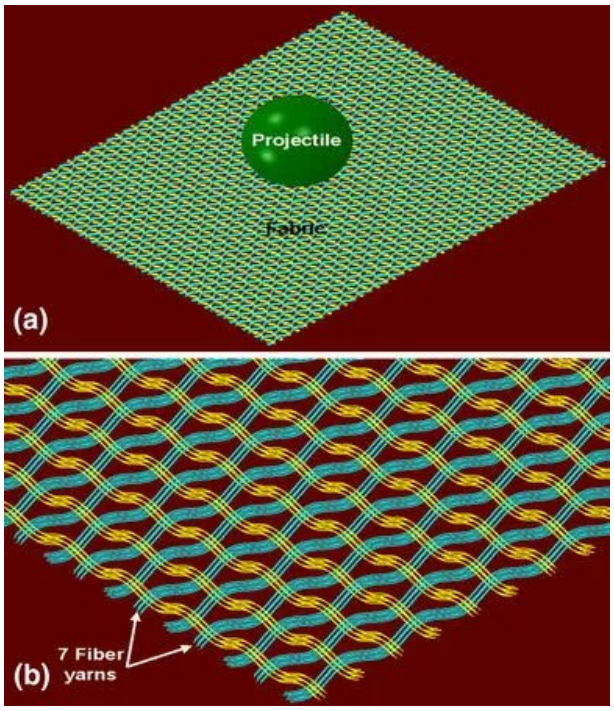

Figure I.34 (a) A geometrical model for the projectile/fabric interaction problem analysed in the present work and (b) a close-up of the fabric region showing sub-yarn microstructure and the yarn-weave pattern [73].

Nilakantan [74] developed the first "fully fibre scale" model of one single straight Kevlar KM2 yarn subjected to ballistic impact. Details of the setup of the model are shown in Figure I.35. The yarn comprised 400 fibres modelled by nine solid elements. Each fibre was assumed to be orthotropic. A close hexagonal packing of the filaments, which ensured the maximum yarn packing density of 0.907, was used. Three extra fibres were placed on the outer edge of the yarn in order to precisely obtain the number of 400

fibres. Two cases, wall constrained (constraining fibres from spreading sidewards) and unconstrained, were investigated. The deformation, mobility, and redistribution of fibres in the case of unconstrained, were observed (Figure I.36). The results showed that the transverse displacement wave propagation, the projectile deceleration rate, and the growth of yarn internal energy rate were not affected by this constraint. The effects of fibre-fibre friction, transverse elastic, and shear moduli on the transverse wave displacement were independent of the constraint as well.

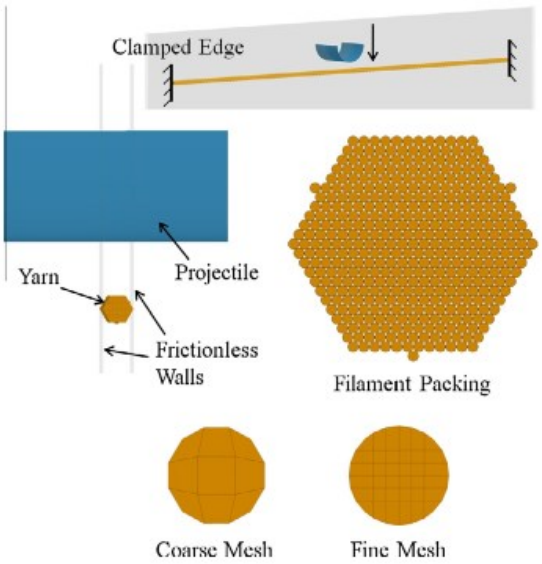

Figure I.35 Setup of the yarn transverse impact test [74].

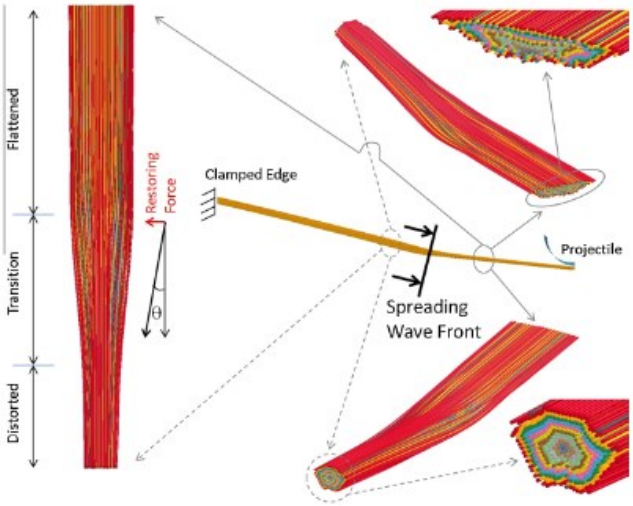

Figure I.36 Propagation of the spreading wave in the unconstrained case with V_i = 100 m/s [74].

Sockalingam *et al.* [75] also conducted a 3D finite element microscopic model of one single Kevlar KM2 yarn subjected to ballistic impact in order to better predict fibre

damage criteria, along with the fibre-fibre and the fibre-projectile interaction. The cross-section was assumed to be an ellipse. Figure I.37 illustrates the arrangement of 400 fibres. The results clearly showed that fibre failure is sensitive to the longitudinal shear modulus. Stress wave propagation, absorbed energy, and deformation of fibres were also observed.

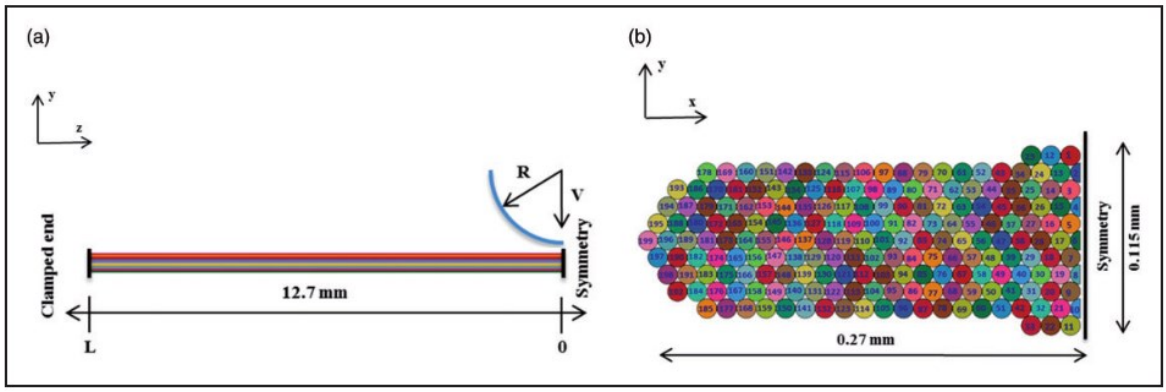

Figure I.37 Quarter symmetric three-dimension fibre-level yarn model [75].

Figure I.38 presents the sub-yarn level model of one single Kevlar KM2 yarn in the work of Chu [4]. In this work, the author proposed the notion of an equivalent fibre with a diameter of 36 µm, representing about ten fibres. Thus, the number of equivalent fibres in a yarn is 42 instead of 400 real fibres (Figure I.38b). The cross-section of the equivalent fibre was modelled by shell elements (Figure I.38c)).

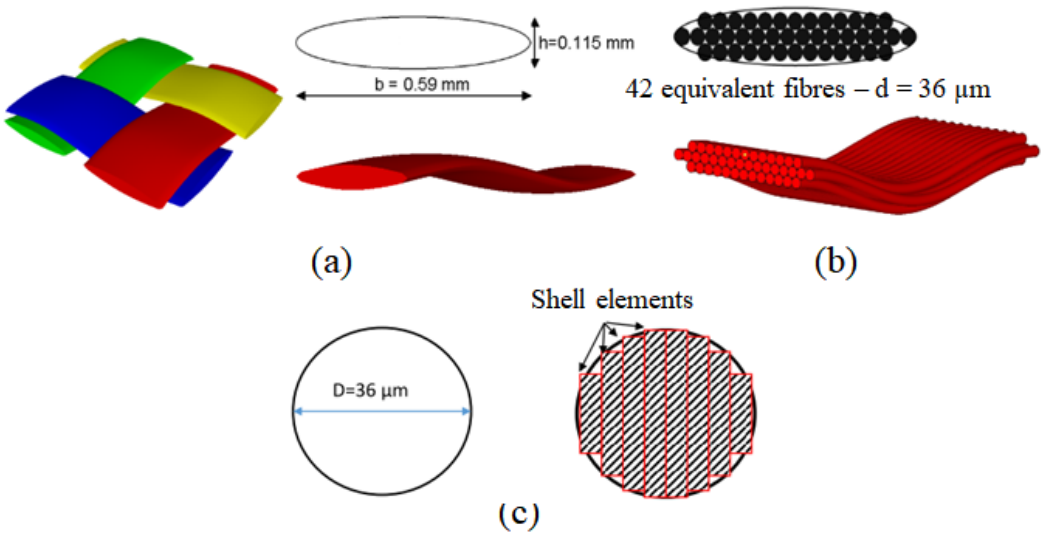

Figure I.38 Model of one fibre (a) mesoscopic model, (b) microscopic model, (c) cross-section of one equivalent fibre [4].

This sub-yarn model is then applied in order to predict the micro behaviour of two primary yarns in a fabric subjected to ballistic impact, as shown in Figure I.39a. Results showed a good agreement with the mesoscopic model (Figure I.39b). However, the fibre-fibre interactions were not fully predicted due to the limits of the shell element.

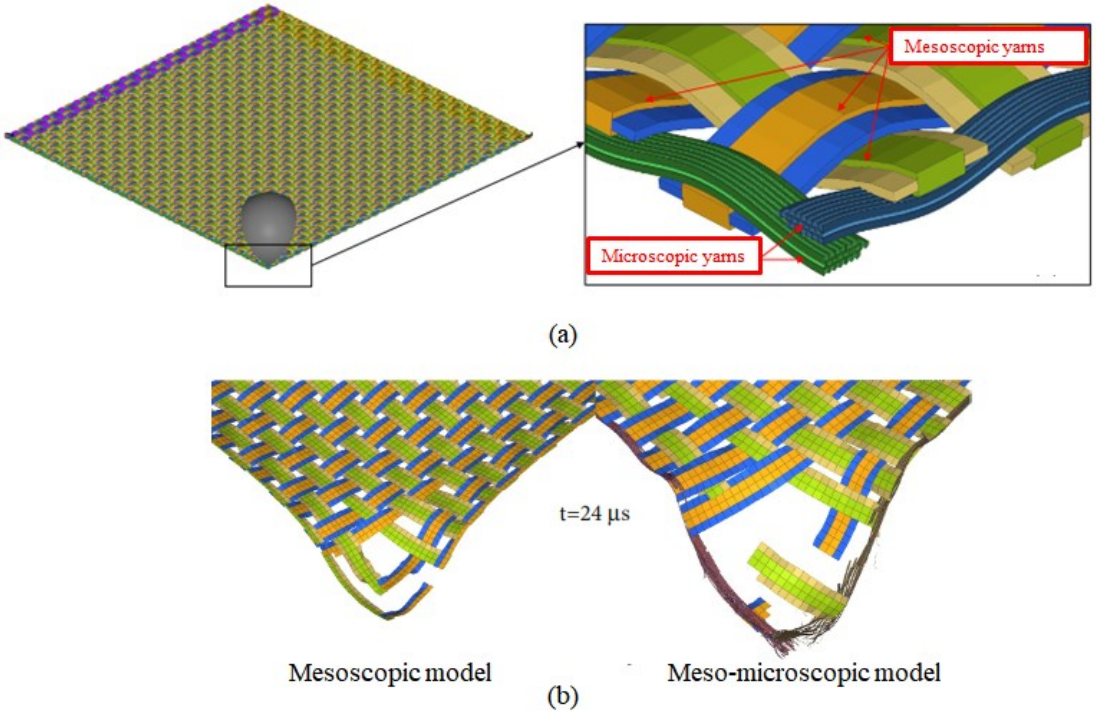

Figure I.39 (a) a quarter of model, (b) Comparison of fabric failure [4].

In reference [4], another micro-mesoscopic multi-scale model of fabric was also proposed (Figure I.40). In this model, the impact zone was modelled on the fibre-scale level, while the rest was at yarn-level scale. Unlike the previous model, in this one, solid elements were utilised. A micro-mesoscopic yarn was also introduced (Figure I.40b). The deformation and distribution of fibres in the impact zone were observed, as shown in Figure I.41.However, this model cannot predict the fibre failure mechanism due to the limit of lateral spreading of fibres in the multi-scale yarn.

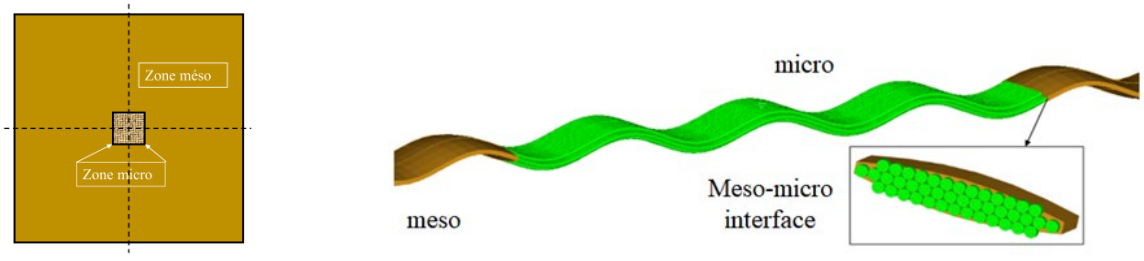

Figure I.40 Micro-mesos multi-scale model (a) global view, (b) multi-scale yarn [4].

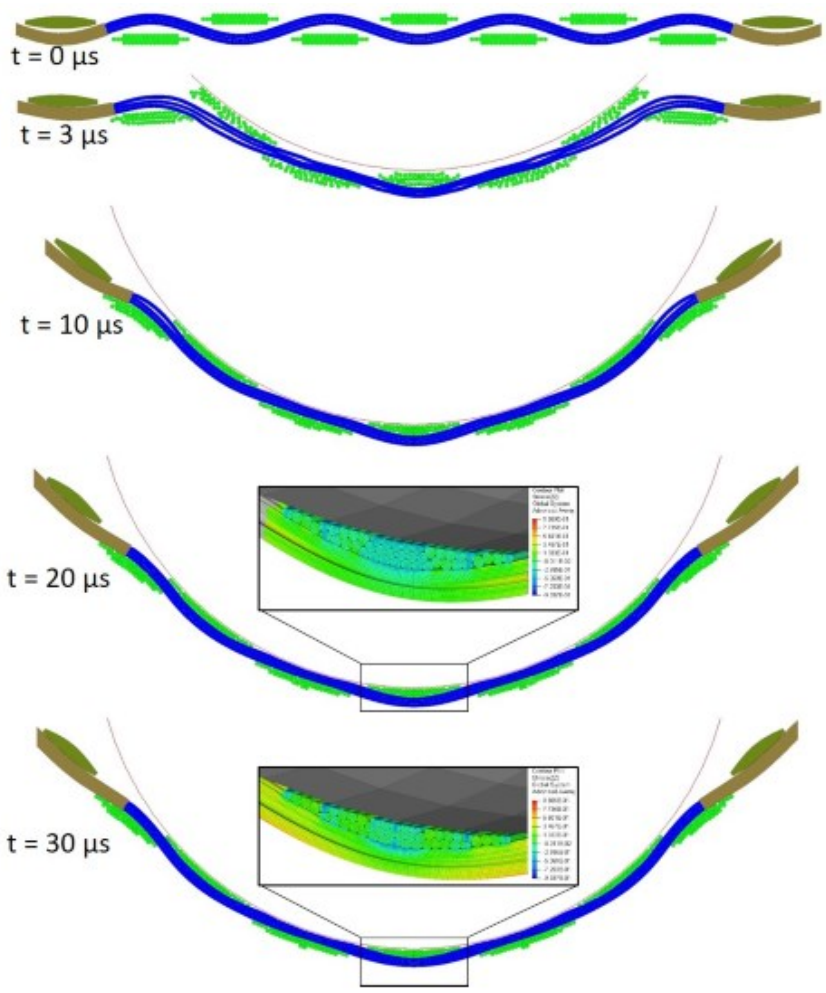

Figure I.41 Fibres deformation and distribution in the impact zone versus time [4].

Recently, Del Sorbo *et al.* [76] also developed a microscopic model of one single Kevlar KM2 yarn, subjected to transverse impact, using a discrete element method (DEM). In this model, truss elements were adopted instead of the 3D solid elements used in the two previous models. Additionally, the cross-section of the yarn was assumed to be circular. Yarn deformation (Figure I.42), projectile velocity, and impact energy were obtained. Sensitivity to friction was also investigated. The results showed a good agreement in comparison with the finite element model of Nilakantan [74]. However, individual fibre deformation was not captured, and there were differences in the post-failure phase.

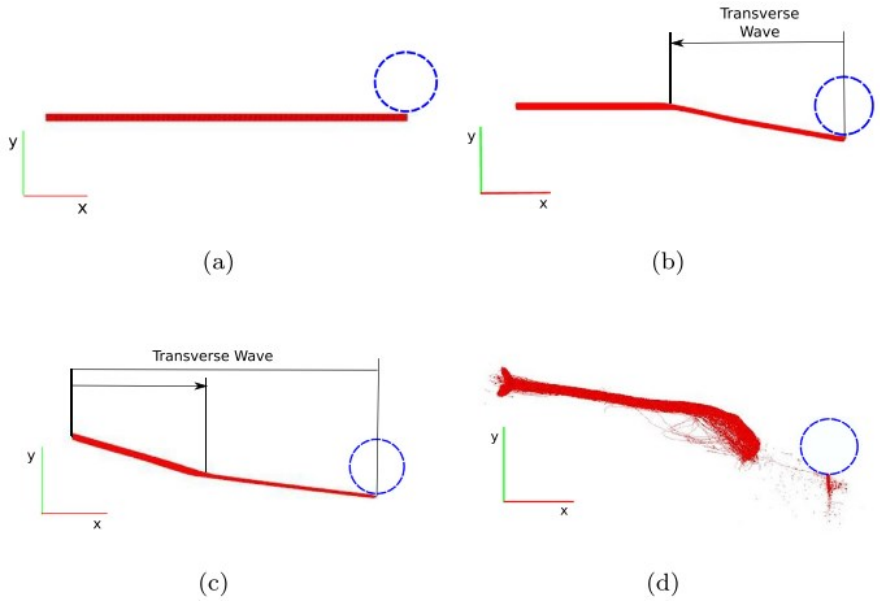

Figure I.42 Deformation of yarn [76].

I.4 Microscopic transverse compressive behaviour of Kevlar fibres

In this part, the state of the art in the investigation of microscopic transverse compressive behaviour of Kevlar fibres is presented. Transverse compressive behaviour of Kevlar fibres has been analytically, experimentally and numerically investigated. Up to now, it has been assumed that the fibre material is transversely isotropic with the constitutional relationship shown in the following equation [77]:

$$\begin{Bmatrix}\sigma_{11}\\ \sigma_{22}\\ \sigma_{33}\\ \sigma_{12}\\ \sigma_{23}\\ \sigma_{31}\end{Bmatrix}=\begin{pmatrix}C_{11} & C_{12} & C_{13} & 0 & 0 & 0\\ C_{12} & C_{11} & C_{13} & 0 & 0 & 0\\ C_{13} & C_{13} & C_{33} & 0 & 0 & 0\\ 0 & 0 & 0 & C_{44} & 0 & 0\\ 0 & 0 & 0 & 0 & C_{55} & 0\\ 0 & 0 & 0 & 0 & 0 & C_{55}\end{pmatrix}\begin{Bmatrix}\varepsilon_{11}\\ \varepsilon_{22}\\ \varepsilon_{33}\\ \gamma_{12}\\ \gamma_{23}\\ \gamma_{31}\end{Bmatrix} \tag{I.12}$$

Where the coefficients C_{ij} of the constitutive matrix are as follows:

$$\begin{aligned} &C_{11}=\frac{(1-n\nu_{31}^2)E_1}{AB},\quad C_{12}=\frac{(\nu_{12}+n\nu_{31}^2)E_1}{AB},\quad C_{44}=G_{12}=\frac{E_1}{2A}\\ &C_{13}=\frac{\nu_{31}E_1}{B},\quad C_{33}=\frac{(1-\nu_{12})E_3}{B},\quad C_{55}=G_{13}=G_{23}\\ &A=1+\nu_{12},\quad B=1-\nu_{12}-2n\nu_{31}^2,\quad n=E_1/E_3 \end{aligned} \tag{I.11}$$

Here, E, G and ν represent the Young's modulus, shear modulus, and Poisson's ratios, respectively, and n represents the degree of anisotropy. The longitudinal axis of the fibre is denoted as 1, while 2-3 represent the transverse plane (Figure I.43).

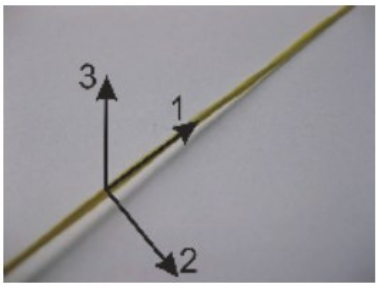

Figure I.43 The direction of the fibre.

I.4.1 Analytical theory

The analytical theory was developed based on the complex variable method for Hertzian contact in the work of M'Ewen [78]. Jawad *et al.* [79] and Cheng *et al.* [77] developed a linear elastic analytical solution for a single fibre transverse compression response. One single fibre was assumed to be compressed by a rigid plate (Figure I.44). No friction was introduced in the contact zone.

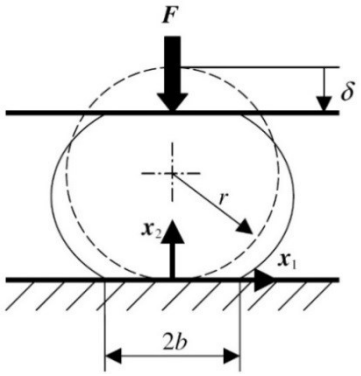

Figure I.44 Schematic of a single fibre compression [77].

As the cross-section dimension of a single fibre can be negligible in comparison with its length, a 2D plane strain problem was considered. The material was assumed to be transversely orthotropic. The load-displacement relationship was proposed as follows:

$$\delta = \frac{4F}{\pi b^2}\left[\left(-\frac{\nu_{12}}{E_1}-\frac{\nu_{31}^2}{E_3}\right)\left(\sqrt{b^2+r^2}-r\right)r+\left(\frac{1}{E_1}-\frac{\nu_{31}^2}{E_3}\right)b^2\ln\frac{\sqrt{b^2+r^2}+r}{b}\right] \tag{I.12}$$

$$b = \sqrt{\frac{4Fr}{\pi}\left(\frac{1}{E_1}-\frac{\nu_{31}^2}{E_3}\right)} \tag{I.13}$$

Where F denotes the load per unit length along the fibre longitudinal direction, E_1, and E_3 are Young's modulus in the transverse plane and the longitudinal direction. b is the contact width, r denotes the radius of the fibre.

I.4.2 Experimental works

Kawabata [80] proposed the first experimental protocol to study the transverse compressive behaviour of Kevlar 29, 49, 119 and 149 single fibre. The result clearly showed a yielding in the transverse compression allowing the author to determine the transverse modulus of the fibre. Afterwards, Singletary *et al.* [81, 82] Cheng *et al.* [77, 83] and Sockalingam *et al.* [84] conducted some transverse compression experiments for the case of one single Kevlar fibre.

Figure I.45 presents loading condition of single fibre compression test of Singletary *et al.* [81, 82]. A single Kevlar 29 fibre was laid on a flat, stiff platen and compressed by another parallel platen. The platen was designed to ensure the smooth contact between fibre and platens. Results showed a nonlinear load-deformation response (Figure I.46).

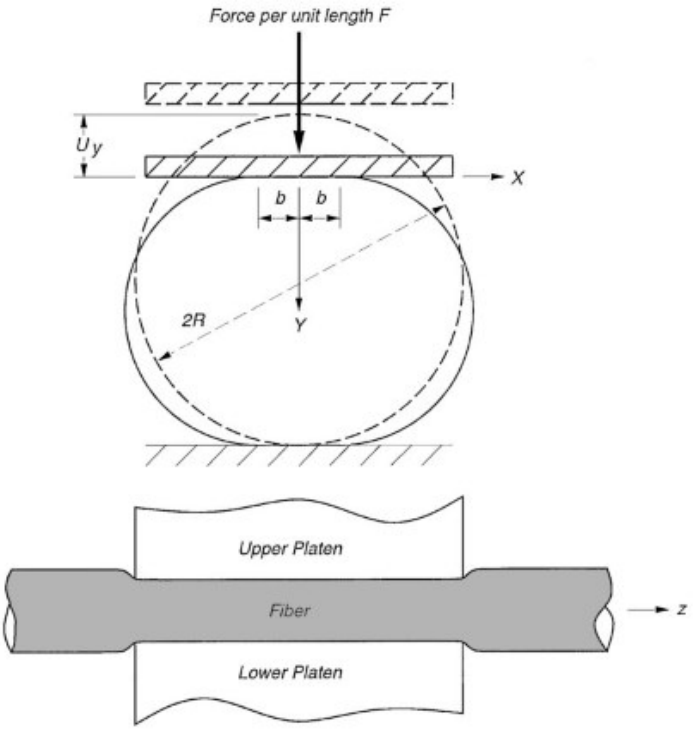

Figure I.45 Loading condition of single fibre compression test [81].

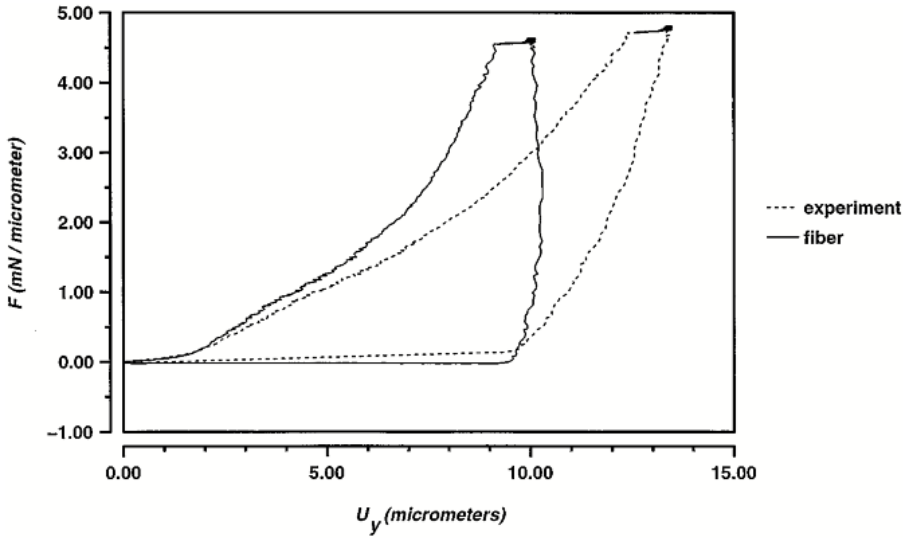

Figure I.46 Experimental and extracted fibre force – deflection curves [81].

In the works of Cheng *et al.* [77, 83], the results showed the nonlinear, pseudo-elastic transverse mechanical properties of Kevlar KM2 fibres in the case of large deformation (Figure I.47). The authors concluded that Kevlar KM2 fibres possess the same phenomena as the nonlinear behaviour of the Mullin's effect in rubber materials. Afterwards, Sockalingam *et al.* [84] also conducted a similar experiment in order to capture the quasi-static transverse deformation behaviour of Kevlar KM2 fibres. Fibre damage evolution, as well as contact width and fibre compressed width in a relationship with the compression load, were obtained.

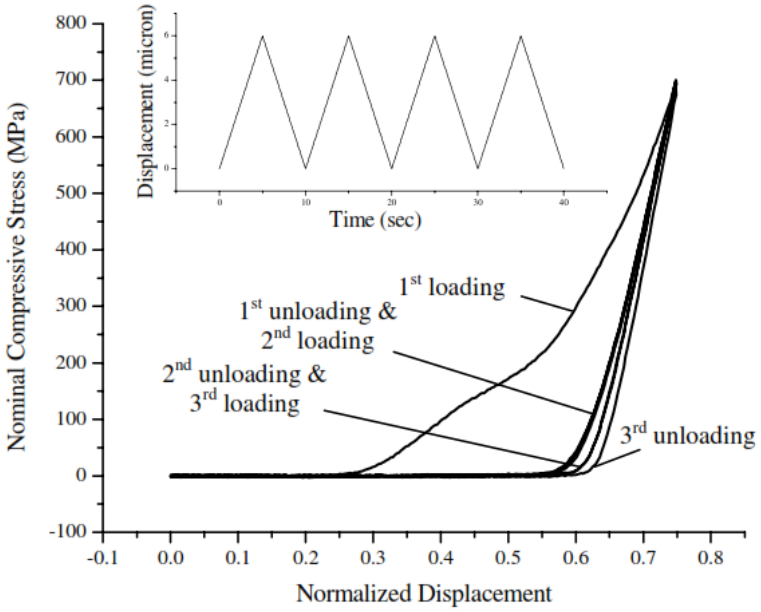

Figure I.47 Cyclic transverse loading of a Kevlar KM2 fibre at a nominal strain rate of 0.075/s [77].

Figure I.48 presents the experiment conducted by Bourgoyne and Brown [85] in order to investigate the transverse properties of a block of Kevlar 49 fibres. A block of fibres removed from a suitably sized parallel-lay rope was placed inside a chamber, as shown in Figure I.48a. The plunger was pushed by an applied force to measure the corresponding displacement. Then a load-displacement curve was obtained (Figure I.48b). The results clearly showed that as the load increased, the fibre block's stiffness changed. Significant differences between the unloading/reloading responses in each loading cycle were also observed.

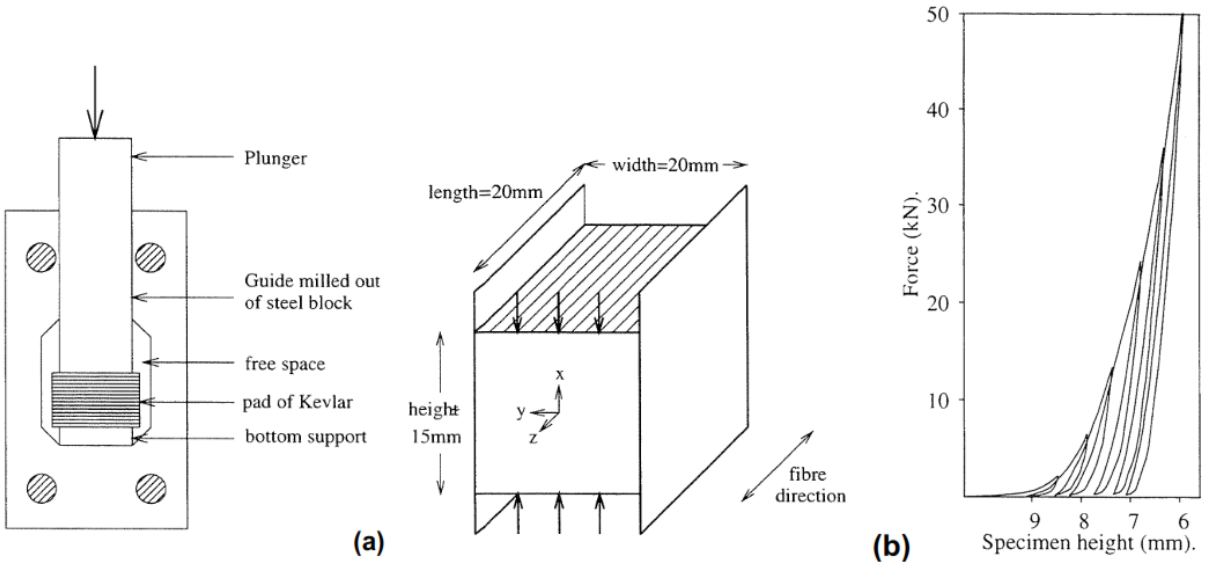

Figure I.48 (a) Compression test rig and fibre layout (b) Typical load-deflection response [4, 85].

I.4.3 Numerical modelling

Besides the experimental part in reference [77], the authors also conducted a numerical model. Nominal stress and nominal strain were introduced. Nominal stress was defined as the load per unit length divided by the initial fibre diameter, while nominal strain was defined as the platen displacement divided by the initial fibre diameter given by the following equations:

$$\bar{\sigma} = \frac{F}{2r} \tag{I.14}$$

$$\bar{\varepsilon} = \frac{\delta}{2r} \tag{I.15}$$

Figure I.49 shows the nominal stress – nominal strain curve in comparison with the experimental data. It is noted that after the nominal strain of about 15%, the numerical model cannot accurately predict the transverse compressive behaviour of the fibre.

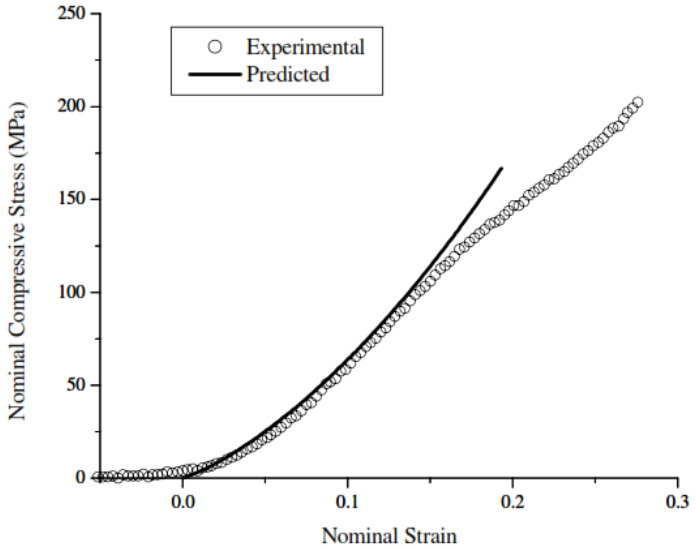

Figure I.49 Comparison between model prediction and experimental data [77].

In 2014, Sockalingam *et al.* investigated transverse compressive behaviour of Kevlar KM2 fibres on the case of one single fibre as well as the case of one single yarn in fibre scale using the finite element method [86]. A 2D plane strain problem was assumed. A mesh convergence was studied. The nominal stress-strain curve of one single fibre was obtained with a good agreement with the analytical and experimental data. Then, the microscopic model of one yarn comprised 400 fibres was conducted. The yarn was compressed by two adjacent ones, which were considered rigid, as shown in Figure I.50.

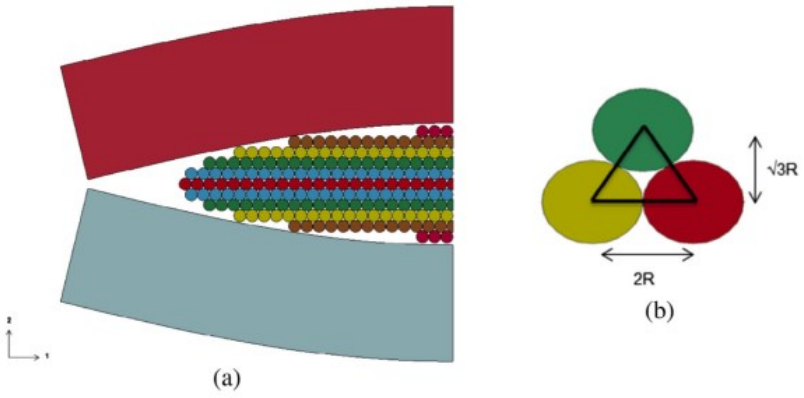

Figure I.50 Fibre scale yarn half symmetric FE model and fibre packing [86].

Figure I.51 shows the results of the model. Force - displacement and apparent stress - apparent strain curves were obtained. It clearly shows a high nonlinearity behaviour.

The effect of friction between fibres was also studied. The authors highlighted the important role of fibre–fibre contact in the spreading, interaction, and deformation of individual fibres.

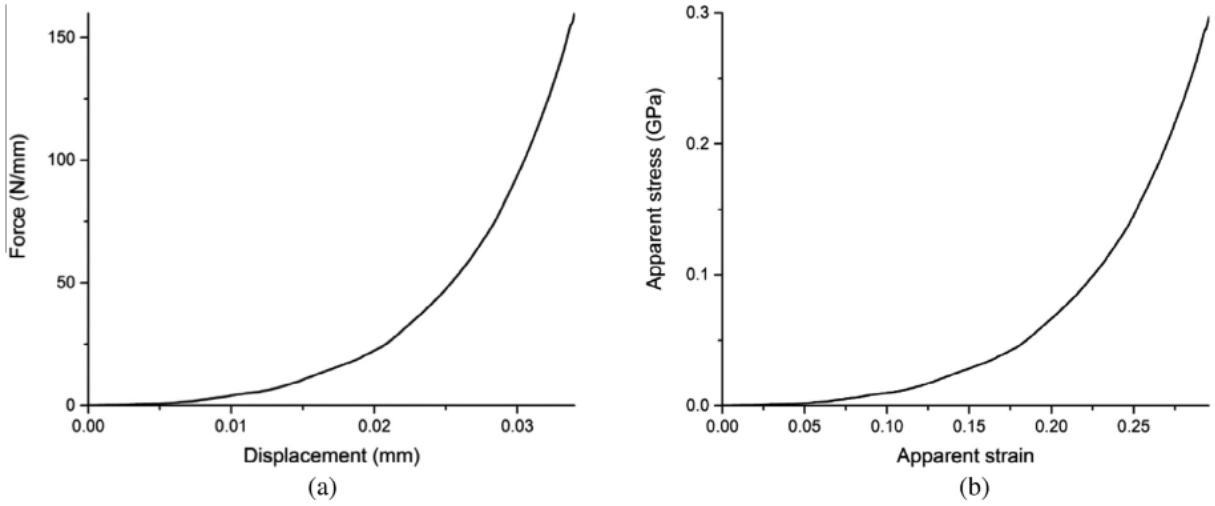

Figure I.51 Yarn transverse compression response predicted (a) force displacement curve (b) apparent stress–apparent strain [86].

I.5 Elementary homogenization approach of transverse compressive behaviour of Kevlar yarns

In this part, the elementary homogenisation approach of transverse compressive behaviour of Kevlar yarns is reviewed. This approach aims to obtain an effective transverse material law for the equivalent homogenised yarn. This homogenised yarn allows not only the obtention of acceptable results, but also a reduction of computation time.

Figure I.52 presents the computational modelling approach for FE analysis of fabric compression of Hua *et al.* [87]. A unit cell was compressed between two parallel plates. The authors proposed a nonlinear material law for one homogenised yarn, in which the nominal stress, strain and Young's modulus are approximated as a power function of the volume fraction, as follows:

$$E_{33} = \frac{\sigma_{33}}{\varepsilon_{33}} = \frac{-a\left(\dfrac{V_{f0}}{e^{\varepsilon_T}}\right)^b + a\left(V_{f0}\right)^b}{\varepsilon_{33}} \tag{I.16}$$

Where σ_{33} and ε_{33} are stress and strain in the longitudinal direction, V_{f0} denotes the initial fibre volume fraction, and a and b are experimentally determined parameters.

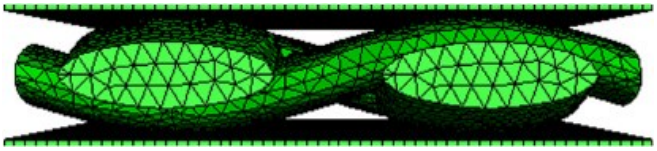

Figure I.52 Simulation setup for plain weave unit cell compression [87].

Numerical models were conducted in order to compare with the experimental data in terms of strain – pressure. Figure I.53 shows a good agreement between the numerical results and experimental data. However, these relationships were obtained by fitting McBride's E-glass yarn compression. This empirical law is very far from reality because no strain rate and interactions were considered.

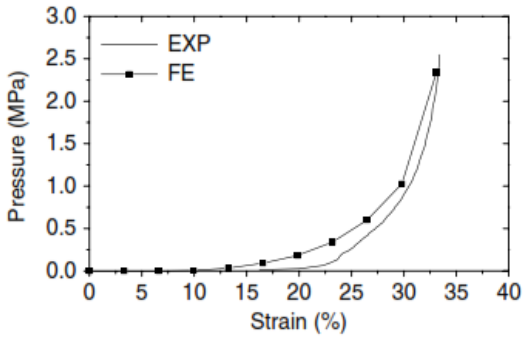

Figure I.53 Comparison between FE analysis and experimental data in the case of plain weave fabric [87].

Figure I.54 presents a homogenised yarn proposed by Sockalingam [86]. An elliptical cross-section was assumed. The material properties were taken from the works of Rao *et al.* [61] (case A), and Cheng *et al.* [83] (case D). The authors also proposed two sets of properties (case B and C). However, the authors did not explain how these properties were obtained. Additionally, the properties were not nonlinear; therefore, the model cannot accurately capture the transverse loading response of the yarn (Figure I.55). Finally, the authors highlighted the need for a nonlinear material law of the homogenised yarn in order to accurately predict the transverse compressive behaviour.

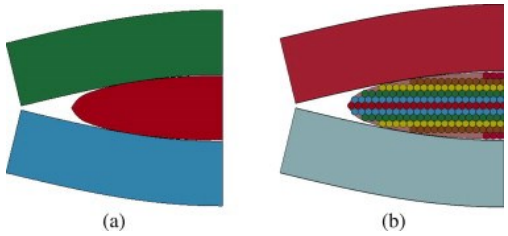

Figure I.54 (a) homogenised yarn model (b) overlay of homogenised yarn and 400-fibre models [86].

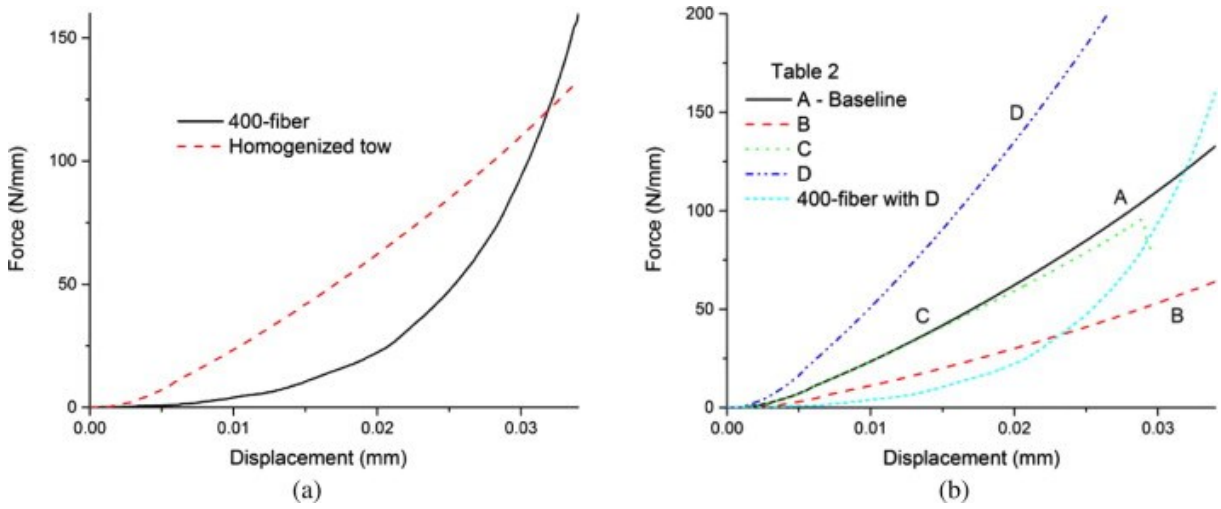

Figure I.55 (a) homogenised yarn model in comparison with the microscopic scale model (b) parametric study [86]

I.6 Synthesis and conclusion

Studies on the ballistic performance of textile fabrics have been reviewed. Deformation mechanisms, including deformation wave propagation and deformation pyramid formation, have been described. The response of the fabric subjected to ballistic impact is very complicated with local and global response modes. This performance is determined by many factors, such as material properties, friction, and projectile properties.

The state of the art in fabric ballistic impact modelling has been presented. Three types of model scale are commonly used: macroscopic, mesoscopic, and microscopic scales. The macroscopic model can predict the global behaviour of the fabric; however, yarn failure and windowing cannot be simulated using this scale. The mesoscopic model has the capacity for these phenomena, but with a higher computational time. Thus, the macro-meso multi-scale model was developed in order to predict the behaviour of textile fabrics on the yarn scale, with a reasonable computational cost. This model consists of mesoscopic and macroscopic regions. The mesoscopic region is located in the impact zone, in which yarn failure occurs, while the macroscopic is placed far away from the impact zone with no failure.

The microscopic model has been developed since the beginning of 2000s. This model can accurately predict the ballistic performance on the fibre scale. However, the computational cost is very high due to a huge number of elements and fibre-fibre interactions. Up to now, there is no fully microscopic model of the fabric. Some models

of the fabric have been developed with the concept of equivalent fibre. A digital element was adopted in order to depict the yarn by a smaller number of digital elements instead of hundreds of fibres. Numerical models of one single yarn have been developed. Fibre failure and fibre-fibre interactions were observed. However, the models have not been validated by the experimental data. Additionally, the configuration of fibres within a yarn is different from a realistic one. Transverse compressive behaviours of one single fibre and one single yarn have been investigated using a 2D plane strain assumption. The results show a highly non-linear elastic behaviour. It was observed that the effect of friction is negligible. The elementary homogenization approach of textile fabrics ballistic performance has also been conducted. In the case of transverse compressive behaviour of one yarn, some effective homogenised material laws have been proposed. However, these laws are empirical, linear elastic, and thus cannot predict the non-linear elastic behaviour.

In the following works of the thesis, the microscopic behaviour of the fibres of woven material will be investigated in the case of transverse compressive behaviour and ballistic responses of a fabric. Microscopic transverse compressive behaviour of fibres will be considered by taking into account the contacts between fibres and the variation of fibre volume fraction. Based on numerical homogenization approach, an effective transverse homogenized material law of one yarn will be obtained. The ballistic responses of the fibres are also analysed using a meso-microscopic multi-scale model. In this case, local fibre failure and the interactions between fibres and fibres-yarn in the impact zone are predicted.

Chapter II

Numerical Analysis of Microscopic Transverse Compressive Behaviour of Fibres

Abstract

In this chapter, the microscopic transverse compressive behaviour of fibres is analysed. Indeed, the study of compression on this scale is motivated by the responses of the projectile in the area affected by the impact. Numerical modelling is developed in four configurations: (i) a single fibre; (ii) two fibres; (iii) a block of fibres; (iv) a yarn. Numerical calculations are performed in the case of transverse compression using the assumption of 2D plane strain. In addition, the mesh convergence is studied in order to find the optimal number of finite elements for a cross-section of a fibre. The interactions with the friction between each fibre are considered. Non-linear evolution of the nominal stress and strain in the case of transverse compression of one and two fibres is obtained. This modelling is verified in the case of two Kevlar fibres (Kevlar® KM2 and Kevlar® 49). In the case of a block of fibres, we investigate the effects of friction on mechanical responses in terms of apparent stress-strain curves. The numerical results are validated by comparison with the experimental data.

Numerical modelling is applied to analyse the behaviour of one yarn composed of 400 fibres subjected to transverse compression, considering the elliptical shape the cross-section of the yarn. The mechanical response in terms of force-displacement curves clearly shows two main zones: (i) a zone of rearrangement of fibres where the volume fraction of the fibres is constant, (ii) a zone of non-linear behaviour corresponding to the compression of fibres where the volume fraction of the fibres increases with displacement. A relationship between the apparent effective strain and the volume fraction is also obtained.

Résumé

Dans ce chapitre, le comportement en compression transversale microscopique des fibres est analysé. En effet, l'étude de la compression à cette échelle est motivée par l'action du projectile dans la zone affectée par l'impact. Une modélisation numérique a été développée dans quatre configurations, à savoir: (i) une seule fibre, (ii) deux fibres, (iii) un bloc de fibres et (iv) un fil. Des calculs numériques sont effectués dans le cas d'une compression transversale en utilisant l'hypothèse d'une déformation plane 2D. De plus, la convergence du maillage est étudiée en vue de vérifier le nombre optimal d'éléments finis pour une section transversale d'une fibre. Les interactions avec la friction entre chaque fibre sont prises en compte. On note bien l'existence d'une évolution no-linéaire de la contrainte et déformation apparentes dans le cas de la compression transversale d'une et de deux fibres. Cette modélisation a été vérifiée dans le cas de deux fibres en Kevlar (Kevlar® KM2, Kevlar® 49). Dans le cas d'un bloc de fibres, nous avons étudié les effets de la friction sur les réponses mécaniques en termes de courbes contrainte-déformation apparentes. Les résultats numériques ont été validés par confrontation avec des données expérimentales.

La modélisation numérique a été appliquée pour analyser le comportement d'un fil composé de 400 fibres soumis à une compression transverse, en prenant en compte l'aspect elliptique du fil. La réponse mécanique en termes de courbes Force-Déplacement a mis en évidence l'existence de deux zones principales : (i) zone de réarrangement des fibres où la fraction volumique des fibres est constante, (ii) zone de comportement non-linéaire correspondant à la compression des fibres où la fraction volumique des fibres augmente avec le déplacement. Ce constat a conduit à l'établissement d'une corrélation entre la déformation effective apparente et la fraction volumique.

Contents

II.1 Introduction

The ballistic impact process of a woven fabric is very complicated due to the high velocity and complex structure of the fabric. It is well known that a fabric consists of many yarns comprising of hundreds of fibres, as shown in Figure II.1. This complex multi-scale structure poses a big challenge in predicting the ballistic behaviour of the material at the fibre scale.

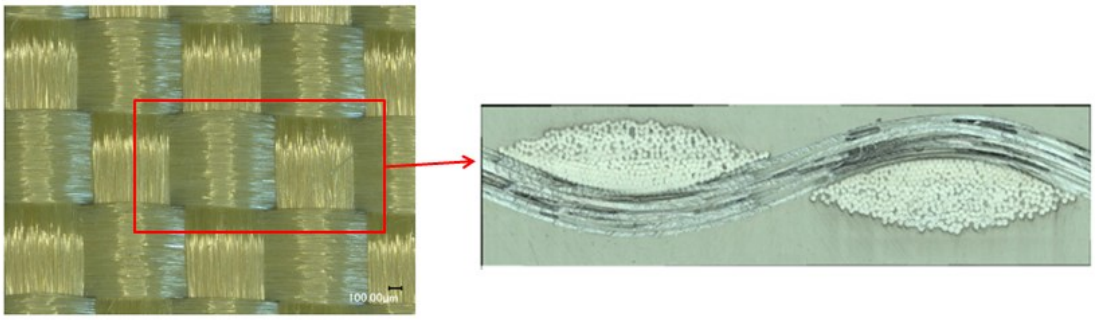

Figure II.1 Multi-scale structure of a fabric [74].

During the impact event, a projectile strikes the fabric resulting in the formation of a deformation pyramid. In the impact zone, yarns are not only locally subjected to longitudinal tensile but also transverse compressive loading, as shown in Figure II.2a. Furthermore, in the yarn-scale model, within the impact zone, transverse compressive behaviour is mainly observed (Figure II.2b). One yarn can be considered to be compressed by the neighbouring ones (Figure II.2c). However, at the yarn-scale, fibre–fibre interaction, fibre deformation, as well as fibre failure have not been sufficiently investigated.

In this chapter, our work focuses on studying the compression behaviour of both fibres and yarn using a microscopic scale approach. This analysis is necessary to better understand and predict the local responses of the fabric under ballistic impact. Indeed, we have developed numerical modelling considering four configurations of transverse compression: (i) one single fibre, (ii) two fibres, (iii) a block of fibres, and (iv) one yarn, as shown in Figure II.3. The results are validated by experimental data. The effects of friction, as well as the block's dimensions, are also investigated.

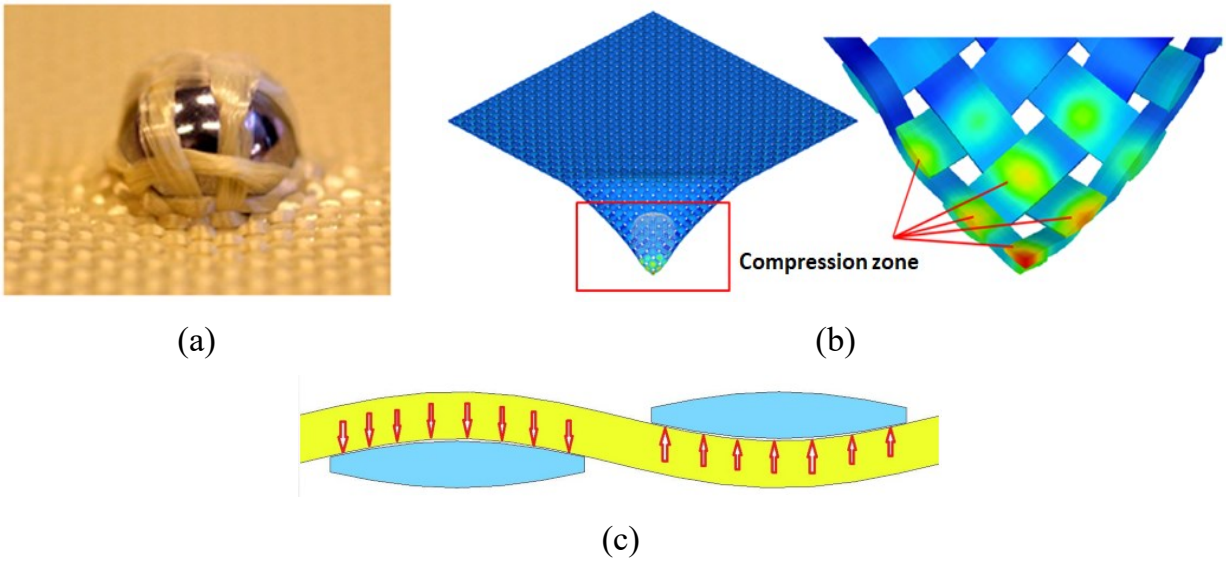

Figure II.2 Example of fabric under ballistic impact, (a) response of fabric [74], (b) compression zone [4], (c) schematic of compression of one yarn [4].

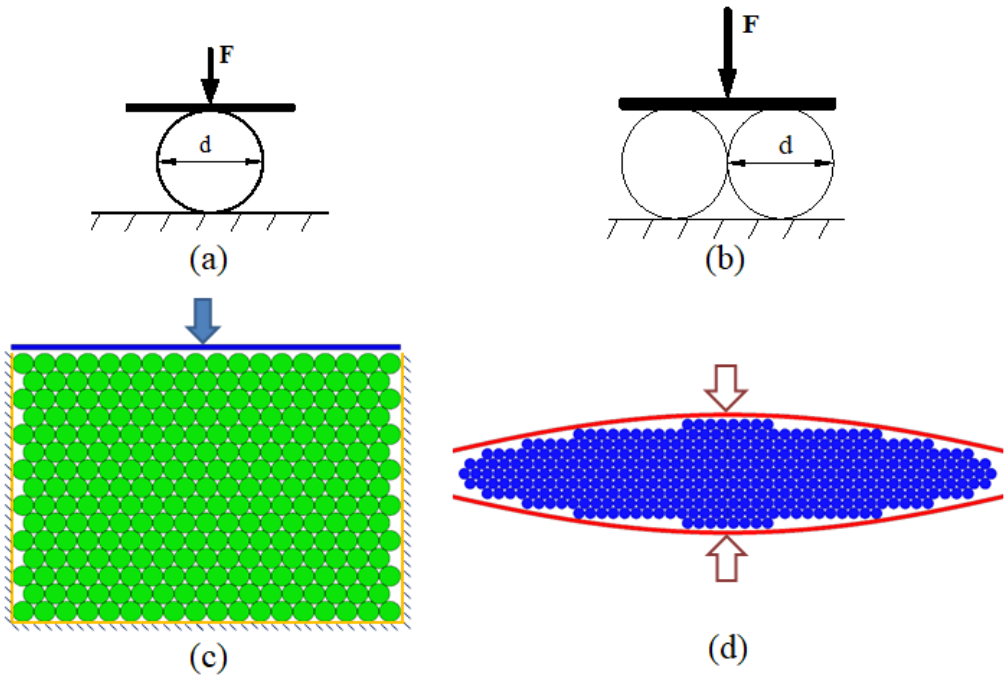

Figure II.3 Schematic of transverse compression of (a) one fibre, (b) two fibres, (c) one block of fibres and (d) one yarn.

II.2 Numerical modelling of transverse compression of one single fibre

II.2.1 Schematic and material

In this section, a model of one single fibre compressed by a rigid plate is conducted, as shown in Figure II.4. Because the diameter of a single fibre can be negligible compared to its length, a 2D plane strain assumption is used for the numerical simulation.

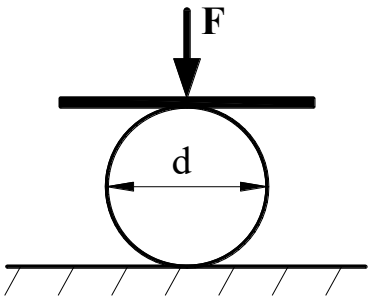

Figure II.4 Schematic of transverse compression of one single fibre.

It is assumed that the material is still in the elastic domain [17]. The properties are shown in Table II.1. Figure II.5 shows a scanning electronic microscope (SEM) micrograph of Kevlar KM2 fibres [77]. The material is considered transversely isotropic with the following constitutional relationship [77]:

$$\begin{Bmatrix}\sigma_{11}\\ \sigma_{22}\\ \sigma_{33}\\ \sigma_{12}\\ \sigma_{23}\\ \sigma_{31}\end{Bmatrix}=\begin{pmatrix}C_{11} & C_{12} & C_{13} & 0 & 0 & 0\\ C_{12} & C_{11} & C_{13} & 0 & 0 & 0\\ C_{13} & C_{13} & C_{33} & 0 & 0 & 0\\ 0 & 0 & 0 & C_{44} & 0 & 0\\ 0 & 0 & 0 & 0 & C_{55} & 0\\ 0 & 0 & 0 & 0 & 0 & C_{55}\end{pmatrix}\begin{Bmatrix}\varepsilon_{11}\\ \varepsilon_{22}\\ \varepsilon_{33}\\ \gamma_{12}\\ \gamma_{23}\\ \gamma_{31}\end{Bmatrix} \tag{II.1}$$

Where the coefficients C_{ij} of the constitutive matrix are as follows:

$$\begin{aligned} &C_{11}=\frac{(1-n\nu_{31}^2)E_1}{AB},\quad C_{12}=\frac{(\nu_{12}+n\nu_{31}^2)E_1}{AB},\quad C_{44}=G_{12}=\frac{E_1}{2A}\\ &C_{13}=\frac{\nu_{31}E_1}{B},\quad C_{33}=\frac{(1-\nu_{12})E_3}{B},\quad C_{55}=G_{13}=G_{23}\\ &A=1+\nu_{12},\quad B=1-\nu_{12}-2n\nu_{31}^2,\quad n=E_1/E_3 \end{aligned} \tag{II.2}$$

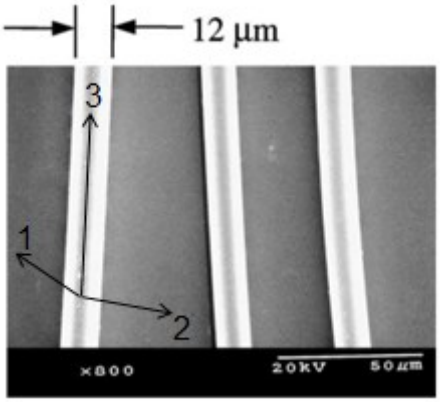

Figure II.5 A SEM micrograph of Kevlar KM2 fibres [77].

Table II.1 Kevlar® 49 and Kevlar® KM2 fibre properties [77, 85, 86]

	ρ (kg/m3)	D (µm)	E_3 (GPa)	E_1 (GPa)	G_{13} (GPa)	ν_{31}	ν_{12}
Kevlar®49	1440	11.3	129.6	2.49	2.01	0.62	0.31
Kevlar®KM2	1440	12.0	84.62	1.34	24.40	0.60	0.24

II.2.2 Boundary conditions and meshing

The numerical model is developed using the commercial FE code Radioss. Due to the symmetric configuration, a quarter model of the single fibre was conducted with associated boundary conditions, as shown in Figure II.6.

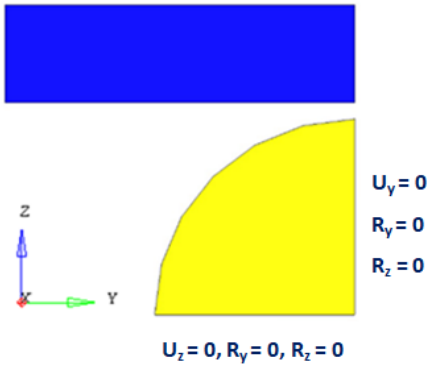

Figure II.6 Boundary conditions.

The platen is considered as a rigid body because the Young's modulus of the fibre is insignificant compared to that of the platen. A constant compression velocity of 0.01m/s is chosen not only to ensure the quasi-static behaviour of the material (kinetic energy is negligible in comparison with internal energy [88]) but also to gain the computation time (approximately 4 minutes using 4 CPU cores in a Windows 64 environment).

As discussed in the reference [86], the effect of the fibre-compressor friction coefficient is insignificant. Therefore, the friction coefficient between the fibre-compressor is supposed to equal to 0.2 based on the references [26, 33, 86]. Moreover, contact between the compressor and the fibre is simulated by penalty contact.

Mesh convergence is studied to find the optimisation of the fibre cross-section mesh in order to reduce the calculation time. The discretisation varies from 84 to 240 finite elements (Figure II.7).

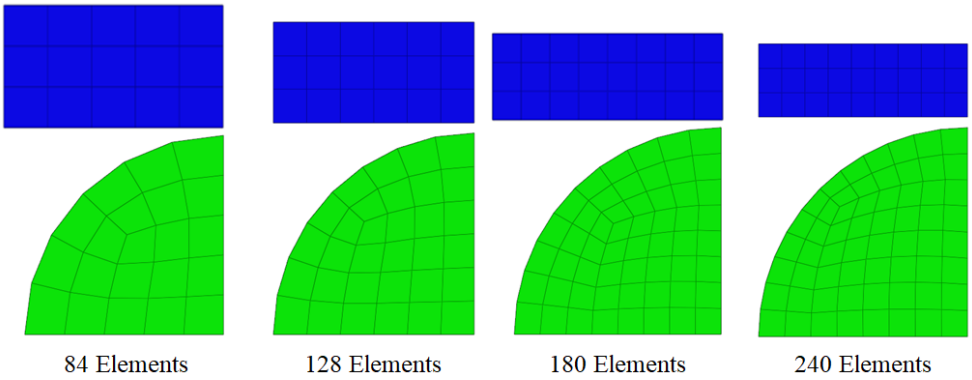

Figure II.7 FE models for mesh convergence study.

II.2.3 Results and discussion

Figure II.8 presents the results of one single Kevlar KM2 fibre in terms of nominal stress/nominal strain compared to the experimental data in references [77, 86]. Nominal stress is defined as the load F per unit length divided by the initial fibre diameter $2r$, while the nominal strain is defined as the platen displacement divided by the initial fibre diameter given by the following equations:

$$\bar{\sigma} = \frac{F}{2r} \tag{II.3}$$

$$\bar{\varepsilon} = \frac{\delta}{2r} \tag{II.4}$$

where δ is the displacement of the platen.

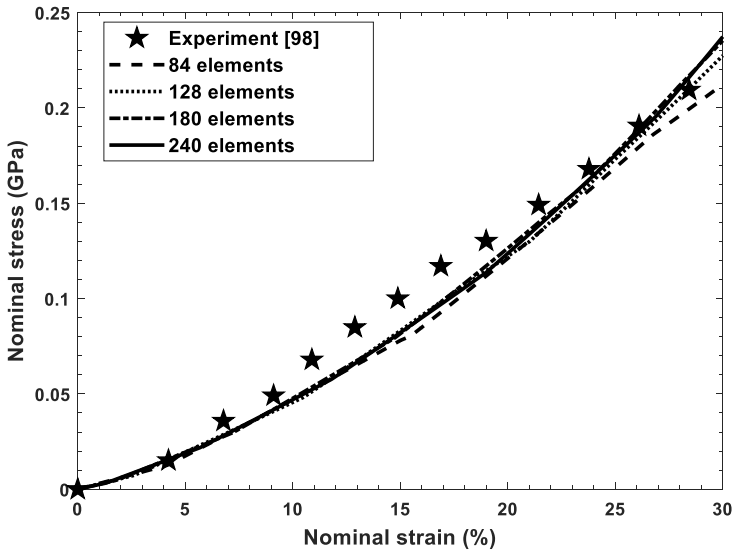

Figure II.8 Mesh density convergence study in comparison with experimental data.

This clearly shows that the curves converge from the mesh of 128 finite elements. Therefore, this one will be used in all simulations. A good agreement between the numerical results and the experimental data (with an average error of 10%) is obtained.

Figure II.9 shows the evolution of the true stress diagram in the Z direction at three different nominal strains. It clearly shows that the maximum compressive stresses are observed at the point of contact between the fibre and the platen. Lower compressive stresses are observed in the centre zone. The compressive stresses are negligible away from the central zone, and the tensile stress in the Z direction is insignificant.

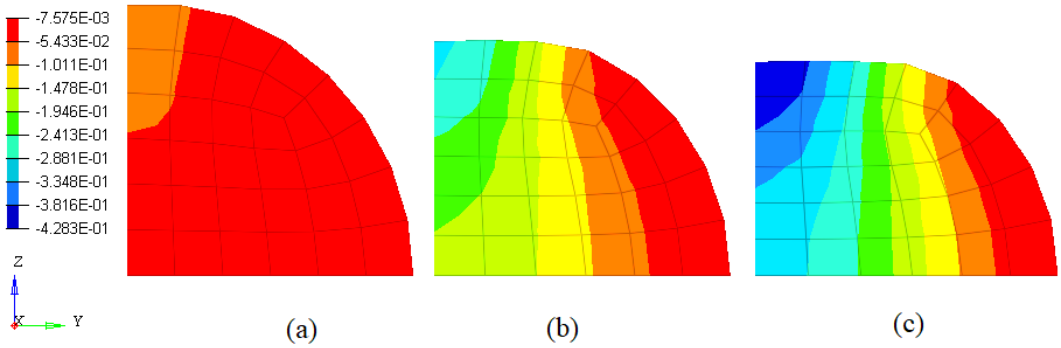

Figure II.9 True stress (GPa) in Z direction of Kevlar KM2 fiber at nominal strain of (a) 0.1, (b) 0.2, (c) 0.25.

True stress in the Y direction is presented in Figure II.10. It is noted that at the contact zone, the fibre is compressed. In contrast, it is under tension at the centre. Thus, maximum tensile stresses are observed in this zone.

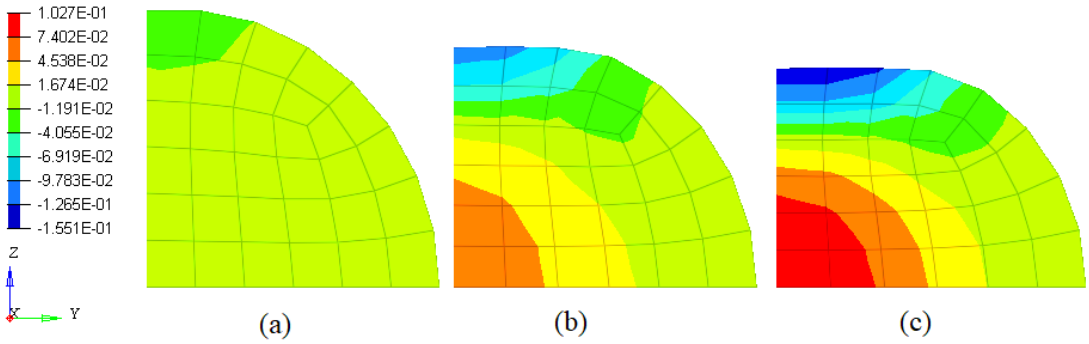

Figure II.10 True stress (GPa) in Y direction of Kevlar KM2 fibre at nominal strain of (a) 0.1, (b) 0.2, (c) 0.25.

Figure II.11 shows the internal and kinetic energies of the 128-elements model. It clearly shows that kinetic energy is approximately 0 and negligible in comparison with the internal energy. Therefore, the velocity of 0.01 m/s ensures the quasi-static behaviour of the material, as mentioned above.

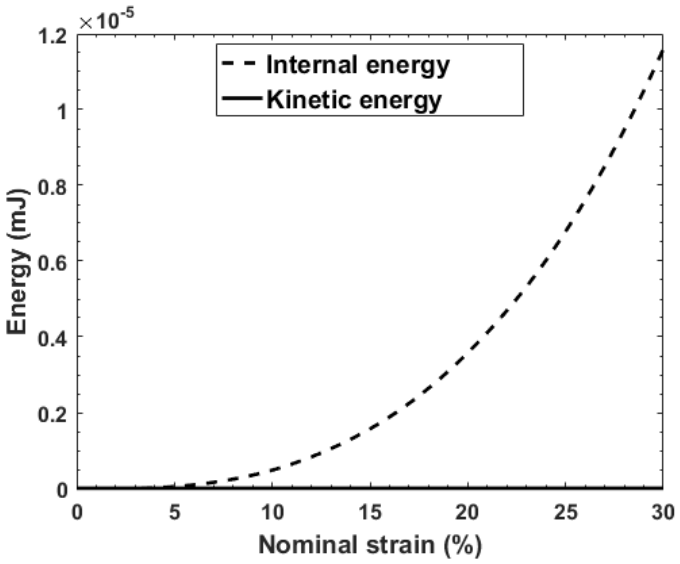

Figure II.11 Energy of the 128-elements model.

The nominal stress-strain curve and the deformation of the fibre are accurate. Thus, the transverse compressive model of one single Kevlar® KM2 fibre is validated. Once this model is validated, it is applied for the case of one single Kevlar® 49 fibre. The results (Figure II.12) clearly show the predominant effect of Young's modulus. The diameters of the two fibres are not significantly different (12 and 11.3μm). Additionally, the transverse Young's modulus of Kevlar® 49 is nearly double that of Kevlar® KM2. Thus, the apparent stress values of Kevlar® 49 are almost double those of Kevlar® KM2 (for example, the stresses are 0.051 and 0.096 GPa at the nominal strain of 10%).

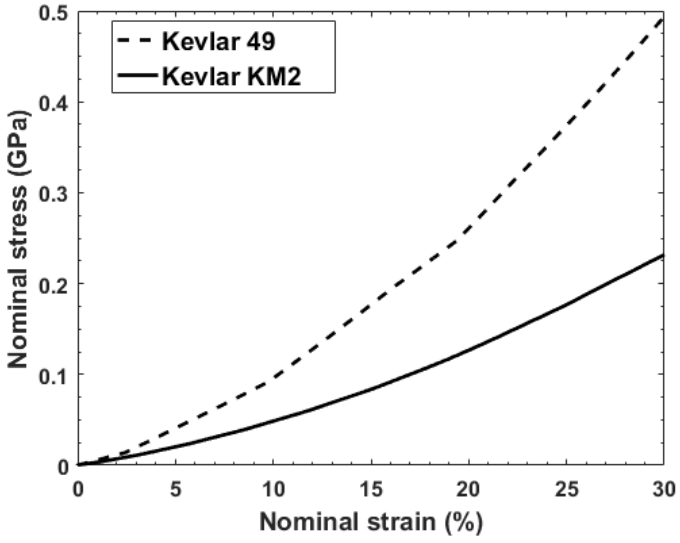

Figure II.12 Nominal stress versus strain: comparison between Kevlar® KM2 and Kevlar® 49.

II.3 Numerical modelling of transverse compression of two fibres

In the previous section, the compressor-fibre contact and fibre deformation are validated. In this section, a numerical model of two fibres subjected to compressive load is simulated to predict and validate the fibre-fibre contact. Because of its symmetric properties (Figure II.13a), a half model is conducted (Figure II.13b). As discussed above, the mesh of 128 elements is used. Penalty contact is defined between the fibres and fibre-compressor.

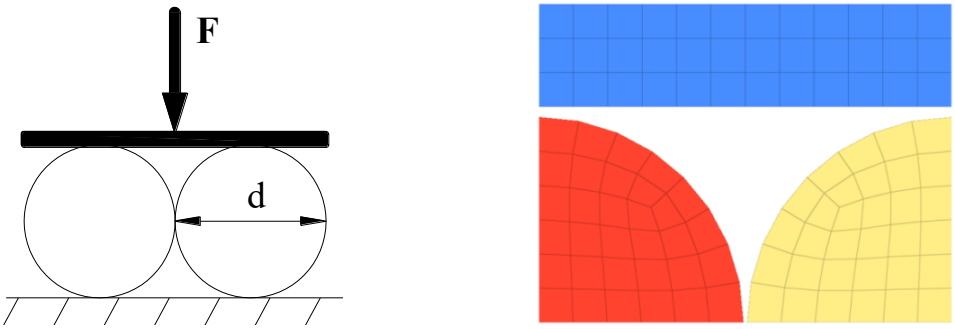

(a) (b)

Figure II.13 Compression of two fibres (a) Schematic (b) Meshing.

True tress in the Z direction is shown in Figure II.14. It can be seen that at the contact zone of the plate and fibres, the maximum compressive stresses occur. Unlike the case of one fibre, in this case, the zone far away from the centre is also compressed due to the interactions between the two fibres.

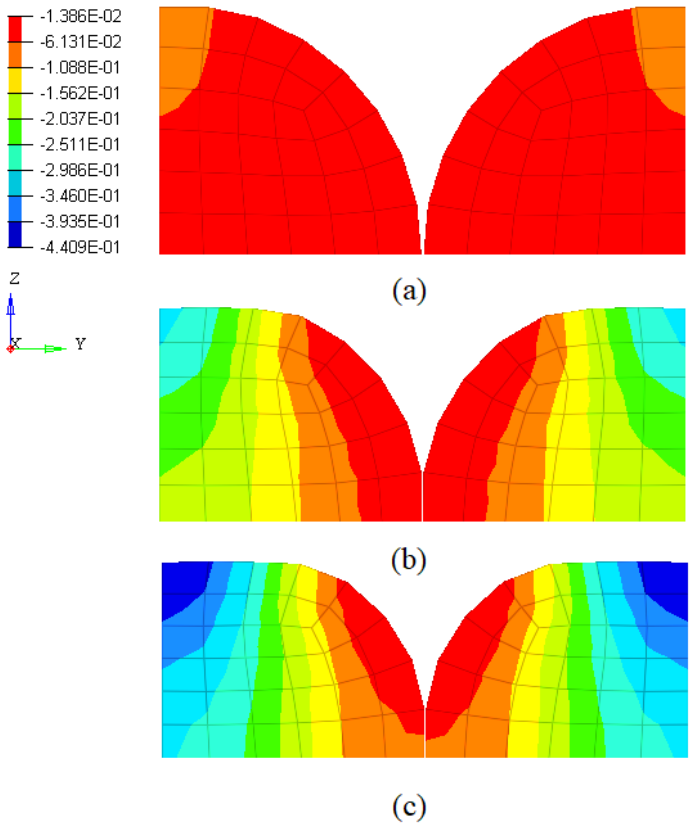

Figure II.14 True Stress (GPa) in Z direction at nominal strain of (a) 0.1, (b) 0.2, (c) 0.25.

The true stress in the Y direction is presented in Figure II.15. Due to the Poisson's effect, the two fibres are under tension at their centre. Thus, the maximum tensile stresses are found there. It should be noted that the fibres are most compressed in the contact zone between them and the platen. In the fibre-fibre contact zone, compressive stresses are also observed.

Figure II.16 presents the nominal stress-strain curves of two fibres. Because of the interactions between two fibres, the nominal stress-strain curve of one fibre, in this case, is a little higher than in the case of one single fibre (Figure II.16a). This can be explained by the fact that due to the fibre-fibre interactions, a higher compressive force is necessary to push one fibre. Meanwhile, similar to the case of one single fibre, the curve of Kevlar® 49 is also double the curve of Kevlar® KM2, as shown in (Figure II.16b). Therefore, the fibre's deformation and contact used in this model are validated.

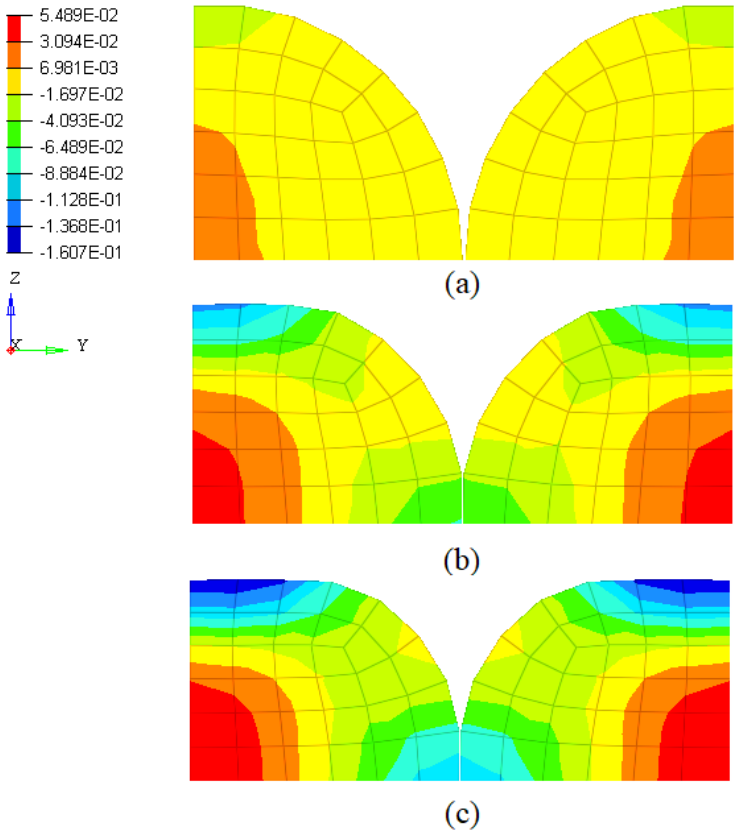

Figure II.15 True stress (GPa) in the Y direction at a nominal strain of (a) 0.1, (b) 0.2, (c) 0.25.

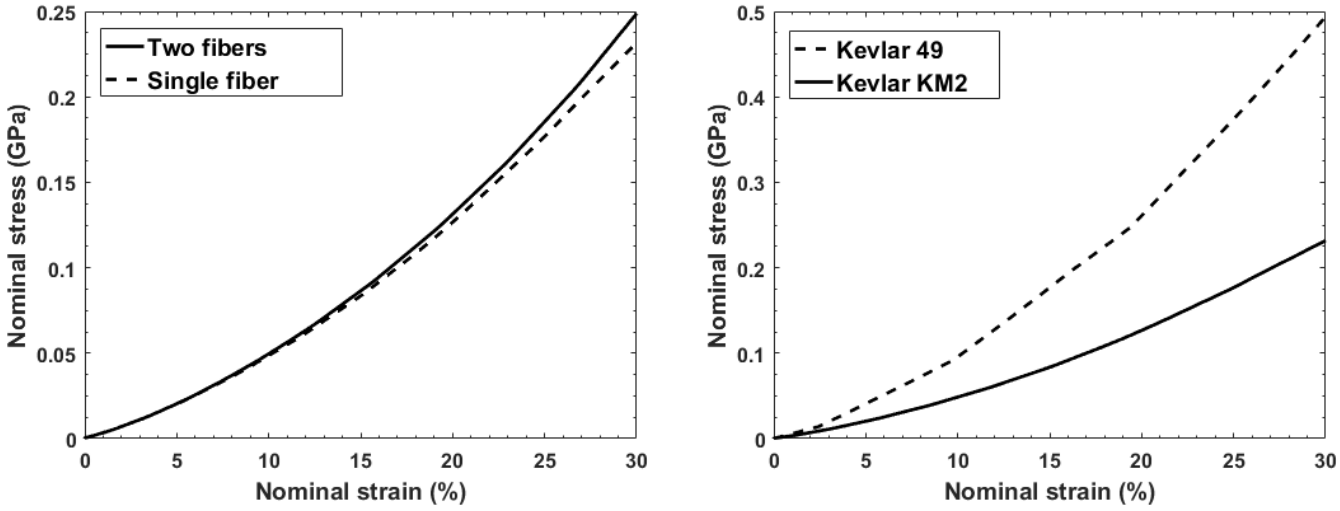

(a) (b)

Figure II.16 Nominal stress versus strain, (a) a single fibre Kevlar® KM2 and one Kevlar® KM2 fibre in the case of two fibre-compression (b) One Kevlar® KM2 and one Kevlar® 49 fibre.

II.4 Numerical modelling of transverse compression of a block of fibres

In this section, a compressive model of a block of Kevlar 49 fibres is developed. A 2D plane strain FE model is conducted with the schematic shown in Figure II.17. In the experiment of Burgoyne and Brown [85], fibres were compressed in a chamber. In the initial state, the block was highly porous. Then, the block of fibres was compressed and became compacted during the unloading/reloading processes. Therefore, the block dimension at the last unloading/reloading cycle (20x7mm) is chosen for this simulation due to the optimal arrangement of the fibres. Due to the calculation limitation, three dimensions of the quarter model are chosen, 35x96µm, 74x203µm and 113x316µm. These dimensions are selected based on the scale 1:1000 of the optimal arrangement state dimension.

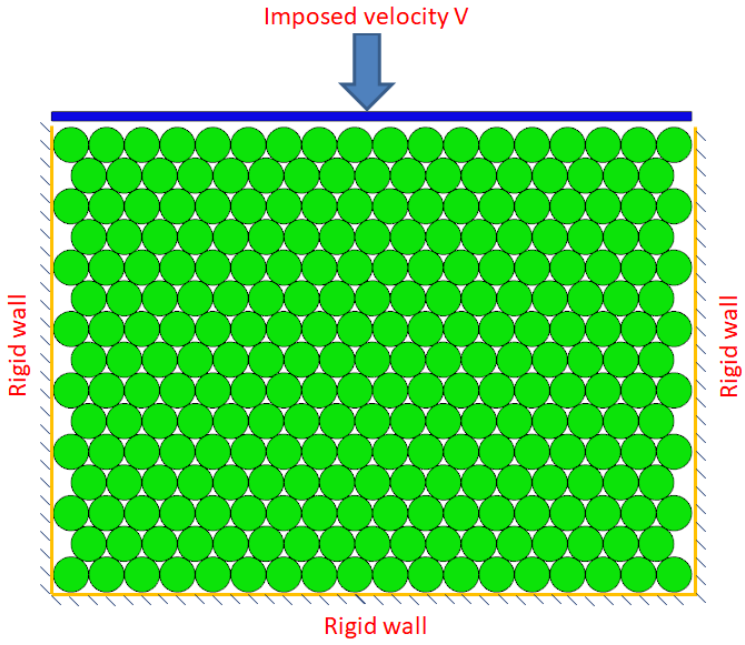

Figure II.17 Schematic description of transverse compressive model of one block of fibres.

Figure II.18 shows the initial and boundary conditions of the numerical model. The compressor is assumed as a rigid body. A constant velocity of 0.1 m/s is imposed on this platen in order to ensure the quasi-static behaviour of the material. Initially, the fibre-fibre and fibre-compressor frictions are assumed to be 0.2 [86]. The effect of friction will be investigated later.

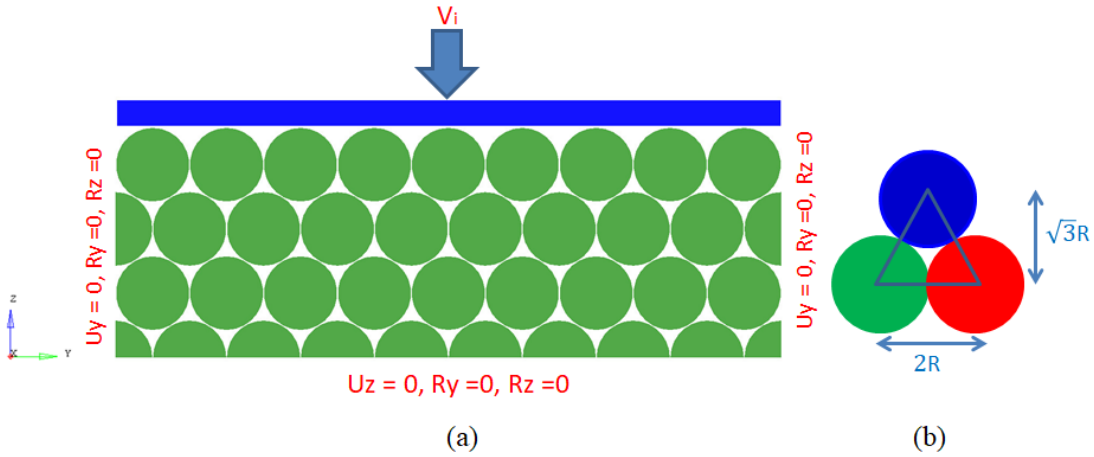

Figure II.18 (a) Boundary conditions, (b) Fibers arrangement.

In this section, apparent stress and strain are introduced, as follows:

$$\bar{\sigma} = \frac{F}{2w} \tag{II.5}$$

$$\bar{\varepsilon} = \frac{\delta}{2h} \tag{II.6}$$

Where F is the reaction force per unit of the platen, and w and h are half of the width and the height of the specimen, respectively. The former is considered as the reaction force per unit of the compressor dived by the specimen width. While the latter is defined as the displacement of the compressor dived by the height of the specimen [86].

Figure II.19 shows the apparent stress-strain curves. The results are compared with the experimental data [85]. At the beginning (apparent strain smaller than 2%), the apparent stress is insignificant because, at this stage, there is no deformation. Afterwards, fibres are compressed, and thus the nominal stress increases. It should be noted that the effect of the block dimension is negligible. Due to a good agreement with experimental data, the 35x96µm model is selected for the next steps. This one also gains computation time as its dimensions are optimal.

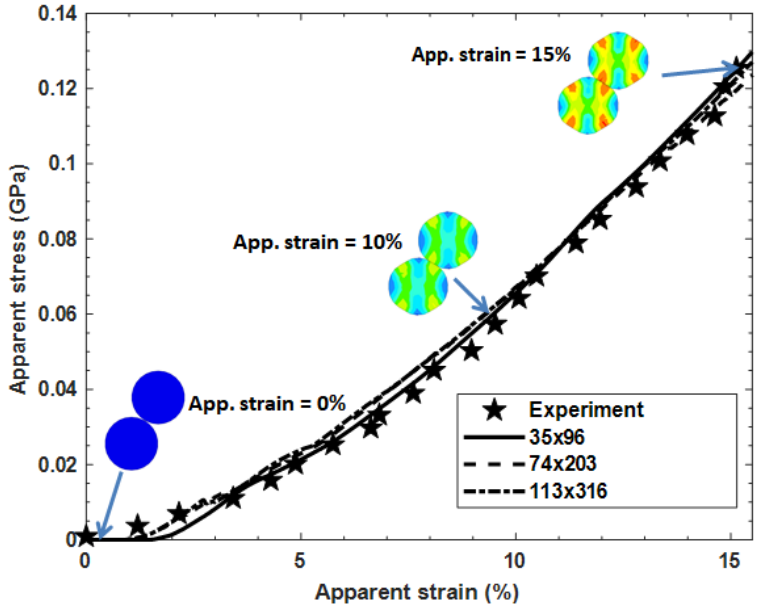

Figure II.19 Apparent stress-strain curves.

Figure II.20 presents the sensitivity of friction. Three friction coefficient values, μ = 0.2, 0.3 and 0.4, are studied. It clearly shows that the effect of friction between the fibres is insignificant.

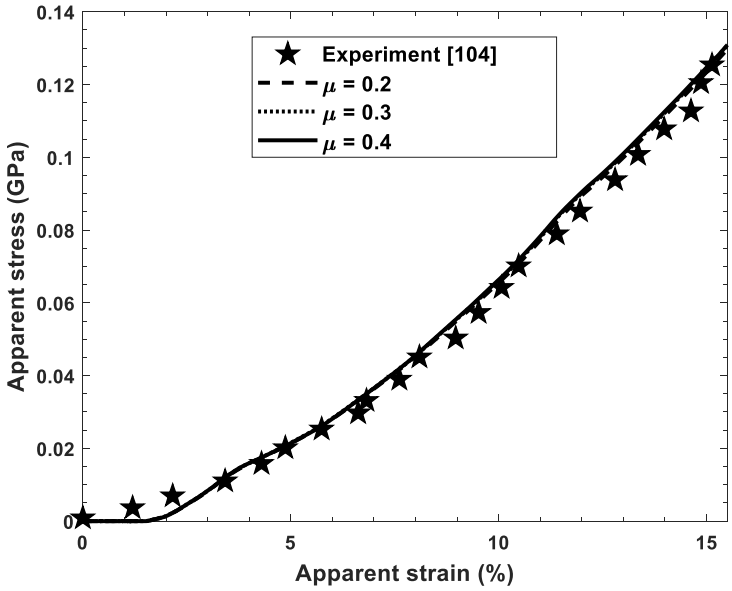

Figure II.20 Sensitivity to friction.

Figure II.21 presents the true stress in the Z direction distribution state of a 70 x 203μm block of fibres in compression, at the apparent strain of 11.4. It can be seen from the figure that stress is concentrated at the boundaries, while in the centre of the block, the distribution of stress is regular. The highest compressive stresses of the fibres occur in the contact zone with the rigid compressor. In contrast, the highest tensile stresses occur

in the two sides. Additionally, the variation of the relative position between fibres is negligible.

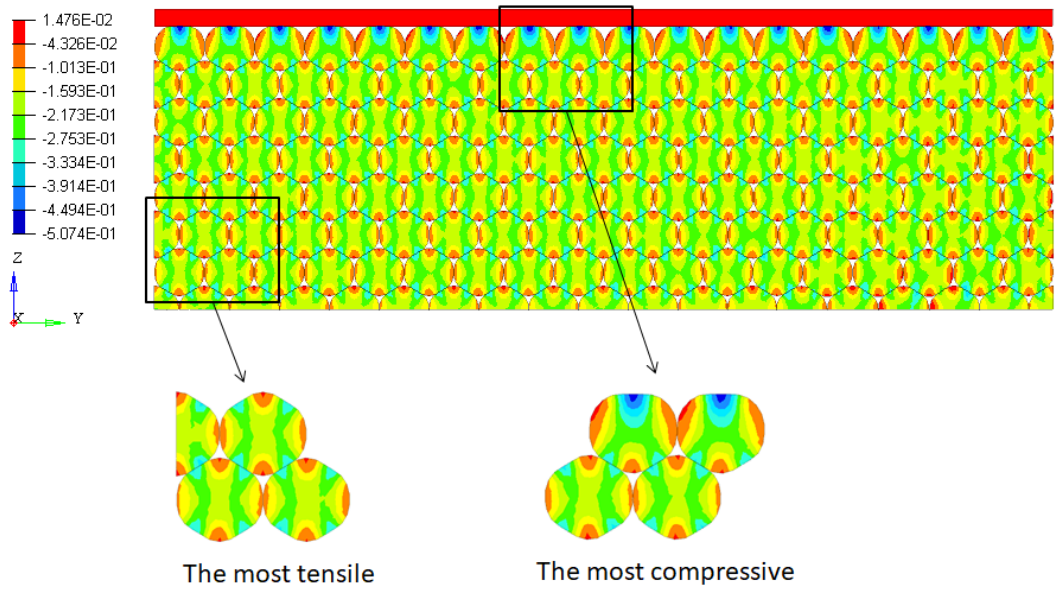

Figure II.21 (a) True stress in the Z direction (GPa) at apparent strain 15.3.

The true stress in the Y direction at the apparent strain of 15.3% is presented in Figure II.22. It clearly shows that fibres are compressed in the contact zone with the compressor. Due to the Poisson's effect, the centres of these fibres are under tension. For the fibres which are not in contact with the compressor, all parts are compressed. The most compressed parts are the parts in contact with the other fibres.

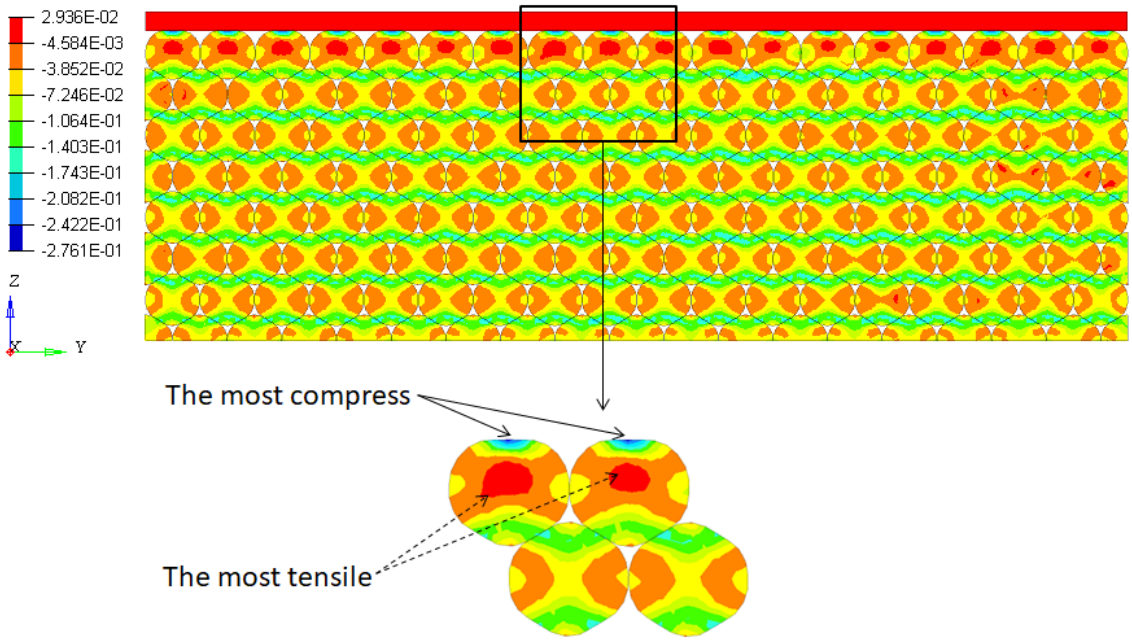

Figure II.22 True stress in the Y direction (GPa) at apparent strain 15.3%.

The revolution of contact width between two regular fibres versus the apparent strain is illustrated in Figure II.23. It should be noted that they are directly proportional. It also proves that the meshing is sufficient for capturing the deformation and fibre-fibre interactions.

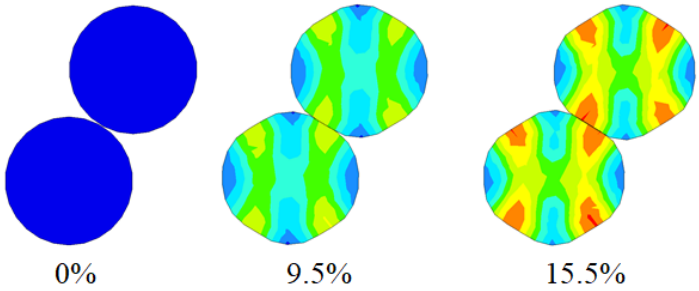

Figure II.23 Contact of two fibres at apparent strain 0%, 9.5% and 15.5%.

Figure II.24 presents the energies of the 35 x 96 µm model. The results clearly show that kinetic energy is approximately 0 and can be considered as negligible, confirming that the behaviour of the material is quasi-static. The compressive energy is almost transformed into deformation (internal) energy.

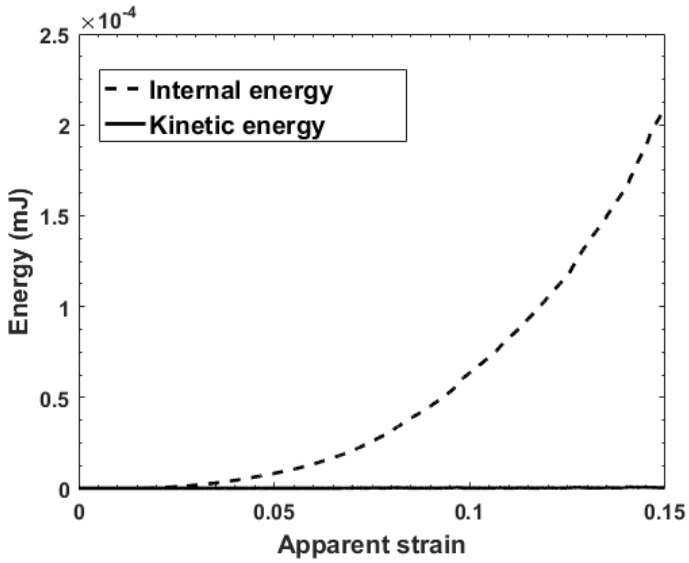

Figure II.24 Energy of the 35x96 µm model.

II.5 Numerical modelling of a transverse compression of one yarn

In this section, the microscopic behaviour of one Kevlar KM2 yarn of Kevlar S706 fabric subjected to transverse compressive loading is investigated. Normally, one yarn consists of about 400 fibres. The yarn cross-section is assumed to be an ellipse (Figure

II.25b). As discussed in reference [67], the centre line of the neighbouring yarn is described by the following equations:

$$y_i^{weft} = \frac{t^{weft}}{2}\cos\left(\frac{\pi x_i^{weft}}{s^{warp}}\right) \tag{II.7}$$

$$y_i^{warp} = \frac{t^{warp}}{2}\cos\left(\frac{\pi x_i^{warp}}{s^{weft}}\right) \tag{II.8}$$

Here, t presents the thickness of yarns, and S is the yarn span. The yarn centre line is along the X axis, and x_i, y_i represent a set of discrete points.

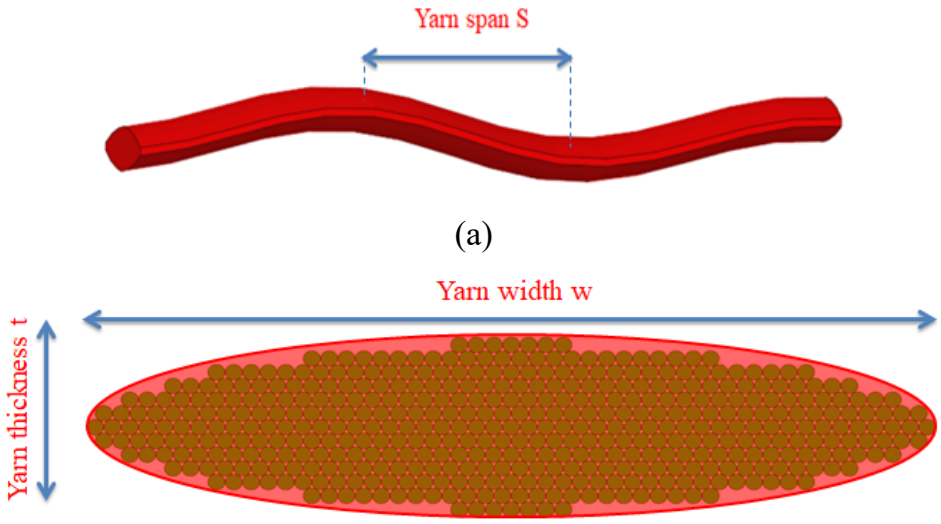

Figure II.25 (a) Yarn path, (b) Yarn ellipse cross-section.

The optimal parameters of the yarn are also proposed in reference [67]. The dimensions of the cross-section are as follows: $t^{weft} = 116$ μm, $t^{warp} = 137$ μm, $S^{weft} = S^{warp} = 747$ μm, and $w^{weft} = 569$ μm. However, in this case, the number of fibres of one yarn is not exactly 400. While the number for the warp yarn is more than 400 (440), this number of the weft yarn is less than 400 (372). This can be explained by the fact that in a realistic fabric, many fibres are tightly packed and thus appear to be not circular (Figure II.26b) as in the ideal configuration in the literature [74]. For simplification, in this work, only the model of one weft yarn is simulated.

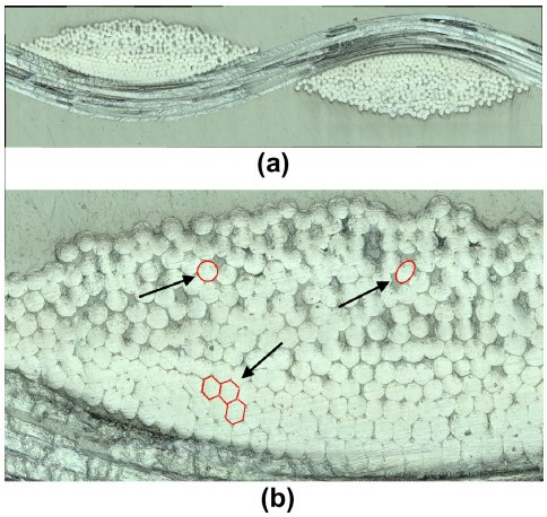

Figure II.26 Greige Kevlar S706 fabric microstructure (a) warp yarn cross-sections, (b) close-up of yarn cross-section showing filament shapes and packing pattern [74].

II.5.1 Numerical model

In this section, a microscopic numerical transverse compression model of one yarn is conducted. Figure II.27 shows the schematic of the numerical FE model. Fibres are distributed within two yarns in nine rectangular zones. In the most compact packing, the initial fibre volume fraction is equal to 0.907=90.7%. The yarn is considered to be compressed by two sinusoidal neighbouring ones. As the dimension of the yarn cross-section is negligible in comparison with its length, a 2D plane strain problem is assumed.

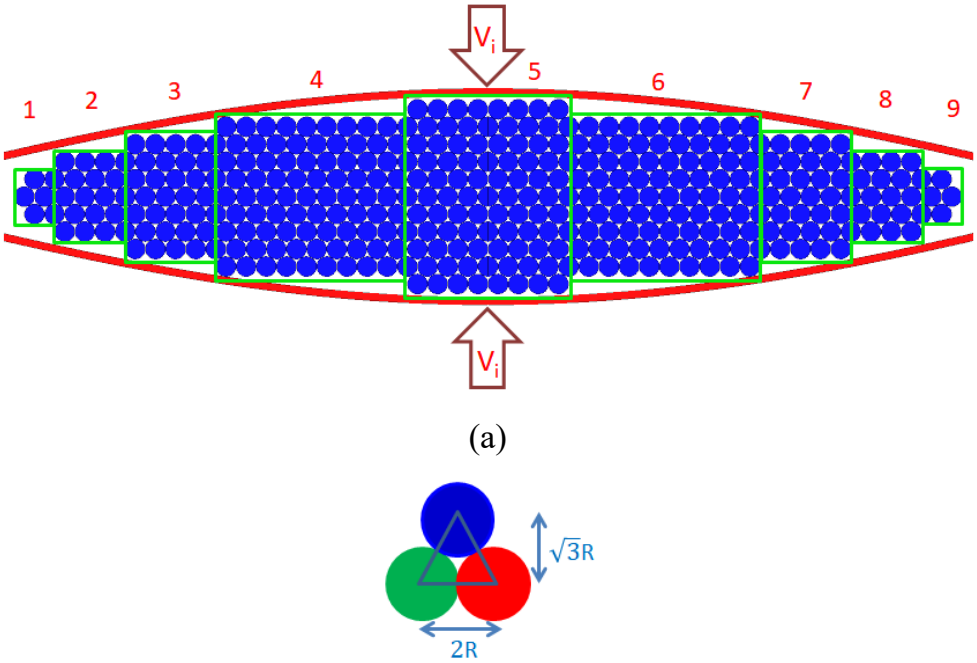

Figure II.27 Schematic of the FE model (a) fibres distribution, (b) fibres packing.

Due to the symmetric geometry and configuration, a half FE model is conducted, as shown in Figure II.28. The fibre's properties and the meshing of the fibre cross-section are taken from section II.2. The friction coefficients between the fibre-compressor and fibre–fibre are supposed to equal 0.2. The two yarns are assumed to be rigid bodies and a constant velocity of 1.0 m/s is imposed.

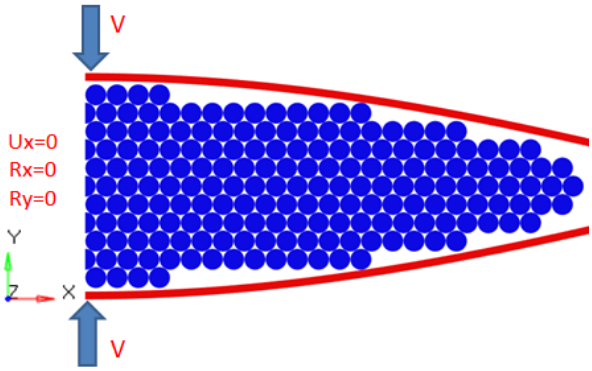

Figure II.28 Boundary condition and geometry of the half numerical model.

II.5.2 Results and discussion

The results in this part can be represented by a typical curve of the compression force versus the total displacement of the compressor, as shown in Figure II.29. This curve clearly shows that the behaviour of the fibres can be divided into two zones: (i) rearrangement, and (ii) nonlinear elastic.

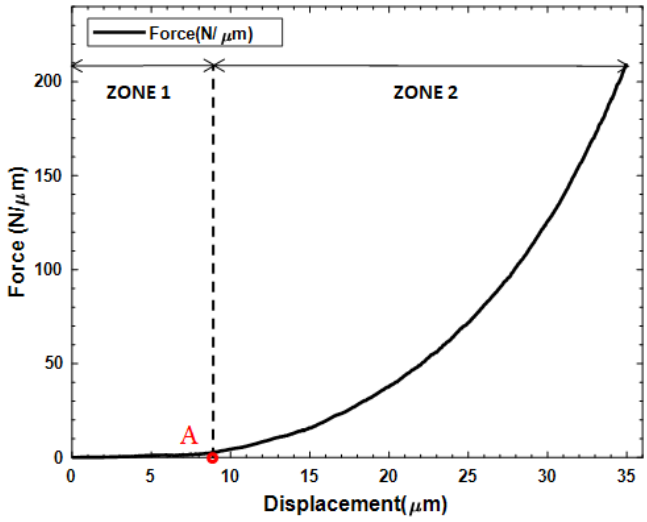

Figure II.29 Typical compression force – displacement curve.

The first zone is named *Rearrangement zone,* in which the fibres are rearranged, and the deformation is negligible. From the displacement of 0 to 9.45 μm (point A), the compression force is approximately 0 due to negligible deformation of the fibres. It

should be noted that even the deformation of fibres is negligible in this zone. At the end of this zone, the fibres start to be compressed.

In the second zone, after being rearranged, the fibres are compressed. Meanwhile, the compression force starts to be positive and increases rapidly. A nonlinear relation between force and displacement is observed. As the material is assumed to be in the elastic domain until failure [17], this zone is called the *Nonlinear elastic zone*.

During the impact, fibres are compressed, and the yarn is compacted. Thus, the fibre volume fraction increases. In this part, the fibre volume fraction is defined as the total area of fibres divided by yarn area (the area inside two neighbouring yarns which equals to total fibre area plus the void area), as shown in Figure II.30.

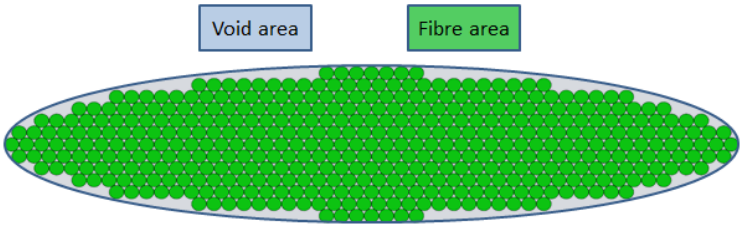

Figure II.30 Schematic of fibre total area and void area.

The evolution of fibre volume fraction versus total displacement of the compressors is presented in Figure II.31. It should be noted that in zone 1 (from the displacement of 0 to 9.45 μm), fibre volume fraction slightly increases as fibres rearrange and the deformation is negligible, whereas, the fibre volume fraction increases rapidly in zone 2.

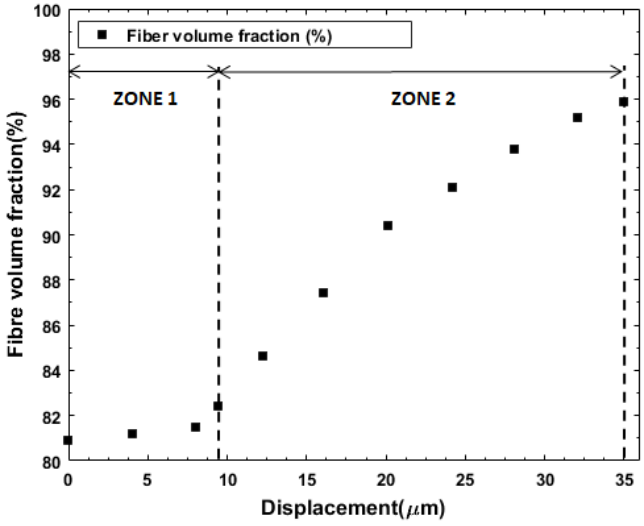

Figure II.31 Evolution of fibre volume fraction.

Results in terms of the distribution of true strain in different displacements in the YY direction are shown in Figure II.32. It clearly shows that in zone 1 (from the displacement of 0 to 9.45 µm), the deformation is negligible. In zone 2, fibres are compacted. The compressive stresses increase from the centre to the side of the yarn due to the distances between the two compressors. At the displacement of 34.5 µm the distribution of strain is very complex. In the furthest part from the centre, the fibres are most compressed (strain of -1.19) while in the centre, a strain of 0.0283 is observed.

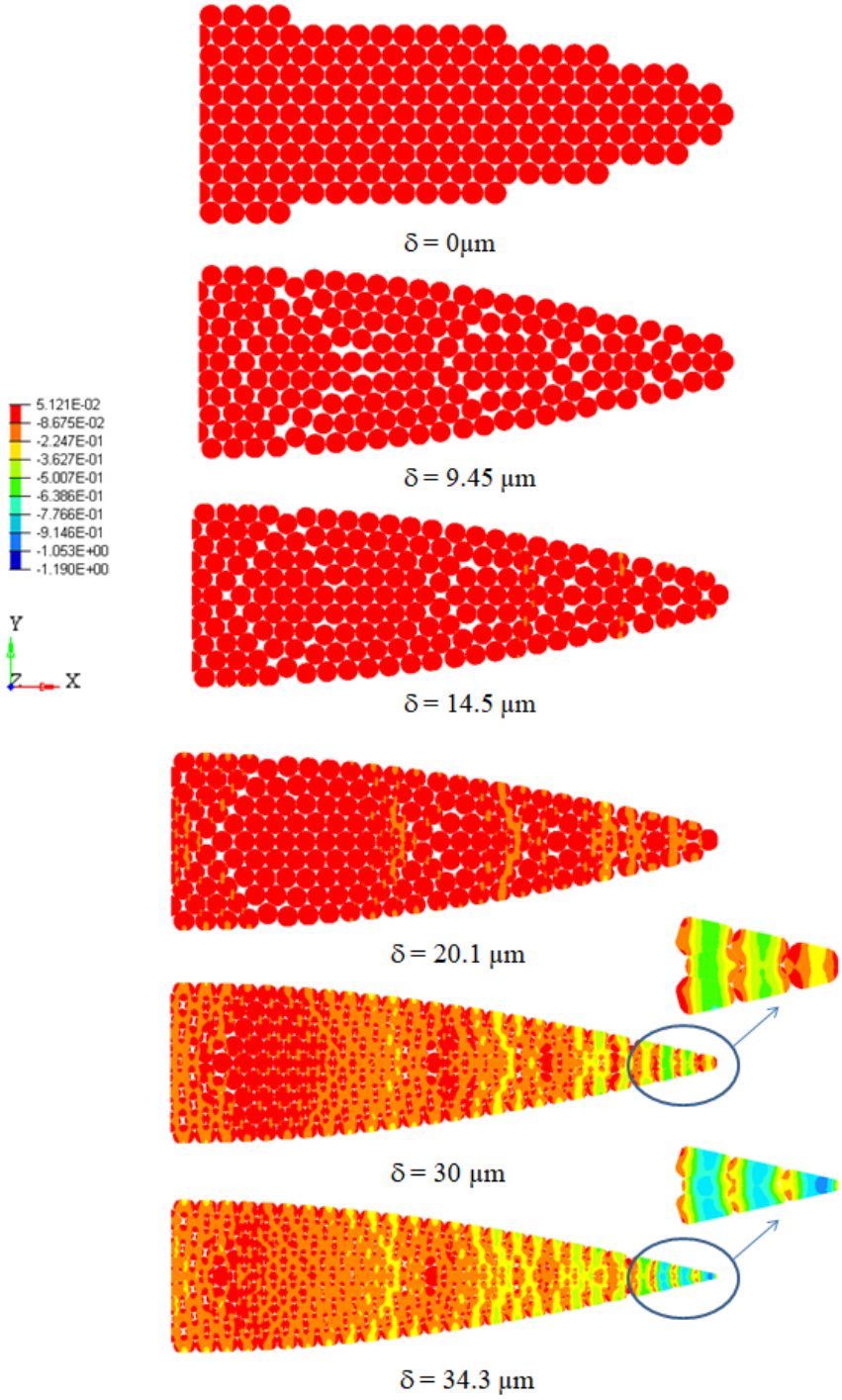

Figure II.32 Evolution of true strain of the fibres in the YY direction.

Figure II.33 presents the evolution of true strain in the XX direction. It should be noted that maximum and minimum strains are also observed on the side of the yarn. Also, fibres in contact with the compressors are more tensile than the others.

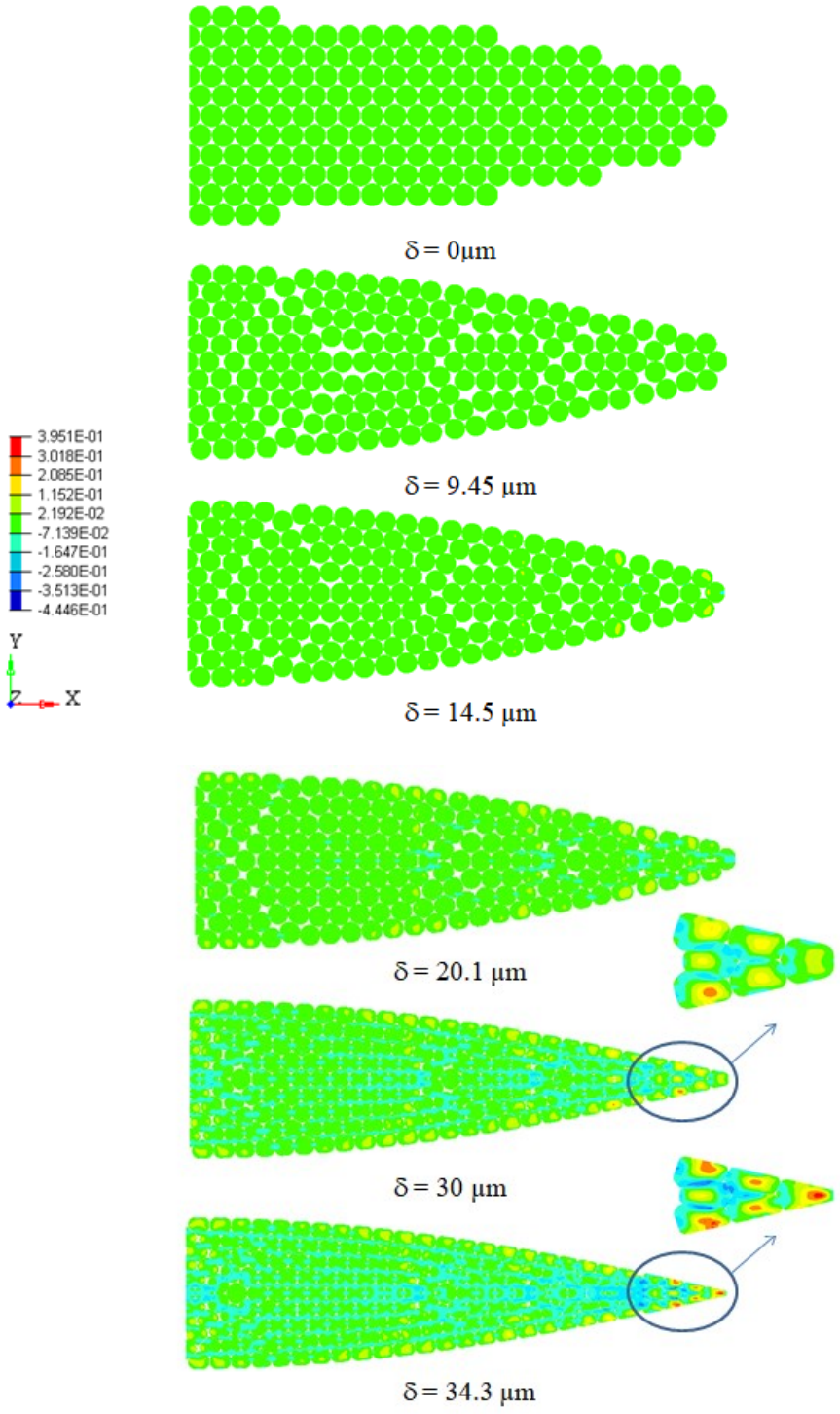

Figure II.33 Evolution of true strain in the XX direction.

The contact between fibres in a typical group during the compression process is illustrated in Figure II.34. It clearly shows that at the beginning of the process, fibres are porous, and some fibres are not in contact with the neighbouring ones. No deformation is

observed. At the displacement of 20.1 µm, the fibres are arranged into the optimal packing with a fibre volume fraction of 90.7 %. All fibres are in contact. At the displacement of 34.5 µm, the fibre volume fraction equals 95.9%, and the deformation is notable.

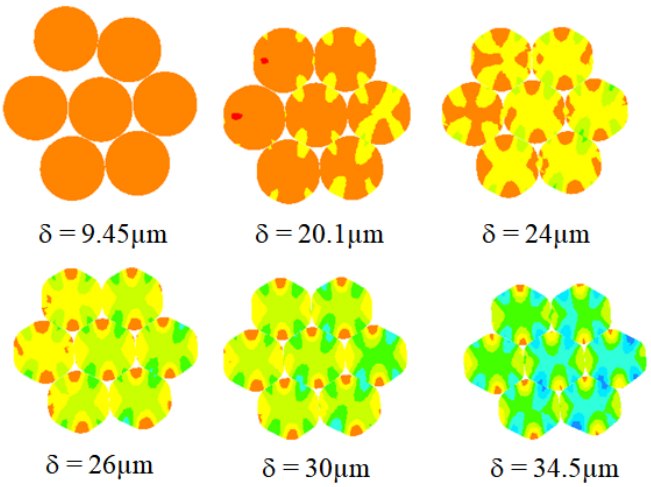

Figure II.34 Contact between fibres in a group.

It should be noted that at the beginning of zone 2, some fibres are not in contact with the neighbouring ones. The contact between all neighbouring fibres occurs at the displacement of 20.1 µm, corresponding with a fibre volume fraction equal to 90.7%. The fibre volume fraction of 90.7% is also equal to the initial fibre volume fraction of the block of fibres at the optimal packing (Figure II.18). This value is the maximum fibre volume fraction in which the fibres are not deformed. Therefore, the displacement from 9.45 to 20.1 µm can be considered as a transit zone of zone 2 (Figure II.35).

Figure II.35 shows the apparent stress-effective apparent strain curve. Since in Zone 1, fibres rearrange, and the deformation is negligible, this zone is not considered. The apparent stress is defined as the reaction force per unit length divided by the length of the major axis of the cross-section, while the effective apparent strain is defined as the effective displacement of the rigid platen δ_R divided by the length of the minor axis of the elliptical cross-section [86], as shown in the following equations:

$$\bar{\sigma} = \frac{F}{w^{weft}} \tag{II.9}$$

$$\bar{\varepsilon} = \frac{\delta_R}{t^{weft}} \tag{II.10}$$

$$\delta_R = \delta - \delta_0 \tag{II.11}$$

Where δ_0 is the displacement of 9.45 µm at point A and δ_R is introduced as the effective displacement. This displacement is counted from the first point of zone 2. The transit zone of zone 2 is also illustrated in this curve. Point B corresponds with the fibre volume fraction of 90.7%.

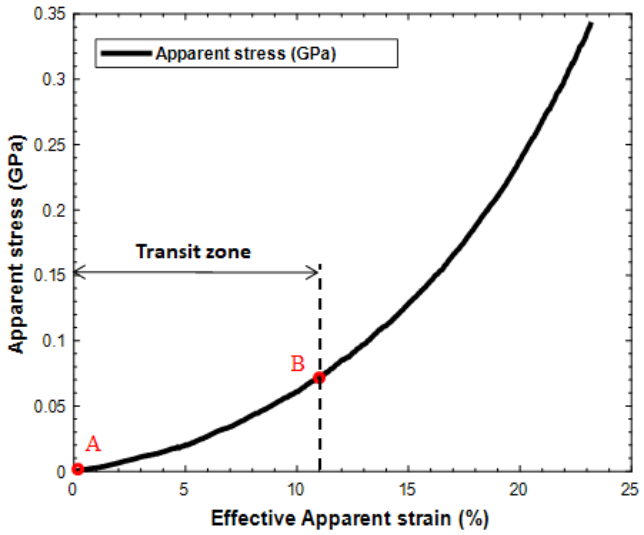

Figure II.35 Evolution of apparent stress.

Figure II.36 presents the fibre volume fraction versus effective apparent strain. It should be noted that the fibre volume fraction $V_f = 82.4\%$ at the effective apparent strain of 0 can be considered as the initial fibre volume fraction V_{f0}. Then, the normalised fibre volume fraction is introduced as $(V_f / V_{f0} - 1)$. This unitless quantity can describe the evolution of the effective apparent strain and the other quantities in the further works.

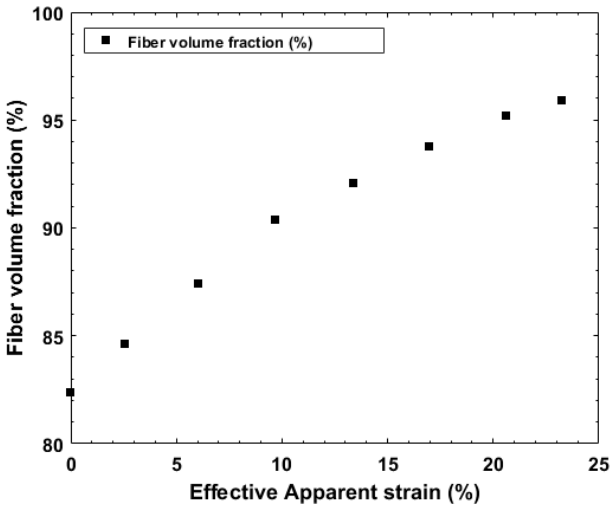

Figure II.36 Fibre volume fraction versus effective apparent strain.

Indeed, the effective apparent strain curve is described by a power law in a relationship with a normalised fibre volume fraction, as shown in Figure II.37, and the following equation:

$$\bar{\varepsilon} = 3.15\left(\frac{V_f}{V_{f0}} - 1\right)^{1.5} \tag{II.12}$$

This is an important remark as the normalised fibre volume fraction is unitless and can be considered as a parameter of a homogenised effective material law, which will be discussed further in the next chapter.

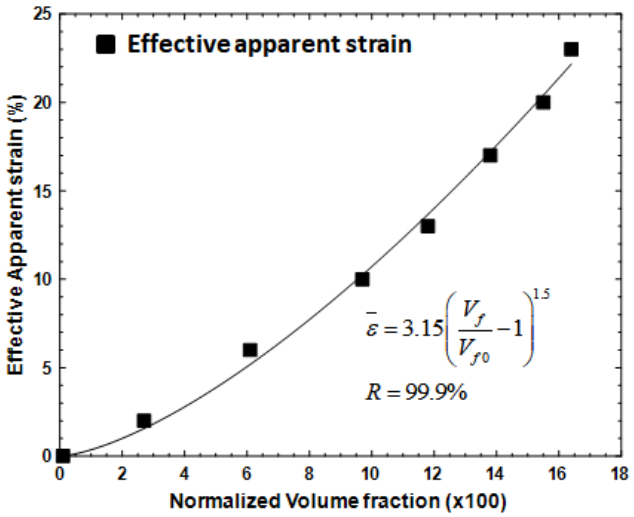

Figure II.37 Effective apparent stain – normalized volume fraction

The evolution of energies of the model is shown in Figure II.38. It clearly shows that kinetic energy can be considered negligible. The compressive energy is almost transformed into deformation (internal) energy. Therefore, with the imposed velocity of 1.0 m/s of the compressors, the material behaviour is quasi-static.

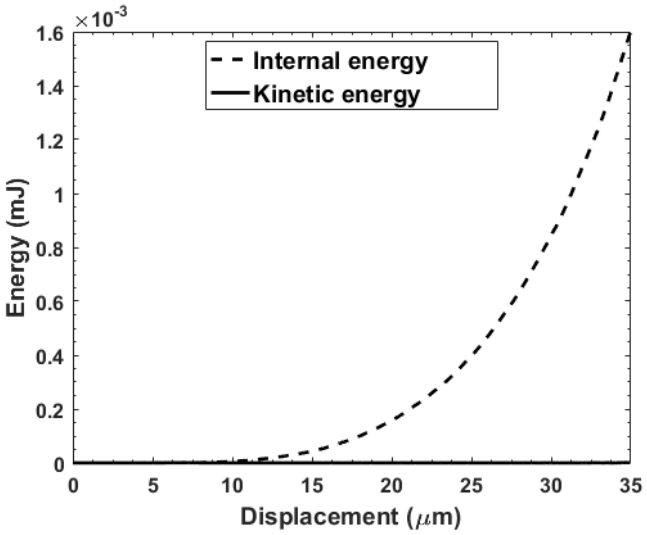

Figure II.38 Model energies.

II.6 Conclusion

In this chapter, the transverse compressive behaviour of Kevlar 49 and Kevlar KM2 fibres in the case of a block of fibres and one yarn is investigated using microscopic numerical approaches.

The transverse compression model of one block of fibres was validated by comparing with data from experimental works in terms of the nominal stress–nominal strain relationship. Non-linear behaviour was observed. The results show the insignificant role of the friction and the dimensions of the block.

In the case of one yarn, the observed behaviour was divided into two zones. Furthermore, the second zone is highly nonlinear elastic. A power-law relationship between effective apparent strain and normalised volume fraction is also captured. The results from microscopic models will be used to validate the homogenised approach in the next chapter.

Chapter III

Homogenization of Transverse Compressive Behaviour of Fibres

Abstract

In this chapter, the transverse compression behaviour of fibres is studied using a numerical elementary homogenization approach. In the first part, an overview of the numerical homogenization method is presented. The concept of numerical homogenization and the most important notions, including the Representative Volume Element (RVE) and boundary conditions, are presented in detail. Several results of previous works concerning the application of the homogenization method on woven materials are presented in this section.

In the second part, the numerical homogenization method is developed to evaluate the effective properties in the case of a block of fibres and one yarn subjected to transverse compression. These homogenized behaviour laws are implemented in the ABAQUS software via a user-defined subroutine and validated by comparison with the results of microscopic models. An Effective Homogenized Material (EHM) for one yarn is proposed, leading to exciting results in terms of apparent stress-strain curves. This modelling allows for a robust model for the study of the impact of woven materials.

Résumé

Dans ce chapitre, le comportement en compression transversale des fibres est étudié en utilisant une approche d'homogénéisation élémentaire numérique. Tout d'abord, dans la première partie, un aperçu de la méthode d'homogénéisation numérique est présenté. Le concept d'homogénéisation numérique et les notions les plus importantes, en particulier, le volume représentatif (VER) et les conditions aux limites, sont présentés en détail. Plusieurs résultats de travaux antérieurs, portant sur l'application de la méthode d'homogénéisation aux matériaux tissés, ont été exposés dans cette partie.

Dans la seconde partie, la méthode d'homogénéisation numérique est développée pour évaluer les propriétés effectives dans le cas de fibres et d'un fil soumis à une compression transversale. Ces lois de comportement homogénéisées sont implémentées dans le logiciel ABAQUS via un sous-programme utilisateur et validées par comparaison avec les résultats des modèles microscopiques. Cette approche a permis de proposer un Matériau Homogène Équivalent (MHE) pour un fil et a conduit à des résultats très intéressants en termes de courbes contrainte-déformation apparentes. Cette modélisation constitue une voie prometteuse pour être utilisée en vue d'établir un modèle robuste pour l'étude de l'impact sur les matériaux tissés.

Contents

Part 1. A Review of Homogenization Method

III.1 Introduction of homogenization method

This part aims to introduce numerical homogenisation using the finite element method. Firstly, we introduce the concept of homogenisation. Then, an overview of numerical homogenisation using the finite element method is briefly presented. The fundamental key points of the method, such as the RVE and boundary conditions, are detailed. Finally, publications regarding the numerical homogenisation of woven fabric composites are reviewed.

III.1.1 Concept of homogenization

Most of the materials, especially composites or porous materials, are heterogeneous at a sufficient scale with many components [89]. Thus, it is very complicated to predict their behaviour. Therefore, the hypothesis of the continuity of a material was proposed. In this hypothesis, the material is considered to be continuous. The concept of homogenisation is to find a homogeneous material representing the heterogeneous one at a macroscopic scale.

The homogenization method aims to derive the effective properties of heterogeneous materials from their constitutive laws and the spatial distribution of their components [90]. In other words, a heterogeneous material is transformed into a homogeneous one called effective homogenised material (EHM), as shown in Figure III.1. The properties of EHM are called effective properties or macro-properties [89]. In general, there are many homogenization methods, such as the rule of mixture, inverse rule of mixture, dilute solution, Mori – Tanaka model, finite element, asymptotic homogenization, fast Fourier transform, and mean-field homogenization. These methods are classified into two main families, analytical and numerical techniques.

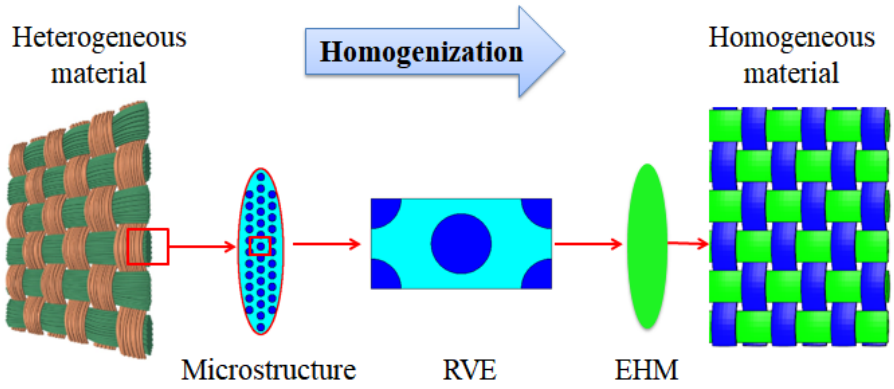

Figure III.1 The concept of homogenization.

III.1.2 Numerical homogenization using finite element method

Numerical homogenization is a robust method to determine the effective properties of heterogeneous materials, which can be applied in all cases of heterogeneous materials, especially composite materials with no restriction on the geometry, material properties or the number of phases. The calculation is rapid, and the results are accurate and reliable.

Numerical homogenization deals with solving a microscale boundary value problem [91]. The local governing behaviour at the macroscopic scale is estimated by solving the microscale boundary value problem. The stress-strain relationship is evaluated at each point of the macroscopic scale through solving the boundary value problem associated with the microscale. In other words, homogenization problems are solved by numerical techniques and simulation on microstructure samples. In the literature, these samples are defined as representative volume element (RVE) for irregular microstructures or unit-cell for periodic ones. The boundary conditions of the microscopic problem are defined such that the strain energy stored in the two scales, known as Hill–Mandel condition, is approximately the same or preserved [92, 93].

Numerical homogenization using the finite element method is a robust and widely used tool to obtain effective properties of heterogeneous materials. In this work, numerical homogenization using the finite element method will be used. Firstly, the basic principle of this method is presented.

The methodology comprises three main steps as follows:

- (i) Representation step: the geometry and mechanical properties of the material (i.e., volume fraction, the length scale of inclusions) are investigated. The representative volume element (RVE) is determined by analysing the microstructure of the material.
- (ii) Localisation step: finite element model is conducted. The RVE is discretised, and appropriate boundary conditions are imposed. In this step, the average fields, such as average stress, strain or energy, are obtained by surface or volume integrals over the RVE.
- (iii) Homogenisation step: this step aims to define the behaviour of the EMH by identifying the macroscopic behaviour through average fields obtained from the

localisation step. In other words, the effective properties of the EHM are deduced from the average fields.

The spatial average stress and strain can be defined as follows:

$$\langle \sigma(x) \rangle = \frac{1}{V} \int_V \sigma(\underline{x}) dV = \Sigma \tag{III.1}$$

$$\langle \varepsilon(x) \rangle = \frac{1}{V} \int_V \varepsilon(\underline{x}) dV = E \tag{III.2}$$

Where $\langle x \rangle$ denotes the spatial average value, $\underline{x}$ stands for spatial vector, V for the volume of the RVE, and Σ and E for the homogenised macroscopic stress and strain, respectively. It should be noted that the RVE and boundary conditions are the essential concepts of this method [90]. Therefore, they will be detailed.

The notion of Representative Volume Element (RVE)

There are many definitions of the RVE. The RVE is generally considered as a volume V of the heterogeneous material, which is large enough to represent the material and ensure the independence of the boundary conditions [90]. Thus, all microstructure heterogeneities, such as grains, fibres, inclusions, and voids, must be included in the RVE. On the other hand, the RVE should also be sufficiently small to be a volume element of the structure. It is concluded that the size of the RVE should be subject to the following condition:

$$d \ll \ll \tag{III.3}$$

Here, L is the characteristic length of the macroscopic structure, l is the characteristic length of the RVE, and d is the characteristic length of the inclusion.

The classic definition of the RVE was proposed by Hill [94] and extensively detailed by Hashin [95, 96]. The authors considered that the RVE is a sample structurally typical of the whole microstructure, and it contains a sufficient number of inclusions or heterogeneities such that the macroscopic properties are independent of the boundary conditions. Additionally, the size of the RVE should be much smaller than the size of the macroscopic body [97].

Sab [98] implied that the RVE should be independent of the type of boundary conditions. That was confirmed by the work of Ostoja Starzewski [99]. Terada *et al.* highlighted that the RVE should be large enough to facilitate the calculations [100]. In contrast, Drugan and Willis [101] stated that "it is the smallest material volume element of the composite for which the usual spatially constant (overall modulus) macroscopic constitutive representation is a sufficiently accurate model to represent the mean constitutive response". In other words, the size of the RVE is the smallest possible one where the macroscopic properties converge and meet.

Ostoja Starzewski [102] implied that the RVE could be defined in two situations:

- The RVE is a repeated unit cell (RUC) in a periodic microstructure.
- The RVE is a statistically representative volume that contains a huge (mathematically infinite) set of microscale elements for a random microstructure.

Thus, in order to determine a RVE, it is necessary to consider [103]:

- The statistical homogeneity and ergodicity of the material. These properties ensure that the RVE is statistically representative of the macro response.
- Length scale l of the RVE which is large enough relative to the micro-scale d of the inclusions. These length scales ensure the independence of the boundary conditions.

In the work of Kanit *et al*. [90], the authors proposed that "the RVE must ensure a given accuracy of the overall estimated properties obtained by spatial averaging of the stress, the strain or the energy fields in a given domain V". A technique for determining the size of the RVE was also introduced. Finite element calculations were applied on 4 or 5 different sample sizes. Different boundary conditions were imposed in order to verify the convergence of effective properties. The chosen size is the smallest one for which the effective properties are independent of the boundary conditions.

Figure III.2 demonstrates a unit cell of a plain-woven fabric. This periodic macro unit cell is the smallest part that can represent the fabric. In the unit cell, the relations between warp and weft yarns are presented. The undulation of warp and fill yarns is described. In the modelling of the fabric geometry, the key parameters are the yarn cross-section, the thickness of the yarn, the yarn span length, the yarn-to-yarn distance and the degree of fibre crimp.

(a) A plain woven fabric

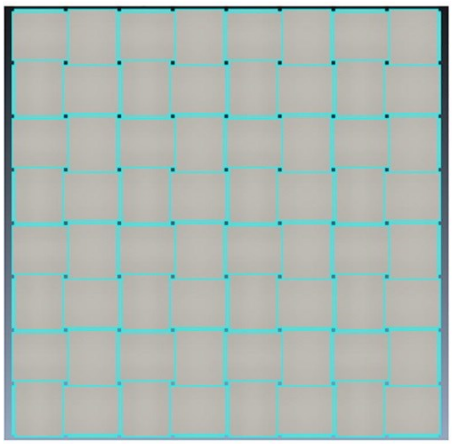

(b) Idealized model

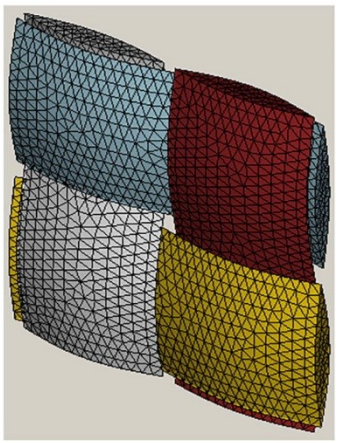

(c) RVE

Figure III.2 Schematics of a unit cell of plain woven fabrics [104].

Boundary conditions

As discussed above, the boundary conditions are defined, such that the Hill–Mandel condition[94, 105] is satisfied. Normally, three boundary conditions, Kinematic Uniform Boundary Conditions (KUBC), Periodic Boundary Conditions (PBC) and Static Uniform Boundary Conditions (SUBC), are widely used.

- KUBC is described by imposing the displacement vector $\underline{u}$ at point position vector $\underline{x}$ which belongs to the boundary ∂V [106]:

$$\underline{u} = \underline{\underline{E}}.\underline{x} \tag{III.4}$$

Where $\underline{\underline{E}}$ is a symmetrical second-order tensor independent of $\underline{x}$ implying that:

$$\underline{\underline{E}} = <\underline{\underline{\varepsilon}}> = \frac{1}{V}\int_V \underline{\underline{\varepsilon}} dV \tag{III.5}$$

The spatial average defines the macroscopic stress tensor:

$$\underline{\underline{\Sigma}} = <\underline{\underline{\sigma}}> = \frac{1}{V}\int_V \underline{\underline{\sigma}} dV \tag{III.6}$$

Here $<\underline{\underline{\varepsilon}}>$, $<\underline{\underline{\sigma}}>$ are spatial average strain and stress tensor.

- SUBC is defined by applying the traction vector at the boundary:

$$\underline{\underline{\sigma}}.\underline{n} = \underline{\underline{\Sigma}}.\underline{n}, \forall \underline{x} \in \partial V \tag{III.7}$$

Where $\underline{\underline{\Sigma}}$ is a symmetrical second-order tensor independent of $\underline{x}$ implying that

$$\underline{\underline{\Sigma}} = <\underline{\underline{\sigma}}> = \frac{1}{V}\int_V \underline{\underline{\sigma}} dV \tag{III.8}$$

Then the macroscopic strain tensor is defined as the spatial average:

$$\underline{\underline{E}} = <\underline{\underline{\varepsilon}}> = \frac{1}{V}\int_V \underline{\underline{\varepsilon}} dV \tag{III.9}$$

- PBC add a periodic fluctuation $\underline{v}$ into the displacement field of KUBC as follows:

$$\underline{u} = \underline{\underline{E}}.\underline{x} + \underline{v}, \forall \underline{x} \in \partial V \tag{III.10}$$

The fluctuation values at two homologous points on the two opposite faces are the same (Figure III.3). Thus, the traction vector at these points takes opposite values.

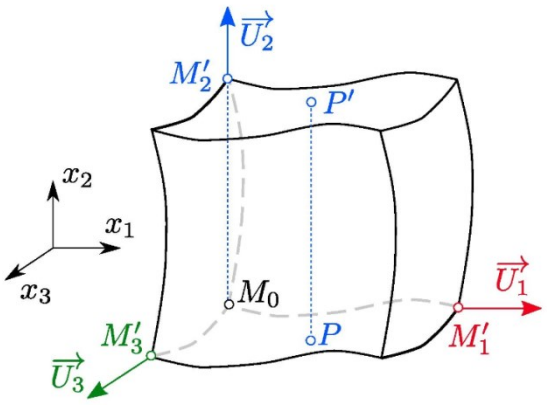

Figure III.3 The fluctuation of nodes [107].

In the case of linear elastic behaviour, each micro-mechanical problem (each boundary condition) admits only one single solution. Thus, it is necessary:

- A fourth-order concentration tensor field $\underset{\sim}{A}$ such that:

$$\underline{\underline{\varepsilon}}(\underline{x}) = \underset{\sim}{A}(\underline{x}) : \underline{\underline{E}} \quad \forall \underline{x} \in V \tag{III.11}$$

and $\forall \underline{\underline{E}}$ for the KUBC problem. Here, the operator : means double dot product between a tensor of order four and a second-order one.

- A fourth-order concentration tensor field $\underset{\sim}{P}$ such that:

$$\underline{\underline{\sigma}}(\underline{x}) = \underset{\sim}{P}(\underline{x}) : \underline{\underline{\Sigma}} \quad \forall \underline{x} \in V \tag{III.12}$$

and $\forall \underline{\underline{\Sigma}}$ for the SUBC problem.

From equations III.11 and III.12, the concentration tensors relate to the fourth-order identity tensor $\underset{\sim}{I}$ operating on the symmetric second-order tensor. These concentration tensors satisfy:

$$\langle \underset{\sim}{A} \rangle_V = \underset{\sim}{I} \qquad \langle \underset{\sim}{P} \rangle_V = \underset{\sim}{I} \tag{III.13}$$

In order to determine the isotropic effective elastic properties, strain and stress tensor $\underline{\underline{E}}$ and $\underline{\underline{\Sigma}}$ are chosen according to the boundary conditions. For KUBC and PBC, the strain tensors are applied to a given V in the same manner [90]:

$$\underline{\underline{E}}_k = \begin{bmatrix} \frac{1}{3} & 0 & 0 \\ 0 & \frac{1}{3} & 0 \\ 0 & 0 & \frac{1}{3} \end{bmatrix} \tag{III.14}$$

$$\underline{\underline{E}}_\mu = \begin{bmatrix} 0 & \frac{1}{2} & 0 \\ \frac{1}{2} & 0 & 0 \\ 0 & 0 & 0 \end{bmatrix} \tag{III.15}$$

Then effective bulk modulus $\bar{k}_{eff}$ and shear modulus $\bar{\mu}_{eff}$ can be calculated as follows:

$$\bar{k}_{eff} = \frac{1}{3} trace\left\langle \underline{\underline{\sigma}} \right\rangle \tag{III.16}$$

$$\bar{\mu}_{eff} = \left\langle \sigma_{12} \right\rangle \tag{III.17}$$

For SUBC, one takes:

$$\underline{\underline{\Sigma}}_k = \begin{bmatrix} 1 & 0 & 0 \\ 0 & 1 & 0 \\ 0 & 0 & 1 \end{bmatrix} \tag{III.18}$$

$$\underline{\underline{\Sigma}}_\mu = \begin{bmatrix} 0 & 1 & 0 \\ 1 & 0 & 0 \\ 0 & 0 & 0 \end{bmatrix} \tag{III.19}$$

Then effective bulk modulus $\bar{k}_{eff}$ and shear modulus $\bar{\mu}_{eff}$ can be defined as follows:

$$\frac{1}{\bar{k}_{eff}} = trace\left\langle \underline{\underline{\varepsilon}} \right\rangle \tag{III.20}$$

$$\frac{1}{\bar{\mu}_{eff}} = 2\left\langle \varepsilon_{12} \right\rangle \tag{III.21}$$

III.1.3 Numerical homogenization of textile woven fabric

Numerical homogenization has been applied in order to predict the macroscopic and mesoscopic behaviour of textile woven fabric. Normally, the multi-scale numerical analysis using homogenization techniques is performed in two steps, as shown in Figure III.4.

- (i) Firstly, the micro-scale RVE is selected as a unit cell of the microstructure. The properties of the homogenized yarn are determined using the properties of the fibres and the matrix on the micro-scale.
- (ii) Secondly, the macro-meso RVE is built using homogenised yarn in order to obtained effective macro properties of the fabric. Appropriate RVE and boundary conditions must be selected and applied in each step.

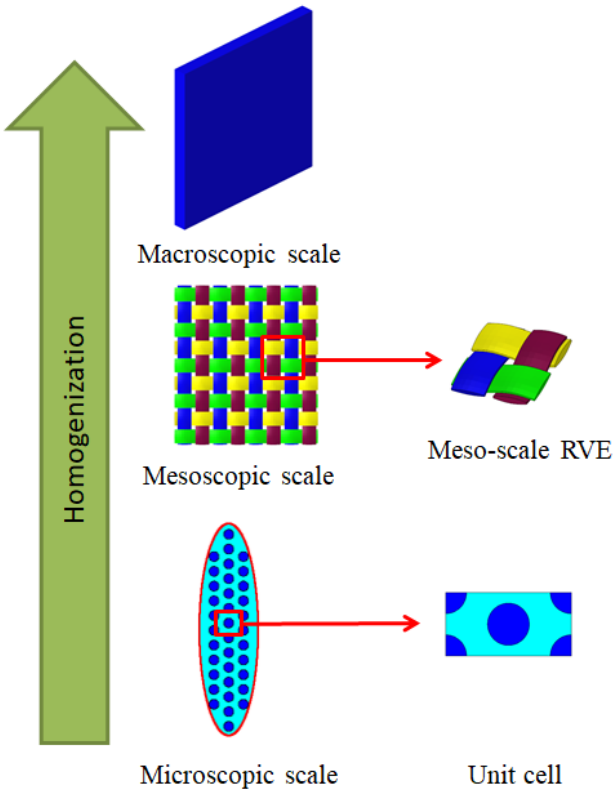

Figure III.4 Schematic of multi-scale numerical homogenization techniques.

Sun et al. [108] stated that in order to estimate the properties of a composite material, a correct RVE must be determined according to the distribution of the fibres. For the periodic fibre distribution, the elastic constants and fibre volume fraction of the RVE and the composite must be the same. Figure III.5 presents the RVE in the square and the hexagonal array, which are commonly used in woven textile composites. Then, appropriate boundary conditions need to be applied to the RVE. Finally, the average stress and strain obtained from boundary displacements are utilised to compute the equivalent properties constants.

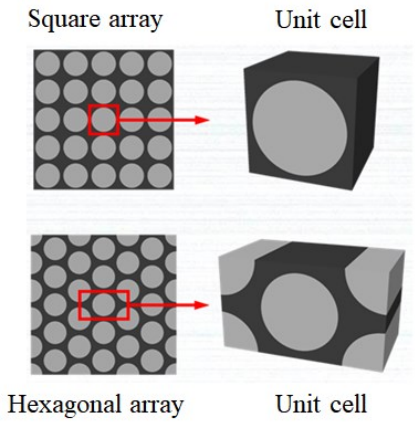

Figure III.5 RVEs in the case of square and hexagonal array configuration [108].

Textile woven fabric has been numerically investigated by the homogenization approach by many authors. Carvelli et al. [109] proposed a procedure for numerical analysis of woven fabric using a homogenization method based on the assumption of the periodic distribution of fibres in the yarns as well as the periodic arrangement of yarns in the fabric. A dual homogenization procedure is applied to the yarns using the microscale and subsequently to the mesoscale representative volume of the fabric. The results were validated by comparing with experimental data, as shown in Figure III.6.

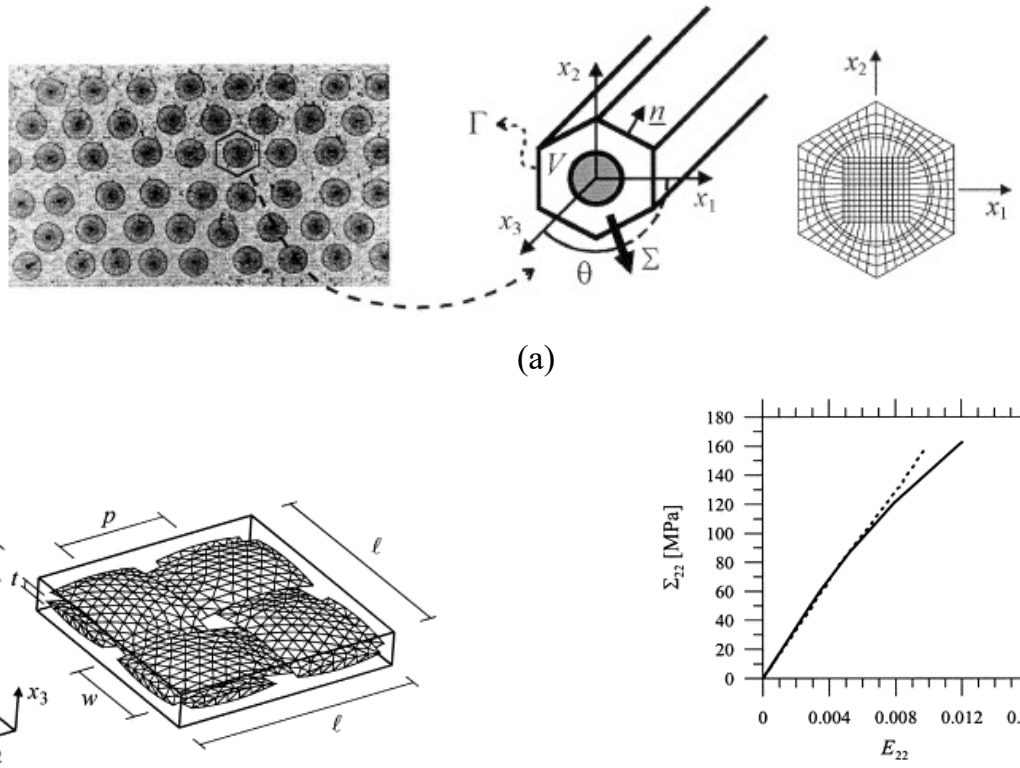

Figure III.6 (a) Micro scale RVE, (b) meso scale RVE, (c) Macroscopic stress–strain relations of woven fabric in comparison with experimental data (dashed line).

Figure III.7 presents the entire procedure proposed by Xiongqi Peng *et al*. [110] in order to predict the effective nonlinear elastic moduli of a plain weave composite using the finite element and the homogenization method.

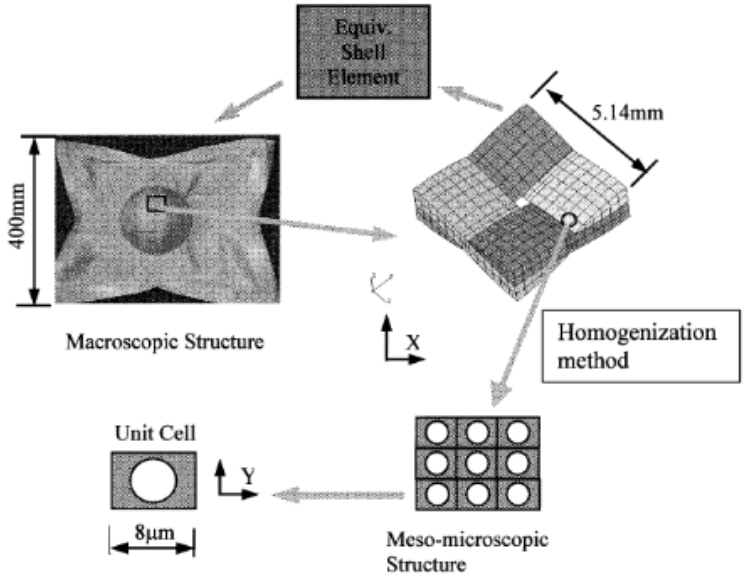

Figure III.7 Multi-scale material characterization approach [110].

A unit cell of fibre yarn was built. Then, homogenization method was applied for this unit cell to obtain the elastic constants of the yarn. Another unit cell was built for the textile composite. By applying numerical trellising and extension tests on this unit cell, the force-displacement curves were obtained. Finally, the equivalent elastic properties of the equivalent shell, which has the same outer dimension as the unit cell, were obtained by correlating these curves, as shown in Figure III.8.

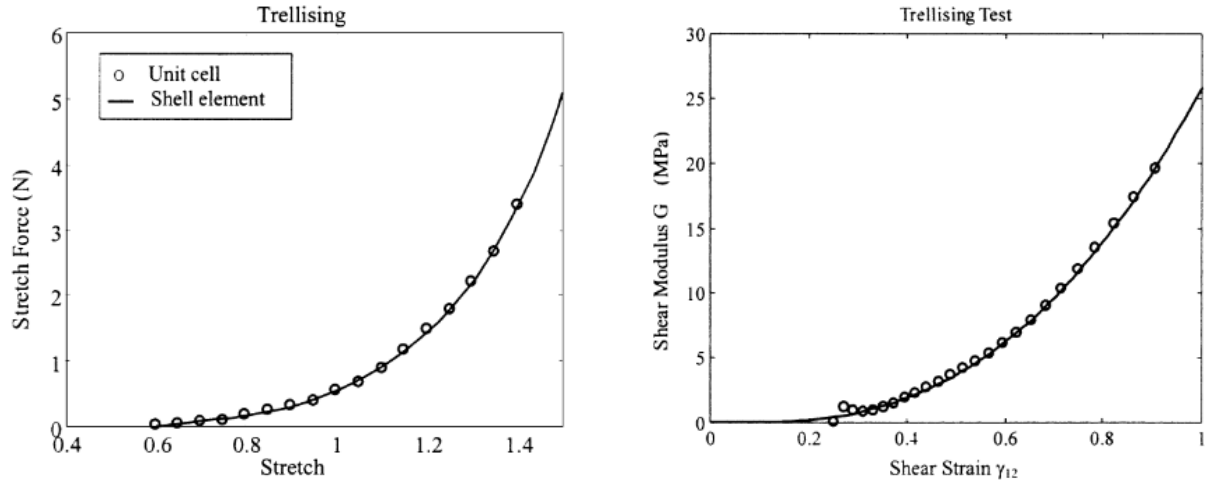

(a) (b)

Figure III.8 (a) Comparison of stretch force, (b) Equivalent shear modulus [110] .

The failure process of the woven fabric under off-axial loading was investigated using homogenization approach in reference [111]. The mesoscopic and microscopic RVEs were identified. In order to obtain the effective properties of the tow, numerical simulation was performed on the microscopic RVE, as shown in Figure III.9. Stress-

strain curves were obtained, and the initial linear portion of the curves was used to determine the particular elastic constants. The predicted yield stress obtained from the stress and strain curves was considered as the corresponding strength value.

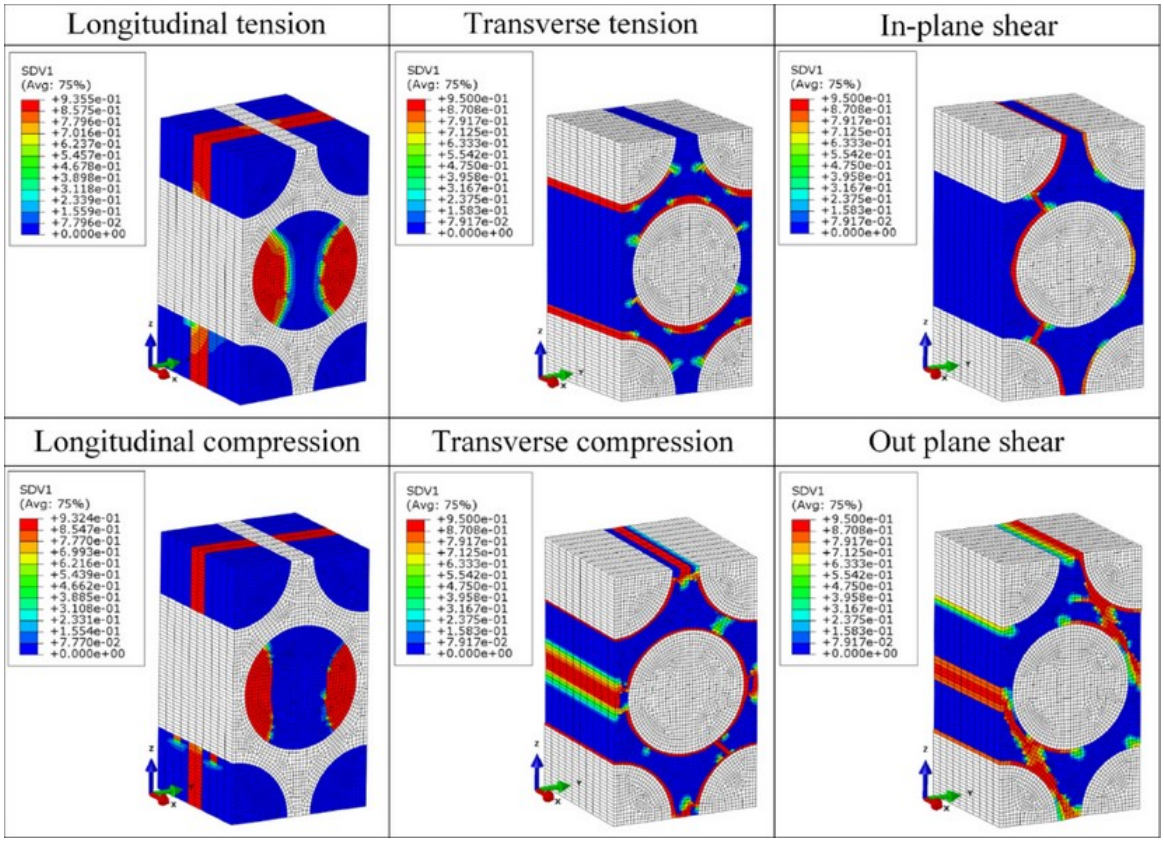

Figure III.9 Failure modes of the tow under different uniaxial loads [111] .

Shear deformed twill woven composite non-linear mechanical behaviour was investigated using a micro-scale and a mesoscale RVE model based on multi-scale progressive failure analysis in the work of Hwang et al. [112]. Failure modes, mechanical properties, and stress-strain curves were predicted. The elastic modulus varied from 4.8 to 23.9 GPa, the tensile strength range in the range of 80 to 375 MPa, and the failure strain varied from 0.018 to 0.13 according to the shear deformed twill woven composite fibre angle. The fibre and matrix failure distribution is illustrated in Figure III.10.

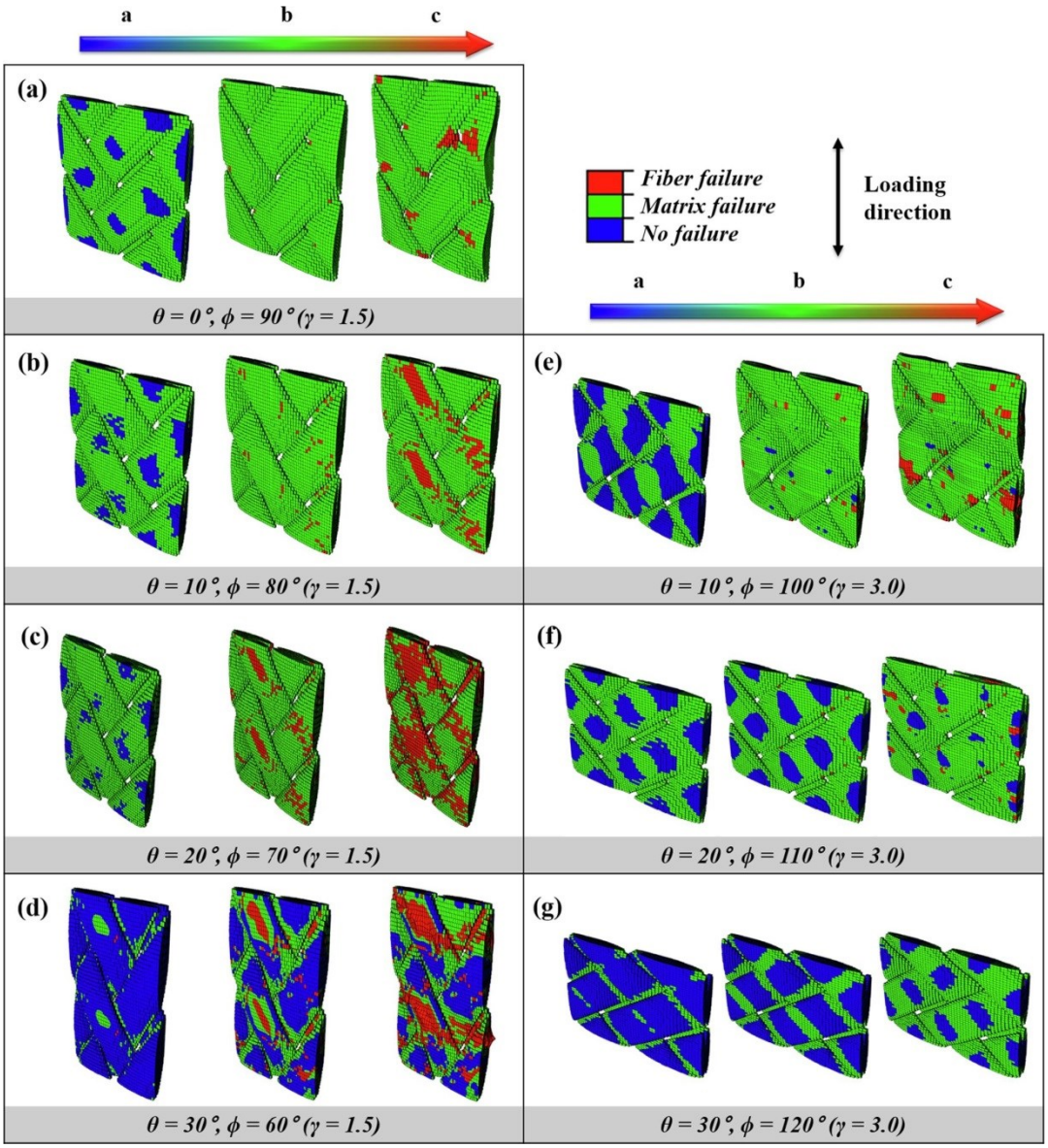

Figure III.10 Fibre and matrix failure distribution of various fibre angle models [112].

Part 2. Homogenization Approach of Fibres

III.2 Homogenization approach of transverse compressive behaviour of a block of fibres

In this section, the transverse compressive behaviour of one block of Kevlar KM2 fibres is analysed using homogenization approach. A new strategy based on the finite element homogenization method, proposed by Kanit *et al.* [90], will be introduced in order to obtain the effective properties which can represent the elastic nonlinearity of the microstructure. Results will be validated by comparing with those of the microscopic approach in section II.4 of Chapter II.

III.2.1 RVE determination

In this calculation, a new strategy is introduced. The RVE is chosen not only at the initial stage (without loading) but also during the deformation process. The initial RVE is selected as the unit cell of the periodic microstructure, as illustrated in Figure III.11. All microscopic characteristics are considered but in optimal size. This one is selected based on the initial fibres packing in which one fibre is in contact with six surrounding ones. The initial fibre volume fraction V_{f0} is equal to 90.8 %.

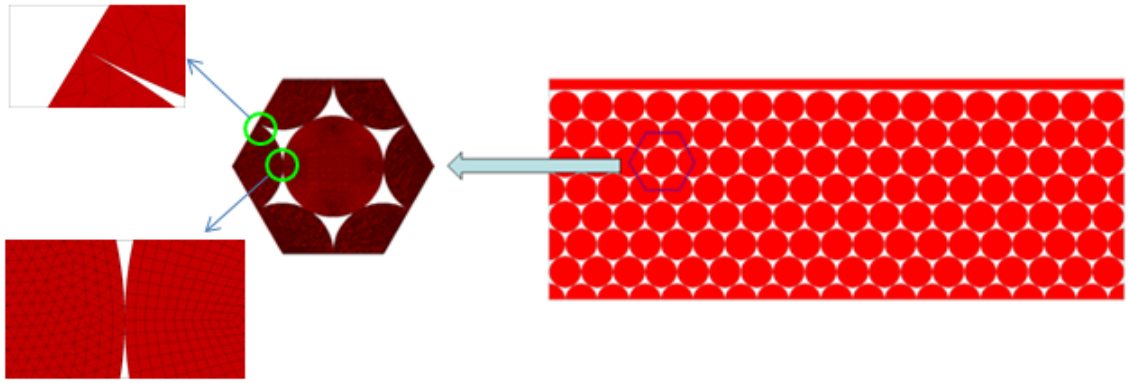

Figure III.11 Initial RVE.

Figure III.11 also illustrates the mesh of the initial RVE. In order to decrease the number of elements, 2D rectangular elements were used to discretise the central fibre, while the others are discretised by triangular elements due to their complex geometry.

During the microscopic deformation process, since the shape and fibre volume fraction of the microstructure change, the initial RVE cannot represent the deformed structure. Thus, a new RVE should be determined in order to address this problem. Due to the symmetry of the deformation, the initial RVE can be considered to transform into a new RVE called “deformed RVE”. Finally, a set of RVEs is obtained by selecting one

deformed RVE at each stage of deformation from the microscopic model. Figure III.12 shows an example of some deformed RVEs.

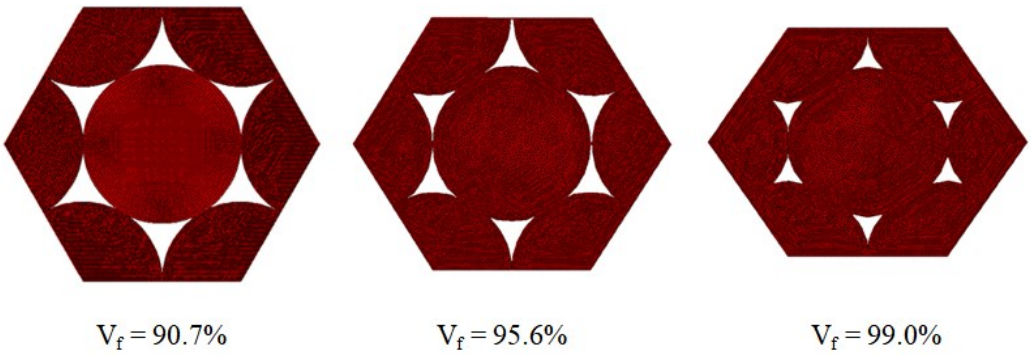

Figure III.12 RVEs correspond with different fibre volume fraction.

III.2.2 Boundary conditions

As discussed in Chapter II, since the cross-section dimension can be negligible compared to the length of the block, a 2D plane strain assumption is used. It should be noted that the RVE is determined as a unit cell due to the periodic microstructure. In this case, the homogenized properties are independent of the boundary conditions [102, 113]. Thus, Kinematic Uniform Boundary Conditions (KUBC) are employed.

In the case of a 2D plane strain problem, KUBC is described by imposing the displacement vector $\underline{u}$ at the point position vector $\underline{x}$ of the boundary ∂s :

$$\underline{u} = \underline{\underline{\Xi}}.\underline{x} \tag{III.22}$$

Where $\underline{\underline{\Xi}}$ is a symmetrical second-order tensor independent of $\underline{x}$

$$\underline{\underline{\Xi}} = <\underline{\underline{\varepsilon}}> = \frac{1}{S}\int_S \underline{\underline{\varepsilon}} dS \tag{III.23}$$

The macroscopic stress tensor is defined by the spatial average:

$$\underline{\underline{\Sigma}} = <\underline{\underline{\sigma}}> = \frac{1}{S}\int_S \underline{\underline{\sigma}} dS \tag{III.24}$$

III.2.3 Effective transverse macroscopic properties

In order to compute the effective transverse bulk modulus of the homogenized material, a strain tensor is imposed as follows:

$$\underline{\underline{\Xi}}_k = \begin{bmatrix} 1 & 0 \\ 0 & 1 \end{bmatrix} \tag{III.25}$$

Then the 2D effective transverse bulk modulus is calculated:

$$\bar{k}_{eff} = \frac{1}{4} trace\left\langle \underline{\underline{\sigma}} \right\rangle \tag{III.26}$$

The 2D effective transverse shear modulus is computed using the following equation:

$$\underline{\underline{\Xi}}_\mu = \begin{bmatrix} 0 & \frac{1}{2} \\ \frac{1}{2} & 0 \end{bmatrix} \tag{III.27}$$

$$\bar{\mu}_{eff} = \left\langle \sigma_{12} \right\rangle \tag{III.28}$$

Because of *in-plane* bulk modulus, the effective properties are computed from these parameters using the following equations [114]:

$$\bar{k} = \frac{\bar{E}}{2(1+\bar{\nu})(1-2\bar{\nu})} \tag{III.29}$$

$$\bar{\mu} = \frac{\bar{E}}{2(1+\bar{\nu})} \tag{III.30}$$

$$\bar{\nu} = \frac{\bar{k} - \bar{\mu}}{2\bar{k}} \tag{III.31}$$

III.2.4 Results and discussion

As mentioned above, a set of RVEs is obtained. For each RVE, boundary conditions are applied. Figure III.13 presents some examples of the deformation and stresses of the RVEs in this calculation. For each RVE, 11 strain and stresses are shown in the case of the bulk modulus calculation, while 12 strain and stresses are shown for the shear modulus.

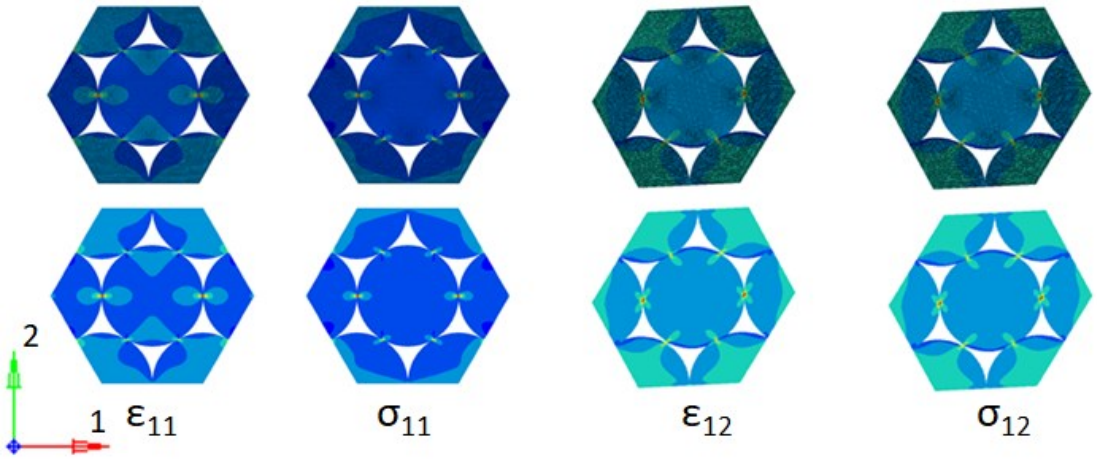

(a)

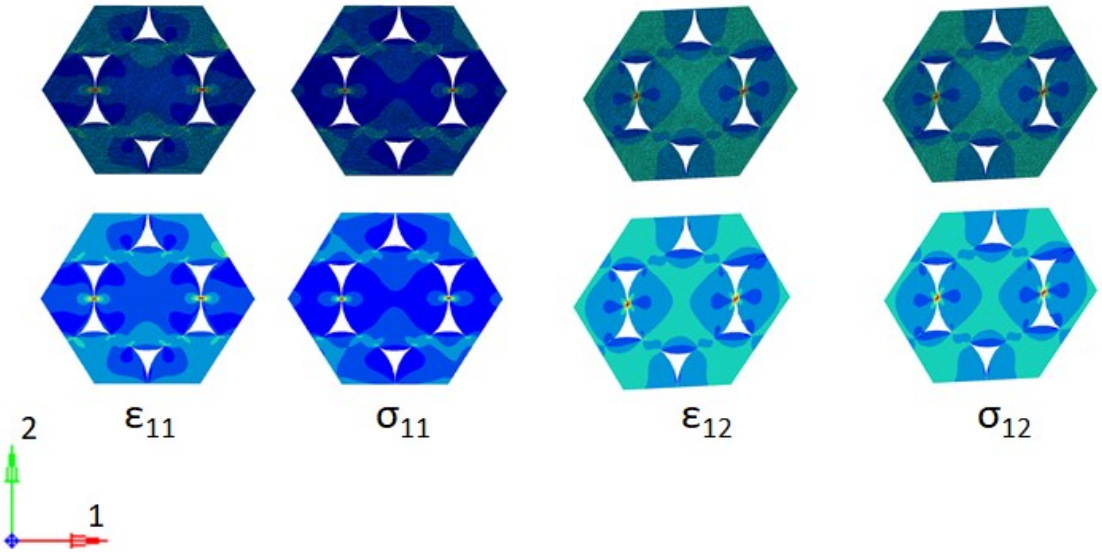

(b)

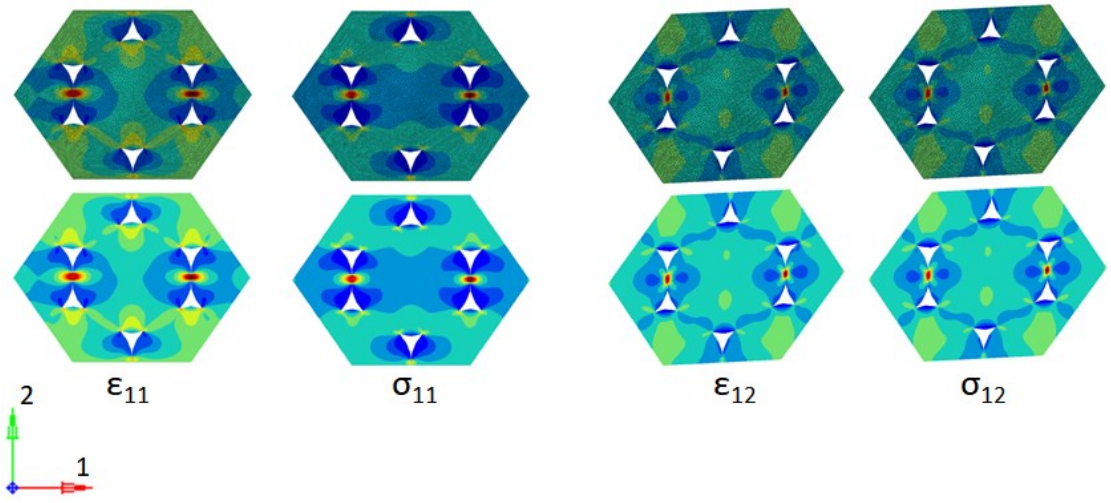

(c)

Figure III.13 Stress and strain of RVEs corresponding with (a) $V_f = 90.7$ %, (b) $V_f = 95.6\%$, (c) $V_f = 99.0\%$.

A set of effective properties is obtained, as shown in the following table:

Table III.1 Effective mechanical properties versus fibre volume fraction

V_f (%)	$\overline{E}[GPa]$	$\overline{\nu}$	$\overline{\varepsilon}$ (%)
90.7	0.56	0.101	0
91.0	0.63	0.139	3.2
91.6	0.69	0.161	4.7
92.2	0.76	0.177	6.3
92.9	0.81	0.180	7.9
94.1	0.90	0.184	9.5
94.7	0.95	0.196	11.0
95.2	0.96	0.198	12.6
95.6	1.04	0.215	14.2
95.9	1.08	0.218	15.8
96.2	1.09	0.216	17.4
96.9	1.14	0.218	20.5
97.6	1.17	0.222	23.7
98.3	1.20	0.226	26.8
99.0	1.29	0.237	30.0

It should be noted that the earlier homogenization theory in which only one RVE is determined in the initial stage provides a linear elastic material law as shown in the first row of Table III.1, while the new strategy can provide a non-linear elastic law. Evolutions of the effective transverse mechanical properties as functions of fibre volume fraction can be deduced from Table III.1. Additionally, the variation of the apparent macroscopic strain $\overline{\varepsilon}$ with the fibre volume fraction V_f is also obtained.

Analysing the microscopic behaviour of the block in Chapter II, the evolution of macroscopic strain $\overline{\varepsilon}$ versus fibre volume fraction V_f is presented in Figure III.14. It clearly shows that as the fibres are compressed, the voids between them decrease, resulting in the increase of the fibre volume fraction. In the initial stage, the strain increases dramatically. However, it shows a slight increase until the fibre volume fraction reaches 95%, then rises sharply.

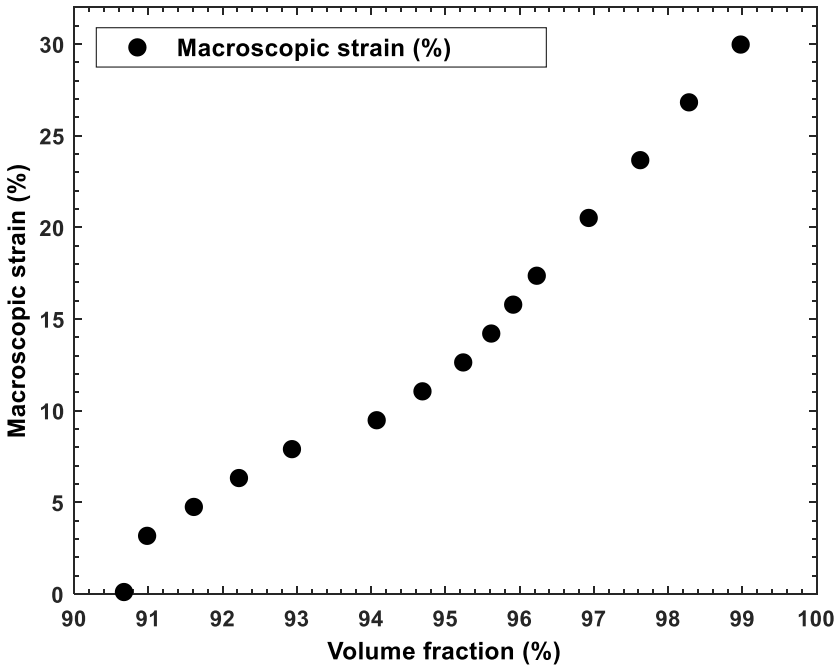

Figure III.14 Evolution of macroscopic strain versus fibre volume fraction.

Figure III.15 shows that the effective transverse modulus $\overline{E}$ has a mostly linear increase with the fibre volume fraction V_f. Thus, it can be concluded that the effective transverse mechanical properties are governed by the variation of the fibre volume fraction.

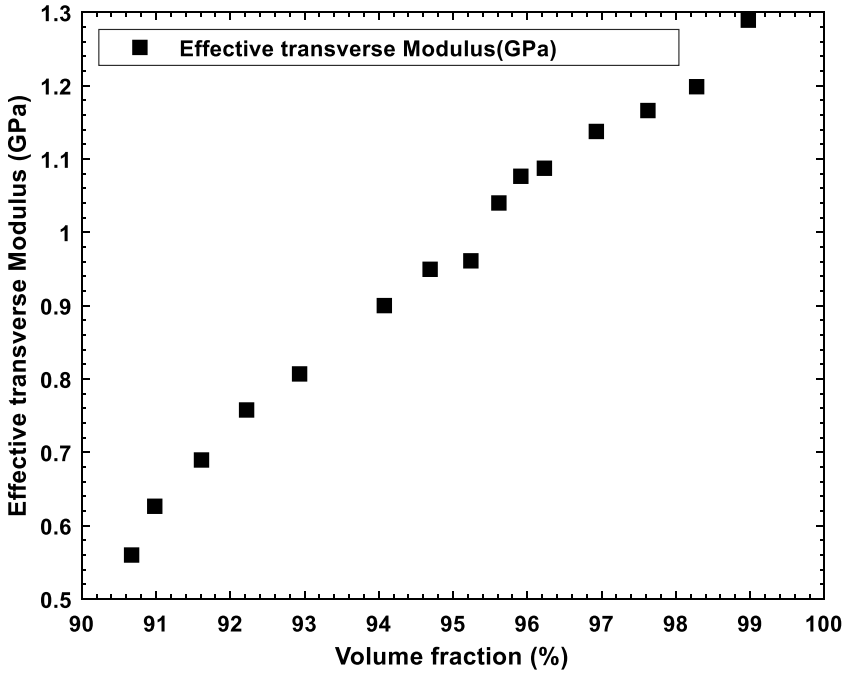

Figure III.15 Effective Young's modulus $\overline{E}$ versus fibre volume fraction V_f.

In order to propose a constitutive material model, the evolutions of the effective transverse Young's modulus $\overline{E}$ and the macroscopic strain $\overline{\varepsilon}$ are analysed as a function of the initial effective transverse Young's modulus $E_0 = 0.56$ GPa and the normalized fibre volume fraction $(V_f / V_{f0} - 1)$. Here V_f is the fibre volume fraction and $V_{f0} = 90.7\%$ is the initial one. Figure III.16 shows the evolution of the macroscopic strain and the effective transverse modulus. It should be noted that the macroscopic strain and effective transverse modulus can be modelled by power functions.

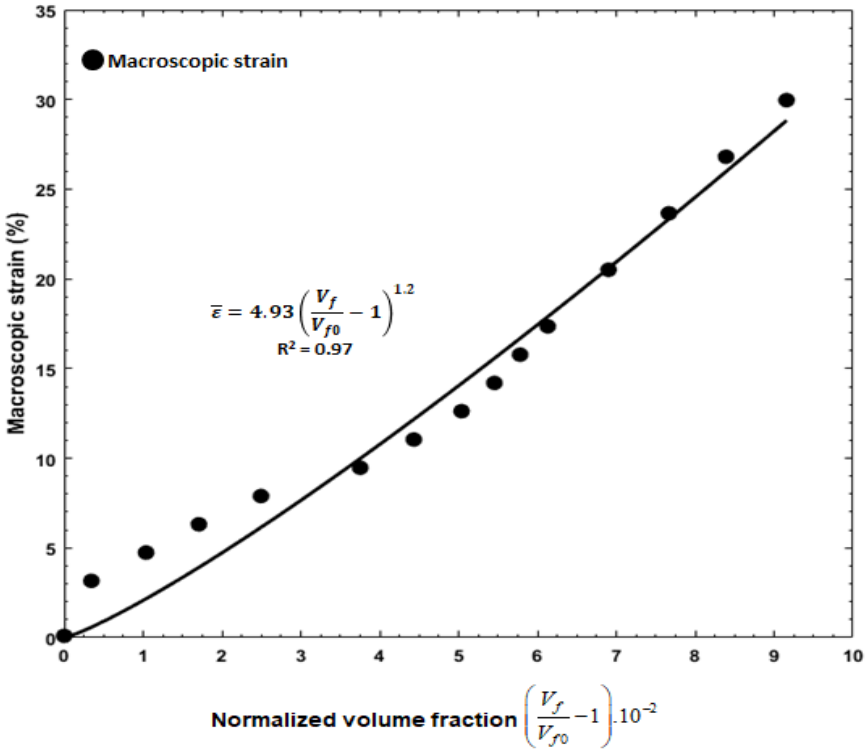

(a)

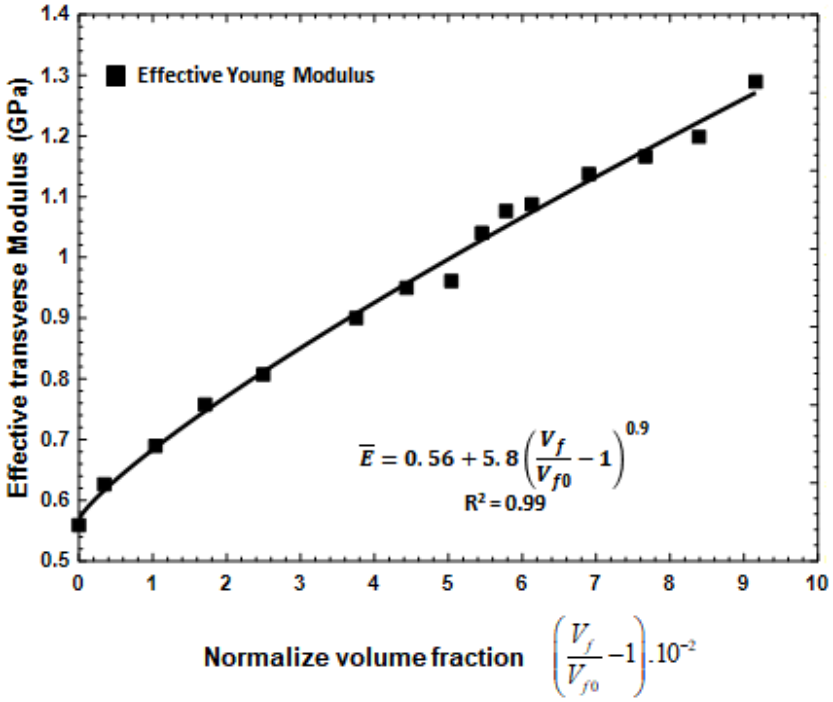

(b)

Figure III.16 (a) Effective transverse modulus and (b) apparent strain versus normalized fibre volume fraction.

The macroscopic apparent strain can be described as follows:

$$\overline{\varepsilon} = a\left(\frac{V_f}{V_{f0}} - 1\right)^b \tag{III.32}$$

Here, $a = 4.93$ and $b = 1.2$ are obtained from curve fitting with $R^2 = 0.97$. The following formula can describe the effective transverse modulus:

$$\overline{E} = E_0 + \alpha\left(\frac{V_f}{V_{f0}} - 1\right)^\beta \tag{III.33}$$

Where $E_0 = 0.56\,\text{GPa}$ is the initial transverse modulus, and $\alpha = 5.8$, $\beta = 0.9$ are also constants obtained from curve fitting with $R^2 = 0.99$. These parameters can be considered as constant properties of the homogenized effective material.

Equations III.32 and III.33 provide the necessary basis to form a relationship between stress and strain of a fibrous material subjected to transverse compression [85, 88]. The above effective transverse Young's modulus can be considered as the tangent

Young's modulus. Then, the stress-strain curve is obtained and compared with the numerical microscopic model, as shown in Figure III.17.

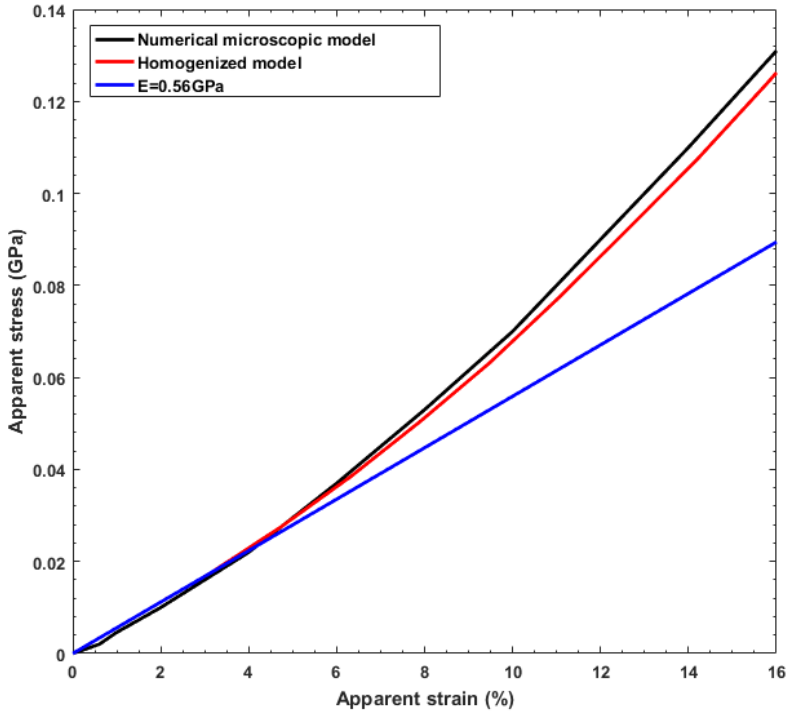

Figure III.17 Comparison of homogenized material and numerical microscopic model.

Figure III.17 clearly shows a good agreement between the two models. Meanwhile, in comparison with the homogenized material obtained from the early homogenization theory in which the effective transverse Young's modulus equals the initial effective transverse Young's modulus $E_0 = 0.56$ GPa, the new strategy provides a sharp improvement. It is noted that the nonlinear behaviour of this structure is highlighted.

III.3 Homogenization approach of transverse compressive behaviour of a yarn

In this section, the transverse compressive behaviour of a Kevlar KM2 yarn is investigated using a homogenization approach. The schema of one homogenized yarn is displayed in Figure III.18. In this case, as a 2D plane strain problem is assumed, the homogenized yarn cross-section is considered sinusoidal due to the compression of two neighbouring sinusoidal ones. A new strategy of finite element homogenization in which the contact between fibres is considered, is introduced. Results will be validated by comparing with those of the microscopic approach in section II.5 of Chapter II.

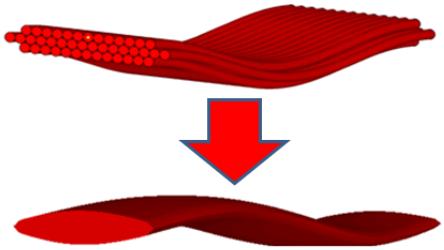

Figure III.18 Schema of one homogenized yarn.

III.3.1 RVE determination

As discussed in section II.5 of Chapter II, in zone 1 of the microscopic behaviour, the fibres rearrange without deformation and contact. Thus, zone 2 will be considered for the homogenization approach. Then, the initial stage of zone 2 (point A in Figure II.35) is considered as the initial stage of the yarn for the homogenization approach.

The initial RVE is determined as a unit cell in the case of a periodic microstructure [113], as shown in Figure III.19. It should be noted that the initial fibre volume fraction of the microscopic structure is equal to 82.4%. Thus, in order to obtain this initial volume fraction, gaps between fibres are added. These gaps also ensure that no contact occurs. The void is assigned as the matrix (the blue part) with the properties of Young's modulus $E_a = 0.00001\,\text{GPa}$ and Poisson's ratio $\nu = 0.499$.

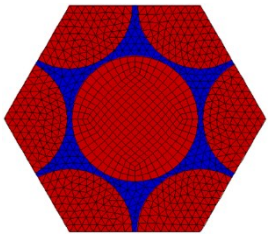

Figure III.19 The initial RVE.

III.3.2 Effective properties

As the RVE is determined as a unit cell in the case of a periodic microstructure, and the homogenized properties are independent of the boundary conditions. Thus, only Kinematic Uniform Boundary Conditions (KUBC) are employed. The boundary conditions were described in section III.2.2.

Bulk modulus

To determine the effective bulk modulus, compressive strain tensor $\underline{\underline{\Xi}}_k$ is imposed.

$$\underline{\underline{\Xi}}_k = \begin{bmatrix} -0.5 & 0 \\ 0 & -0.5 \end{bmatrix} \tag{III.34}$$

This tensor ensures that the deformation of the RVE is not too large, and no damage occurs. Then bulk modulus is calculated as follows:

$$\bar{k}_{eff} = \frac{trace\langle \underline{\underline{\sigma}} \rangle}{trace\langle \underline{\underline{\varepsilon}} \rangle} \tag{III.35}$$

As mentioned in references [87, 115, 116], the effective transverse properties vary during the compression process as the volume fraction increases, and contact between fibres also occur. However, using the procedure above, only a constant bulk modulus is obtained. To solve this issue, the gap between the fibres of the RVE is gradually decreased. Then, a series of similar RVEs with different volume fractions is obtained. KUBC is then applied in each RVE. Finally, the variation of bulk modulus versus volume fraction is observed.

Figure III.20 presents the stress and strain of the RVE corresponding with the initial fibre volume fraction of 82.4%

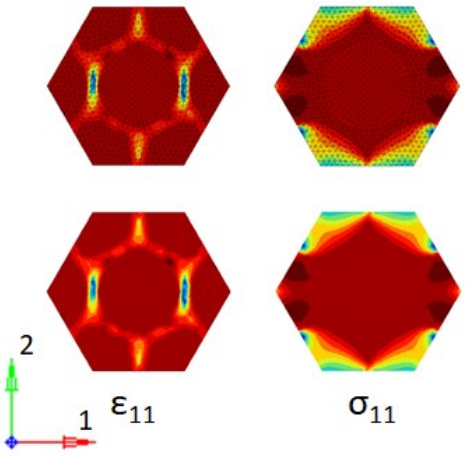

Figure III.20 Stress and strain in the case of the RVE corresponding with $V_{f0} = 82.4\%$.

Nevertheless, during the compression process, the matrix of the RVE will be too deformed, and the calculation does not converge. To overcome this problem, contacts between fibres are added. The process is divided into two steps, as follows:

- First step: the gap between fibres is decreased until approximately 0, but no contact occurs. The initial effective bulk modulus $k_0 = 0.146\,\text{GPa}$ is obtained. In this step, the initial RVE ($V_f = 82.4\%$) and two other similar ones with volume fraction of

$V_f = 87.6\%$ and $V_f = 90.7\%$ are used for the computation. This step considers the transit zone of the behaviour discussed in Chapter II.

- Second step: The RVE in the final stage of the first step in which the gap between the fibres is approximately 0 is selected as the new RVE of the second step. The void mesh is removed (Figure III.21). Additionally, contacts between fibres are considered. Unlike step 1, in this step, only one RVE is used. However, the tensor strain is applied by gradually increasing the value of strain from 0 to -0.2 in several increments. Each increment corresponds with a pair of volume fraction and effective bulk modulus.

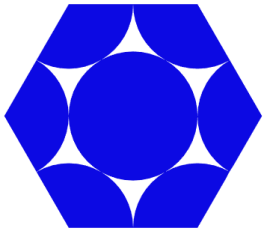

Figure III.21 RVE without void mesh.

In this calculation, penalty contact is implemented. The contact behaviour is defined in terms of normal σ and tangent τ contact stresses. It allows the contact constrains to be violated using the penalty parameters in the normal γ_n and tangential γ_t directions. Two auxiliary forces are defined as follows:

$$\sigma = \sigma - \left[\gamma_n^{-1}\sigma + k_n\left(u_n + \gamma_n^{-1}du_n\right)\right] \tag{III.36}$$

$$\hat{} \quad \llcorner \quad {}^{-1}d\tau + k_t du_t \rceil \tag{III.37}$$

Here, u_n stands for the normal displacement between potential contacting surfaces. du_t is the incremental tangent displacement, and k_n and k_t are the contact stiffness in the normal and tangent directions, respectively. Then the penalty contact model is expressed as follows:

If $\sigma > 0$

then $\gamma_n^{-1}\sigma + k_n\left(u_n + \gamma_n^{-1}du_n\right) = 0$

if $|\tau| < \mu\sigma$

then $\gamma_t^{-1}d\tau + k_t du_t = 0$

else $\tau = \mu\sigma n_t$ with $n_t = \hat{} \quad \hat{}$

else $\sigma = 0, \tau = 0$

Figure III.22 shows stress and strain of the RVE

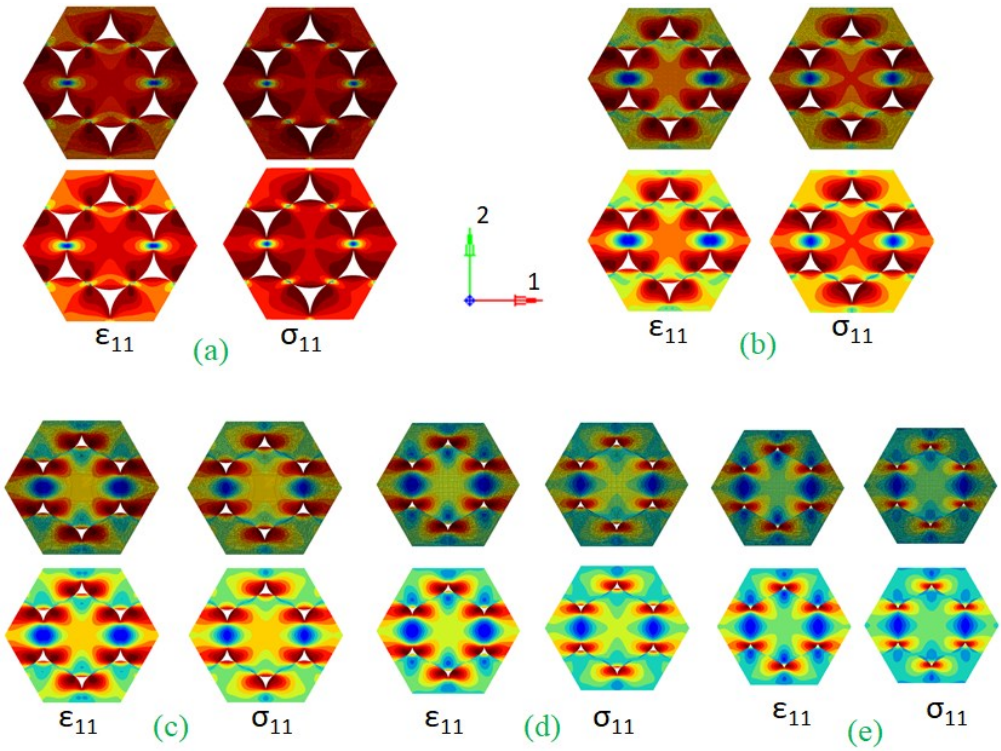

Figure III.22 Stress and strain of RVEs corresponding with (a) $V_f = 90.7$ %, (b) $V_f = 94.9\%$, (c) $V_f = 97.3\%$, (d) $V_f = 98.7\%$, (d) $V_f = 99.5\%$.

The variation of effective bulk modulus versus the volume fraction is shown in Figure III.23. It clearly shows the effect of contacts between fibres. Once it occurs (volume fraction $V_f > 90.7\%$), the bulk modulus increases sharply. In fact, without contact, the effect of the matrix (void) is insignificant, and thus the bulk modulus only changes slightly.

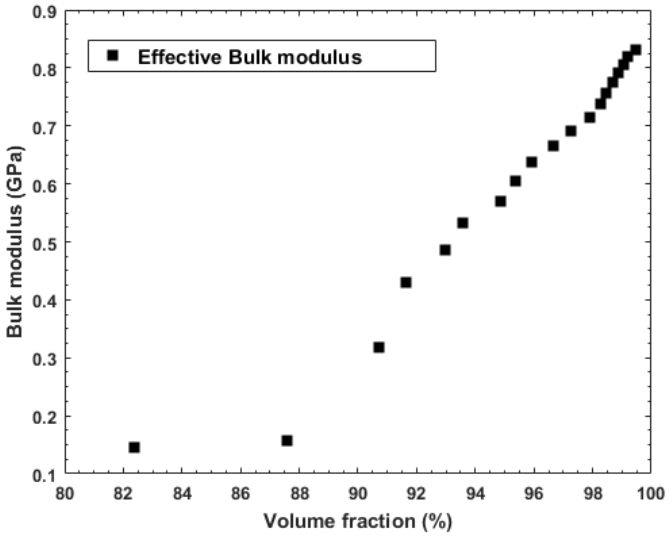

Figure III.23 Effective bulk modulus versus volume fraction.

Effective shear modulus

In order to obtain effective shear modulus, the strain tensor $\underline{\underline{\Xi}}_{\mu}$ is introduced:

$$\underline{\underline{\Xi}}_{\mu} = \begin{bmatrix} 0 & -0.5 \\ -0.5 & 0 \end{bmatrix} \tag{III.38}$$

Then, the effective shear modulus is computed as follows:

$$\mu_{eff} = \frac{<\sigma_{12}>}{2<\varepsilon_{12}>} \tag{III.39}$$

Stress and strain of the RVE are shown in Figure III.24. The initial effective shear modulus $\mu_0 = 0.254\,\text{GPa}$ is obtained.

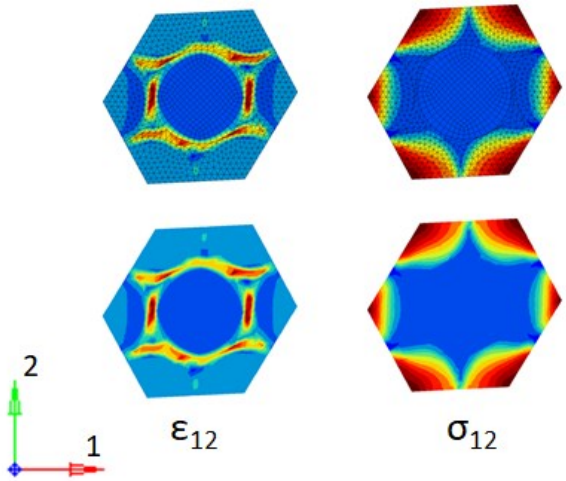

Figure III.24 Stress and strain of RVE.

However, using the same procedure as effective bulk modulus, it is impossible to obtain the variation of effective shear modulus versus fibre volume fraction because the volume fraction changes slightly in the case of pure shear. The most deformed stage of the RVE corresponds to the volume fraction of 90.9% (Figure III.25).

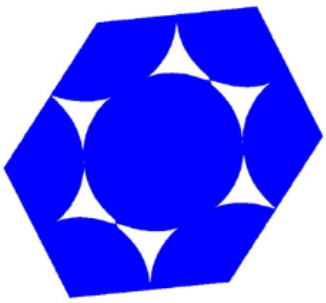

Figure III.25 The most deformed shape of RVE in shear loading.

It should be noted that in the most compact stage of the yarn, the volume fraction approaches 99.99%. Thus, in the case of no matrix, the effective properties are almost the same as the properties of the inclusion (fibres). Therefore, it can be assumed that the effective shear modulus linearly increases from $\mu_0 = 0.254\,\text{GPa}$ $(V_f = 82.4\%)$ to $\mu_{fibre} = 0.54\,\text{GPa}$ $(V_f = 99.99\%)$.

Once, the effective bulk and shear moduli are obtained, the effective transverse modulus is computed by using equations III.29, III.30 and III.31. The results are shown in Figure III.26. The homogenized nonlinear elastic effective transverse modulus is deduced and described by a power-law formula in the relationship with the normalized volume fraction $(V_f / V_{f0} - 1)$ by curve fitting with $R^2 = 0.99$, as shown in the following equation:

$$\overline{E} = 0.25 + 12.3\left(\frac{V_f}{V_{f0}} - 1\right)^{1.6} \tag{III.40}$$

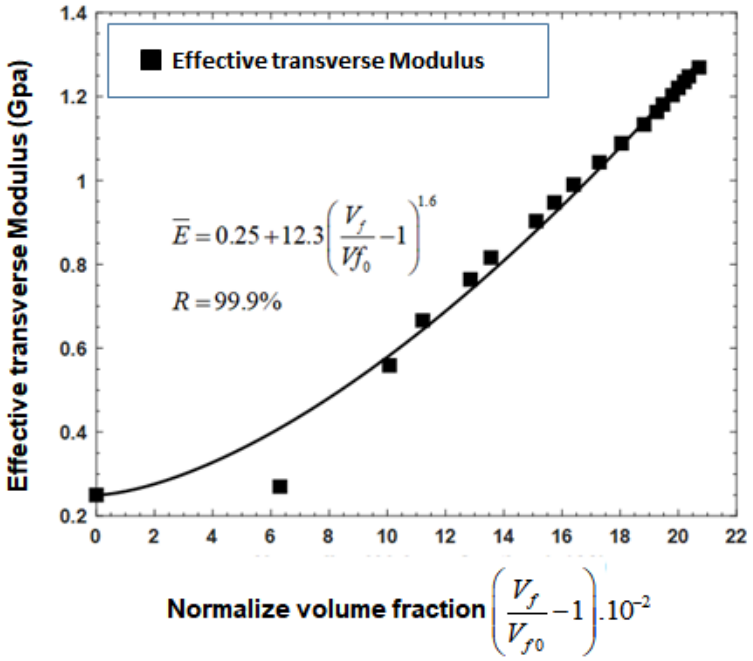

Figure III.26 Effective transverse modulus versus normalized volume fraction.

III.3.3 Numerical homogenization results

In this section, the homogenized model is conducted using the nonlinear elastic behaviour law deduced from equation II.12 (Chapter II) and equation III.40. This law is

implemented into ABAQUS/Standard through a user-subroutine. A half 2D plane strain homogenized model is utilised with boundary conditions shown in Figure III.27.

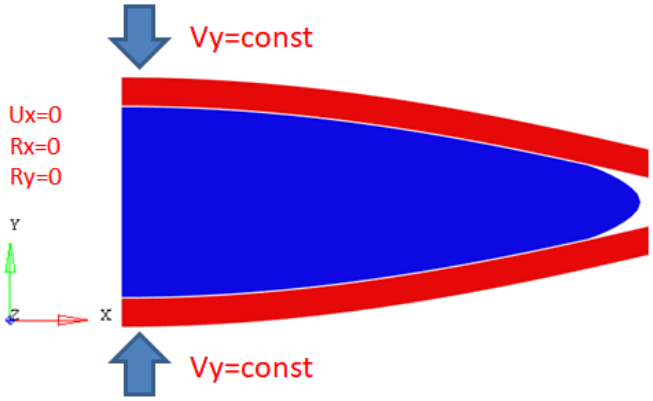

Figure III.27 Homogenized model.

As ABAQUS/Standard does not support the tangent modulus, the equivalent secant modulus is used instead. The average Poisson's ratio $\bar{\nu} = 0.16$ is assumed. Figure III.28 displays the true strain at the effective displacement $\delta_R = 21$ μm. It clearly shows that the parts furthest from the centre of the yarns are more compressed than the centre part. Additionally, the furthest part is not the most compressed part. This result is consistent with the result of the microscopic model in Chapter II.

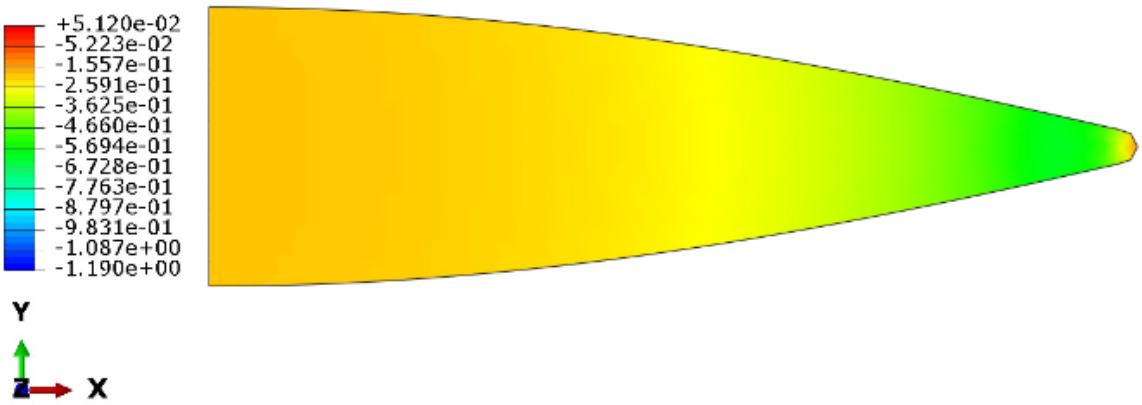

Figure III.28 True strain in YY direction at effective displacement $\delta_R = 21\mu m$

The effective properties are validated by comparing the homogenized model with the microscopic one in Chapter II. A good agreement between the homogenized model and the microscopic one is obtained (Figure III.29). Nonlinear elastic behaviour is also observed. Therefore, the effective homogenized material law is validated. This homogenized material law can be implemented into the FE code in further studies of Kevlar® KM2 fabric textile behaviour.

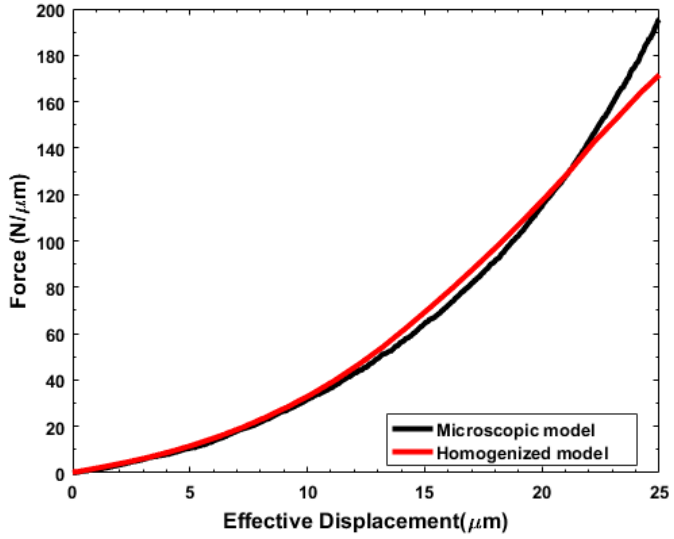

(a)

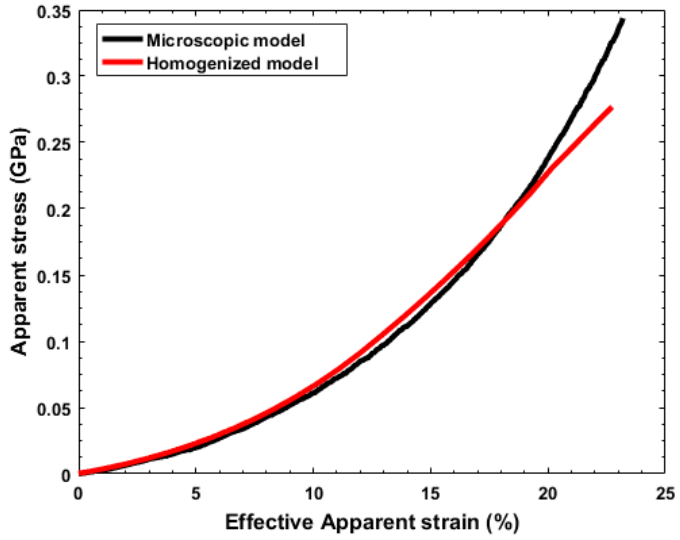

(b)

Figure III.29 Microscopic versus homogenized model.

It should be noticed that differences between the two curves are also observed after the effective apparent strain of approximately 20%. This can be explained by the fact that in this stage, the contact mechanism of the microscopic model is very complex due to the very large deformation of fibres at the right end.

III.4 Conclusion

In this chapter, a brief review of the homogenization method and its application in textile woven fabrics are presented. Then, using numerical finite element homogenization techniques, effective homogenised behaviour laws representing the elastic nonlinearity of one block of Kevlar KM2 fibres and one Kevlar KM2 yarn are obtained. In these

techniques, the shape of the RVE is updated during the compression process. Additionally, the contacts between fibres within the RVE are also considered.

The variation of the effective transverse modulus with the normalised volume fraction and apparent strain is described by a power-law function. The behaviour law is implemented into the FEA ABAQUS/Standard and validated by a good agreement in comparison with the microscopic one. This law allows a more accurate prediction of Kevlar KM2 fabric behaviour subjected to ballistic impact in future works.

Chapter IV

Microscopic Behaviour of a Fabric Subjected to Ballistic Impact

Abstract

In this chapter, the behaviour of the woven material subjected to a ballistic impact (impact velocity of 245 m/s) is studied using a microscopic approach in the case of (i) a single crimped yarn and (ii) one fabric. In the case of a single crimped yarn, two numerical fibre-scale models, in which 400 fibres are represented by 42 and 98 equivalent fibres, respectively, are conducted. The two models are compared by analysing the energies of the yarn, the propagation of the transverse waves and the velocity of the projectile versus time. The tension forces of each fibre are observed. The results are compared with those obtained via mesoscopic modelling. Fibre failure during impact is analysed, resulting in exciting information regarding the damage process of the yarn in contact with a projectile.

Subsequently, a micro-mesoscopic multi-scale model of tissue is developed. Indeed, we consider a fabric with two primary yarns modelled on the microscopic scale (fibre scale) and the rest is modelled as a mesoscopic model. This approach allows for a better analysis of the physical mechanisms occurring in the impact zone under the projectile. It highlights the sliding phenomena and fibre failure, as well as the fibre-fibre and fibre-yarn interactions. This multi-scale model is also compared with a validated mesoscopic model.

Résumé

Dans ce chapitre, le comportement du matériau tissé soumis à un impact balistique (vitesse d'impact de 245 m/s) est étudié en utilisant une approche microscopique dans le cas (i) d'un seul fil ondulé et (ii) d'un tissu. Dans le cas d'un seul fil ondulé, deux modèles numériques à l'échelle des fibres dans lesquels les 400 fibres sont représentées respectivement par 42 et 98 fibres équivalentes sont réalisés. Les deux modèles sont comparés en analysant les énergies des fils, la propagation des ondes transversales et la vitesse du projectile en fonction du temps. Les forces à l'échelle de chaque fibre sont analysées. Les résultats sont comparés à ceux obtenus via une modélisation mésoscopique. Les ruptures des fibres au cours de l'impact sont analysées ce qui permet d'avoir accès à des informations très intéressantes dans le processus d'endommagement d'un fil au contact d'un projectile.

Par la suite, un modèle multi-échelle micro-mésoscopique de tissu a été développée. En effet, nous considérons un tissu avec deux fils primaires qui sont modélisés à l'échelle microscopique (échelle des fibres) et le reste est basé sur un modèle mésoscopique. Cette démarche permet de mieux analyser les mécanismes physiques se produisant dans la zone du tissu affectée par l'impact sous le projectile. Elle met en évidence les phénomènes de glissement et les ruptures des fibres, ainsi que les interactions entre fibre/fibre et fibres/fils. Cette modélisation multi-échelle (micro/méso) a été comparée à une modélisation mésoscopique.

Contents

IV.1 Behaviour of one single crimped yarn

The main objective of this part is investigating the behaviour at the fibre scale of one single crimped Kevlar KM2 yarn which is considered to behave almost like a yarn inserted into a realistic fabric [21]. In order to gain the computation time, two numerical sub-yarn level models in which 400 fibres are represented by 42 and 98 equivalent fibres respectively, are conducted. Each model will be evaluated by comparing and analysing yarn energies, deformation wave propagation and projectile velocity evolution.

IV.1.1 Schematic and initial conditions

In this section, a Kevlar KM2 yarn is investigated. The yarn comprised 400 fibres. The properties of Kevlar KM2 fibres have been introduced in 0. The cross-section of the yarn is considered as an ellipse with the major and minor axes being 0.590 and 0.112 mm, respectively [67].

In order to gain computation time, the concept of *Equivalent Fibre* is introduced, as shown in Figure IV.1. A set of fibres is represented by an equivalent fibre such that its area equals the total area of the fibres. Thus, the diameter of the equivalent fibre can be calculated as follows:

$$d_{eq} = 2\sqrt{\frac{2S_{total}}{n\pi}} \tag{IV.1}$$

Here, S_{tot} is the total area of 400 fibres, and n is the number of equivalent fibres representing for 400 fibres.

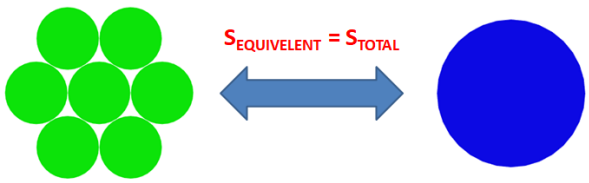

Figure IV.1 The concept of equivalent fibre.

Two sub-yarn level models are conducted: a 42-fibres model and a 98-fibres model. For the 42-fibres model, 400 fibres are represented by 42 equivalent fibres. The diameter of the equivalent fibre, in this case, is 37 µm. While for the 98-fibres model, the number of equivalent fibres is 98, and the diameter of the equivalent fibre is 24 µm.

Figure IV.2 presents the yarn cross-sections in the case of the 42-fibres model, the 98-fibres model, and the realistic yarn. It should be noted that in the case of the 42 equivalent fibres, the number of fibre rows in the yarn cross-section is three, while this number is five in the case of the 98 equivalent fibres and 11 for the realistic one.

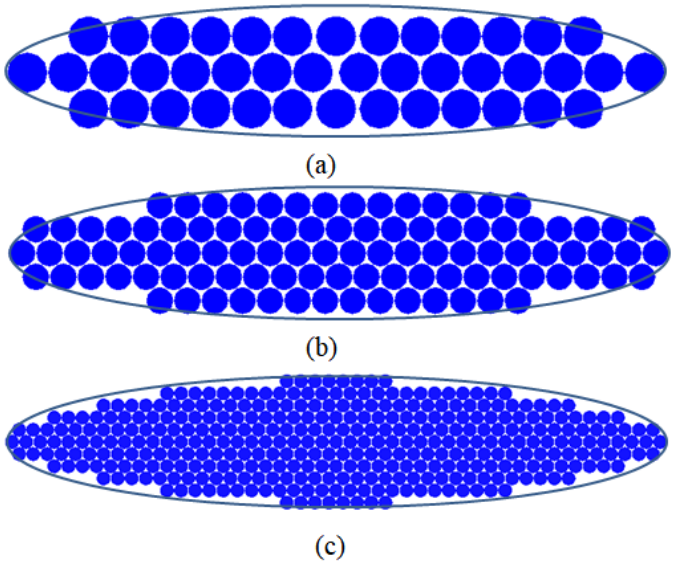

Figure IV.2 Yarn cross section (a) 42 equivalent fibres (b) 98 equivalent fibres (c) realistic yarn.

The schematic and boundary conditions of the model are shown in Figure IV.3. The numerical models are conducted using Finite Element code Radioss. Because of the symmetric configuration, a quarter of the FE model is conducted. The yarn's length is 50.6 mm. The projectile is spherical with a diameter of 5.33 mm and a mass of 0.625 mg. As the steel projectile has a very high Young's modulus in comparison with the fibres, it is assumed to be rigid. The chosen initial impact velocity is 245 m/s.

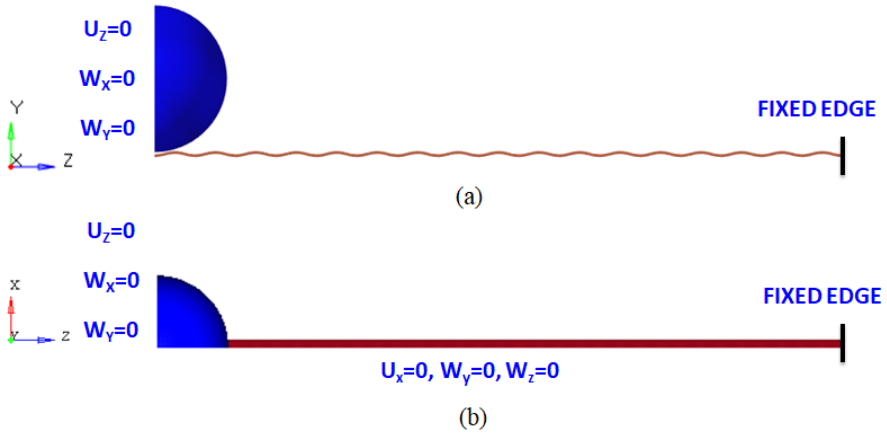

Figure IV.3 Schematic and boundary conditions (a) horizontal view, (b) vertical view of a quart of model.

Figure IV.4 shows the mesh of one equivalent fibre. The cross-section is discretised with nine brick elements. This mesh was proved to be sufficient for the inter-fibre contact interactions in reference [74]. In this chapter, one mesoscopic model is also conducted using shell elements. Details of this model are discussed in references [59].

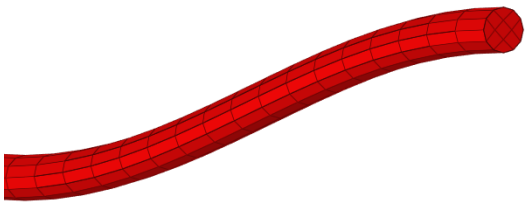

Figure IV.4 Mesh of one equivalent fibre.

It is assumed that fibres are in the elastic domain until failure [6, 17, 21, 33, 38, 77]. As discussed in reference [74], the transverse shear and crush strength are still not well known. Failure based on compressive strength insignificantly affects the tensile strength. Additionally, transverse shear failure, crush strength and compressive failure are not expected to occur during the transverse impact process. Therefore, only axial tension is considered in the failure mode. In this study, the tensile strength of 3.88 GPa from reference [83] is used.

The Hashin damage mode [117] is chosen as the damage criterion of all models. This damage mode can predict fibre tension, fibre compression, matrix tension and matrix compression. In the case of no matrix, matrix properties can be considered as the same as those of the fibre [70]. As only axial tension is expected, in the numerical models, the longitudinal tensile strength, longitudinal compressive strength, transverse tensile strength, transverse compressive strength, the longitudinal shear strength and the transverse shear strength can be considered to be infinite. Thus, only one equation rules the fibre tension mechanism, as follows:

$$F_1 = \left(\frac{\sigma_{11}}{\sigma_1^t} \right)^2 \tag{IV.2}$$

Here, σ_{11} is the tension stress in the longitudinal direction of the fibre, and $\sigma_1^t = 3.88$ GPa is the longitudinal tensile strength. If F_1 equals 1, the failure criterion is reached, and the element is deleted.

IV.1.2 Results and discussion

Residual velocity and contact force

The evolution of projectile velocity versus time is displayed in Figure IV.5. There is an insignificant difference between the residual velocities of the three models. The residual velocity of the mesoscopic model is 244.05 m/s, while the 42 fibres-model has the highest residual velocity of 244.26 m/s. Two phases are observed: de-crimping and tension.

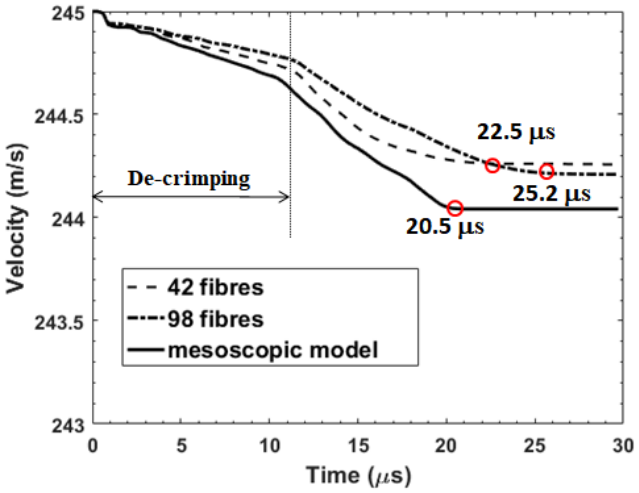

Figure IV.5 Projectile velocity.

It clearly shows that the de-crimping phases of the three models are almost the same (from 0 to around 11.1 μs). This can be explained by the fact that in this phase, crimped fibres straighten or decrimp; and the tension is negligible. Thus, the influence of the yarn's microstructure is insignificant, resulting in the same behaviour of the three models.

The tension phase begins after the de-crimping one and lasts until the moment that the yarn is completely damaged. Fibres start to dissipate the projectile energy via tensile deformation. Because in this phase the fibre-fibre interactions of each model are different, their durations are different. While this phase of mesoscopic model ends earliest at around 20.5 μs, that of 42-fibres model is 22.5 μs, and 25.2 μs for the case of the 98-fibres model. This is because in the case of the sub-yarn level models, the fibres spread horizontally. Thus, they are under less tension compared to the mesoscopic yarn.

Figure IV.6 illustrates the evolution of the impact force during the de-crimping phrase. The initial contact is the same (form 0 to 1 μs). Here, peak values observed indicate the first contacts of the projectile with the fibres.

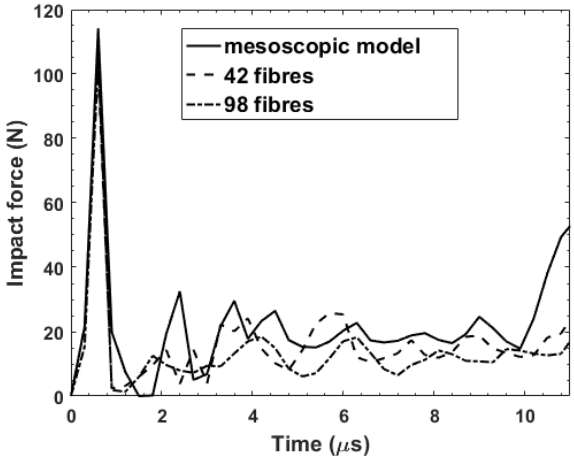

Figure IV.6 Impact force during the de-crimping process.

Figure IV.7 shows the deformation of fibres just after the initial contact with the projectile (0.9 μs). After the peaks, the force decreases rapidly to about 0. This result is consistent with the results of Sockalingam in reference [75]. The reason is that after the first contact, the projectile velocity decreases dramatically while the velocity of the upper part of the fibres is the same as the initial velocity of the projectile. The fibres are not in contact with the edge of the projectile. This corresponds with the sharp decrease of projectile velocity at 0.9 μs, as shown in Figure IV.5.

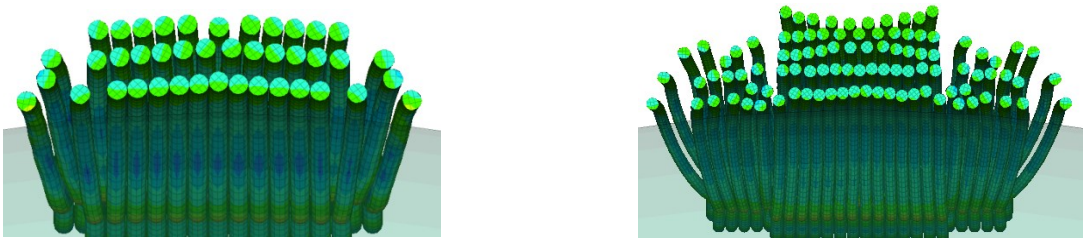

(a) (b)

Figure IV.7 Deformation of yarns at 0.9μs (a) 42-fibres (b) 98-fibres model.

It is observed that during the de-crimping process, there is no damage in the case of the mesoscopic and 42-fibres models. However, in the case of the 98-fibres model, the first failure (18 fibres) is observed at around 2.1 μs (Figure IV.8). It should also be noted that while the width of the mesoscopic yarn is unchanged, the width of the sub-microscopic yarn increases as the fibres spread horizontally. The numbers of fibres in contact with the projectile in the case of 42-fibres and 98-fibres models are 15/42 and 32/98, respectively. Until the end of the de-crimping process (11.1 μs), no more damage occurs.

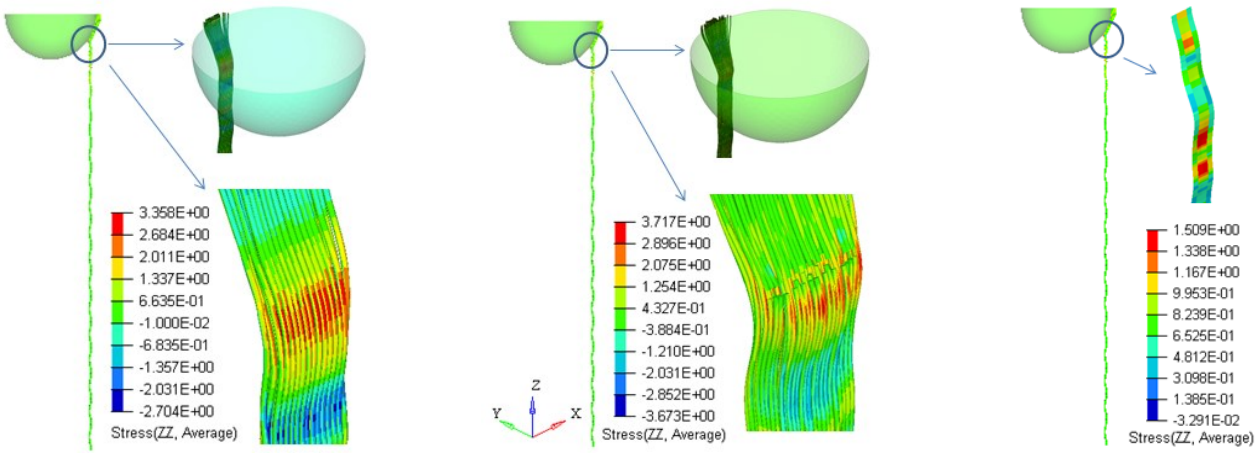

(a) (b) (c)

Figure IV.8 Deformation at 2.1µs (a) 42-fibres (b) 98-fibres (c) mesoscopic model.

Figure IV.9 shows the first failure of the 42-fibres model at 11.4 µs, just after the de-crimping process. It can be seen that in the case of 98-fibres model, 18 fibres which failed at 2 µs are still in contact with the lower part of the projectile and resist the projectile until the end of the de-crimping process. This is important regarding the differences between the two sub-yarn level models. It clearly shows that the three layers of fibres of the 42-fibres model are insufficient to describe the yarn's local damage, while with five layers of fibres, the 98-fibres model is able to simulate this phenomenon.

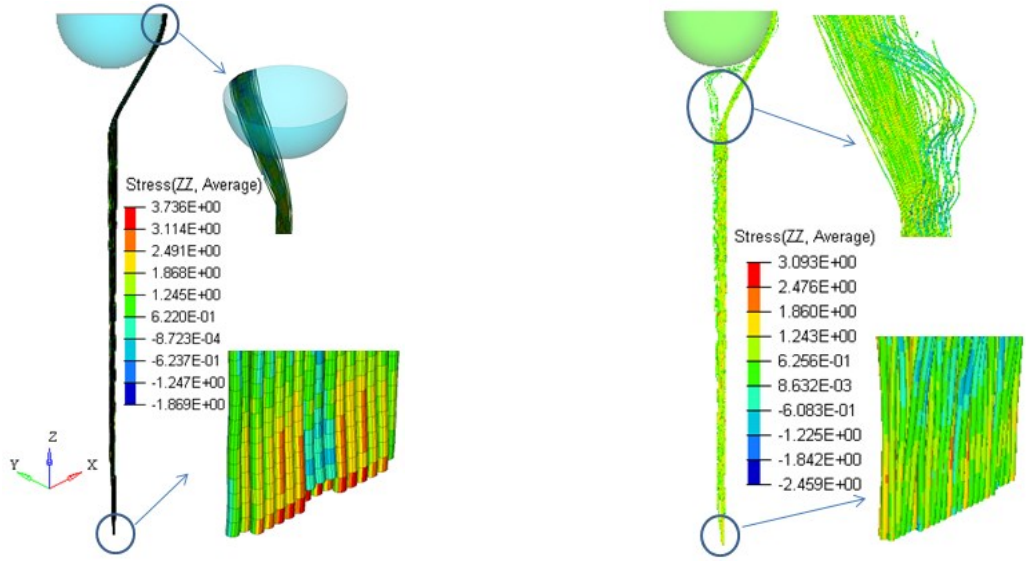

(a) (b)

Figure IV.9 Deformation of yarns at 11.4µs (a) 42-fibres (b) 98-fibres.

In this section, the projectile velocity is analysed. Yarn's contact force and deformation during the de-crimping process are also investigated. The results show that globally, the behaviours of yarns in the three models are almost the same. However, the local failure mechanism is different. The 98-fibres model can predict the initial failure of the yarn just after the initial impact. In contrast, the mesoscopic and 42-fibres model cannot predict the initial failure due to the lack of fibre-fibre internal interactions.

Energy analysis

In this subsection, the energy of the yarn will be analysed. The total energy of the yarn is equal to the lost energy of the projectile absorbed by the fabric and converted into yarn deformation energy E_{fd}, the yarn kinetic energy E_{fk} and the energy lost in frictional sliding E_f, as shown in the following equation [23]:

$$\Delta E_{pk} = \frac{1}{2} m(v_i^2 - v_r^2) = E_{fd} + E_{fk} + E_f \tag{IV.3}$$

Where v_i, v_r are the initial velocity and the residual velocity of the projectile, respectively, and m denotes projectile mass.

Figure IV.10 presents the evolution of the energies of each model versus time. It clearly shows that in all models, the yarn total energy is dominated by kinetic energy. In particular, the contact energy is insignificant in the case of the mesoscopic model, while in the case of the sub-yarn level ones, the contact energy is notable due to fibre-fibre interactions. Residual total energies appear at the same moment as the residual velocities.

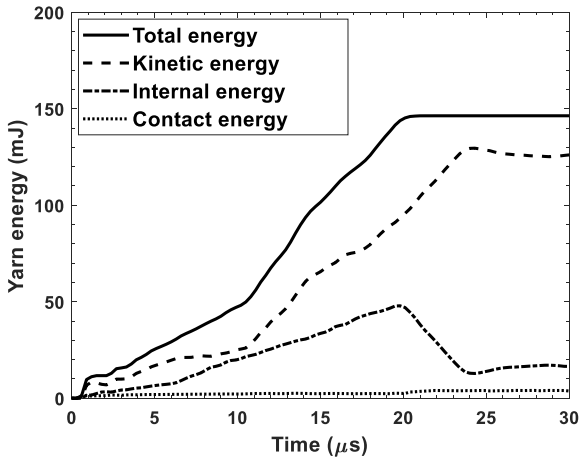

(a) Mesoscopic model

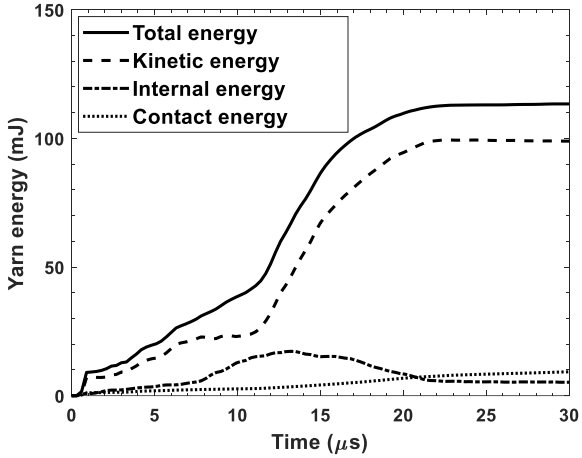

(b) 42-fibres model

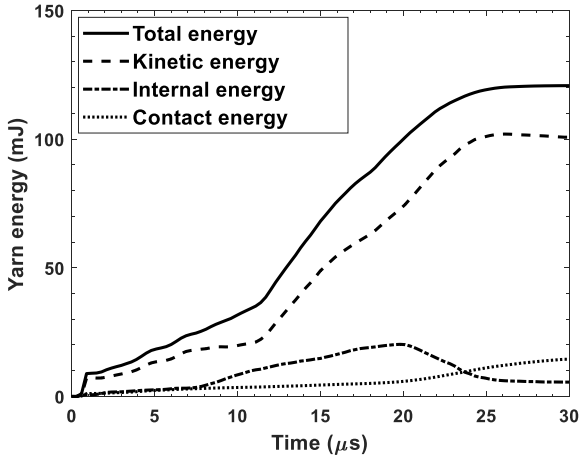

(c) 98-fibres model

Figure IV.10 Evolution of energy versus time.

The total yarn energies of the three models are compared in Figure IV.11. It clearly shows an insignificant difference between the three models during the de-crimping process. However, there is a notable difference between the mesoscopic and the others in the tension phase. The mesoscopic model absorbs the highest projectile energy, while the amounts of energy absorbed by the two sub-yarn level models are lower and almost the same.

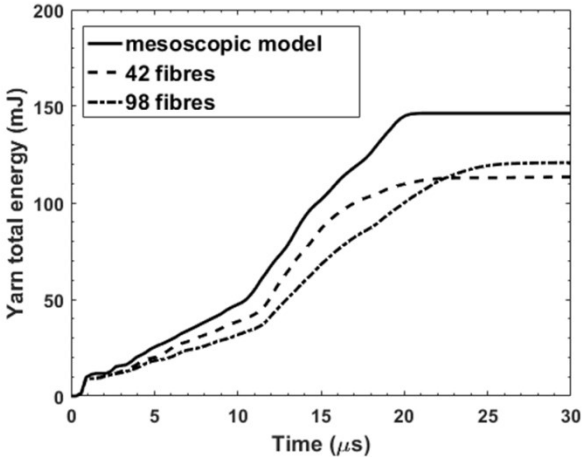

Figure IV.11 Yarn total energy.

Yarn kinetic energies are shown in Figure IV.12. After 19.5 μs, there is a sharp difference between the mesoscopic model and the two sub-yarn level ones. It clearly shows that the difference between the three models is insignificant during the de-crimping process. This can be explained by the fact that the velocity of the projectile is almost the same in this process. At the end of the impact, the residual kinetic energies of the two sub-yarn level models are almost the same.

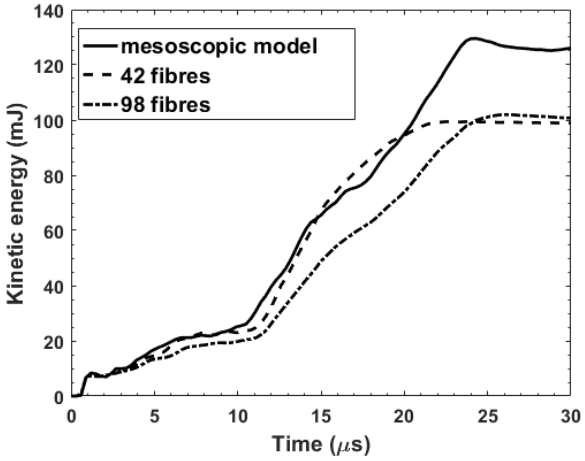

Figure IV.12 Kinetic energy.

Figure IV.13 shows the evolution of internal energy. The transverse wave reflection and catastrophic failure of each model are observed. The internal energy increases gradually until the transverse wave displacement travels to the boundary. This instant is observed at 6 μs in the mesoscopic model, and at around 7.5 μs for the 42-fibres and 98-fibres models. Then, internal energy increases rapidly to the peak value corresponding with catastrophic failure. Catastrophic failure of the 42-fibres model appears first at 13.2

µs, while those of the mesoscopic and 98-fibres models occur almost at the same instant (19.8 µs).

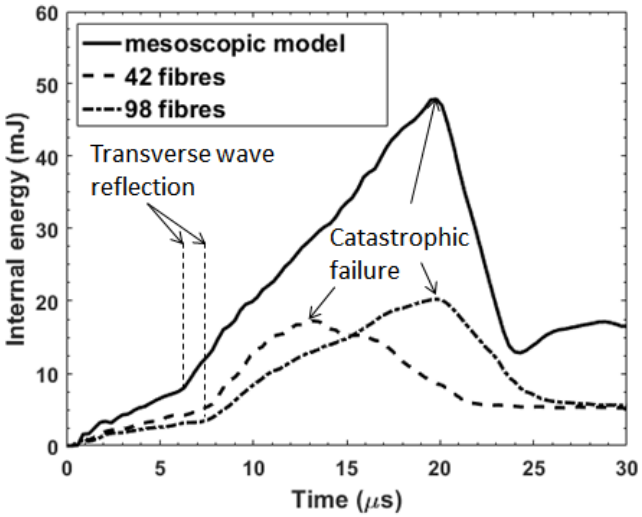

Figure IV.13 Yarn internal energy histories.

Figure IV.14 presents the deformation at 19.8 µs at which catastrophic failures of the mesoscopic and 98-fibres models are observed. At this moment, the initial failure of the mesoscopic yarn occurs later. While the 36 equivalent fibres of the 42-fibres model have failed, this number is 56 in the case of the 98-fibres model. After the peak value, there is a sharp decrease in internal energy followed by the complete failure of the fibres.

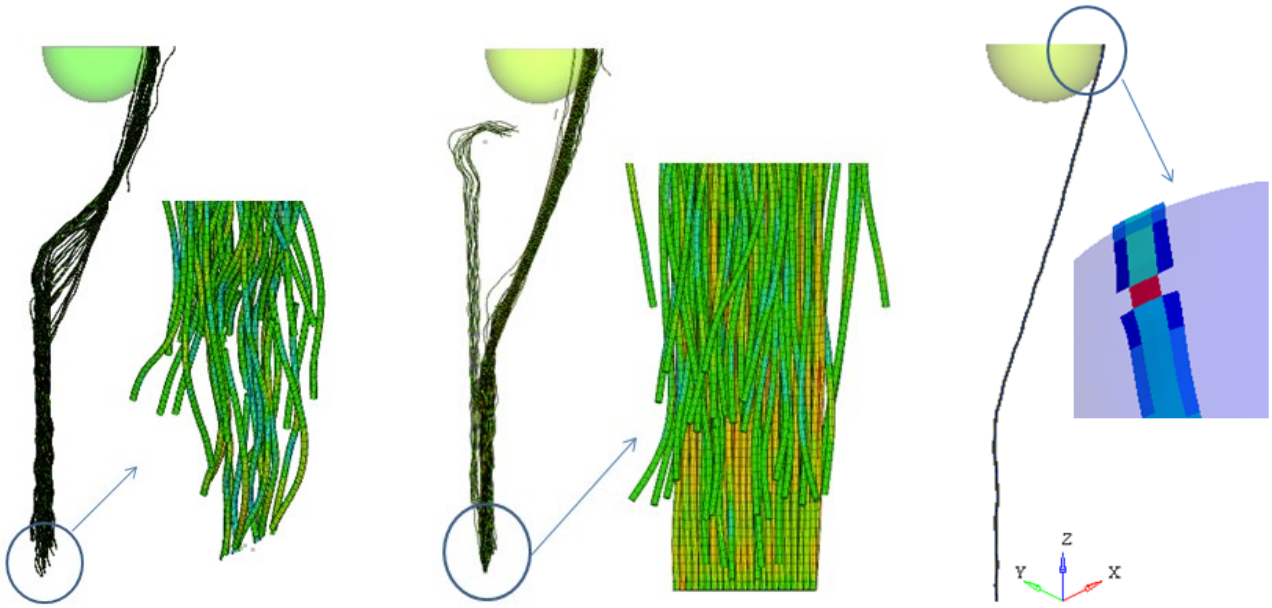

(a) (b) (c)

Figure IV.14 Deformation of yarns at 19.8 µs (a) 42-fibres (b) 98-fibres (c) mesoscopic model.

It should be noted that the failure duration of the mesoscopic yarn is shorter (from 19.8 to 24 μs) in comparison with the 42-fibres model (from 13.2 to 22.5 μs) and the 98-fibres model (from 19.8 to 25.2 μs). This can be explained by the fact that the failure mechanism of the sub-yarn level models is more complex. Failure can occur in every position of the fibres, not only at the contact zone with the projectile as in the case of the mesoscopic model. Moreover, partial failure occurs during the de-crimping phrase in the 98-fibre model, as discussed above.

Figure IV.15 presents the contact energy. It can be seen that the contact energy of the mesoscopic model is insignificant in comparison with the other two as there is no internal contact within the mesoscopic yarn. On the other hand, the contact energy of the 98-fibres model is higher than the 42-fibres model because the 98-fibres model has a higher number of equivalent fibres leading to higher internal contact. At the instance of catastrophic failure, a sharp increase is observed.

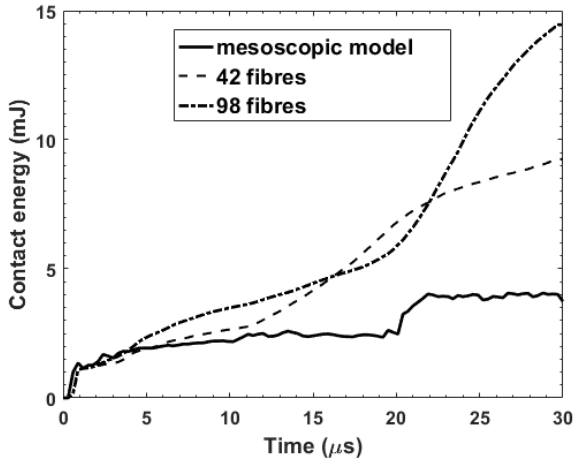

Figure IV.15 Contact energy.

Transverse wave propagation

In this subsection, the propagation of the transverse wave and the evolution of the impact zone dimension will be investigated. The dimension of the impact zone is characterised by the width W and the height H of the V-shape region. Results are shown in Table IV.1.

It should be noted that the shell elements seem to be softer than the solid ones. Thus, the yarn is easier to straighten. It also clearly shows that the transverse wave of the mesoscopic model propagates more rapidly than the others, and its V-shape region is wider than the others. That is why the mesoscopic yarn can absorb more energy, and its

initial failure appears later. During the de-crimping process, the propagation speeds of the two sub-yarn level models are almost the same. Then, the transverse wave of the 98-fibres model propagates more rapidly.

Table IV.1 Evolution of V-shape region.

Time (μs)		W (μm)	H(μm)
2.1	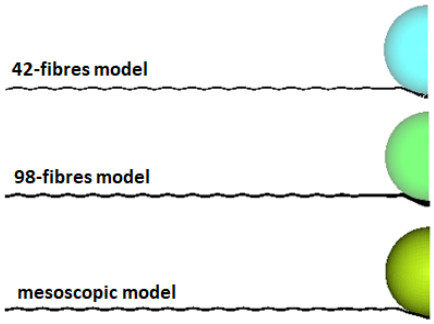	1535 1555 2080	525 550 610
11.1	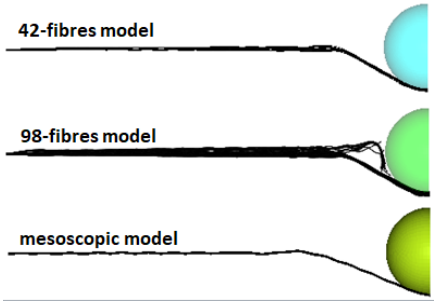	5245 5330 7785	2490 2380 2765
13.2	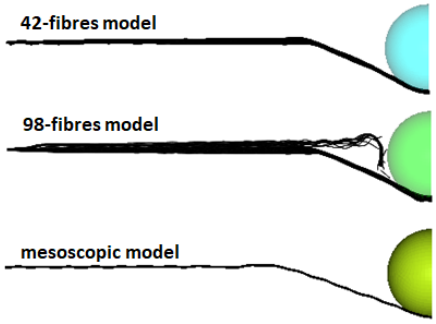	6745 6755 9430	2920 2850 3200
19.5	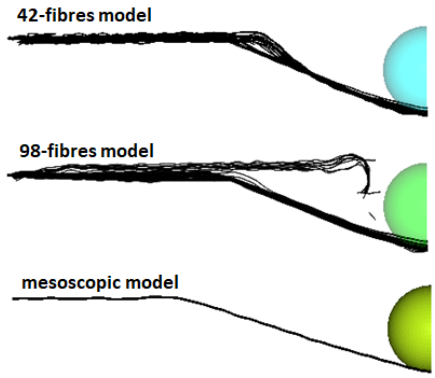	9920 12070 15400	4565 4250 4700

22.5	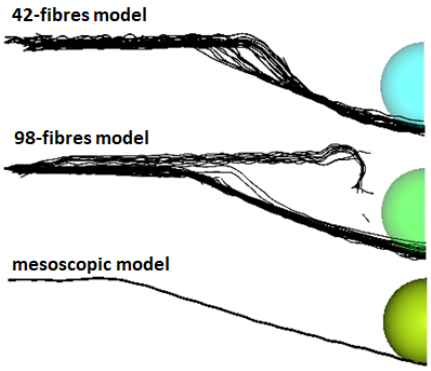	10100 14480 18600	5350 4750 5395
25.2	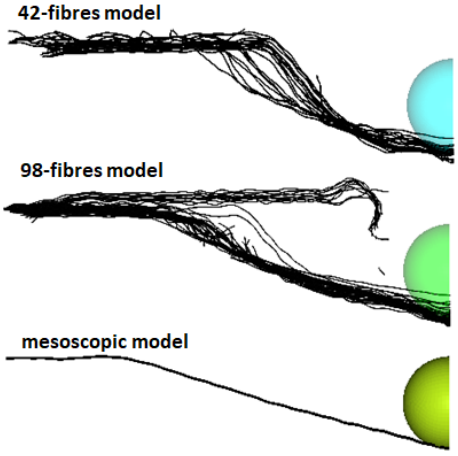	10710 17000 21385	6090 6050 6050

Figure IV.16 presents the tensile force and nominal stress in the longitudinal direction of the equivalent fibre in the centre of the yarn. The nominal stress is equal to the tensile force divided by the cross-sectional area. Forces and stresses are observed in the position of the fixed edge of the yarn (Figure IV.16a). This clearly shows that for both models, the tensile forces start to be positive at around 4 µs. It means that the longitudinal strain waves first reach the encastre at this moment. It can also be seen that in the case of 42-fibres model, the centre-fibre fails at the encastre after the end of the de-crimping process (around 11.1 µs), as the tension force is equal to 0. In the case of 98-fibres, the sharp decrease at 21.3 µs indicates fibre failure. Because the failure does not occur at the encastre, the tensile force does not equal 0 until the end of the impact.

(a)

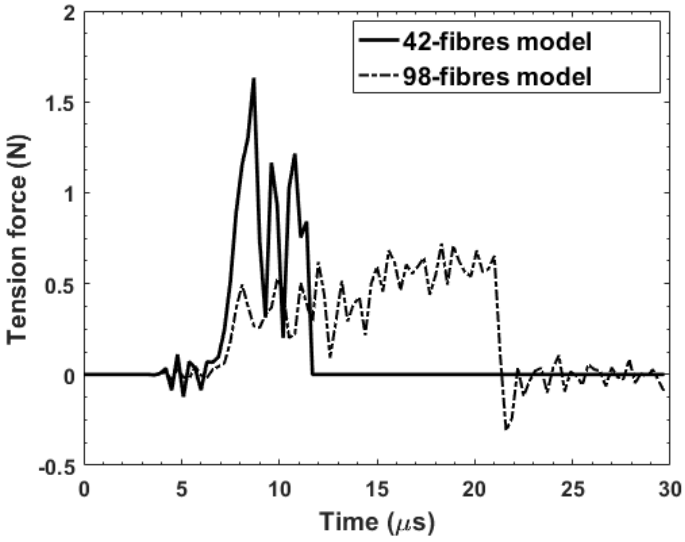

(b)

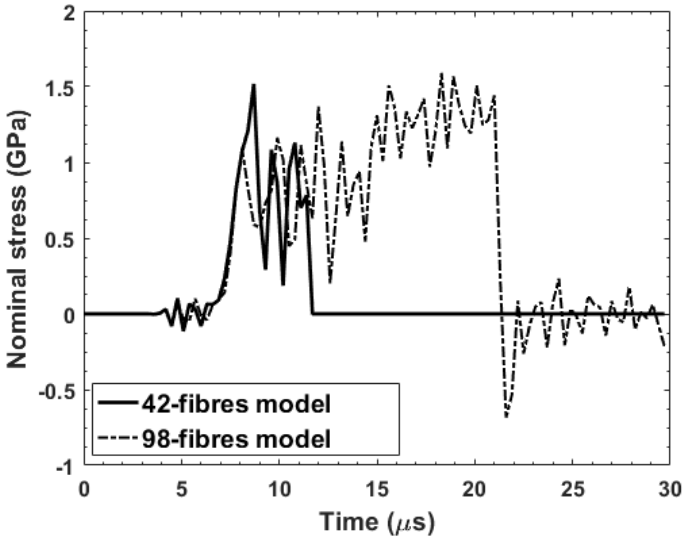

(c)

Figure IV.16 Tensile force and nominal stress at the encastre of the centre fibre (a) schema (b) tensile force (c) nominal stress.

Figure IV.17 displays the nominal stress of each equivalent fibre in the fixed edge. It can be seen that the longitudinal waves first travel to the encastre at 4 μs. This clearly

shows that for the 42-fibres model, most of the fibres fail from 11 to 12 µs (after de-crimping), with the rest failing at 22.5 µs. For the case of 98-fibres model, the fibre failure process is more complex. The first set of fibres (18 fibres) fail at 2 µs. Then fibres gradually fail after the de-crimping process.

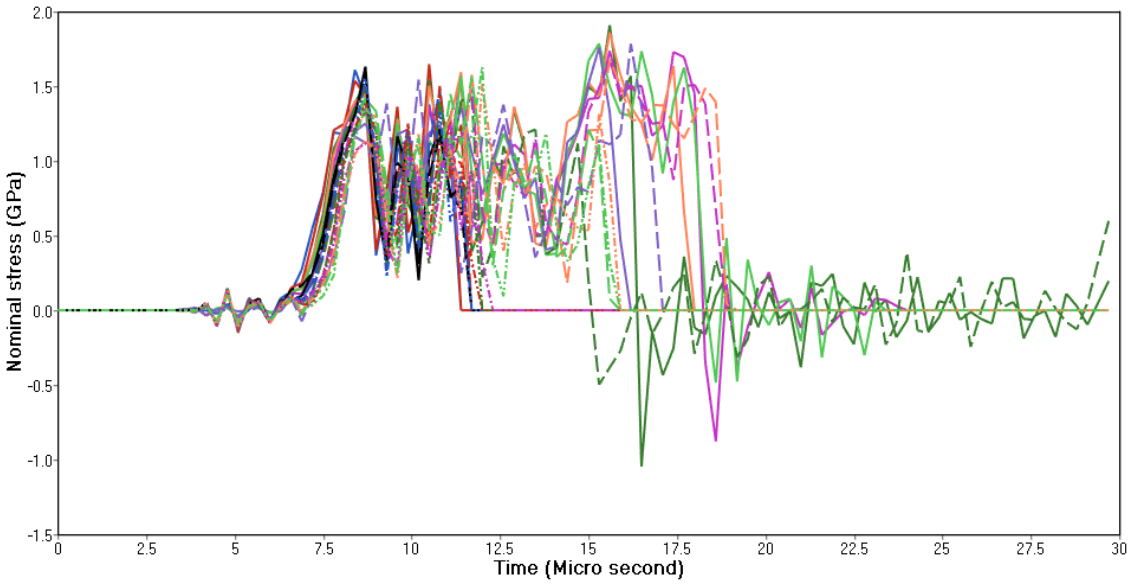

(a)

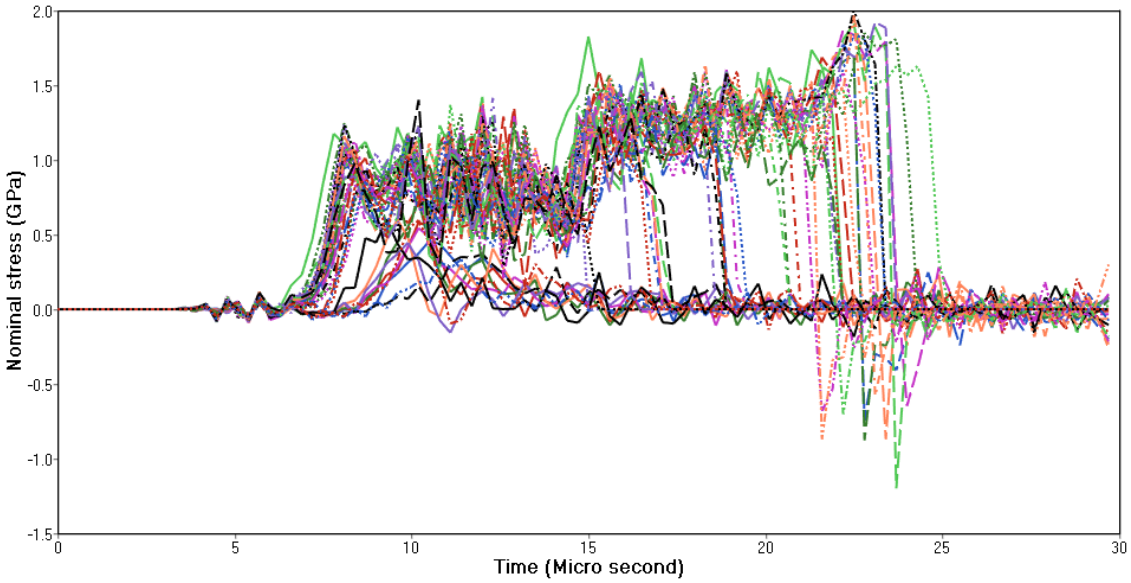

(b)

Figure IV.17 Nominal stress of each fibre at the encastre (a) 42-fibre model (b) 98-fibres model.

IV.1.3 Conclusion

In this part, the behaviour of one single crimped Kevlar KM2 yarn is investigated using mesoscopic and sub-yarn level models. In the case of the sub-yarn level models, 400 realistic fibres of yarn are represented by 42 and 98 equivalent fibres, respectively. It is noted that there is an insignificant difference between the three models in terms of yarn total energy and projectile velocity. Two phases are observed, including de-crimping and tension phases.

In the case of the mesoscopic model, as the yarn cross-section width is unchanged during the impact process, the mesoscopic yarn deformation energy is markedly higher in comparison with the others. It is also noted that the initial failure duration of the mesoscopic yarn is shorter. The mesoscopic yarn rapidly fails in a short period. The fibres of the 42-fibres model start to fail after the de-crimping process, then show the earliest complete failure. On the other hand, the first fibre failure of the 98-fibres model appears rapidly, just after the first contact with the projectile. Two sets of fibres can be observed. The first one consists of fibres which failed early, but they continue to resist the projectile until the end of the de-crimping process. The second is the rest of the fibres. These fibres start to fail after the de-crimping process and mainly resist the projectile.

In conclusion, the three models can describe the general behaviour of a Kevlar KM2 yarn. However, due to the lack of interaction between fibres, the mesoscopic and 42-fibres models cannot describe the local failure and fibre-fibre interaction. The 98-fibres model can describe these phenomena and thus can be used in the multi-scale model, with a combination of micro and mesoscopic scales, to capture the micro-interactions within the fabric in the next part.

IV.2 Micro–meso multi-scale model of one fabric

IV.2.1 Schematic and initial conditions

The schematic of the numerical micro-mesoscopic model is presented in Figure IV.18. As discussed above, the 98-fibres model can predict the micro-behaviour of one single crimped yarn; thus, the two centre yarns, which are in contact with the projectile, are modelled on the microscopic scale. In order to gain computation time, the rest of the fabric is modelled as a mesoscopic model.

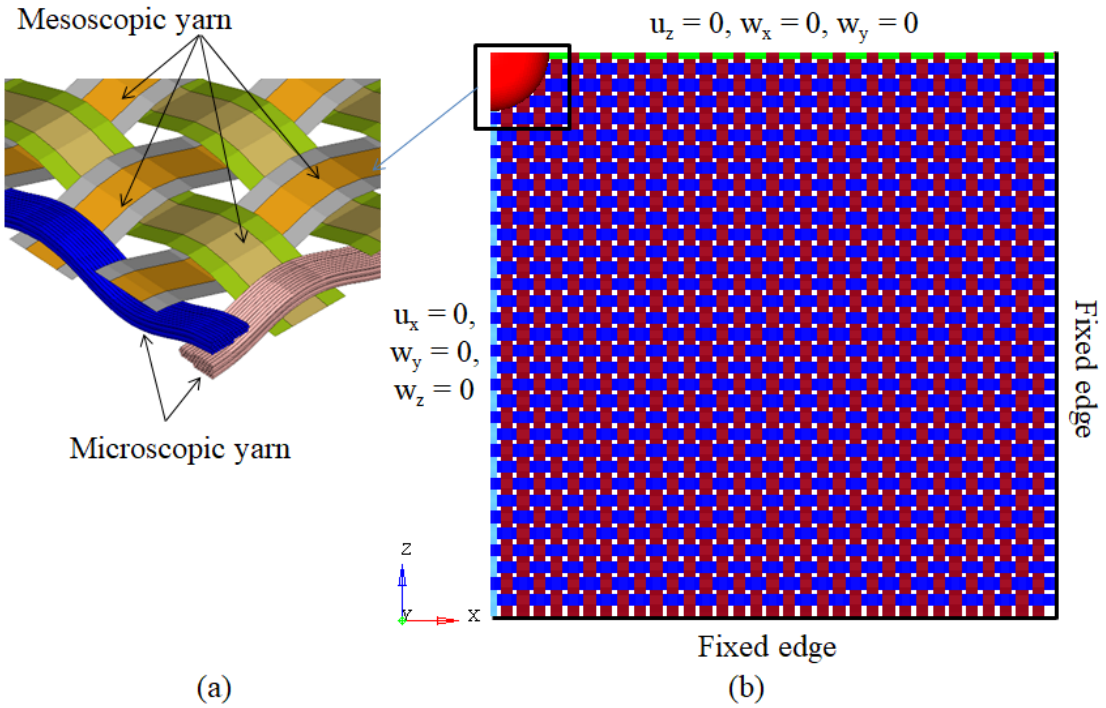

Figure IV.18 Schematic of the micro-meso model (a) the centre zone (b) fabric quarter symmetric FE model.

Due to the symmetry of the geometry, a quarter symmetric model is conducted. The dimensions of the fabric are 50.6 x 50.6 mm. The projectile is spherical, with a diameter of 5.33 mm and a mass of 0.625 mg. As the steel projectile has a very high Young's modulus compared to the fibres, it is assumed to be rigid. The initial impact velocity of the projectile is 245 m/s. The properties of Kevlar KM2 material have been introduced in 0. Yarn-yarn and fibre-fibre friction coefficients are equal to 0.2.

IV.2.2 Result and discussion

Evolution of projectile velocity

Figure IV.19 presents the evolution of the projectile velocity in comparison with the mesoscopic model. The mesoscopic model has been validated in our previous works [23, 58]. It is observed that the two curves are almost similar. The velocity of the mesoscopic is lower. This is because the two mesoscopic primary yarns modelled by shell elements are stiffer than the microscopic ones and the microscopic yarn fails earlier, as discussed in the previous section.

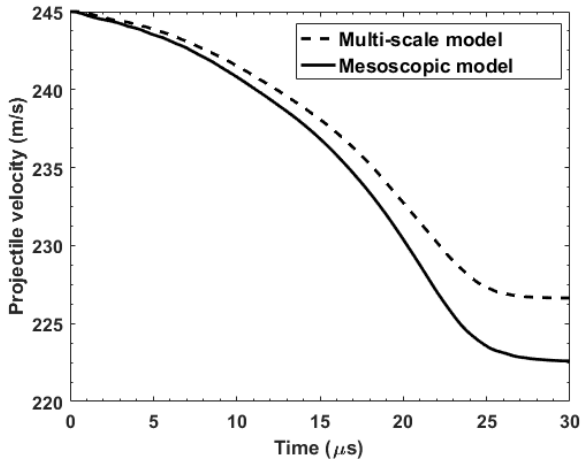

Figure IV.19 Evolution of the projectile velocity.

Deformation waves and deformation pyramid

The propagation of the deformation wave in the fabric is shown in Figure IV.20. The formation of the deformation pyramid is observed. The longitudinal wave propagates with a higher speed in the primary yarns. Also, the transverse wave propagates at a lower speed, and the material behind the wavefront moves transversely, forming the deformation pyramid.

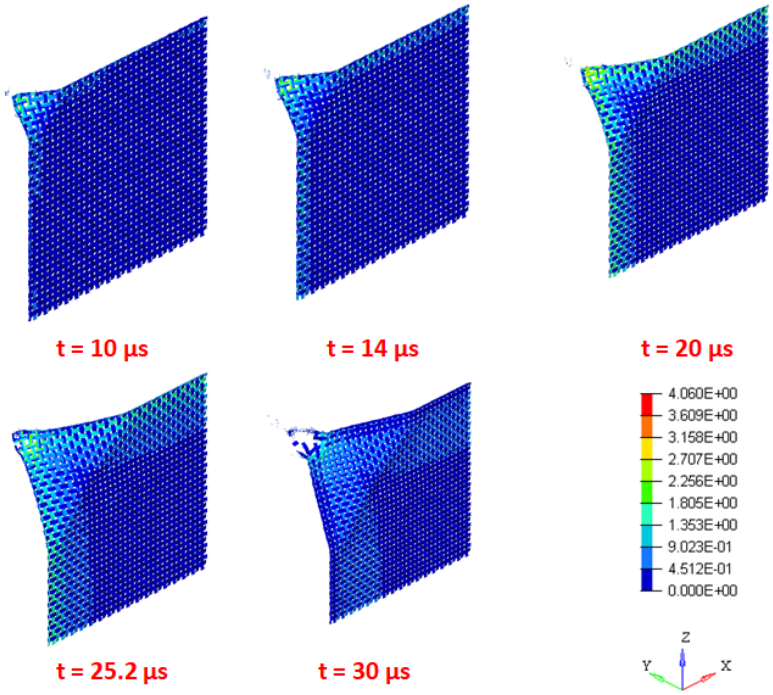

Figure IV.20 Propagation of the deformation wave.

Table IV.2 presents the comparison between the pyramid deformation of the multi-scale and mesoscopic scale models. It clearly shows that in the case of the mesoscopic model, the pyramid is bigger. This can be explained by the fact that in the mesoscopic

model, no failure occurs until 20 μs. Thus the primary yarns can transfer more deformation to the secondary ones, resulting in a higher speed transverse wave.

Table IV.2 Comparison of deformation pyramid.

Time (μs)		W (μm)	H(μm)
10	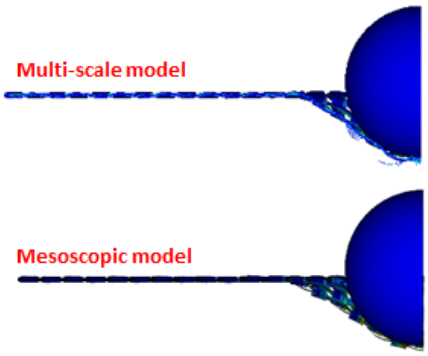	4300 4950	2260 2340
14	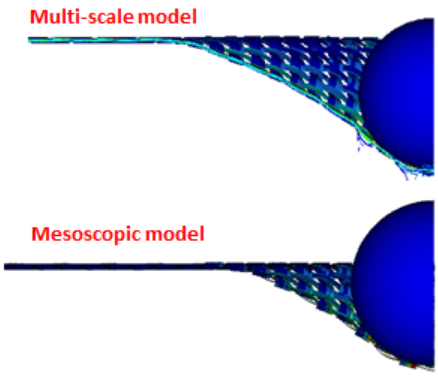	5760 6455	3160 3260
20	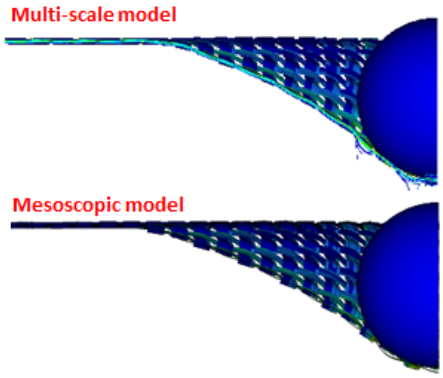	9640 9985	4560 4660

25.2	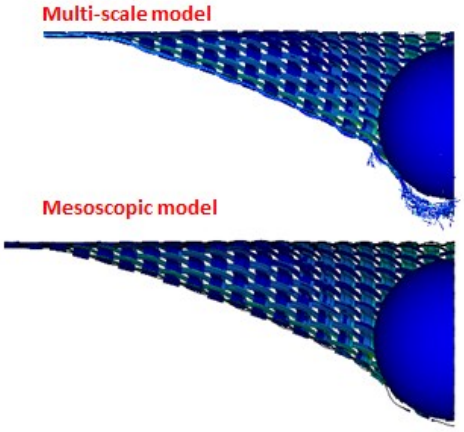	13090 9640	5790 4560
30	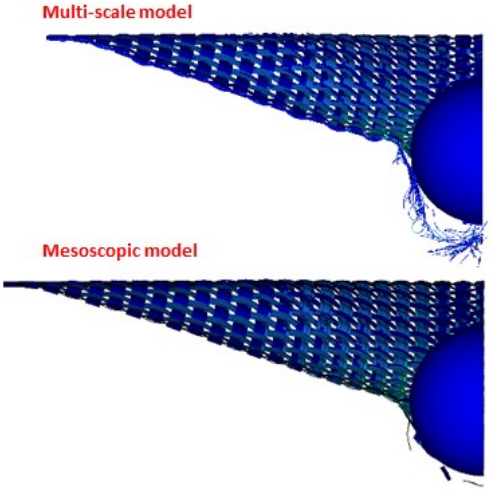	15000 16300	6820 6880

Fibre failure and yarn-yarn interactions

The fabric deformation and fibre failure of the yarns in the impact zone are also observed. For convenience, yarns in the contact zone with the projectile are numbered from 1 to 6, as shown in Figure IV.21.

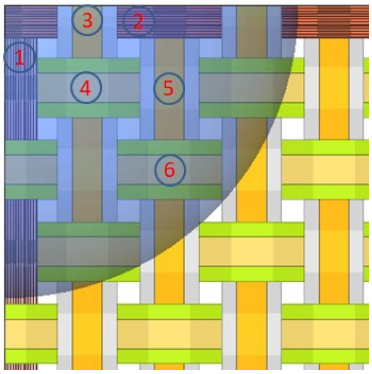

Figure IV.21 Numbering of yarns in the impact zone.

The first fibre failures of the two microscopic yarns are observed at about 1.75 and 7.35 μs, as shown in Figure IV.22. It should be noted that fibres in the primary yarn 1,

which is indirectly contacted by the projectile, fail first. The reason is that the two yarns can be considered to be supported by the other yarns. While yarn 1 is supported by yarn 4, yarn 2 is supported by yarn 5. As the span of yarn 1 is shorter, it is under more tensile.

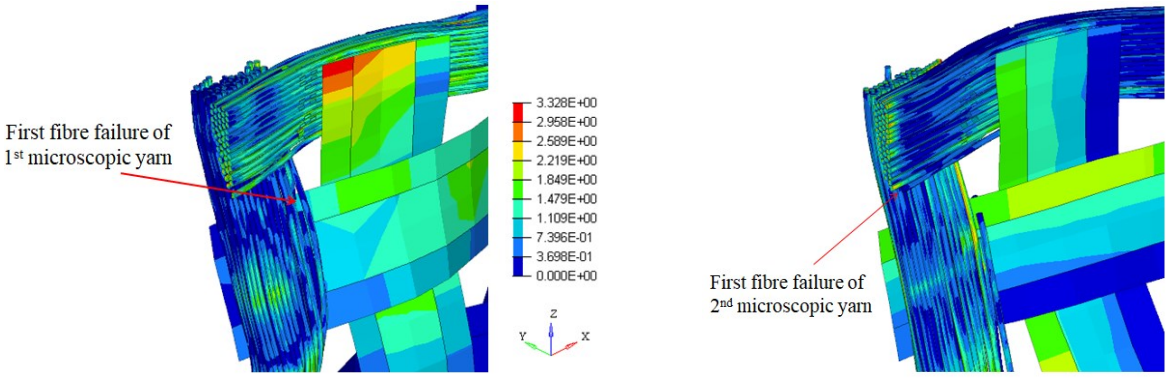

(a) (b)

Figure IV.22 Deformation of fabric at (a) 1.75 µs, (b) 7.35 µs.

The total failure of the primary yarns is shown in Figure IV.23. Yarn 1 totally fails first at 20.3 µs. Then yarn 2 totally fails at 22.4 µs. Yarn 3, yarn 4 and yarns 5, 6 totally fail at 25.2, 26.95 and 29.05, respectively. The windowing process is also observed. After 29.05 µs, the fabric cannot resist the projectile.

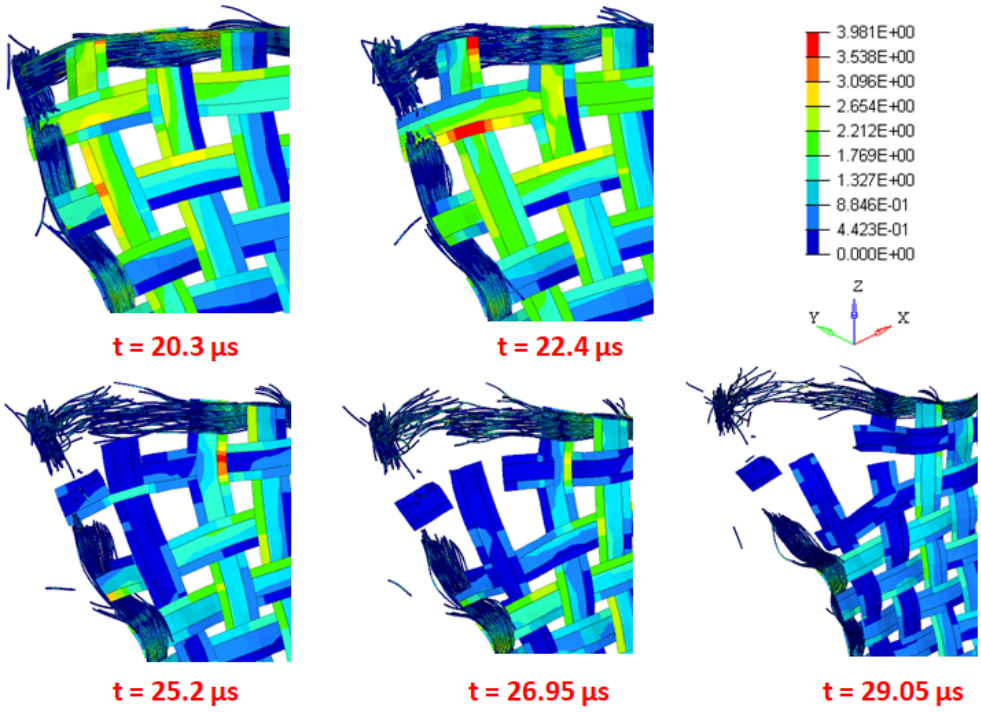

Figure IV.23 Total failure of primary yarns.

Figure IV.24 shows the interactions between two primary yarns in the zone under the projectile until 20 µs. At 0.7 µs, the projectile strikes yarn 2 and fibres in this yarn are compacted but not yet in contact with yarn 1. Then, interactions between the fibres in the two yarns are observed. It is noted that after 4.9 µs, the Von Mises stress does not vary significantly as the two yarns move with the projectile, and the relative position does not change. Additionally, fibres can laterally spread as they are compressed.

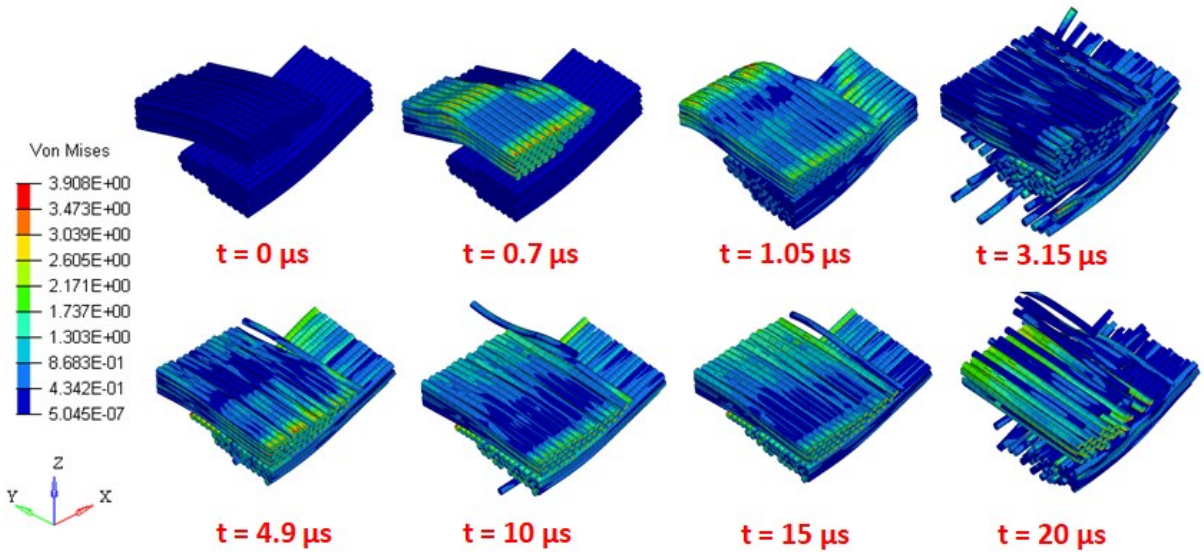

Figure IV.24 Interactions between two primary yarns of the multi-scale model under the projectile.

Figure IV.25 presents the counterpart of the mesoscopic model. It clearly shows significant differences in comparison with the multi-scale model. The cross-sections of the yarns are the same during the impact. In addition, the Von Mises stress proportionally increases with time. Furthermore, no local failure is observed.

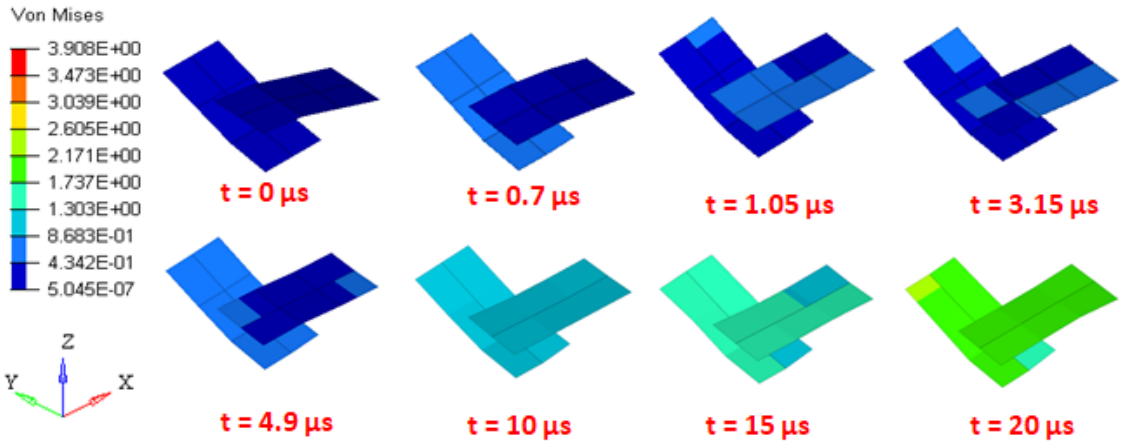

Figure IV.25 Interactions between two primary yarns of the mesoscopic model under the projectile.

The tensile force of each fibre of the primary yarn 2 is shown in Figure IV.26. It clearly shows that the longitudinal wave propagates to the encastre at about 4 µs. The de-crimping process ends at about 11 µs when the tensile force sharply increases. It should be noted that the primary yarn 2 undergoes total failure at 22.4 µs. Then, due to the fibre-fibre and fibre-projectile friction, fibres are still under tension up to 30 µs.

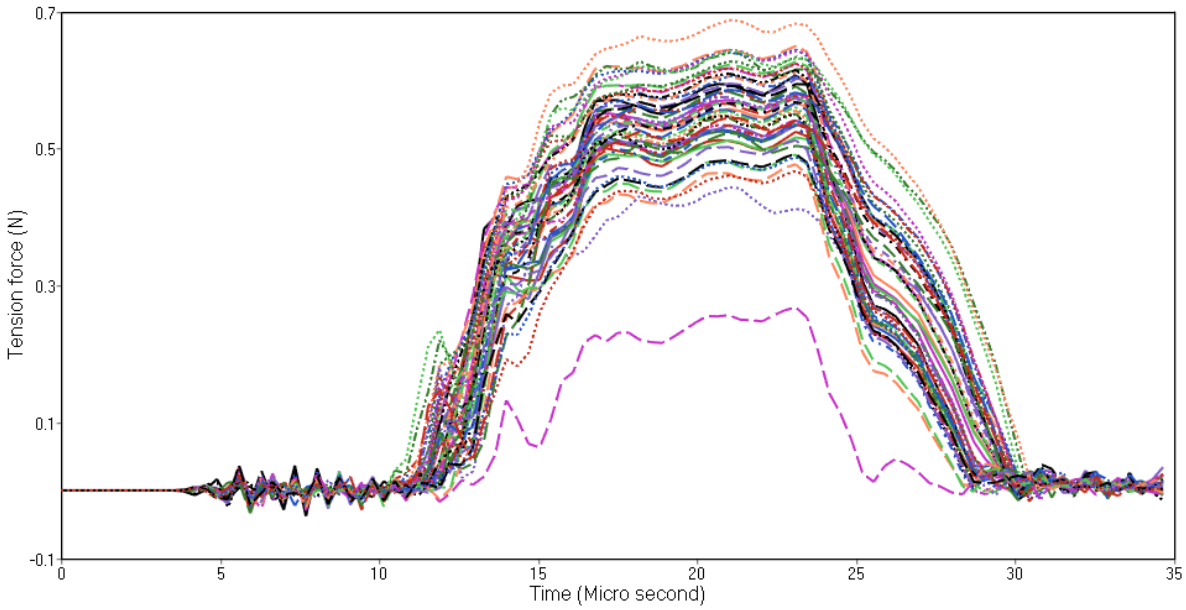

Figure IV.26 Tensile force of individual fibres.

The total tensilen force of the microscopic yarn 2 is compared with the counterpart of the mesoscopic yarn in Figure IV.27. It clearly shows that because of the "early local failure", the value of the microscopic yarn is lower than the mesoscopic one.

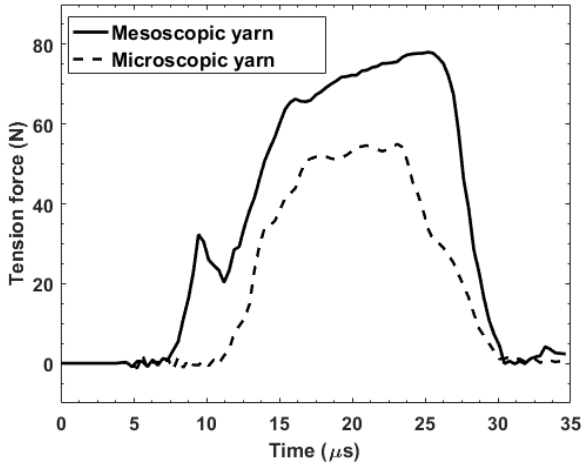

Figure IV.27 Total tensile force of the primary yarn 2.

Transverse compressive behaviour of fibres

In this sub-section, the transverse compressive behaviour of fibres of yarn 2 is analysed. Figure IV.28 shows the fibres compression and fibre-fibre contacts at the initial impact with the projectile. It clearly shows that the zone in contact with the projectile is the most compressed. At 0.7 µs, interactions between the two yarns have not yet been observed. Fibres of yarn 2 are only compressed by the projectile. The fibres in the contact zone are compacted, while in the farther zone, fibres are insignificantly deformed.

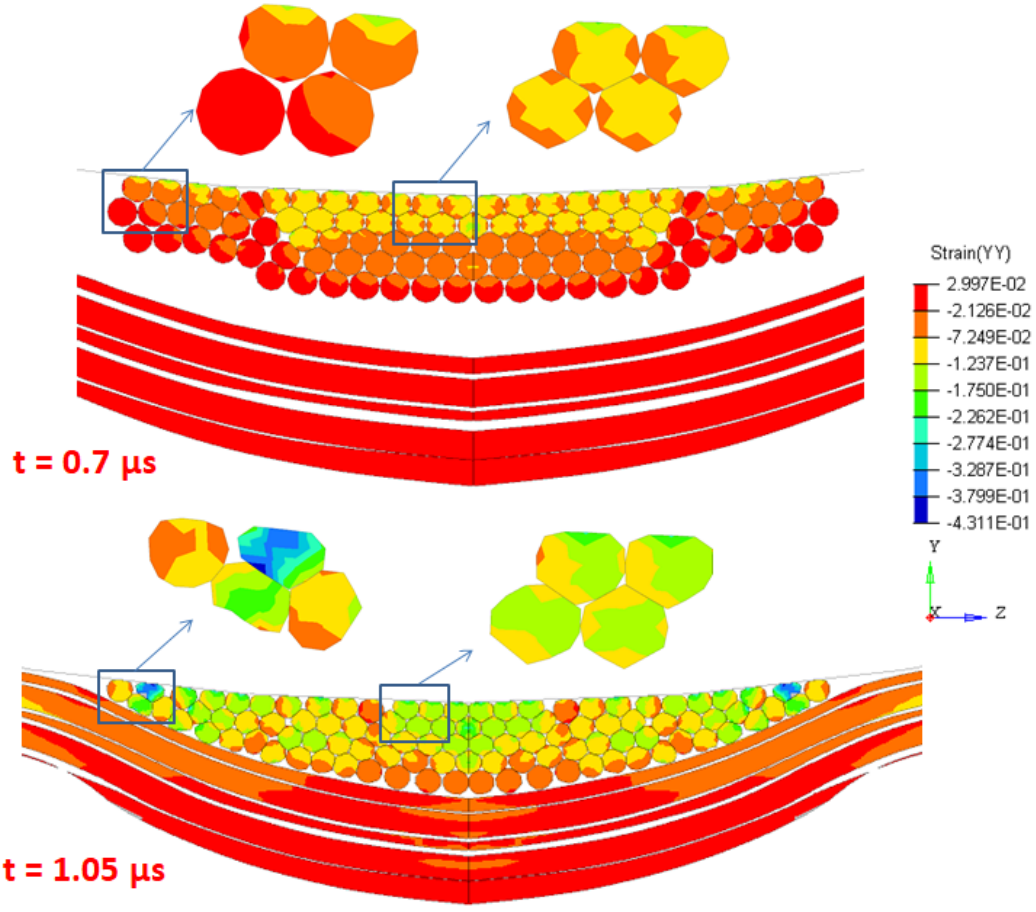

Figure IV.28 Transverse compression of fibres in the initial stage.

The highest compression of the fibres is observed at 1.05 µs. At this moment, the fibres of yarn 2 are compressed by the projectile and yarn 1. As yarn 1 has not moved, most of the fibres are compressed. On the edge of the yarn 2, fibres are most deformed as the distance between the projectile and yarn 1 is the smallest.

Figure IV.29 shows the compression and the distribution of the fibres after the initial stage. After the most compressive moment, as yarn 1 moves with the projectile, the fibres are less compressed. It can be seen that fibres near the central zone are more compressed. As yarn 2 is not rigid, the compressive strain varies and not linear increases.

While in the initial stage, the maximum compressed strain of 0.41 is observed, in this stage, the maximum compressed strain is 0.15.

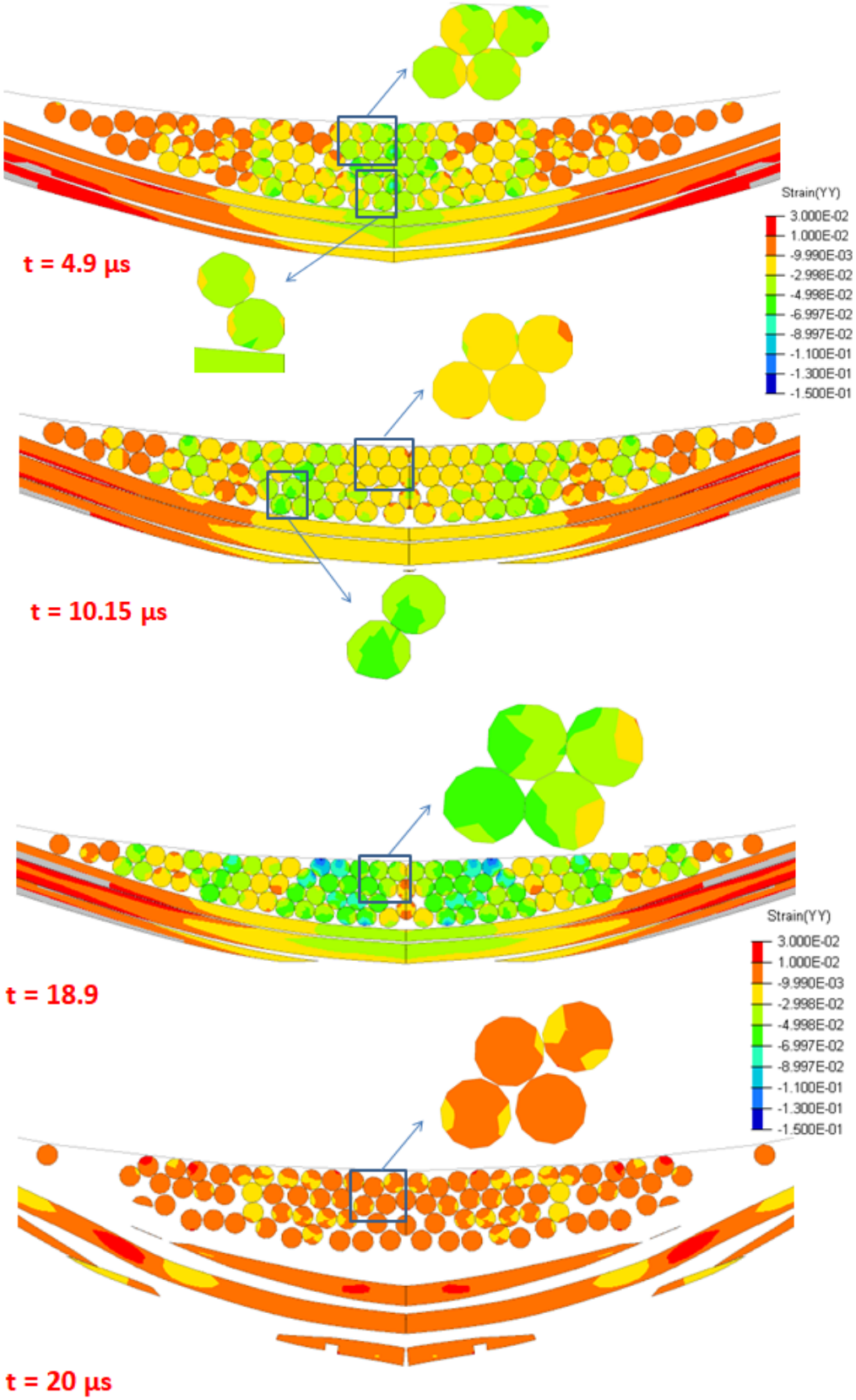

Figure IV.29 Transverse compression of fibres after the initial stage.

Energy analysis

Figure IV.30 presents the evolution of the fabric energies, including the total, kinetic, internal, and contact energy. The total fabric energy is equal to the total loss energy of the projectile. The energy of the projectile is absorbed by the fabric via kinetic, internal, and contact energy.

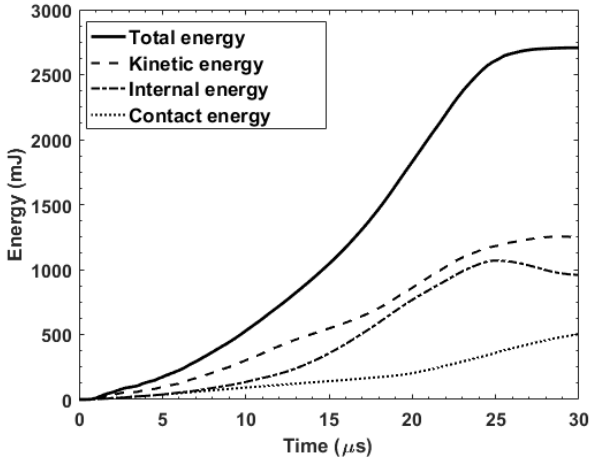

Figure IV.30 Evolution of multi-scale fabric energies.

The fabric energies are also compared with the mesoscopic model in Figure IV.31. It clearly shows that the shapes of the curves are almost similar. However, the total energy of the mesoscopic model is higher. The reason is that while in the mesoscopic model the initial failure occurs at around 20 μs, the initial failure of the multi-scale model occurs at 1.75 μs. Afterwards, fibre failure is observed in the two microscopic yarns until the end of the impact event. Due to this local failure, the deformation and kinetic energies of the two microscopic yarns are lower than those of the corresponding mesoscopic ones, as shown in Figures IV.31b and c. In other words, with the later failure, the mesoscopic model can resist the projectile better than the mesoscopic one.

It is noted that the peak of the internal energy curve is at 25 μs after the total failure of the three primary centre yarns. The internal energy gradually decreases after 25 μs. However, the kinetic energy gradually increases until 29 μs because material in the deformation pyramid keeps moving after the projectile. Thus, the residual total energy is observed from this moment.

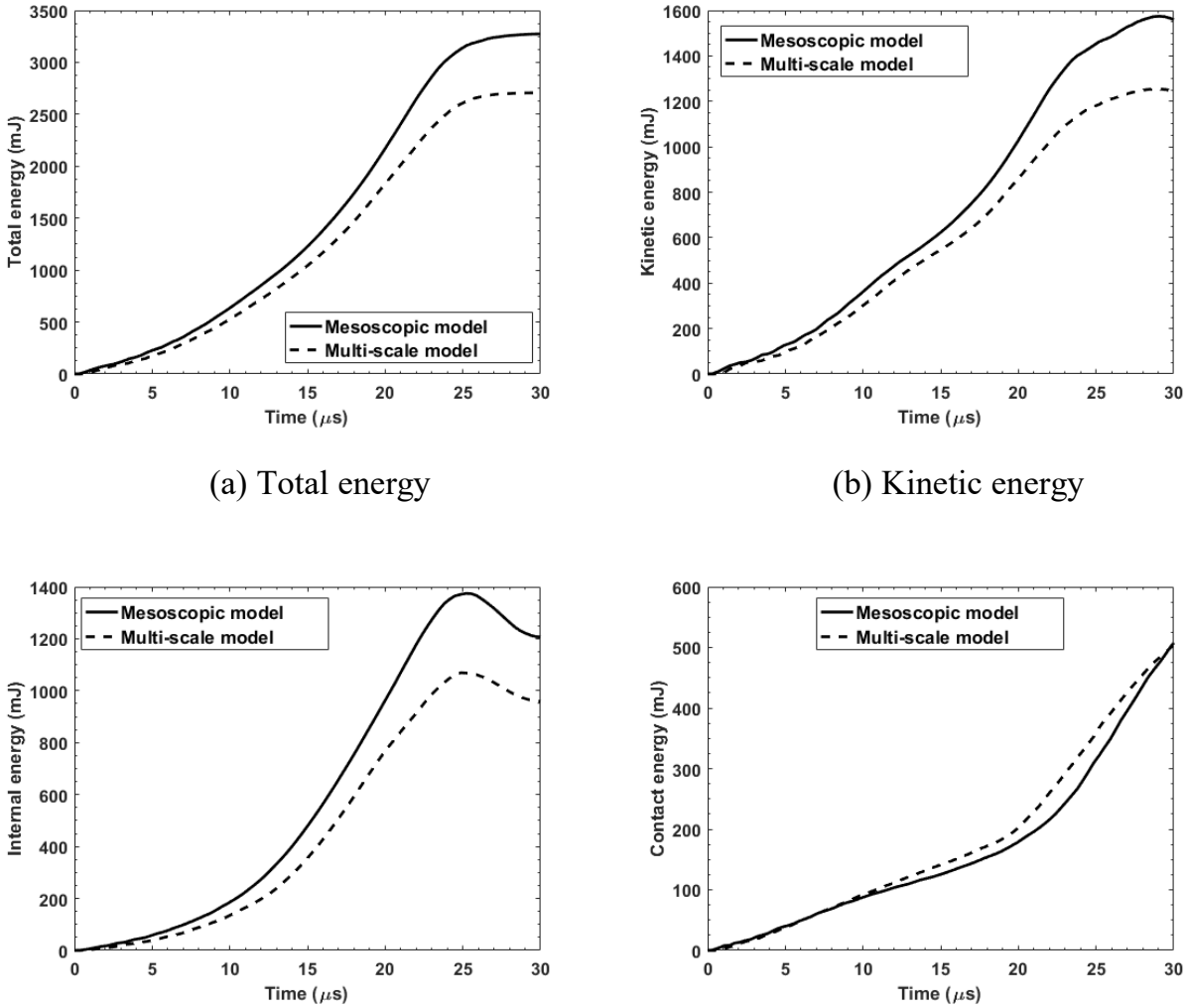

(a) Total energy (b) Kinetic energy

(c) Internal energy (d) Contact energy

Figure IV.31 Comparison of fabric energies.

Figure IV.31d presents a comparison of contact energies. It should be noted that in the first 20 μs, before the total failure of the first microscopic yarn, the two curves are almost the same as the sliding friction between fibres mostly contributes to this energy in this period. After the first total failure, there is a sharp increase in the two curves. The reason is that the yarns fail, and the windowing process occurs so increasing the fibre-projectile friction. Due to the effects of the two microscopic yarns, this value is higher in the case of the multi-scale model.

Figure IV.32 shows the time history of the impact forces. Before 20 μs, the two curves are similar. However, from 19 to 22 μs, there is a significant difference. While the curve of the mesoscopic model sharply increases, the curve of the microscopic model

fluctuates. This can be explained by the complex catastrophic failure of the two microscopic yarns.

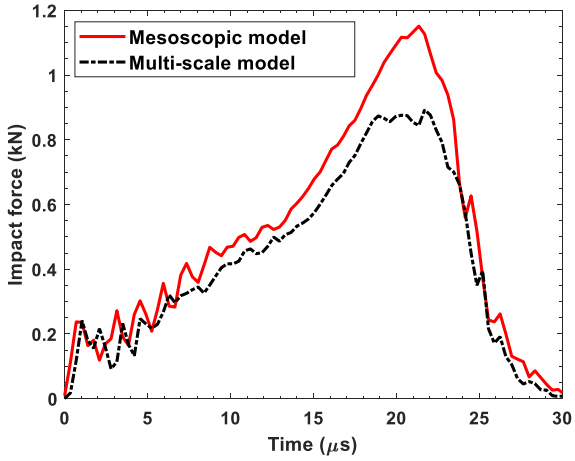

Figure IV.32 Comparison of impact force.

IV.3 Conclusion

In this chapter, the microscopic behaviour of Kevlar KM2 fibres subjected to ballistic impact is investigated in the case of one single crimped yarn and fabric. In order to gain computation time, the concept of an equivalent fibre is introduced. One equivalent fibre represents a set of fibres such that its cross-section area is equal to the total area of the cross-section of the fibres in the set.

The behaviour of one single crimped Kevlar KM2 yarn is investigated using mesoscopic and two sub-yarn level models. In the case of sub-yarn level models, 400 realistic fibres of yarn are represented by 42 and 98 equivalent fibres, respectively. The two models can predict the general behaviour of a Kevlar KM2 yarn. Globally, there is an insignificant difference between the two models in term of yarn total energy and projectile velocity. Two phases, including de-crimping and tension, are observed. However, due to the lack of interaction between the fibres, the 42-fibres models cannot fully describe the local failure and fibre-fibre interaction. The 98-fibres model has the capacity to describe these phenomena and thus can be used in the multi-scale model with a combination of micro and mesoscopic scales in order to capture micro-interactions within the fabric.

In the case of one fabric, a micro-mesoscopic multi-scale model is conducted. In this model, the two primary yarns are modelled on the microscopic scale, while the others are modelled on a mesoscopic one. The evolution of the projectile velocity and the tensile

force of each fibre are investigated. The results show two phases, including de-crimping and the tensile process of the fibres. The deformation pyramid and interactions of the two microscopic yarns under the impact zone are analysed. Results show that fibres are transversely compressed and also laterally spread during the impact. Fibre failure mechanisms are also investigated. It is noted that, in a micro-scale yarn, fibres fail locally during the impact before the moment of catastrophic failure. Energies of the fabric are analysed and compared with the mesoscopic model. In general, the curves are similar. However, the values in the case of the multi-scale model are lower due to the micro-interactions and fibre failure.

Conclusions and perspectives

General conclusions

The state of the art analysis showed an interest in the study of fabric performance under ballistic impact. It is noted that a number of research works have been dedicated to the understanding and modelling of the physical phenomena that occur. Indeed, the development of numerical tools has allowed researchers to develop numerical approaches for modelling the behaviour of fabric at different scales: macroscopic (fabric scale), mesoscopic (yarn scale) and microscopic (fibre scale).

This thesis focused on the numerical study of the behaviour at the microscopic scale of woven material using a microscopic approach based on numerical homogenization. During ballistic impact, the fabric's impact zone is subjected to local compression of the fibres, leading to the analysis of fibre responses under transverse compressive loading at different scales. In this case, we have proposed four transverse compressive 2D plane strain models of (i) a single fibre, (ii) two fibres, (iii) a block of fibres and (iv) a single yarn. The mesh sensitivity study was carried out. The results showed a non-linear behaviour of fibres subjected to transverse compression. This behaviour can be divided into two zones: (i) zone of rearrangement of fibres and (ii) zone of non-linear behaviour.

Furthermore, in the second zone, the volume fraction of the fibres increases with displacement. It is noted that the evolution of apparent strain has been described from the evolution of the fibre volume fraction. It clearly showed that the role of friction between fibres is insignificant.

Fibre-fibre interactions have also been observed. The results were validated by comparison with data from experimental work in terms of the apparent stress-strain relationship.

Using numerical finite element homogenization technique, calculations were performed at the Representative Volume Element (RVE), considering the periodic distribution of the yarn and fibre-fibre interactions. The variation of the transverse effective elastic modulus E with the normalized volume fraction and the apparent strain was described by a power-law function. The homogenized behaviour law has been

implemented in the ABAQUS software. The results obtained show a good agreement with those obtained from the microscopic law analysis.

The numerical finite element homogenization technique was applied in the case of a single crimped yarn subjected to ballistic impact, with an impact velocity of 245 m/s, considering the interactions between the fibres. In order to optimise the calculations, the notion of equivalent fibre was introduced to gain calculation time. An equivalent fibre represented a set of fibres so that its cross-section is equal to the total cross-section of the set. This analysis was carried out by considering two cases, in which 42 and 98 equivalent fibres represent 400 fibres of one yarn. The results showed two phases, including the process of de-crimping and tension of the fibres. The 98-fibre model can describe the local failure and fibre-fibre interactions, and thus be used in the multi-scale model with a combination of micro and mesoscopic scales to predict micro-interactions within the fabric.

A multi-scale micro-mesoscopic model of a fabric subjected to ballistic impact has also been developed. In this model, the two primary yarns were modelled on the microscopic scale, while the others were modelled on a mesoscopic one. The evolution of the projectile velocity and the tension force of each fibre were obtained. The deformation pyramid and the interactions of the two microscopic yarns in the area affected by the impact were analysed. The results showed that the fibres were compressed transversely and spread laterally during the impact. The mechanisms of fibre failure were also studied. It should be noted that, in the case of a microscopic yarn, the fibres fail locally during the impact before the catastrophic failure of the yarn. The results were compared with those obtained by mesoscopic modelling to show the advantages of taking into account primary yarns at the fibre scale.

Perspectives

This thesis opens new sceneries in woven fabric modelling:

- The micro behaviour of fibres in a fabric subjected to ballistic impact can be thoroughly investigated by developing the micro-meso multi-scale model of the fabric. The number of microscopic yarns should be increased in the impact zone. Hybrid element analysis can be applied in order to gain computation time.

- The effective homogenized transverse compressive behaviour law can be implemented into the mesoscopic numerical models, allowing a more accurate prediction of woven fabric behaviour taking into account the variation of transverse Young's modulus of yarn.
- It is now also possible to take into account the entire anisotropy of the material by homogenizing the matrix of elastic coefficients as a whole and not only the transverse compression behaviour.
- A further study can also follow this work by investigating at the homogenized elastic properties, such as effective bulk modulus and effective shear modulus, to build a complete homogenized behaviour law.
- Given the mastery of this technique, it is also desirable to address other mechanical behaviours, i.e. non-linear behaviour.
- One can also imagine performing the inverse process of homogenization. Starting from a fixed mechanical behaviour, one goes back to the ideal morphology or the ideal matrix of the elastic coefficients of yarn which may be behind the adequate mechanical behaviour. This falls within the context of the so-called optimal morphology design of numerical materials.

Conclusions et perspectives

Conclusions générales

L'analyse de l'état de l'art a montré l'intérêt porté à l'étude de la performance des tissus sous impact balistique. On note qu'un nombre important de travaux de recherche ont été consacrés à la compréhension et à la modélisation des phénomènes physiques qui se produisent. En effet, le développement des outils numériques a permis manifestement aux chercheurs de proposer des approches numériques pour une modélisation du comportement des tissus à différentes échelles : macroscopique (échelle du tissu), mésocopique (échelle de fil) et microscopique (échelle de fibre).

Cette thèse a porté sur l'étude numérique du comportement à l'échelle microscopique d'un matériau tissé en utilisant une approche microscopique basée sur l'homogénéisation numérique. Quand un tissu est soumis à un impact balistique, la zone affectée par le projectile est sujette à une compression locale des fibres. Ceci a motivé l'analyse des réponses des fibres sous chargement en compression transversale à différentes échelles. Dans ce cas, nous avons proposé quatre modèles de déformation plane en 2D, pour : (i) une fibre unique, (ii) deux fibres, (iii) un bloc de fibres et (iv) un fil unique. L'étude de la sensibilité au maillage a été réalisée. Les résultats ont montré l'existence d'un comportement non-linéaire des fibres soumis à une compression transversale. Ce comportement peut être divisé en deux zones : (i) zone de réarrangement des fibres et (ii) zone de comportement non linéaire. De plus, dans la seconde zone, la fraction volumique des fibres augmente avec le déplacement. On note que l'évolution de la déformation apparente a été décrite à partir de l'évolution de la fraction volumique des fibres. Il a clairement montré que le rôle de la friction entre les fibres est insignifiant.

Des interactions fibre-fibre ont été observées. Les résultats ont été validés par confrontation avec les données de travaux expérimentaux en termes de relation contrainte apparente-déformation apparente.

En utilisant la technique d'homogénéisation numérique par éléments finis, les calculs ont été effectués à l'échelle du Volume Elémentaire Représentatif (VER), en prenant en compte la distribution périodique du fil et des interactions fibre-fibre. La variation du module élastique effectif transversal E avec la fraction volumique

normalisée et la déformation apparente a été décrite par une fonction de loi puissance. La loi de comportement homogénéisée a été implémentée dans la logiciel ABAQUS. Les résultats obtenus montrent un bon accord avec ceux obtenus à partir de l'analyse avec la loi microscopique.

La technique d'homogénéisation a été aussi appliquée dans le cas d'un fil unique soumis à un impact balistique, avec une vitesse d'impact de 245 m/s, en prenant en compte les interactions entre les fibres. Dans un souci d'optimiser les calculs, la notion de fibre équivalente a été introduite afin de gagner du temps de calculs. Une fibre équivalente représentait un ensemble de fibres de telle sorte que sa section transversale soit égale à la section transversale totale de l'ensemble. Cette analyse a été réalisée en considérant un nombre de fibres de 42 et 98, équivalent aux 400 fibres constituant un fil. Les résultats ont montré deux phases, dont le processus de déondulation et de tension des fibres. Le modèle à 98 fibres a la capacité de décrire la défaillance locale et l'interaction fibre-fibre et peut donc être utilisé dans le modèle multi-échelle avec une combinaison d'échelles micro et mésoscopiques afin de capturer les micro-interactions au sein du tissu.

Un modèle micro-mesoscopique multi-échelle d'un tissu soumis à un impact balistique a également été développé. Dans ce modèle, les deux fils primaires ont été modélisés à l'échelle microscopique, tandis que les autres ont été modélisés à l'échelle mésoscopique. Les évolutions de la vitesse du projectile et la force de tension de chaque fibre ont été analysées. La pyramide de déformation et les interactions des deux fils microscopiques dans la zone affectée par l'impact ont été analysées. Les résultats ont montré que les fibres ont été comprimées transversalement et écartées latéralement pendant l'impact. Les mécanismes de rupture des fibres ont également été étudiés. Il est à noter que, dans le cas d'un fil à l'échelle microscopique, les fibres se rompent localement pendant l'impact avant le moment de rupture finale du fil. Les résultats ont été confrontés avec ceux obtenus avec une modélisation mésoscopique pour montrer en évidence les apports intéressants de la prise en compte des fils primaires à l'échelle des fibres.

Perspectives

Cette thèse ouvre de nouveaux horizons dans le modélisation des tissus soumis à un impact balistique:

- Le micro-comportement des fibres dans un tissu soumis à un impact balistique peut être entièrement étudié en développant le modèle micro-meso multi-échelle du tissu. Le nombre de fils microscopiques devrait être augmenté dans la zone d'impact. L'analyse des éléments hybrides peut être appliquée afin de gagner du temps de calcul.
- La loi de comportement en compression transversale homogénéisée effective peut être mise en œuvre dans les modèles numériques mésoscopiques, permettant une prédiction plus précise du comportement du tissu en tenant compte de la variation du module de Young transversal du fil.
- Il est aussi maintenant possible de tenir compte de l'entière anisotropie du matériau en homogénéisant la matrice des coefficients élastiques dans sa globalité et pas que le comportement en compression transversale.
- Ce travail peut être aussi suivi par une étude plus profonde en s'intéressant aux propriétés élastique homogénéisées, à savoir le module effectif de compressibilité et le module effectif de cisaillement afin de construire une loi de comportement homogénéisée assez complète.
- Vu la maîtrise de cette technique, il est également souhaitable d'aborder d'autres comportements mécaniques, à savoir le comportement non linéaire par exemple.
- On peut également imaginer faire le processus inverse de l'homogénéisation, c'est-à-dire, à partir d'un comportement mécanique figé, on remonte à la morphologie idéale ou à la matrice idéale des coefficients élastiques des fils qui peut être derrière le comportement mécanique adéquat. Ceci rentre dans le cadre de ce qu'on appelle le design de morphologie optimale des matériaux numériques.

Publications

Articles

Q. Hoan-Pham, C. Ha-Minh, T. Long-Chu, T. Kanit and A. Imad

Analysis of the transverse compressive behavior of Kevlar fibers using microscopic scale approach

International Journal of Mechanical Sciences,164,105149, 2019.

DOI: 10.1016/j.ijmecsci.2019.105149

Q. Hoan-Pham, C. Ha-Minh, T. Long-Chu, T. Kanit and A. Imad

On microscopic and homogenized macroscopic analysis of one Kevlar® yarn under transverse compressive loading

Mechanics Research Communications 104, 103496, 2020.

DOI: 10.1016/j.mechrescom.2020.103496

References

[1] T. M. Loganathan, M. T. H. Sultan, M. K. Gobalakrishnan, and G. Muthaiyah, "10 - Ballistic impact response of laminated hybrid composite materials," *Mechanical and Physical Testing of Biocomposites, Fibre-Reinforced Composites and Hybrid Composites*, M. Jawaid, M. Thariq and N. Saba, eds., pp. 171-191: Woodhead Publishing, 2019.

[2] R. L. Ellis, "Ballistic impact resistance of graphite epoxy composites with shape memory alloy and extended chain polyethylene spectra hybrid components," Master of science thesis, Virginia Polytechnic Institute and State University, 1996.

[3] C. Ha-Minh, "Comportement mécanique des matériaux tissés soumis à un impact balistique: approches expérimentale, numérique et analytique," Lille 1, 2011.

[4] T.-L. Chu, "Étude du comportement mécanique d'un matériau tissé soumis à un impact balistique basée sur une approche multi-échelle," 2016.

[5] A. Majumdar, B. S. Butola, and A. Srivastava, "An analysis of deformation and energy absorption modes of shear thickening fluid treated Kevlar fabrics as soft body armour materials," *Materials & Design,* vol. 51, pp. 148-153, 2013.

[6] A. Tabiei, and G. Nilakantan, "Ballistic Impact of Dry Woven Fabric Composites: A Review," *Applied Mechanics Reviews,* vol. 61, no. 010801, 2008.

[7] B. A. Cheeseman, and T. A. Bogetti, "Ballistic impact into fabric and compliant composite laminates," *Composite Structures,* vol. 61, no. 1, pp. 161-173, 2003.

[8] W. K. Stone, H. F. Schiefer, and G. Fox, "Stress-Strain Relationships in Yarns Subjected to Rapid Impact Loading: Part I: Equipment, Testing Procedure, and Typical Results1,2," *Textile Research Journal,* vol. 25, no. 6, pp. 520-528, 1955.

[9] J. C. Smith, F. L. McCrackin, and H. F. Schiefer, "Stress-Strain Relationships in Yarns Subjected to Rapid Impact Loading: Part III. Effect of Wave Propagation," *Textile Research Journal,* vol. 25, no. 8, pp. 701-708, 1955.

[10] J. C. Smith, F. L. McCrackin, H. F. Schiefer, W. K. Stone, and K. M. Towne, "Stress-Strain Relationships in Yarns Subjected to Rapid Impact Loading: Part IV: Transverse Impact Tests," *Textile Research Journal,* vol. 26, no. 11, pp. 821-828, 1956.

[11] J. C. Smith, F. L. McCrackin, and H. F. Schiefer, "Stress-Strain Relationships in Yarns Subjected to Rapid Impact Loading: Part V: Wave Propagation in Long Textile Yarns Impacted Transversely," *Textile Research Journal,* vol. 28, no. 4, pp. 288-302, 1958.

[12] J. C. Smith, C. A. Fenstermaker, and P. J. Shouse, "Stress-Strain Relationships in Yarns Subjected to Rapid Impact Loading: Part XI: Strain Distributions Resulting from Rifle Bullet Impact1," *Textile Research Journal,* vol. 35, no. 8, pp. 743-757, 1965.

[13] B. Song, H. Park, W.-Y. Lu, and W. Chen, "Transverse Impact Response of a Linear Elastic Ballistic Fiber Yarn," *Journal of Applied Mechanics,* vol. 78, no. 051023, 2011.

[14] S. Chocron, E. Figueroa, N. King, T. Kirchdoerfer, A. E. Nicholls, E. Sagebiel, C. Weiss, and C. J. Freitas, "Modeling and validation of full fabric targets under ballistic impact," *Composites Science and Technology,* vol. 70, no. 13, pp. 2012-2022, 2010.

[15] M. Hudspeth, J.-m. Chu, E. Jewell, B. Lim, E. Ytuarte, W. Tsutsui, S. Horner, J. Zheng, and W. Chen, "Effect of projectile nose geometry on the critical velocity and failure of yarn subjected to transverse impact," *Textile Research Journal,* vol. 87, no. 8, pp. 953-972, 2016.

[16] A. Shahkarami, E. Cepus, R. Vaziri, and A. Poursartip, "3 - Material responses to ballistic impact," *Lightweight Ballistic Composites*, A. Bhatnagar, ed., pp. 72-100: Woodhead Publishing, 2006.

[17] C. Ha-Minh, F. Boussu, T. Kanit, D. Crépin, and A. Imad, "Analysis on failure mechanisms of an interlock woven fabric under ballistic impact," *Engineering Failure Analysis,* vol. 18, no. 8, pp. 2179-2187, 2011.

[18] B. Provost, F. Boussu, J. Nussbaum, and M. Lefebvre, "Use of new warp interlock structures against high velocity impact."

[19] G. Nilakantan, S. Horner, V. Halls, and J. Zheng, “Virtual ballistic impact testing of Kevlar soft armor: Predictive and validated finite element modeling of the V0-V100 probabilistic penetration response,” *Defence Technology,* vol. 14, no. 3, pp. 213-225, 2018.
[20] E. M. Parsons, T. Weerasooriya, S. Sarva, and S. Socrate, “Impact of woven fabric: Experiments and mesostructure-based continuum-level simulations,” *Journal of the Mechanics and Physics of Solids,* vol. 58, no. 11, pp. 1995-2021, 2010.
[21] C. Ha-Minh, A. Imad, F. Boussu, T. Kanit, and D. Crépin, “Numerical study on the effects of yarn mechanical transverse properties on the ballistic impact behaviour of textile fabric,” *The Journal of Strain Analysis for Engineering Design,* vol. 47, no. 7, pp. 524-534, 2012.
[22] Y. Duan, M. Keefe, T. A. Bogetti, B. A. Cheeseman, and B. Powers, “A numerical investigation of the influence of friction on energy absorption by a high-strength fabric subjected to ballistic impact,” *International Journal of Impact Engineering,* vol. 32, no. 8, pp. 1299-1312, 2006.
[23] T.-L. Chu, C. Ha-Minh, and A. Imad, “A numerical investigation of the influence of yarn mechanical and physical properties on the ballistic impact behavior of a Kevlar KM2® woven fabric,” *Composites Part B: Engineering,* vol. 95, pp. 144-154, 2016.
[24] B. Gu, “Analytical modeling for the ballistic perforation of planar plain-woven fabric target by projectile,” *Composites Part B: Engineering,* vol. 34, no. 4, pp. 361-371, 2003.
[25] P. M. Cunniff, “An Analysis of the System Effects in Woven Fabrics under Ballistic Impact,” *Textile Research Journal,* vol. 62, no. 9, pp. 495-509, 1992.
[26] B. J. Briscoe, and F. Motamedi, “The ballistic impact characteristics of aramid fabrics: The influence of interface friction,” *Wear,* vol. 158, no. 1, pp. 229-247, 1992.
[27] D. Starratt, T. Sanders, E. Cepuš, A. Poursartip, and R. Vaziri, “An efficient method for continuous measurement of projectile motion in ballistic impact experiments,” *International Journal of Impact Engineering,* vol. 24, no. 2, pp. 155-170, 2000.
[28] T.-L. Chu, C. Ha-Minh, and A. Imad, “Analysis of local and global localizations on the failure phenomenon of 3D interlock woven fabrics under ballistic impact,” *Composite Structures,* vol. 159, pp. 267-277, 2017.
[29] D. Roylance, A. Wilde, and G. Tocci, “Ballistic Impact of Textile Structures,” *Textile Research Journal,* vol. 43, no. 1, pp. 34-41, 1973.
[30] D. Roylance, and S. S. Wang, "Chapter 12 - Penetration Mechanics of Textile Structures," *Methods and Phenomena*, R. C. Laible, ed., pp. 273-292: Elsevier, 1980.
[31] R. A. Prosser, S. H. Cohen, and R. A. Segars, “Heat as a Factor in the Penetration of Cloth Ballistic Panels by 0.22 Caliber Projectiles,” *Textile Research Journal,* vol. 70, no. 8, pp. 709-722, 2000.
[32] P. Cunniff, “Dimensionless Parameters for Optimization of Textile Based Body Armor Systems,” in the 18th International and Symposium on Ballistics, San Antonio, TX, 1999, pp. 1303–1310.
[33] M. P. Rao, Y. Duan, M. Keefe, B. M. Powers, and T. A. Bogetti, “Modeling the effects of yarn material properties and friction on the ballistic impact of a plain-weave fabric,” *Composite Structures,* vol. 89, no. 4, pp. 556-566, 2009.
[34] M. A. Martínez, C. Navarro, R. Cortés, J. Rodríguez, and N. Sanchez-Galvez, “Friction and wear behaviour of Kevlar fabrics,” *Journal of Materials Science,* vol. 28, no. 5, pp. 1305-1311, 1993.
[35] S. Bazhenov, “Dissipation of energy by bulletproof aramid fabric,” *Journal of Materials Science,* vol. 32, no. 15, pp. 4167-4173, 1997.
[36] K. Bilisik, “Experimental determination of yarn pull-out properties of para-aramid (Kevlar®) woven fabric,” *Journal of Industrial Textiles,* vol. 41, no. 3, pp. 201-221, 2011.
[37] J. E. Kirkwood, K. M. Kirkwood, Y. S. Lee, R. G. Egres, N. J. Wagner, and E. D. Wetzel, “Yarn Pull-Out as a Mechanism for Dissipating Ballistic Impact Energy in Kevlar® KM-2 Fabric: Part II: Predicting Ballistic Performance,” *Textile Research Journal,* vol. 74, no. 11, pp. 939-948, 2004.
[38] Y. Duan, M. Keefe, T. A. Bogetti, and B. A. Cheeseman, “Modeling friction effects on the ballistic impact behavior of a single-ply high-strength fabric,” *International Journal of Impact Engineering,* vol. 31, no. 8, pp. 996-1012, 2005.
[39] Y. Duan, M. Keefe, T. A. Bogetti, and B. A. Cheeseman, “Modeling the role of friction during ballistic impact of a high-strength plain-weave fabric,” *Composite Structures,* vol. 68, no. 3, pp. 331-337, 2005.

[40] Y. Duan, M. Keefe, T. A. Bogetti, and B. Powers, “Finite element modeling of transverse impact on a ballistic fabric,” *International Journal of Mechanical Sciences,* vol. 48, no. 1, pp. 33-43, 2006.
[41] C. Ha-Minh, F. Boussu, T. Kanit, D. Crépin, and A. Imad, “Effect of Frictions on the Ballistic Performance of a 3D Warp Interlock Fabric: Numerical Analysis,” *Applied Composite Materials,* vol. 19, no. 3, pp. 333-347, 2012.
[42] Y. Chu, S. Min, and X. Chen, “Numerical study of inter-yarn friction on the failure of fabrics upon ballistic impacts,” *Materials & Design,* vol. 115, pp. 299-316, 2017.
[43] T. G. Montgomery, P. L. Grady, and C. Tomasino, “The Effects of Projectile Geometry on the Performance of Ballistic Fabrics,” *Textile Research Journal,* vol. 52, no. 7, pp. 442-450, 1982.
[44] V. B. C. Tan, C. T. Lim, and C. H. Cheong, “Perforation of high-strength fabric by projectiles of different geometry,” *International Journal of Impact Engineering,* vol. 28, no. 2, pp. 207-222, 2003.
[45] C. T. Lim, V. B. C. Tan, and C. H. Cheong, “Perforation of high-strength double-ply fabric system by varying shaped projectiles,” *International Journal of Impact Engineering,* vol. 27, no. 6, pp. 577-591, 2002.
[46] M. De Araújo, "1 - Natural and man-made fibres: Physical and mechanical properties," *Fibrous and Composite Materials for Civil Engineering Applications*, R. Fangueiro, ed., pp. 3-28: Woodhead Publishing, 2011.
[47] G. Nilakantan, E. D. Wetzel, T. A. Bogetti, and J. W. Gillespie, “A deterministic finite element analysis of the effects of projectile characteristics on the impact response of fully clamped flexible woven fabrics,” *Composite Structures,* vol. 95, pp. 191-201, 2013.
[48] G. Nilakantan, E. D. Wetzel, T. A. Bogetti, and J. W. Gillespie, “Finite element analysis of projectile size and shape effects on the probabilistic penetration response of high strength fabrics,” *Composite Structures,* vol. 94, no. 5, pp. 1846-1854, 2012.
[49] G. Nilakantan, and J. W. Gillespie, “Yarn pull-out behavior of plain woven Kevlar fabrics: Effect of yarn sizing, pullout rate, and fabric pre-tension,” *Composite Structures,* vol. 101, pp. 215-224, 2013.
[50] D. Roylance, *Numerical analysis of projectile impact in woven texile structures*, Nasa Report CP-2017, 1977.
[51] D. Roylance, “Wave Propagation in a Viscoelastic Fiber Subjected to Transverse Impact,” *Journal of Applied Mechanics,* vol. 40, no. 1, pp. 143-148, 1973.
[52] D. Roylance, P. Hammas, J. Ting, H. Chi, and B. Scott, “Numerical modeling of fabric impact,” *ASME-PUBLICATIONS-AD,* vol. 48, pp. 155-160, 1995.
[53] D. Roylance, and S.-S. Wang, *Penetration mechanics of textile structures*, Massachusetts Inst of Tech Cambridge, 1979.
[54] D. Roylance, “Stress wave propagation in fibres: Effect of crossovers,” *Fibre Science and Technology,* vol. 13, no. 5, pp. 385-395, 1980.
[55] V. P. W. Shim, V. B. C. Tan, and T. E. Tay, “Modelling deformation and damage characteristics of woven fabric under small projectile impact,” *International Journal of Impact Engineering,* vol. 16, no. 4, pp. 585-605, 1995.
[56] C. T. Lim, V. P. W. Shim, and Y. H. Ng, “Finite-element modeling of the ballistic impact of fabric armor,” *International Journal of Impact Engineering,* vol. 28, no. 1, pp. 13-31, 2003.
[57] I. Ivanov, and A. Tabiei, “Loosely woven fabric model with viscoelastic crimped fibres for ballistic impact simulations,” *International Journal for Numerical Methods in Engineering,* vol. 61, no. 10, pp. 1565-1583, 2004.
[58] C. Ha-Minh, T. Kanit, F. Boussu, and A. Imad, “Numerical multi-scale modeling for textile woven fabric against ballistic impact,” *Computational Materials Science,* vol. 50, no. 7, pp. 2172-2184, 2011.
[59] C. Ha-Minh, A. Imad, T. Kanit, and F. Boussu, “Numerical analysis of a ballistic impact on textile fabric,” *International Journal of Mechanical Sciences,* vol. 69, pp. 32-39, 2013.

[60] B. Gu, “Ballistic Penetration of Conically Cylindrical Steel Projectile into Plain-woven Fabric Target – A Finite Element Simulation,” *Journal of Composite Materials,* vol. 38, no. 22, pp. 2049-2074, 2004.
[61] M. P. Rao, G. Nilakantan, M. Keefe, B. M. Powers, and T. A. Bogetti, “Global/Local Modeling of Ballistic Impact onto Woven Fabrics,” *Journal of Composite Materials,* vol. 43, no. 5, pp. 445-467, 2009.
[62] G. Nilakantan, M. Keefe, E. D. Wetzel, T. A. Bogetti, and J. W. Gillespie, “Computational modeling of the probabilistic impact response of flexible fabrics,” *Composite Structures,* vol. 93, no. 12, pp. 3163-3174, 2011.
[63] G. Nilakantan, M. Keefe, E. D. Wetzel, T. A. Bogetti, and J. W. Gillespie, “Effect of statistical yarn tensile strength on the probabilistic impact response of woven fabrics,” *Composites Science and Technology,* vol. 72, no. 2, pp. 320-329, 2012.
[64] G. Nilakantan, and J. W. Gillespie, “Ballistic impact modeling of woven fabrics considering yarn strength, friction, projectile impact location, and fabric boundary condition effects,” *Composite Structures,* vol. 94, no. 12, pp. 3624-3634, 2012.
[65] G. Nilakantan, and S. Nutt, “Effects of clamping design on the ballistic impact response of soft body armor,” *Composite Structures,* vol. 108, pp. 137-150, 2014.
[66] G. Nilakantan, and S. Nutt, “Effects of fabric target shape and size on the V50 ballistic impact response of soft body armor,” *Composite Structures,* vol. 116, pp. 661-669, 2014.
[67] G. Nilakantan, “Virtual microstructure generation using thermal growth: Case study of a plain-weave Kevlar fabric,” *Finite Elements in Analysis and Design,* vol. 147, pp. 21-33, 2018.
[68] R. Barauskas, and A. Abraitienė, “Computational analysis of impact of a bullet against the multilayer fabrics in LS-DYNA,” *International Journal of Impact Engineering,* vol. 34, no. 7, pp. 1286-1305, 2007.
[69] T. L. Chu, “Study of the mechanical behavior of a woven material subjected to a ballistic impact based on a multi-scale approach,” Phd Thesis, University of Lille, 2016.
[70] H. López-Gálvez, and X. Soldani, “Suitability of numerical model from low to high velocity impacts against KM2 fabrics with isotropic hypothesis,” *Composite Structures,* vol. 214, pp. 390-396, 2019.
[71] G. Zhou, X. Sun, and Y. Wang, “Multi-chain digital element analysis in textile mechanics,” *Composites Science and Technology,* vol. 64, no. 2, pp. 239-244, 2004.
[72] Y. Wang, Y. Miao, D. Swenson, B. A. Cheeseman, C.-F. Yen, and B. LaMattina, “Digital element approach for simulating impact and penetration of textiles,” *International Journal of Impact Engineering,* vol. 37, no. 5, pp. 552-560, 2010.
[73] A. H. M. Grujicic, B. Pandurangan, C.F. Yen, B.A. Cheeseman, Y. Wang, Y. Miao, J.Q. Zheng, “Fiber-Level Modeling of Dynamic Strength of Kevlar® KM2 Ballistic Fabric,” *J. of Materi Eng and Perform,* vol. 21, pp. 1107-1119, 2012.
[74] G. Nilakantan, “Filament-level modeling of Kevlar KM2 yarns for ballistic impact studies,” *Composite Structures,* vol. 104, pp. 1-13, 2013.
[75] S. Sockalingam, J. W. Gillespie, and M. Keefe, “Modeling the fiber length-scale response of Kevlar KM2 yarn during transverse impact,” *Textile Research Journal,* vol. 87, no. 18, pp. 2242-2254, 2016.
[76] P. del Sorbo, J. Girardot, F. Dau, and I. Iordanoff, “Numerical investigations on a yarn structure at the microscale towards scale transition,” *Composite Structures,* vol. 183, pp. 489-498, 2018.
[77] M. Cheng, W. Chen, and T. Weerasooriya, “Experimental investigation of the transverse mechanical properties of a single Kevlar® KM2 fiber,” *International Journal of Solids and Structures,* vol. 41, no. 22, pp. 6215-6232, 2004.
[78] E. M'Ewen, “XLI. Stresses in elastic cylinders in contact along a generatrix (including the effect of tangential friction),” *The London, Edinburgh, and Dublin Philosophical Magazine and Journal of Science,* vol. 40, no. 303, pp. 454-459, 1949.
[79] S. A. Jawad, and I. M. Ward, “The transverse compression of oriented nylon and polyethylene extrudates,” *Journal of Materials Science,* vol. 13, no. 7, pp. 1381-1387, 1978.

[80] Kawabata, “Measurement of the transverse mechanic properties of high-performance fibers,” *Journal of the Textile Insitute,* vol. 81, no. 4, pp. 432-447, 1990.
[81] J. Singletary, H. Davis, M. K. Ramasubramanian, W. Knoff, and M. Toney, “The transverse compression of PPTA fibers Part I Single fiber transverse compression testing,” *Journal of Materials Science,* vol. 35, no. 3, pp. 573-581, 2000.
[82] J. Singletary, H. Davis, Y. Song, M. K. Ramasubramanian, and W. Knoff, “The transverse compression of PPTA fibers Part II Fiber transverse structure,” *Journal of Materials Science,* vol. 35, no. 3, pp. 583-592, 2000.
[83] M. Cheng, W. Chen, and T. Weerasooriya, “Mechanical Properties of Kevlar® KM2 Single Fiber,” *Journal of Engineering Materials and Technology,* vol. 127, no. 2, pp. 197-203, 2005.
[84] S. Sockalingam, J. W. G. Jr., and M. Keefe, “Transverse compression behavior of Kevlar KM2 single fiber,” *Composites Part A 2016*, no. 81, pp. 271–281, 2016.
[85] C J Bourgoyne, and I. F. Brown, “Transverse properties of bulk aramid fibres,” *3rd Int. Symp. Non-Met. FRP Reinf. Concr. Struct. FRPRCS-3*, pp. 35-42, 1997.
[86] S. Sockalingam, J. W. G. Jr., and M. Keefe, “On the transverse compression response of Kevlar KM2 using fiber-level finite element model,” *International Journal of Solids and Structures*, no. 51, pp. 2504–2517, 2014.
[87] H. Lin, M. Sherburn, J. Crookston, A.C. Long, M.J. Clifford, and I. A. Jones, “Finite element modelling of fabric compression,” *Model. Simul. Mater. Sci. Eng,* vol. 16, pp. 16, 2008.
[88] J. M. Staniszewski, S. Sockalingam, T. A. Bogetti, and J. W. Gillespie, “Modeling the Fibrillation of Kevlar® KM2 Single Fibers Subjected to Transverse Compression,” *Fibers and Polymers,* vol. 19, no. 7, pp. 1479-1489, 2018.
[89] S. Kurukuri, and S. Eckardt, “A review of homogenization techniques for heterogeneous materials,” 2004.
[90] T. Kanit, S. Forest, I. Galliet, V. Mounoury, and D. Jeulin, “Determination of the size of the representative volume element for random composites: statistical and numerical approach,” *International Journal of Solids and Structures,* vol. 40, no. 13-14, pp. 3647-3679, 2003.
[91] P. R. Budarapu, X. Zhuang, T. Rabczuk, and S. P. A. Bordas, "Chapter One - Multiscale modeling of material failure: Theory and computational methods," *Advances in Applied Mechanics*, M. I. Hussein, ed., pp. 1-103: Elsevier, 2019.
[92] L. Qi, W. Tian, and J. Zhou, “Numerical evaluation of effective elastic properties of composites reinforced by spatially randomly distributed short fibers with certain aspect ratio,” *Composite Structures,* vol. 131, pp. 843-851, 2015.
[93] S. Saeb, P. Steinmann, and A. Javili, “Aspects of Computational Homogenization at Finite Deformations: A Unifying Review From Reuss' to Voigt's Bound,” *Applied Mechanics Reviews,* vol. 68, no. 050801, 2016.
[94] R. Hill, “Elastic properties of reinforced solids: Some theoretical principles,” *Journal of the Mechanics and Physics of Solids,* vol. 11, no. 5, pp. 357-372, 1963.
[95] Z. Hashin, “The Elastic Moduli of Heterogeneous Materials,” *Journal of Applied Mechanics,* vol. 29, no. 1, pp. 143-150, 1962.
[96] Z. Hashin, *Theory of mechanical behavior of heterogeneous media*, TOWNE SCHOOL OF CIVIL AND MECHANICAL ENGINEERING PHILADELPHIA PA, 1963.
[97] Z. Hashin, “Analysis of Composite Materials—A Survey,” *Journal of Applied Mechanics,* vol. 50, no. 3, pp. 481-505, 1983.
[98] K. Sab, “On the homogenization and the simulation of random materials,” *European journal of mechanics. A. Solids,* vol. 11, no. 5, pp. 585-607, 1992.
[99] M. Ostoja-Starzewski, “Random field models of heterogeneous materials,” *International Journal of Solids and Structures,* vol. 35, no. 19, pp. 2429-2455, 1998.
[100] K. Terada, M. Hori, T. Kyoya, and N. Kikuchi, “Simulation of the multi-scale convergence in computational homogenization approaches,” *International Journal of Solids and Structures,* vol. 37, no. 16, pp. 2285-2311, 2000.

[101] W. J. Drugan, and J. R. Willis, “A micromechanics-based nonlocal constitutive equation and estimates of representative volume element size for elastic composites,” *Journal of the Mechanics and Physics of Solids,* vol. 44, no. 4, pp. 497-524, 1996.
[102] M. Ostoja-Starzewski, “Microstructural Randomness Versus Representative Volume Element in Thermomechanics,” *Journal of Applied Mechanics,* vol. 69, no. 1, pp. 25-35, 2001.
[103] I. M. Gitman, H. Askes, and L. J. Sluys, “Representative volume: Existence and size determination,” *Engineering Fracture Mechanics,* vol. 74, no. 16, pp. 2518-2534, 2007.
[104] X.-Y. Zhou, X. Ruan, S. Zhang, W. Xiong, and Z. Ullah, “Design optimization for thermal conductivity of plain-woven textile composites,” *Composite Structures,* vol. 255, pp. 112830, 2021.
[105] J. Mandel, "Contribution théorique à l’étude de l’écrouissage et des lois de l’écoulement plastique," *Applied Mechanics*, pp. 502-509: Springer, 1966.
[106] C. Huet, “Application of variational concepts to size effects in elastic heterogeneous bodies,” *Journal of the Mechanics and Physics of Solids,* vol. 38, no. 6, pp. 813-841, 1990.
[107] S. Sádaba, M. Herráez, F. Naya, C. González, J. Llorca, and C. S. Lopes, “Special-purpose elements to impose Periodic Boundary Conditions for multiscale computational homogenization of composite materials with the explicit Finite Element Method,” *Composite Structures,* vol. 208, pp. 434-441, 2019.
[108] C. T. Sun, and R. S. Vaidya, “Prediction of composite properties from a representative volume element,” *Composites Science and Technology,* vol. 56, no. 2, pp. 171-179, 1996.
[109] V. Carvelli, and C. Poggi, “A homogenization procedure for the numerical analysis of woven fabric composites,” *Composites Part A: Applied Science and Manufacturing,* vol. 32, no. 10, pp. 1425-1432, 2001.
[110] X. Peng, and J. Cao, “A dual homogenization and finite element approach for material characterization of textile composites,” *Composites Part B: Engineering,* vol. 33, no. 1, pp. 45-56, 2002.
[111] L. Wang, B. Zhao, J. Wu, C. Chen, and K. Zhou, “Experimental and numerical investigation on mechanical behaviors of woven fabric composites under off-axial loading,” *International Journal of Mechanical Sciences,* vol. 141, pp. 157-167, 2018.
[112] Y.-T. Hwang, K.-H. Choi, J.-I. Kim, J. Lim, B. Nam, and H.-S. Kim, “Prediction of non-linear mechanical behavior of shear deformed twill woven composites based on a multi-scale progressive damage model,” *Composite Structures,* vol. 224, pp. 111019, 2019.
[113] M. Ostoja-Starzewski, “Material spatial randomness: From statistical to representative volume element,” *Probabilistic Engineering Mechanics,* vol. 21, no. 2, pp. 112-132, 2006.
[114] D. Beicha, T. Kanit, Y. Brunet, A. Imad, A. E. Moumen, and Y. Khelfaoui, “Effective transverse elastic properties of unidirectional fiber reinforced composites,” *Mechanics of Materials,* vol. 102, pp. 47-53, 2016.
[115] C. T. Herakovich, “Mechanics of composites: A historical review,” *Mechanics Research Communications,* vol. 41, pp. 1-20, 2012.
[116] A. Benhizia, T. Kanit, T. Outtas, S. Madani, and A. Imad, “Computation of effective behavior of isotropic transverse composite in nonlinear problems,” *Mechanics Research Communications,* vol. 59, pp. 6-13, 2014.
[117] Z. Hashin, “Failure Criteria for Unidirectional Fiber Composites,” *Journal of Applied Mechanics,* vol. 47, no. 2, pp. 329-334, 1980.